THE UNIVERSITY OF CHICAGO

QUANTUM SIMULATIONS FOR QUANTUM TECHNOLOGIES

A DISSERTATION SUBMITTED TO
THE FACULTY OF THE DIVISION OF THE PHYSICAL SCIENCES
IN CANDIDACY FOR THE DEGREE OF
DOCTOR OF PHILOSOPHY

DEPARTMENT OF CHEMISTRY

BY
BENCHEN HUANG

CHICAGO, ILLINOIS
JUNE 2024

To my family

CONTENTS

LIST OF FIGURES

LIST OF TABLES

ACKNOWLEDGMENTS

First and foremost, I would like to thank my advisor, Prof. Giulia Galli, for giving me the opportunity to pursue this research and looking after my development, both personally and academically, in countless ways. Anyone who has ever worked with Giulia will surely be impressed by her insightfulness and elegant work, so there is hardly a need for further elaboration. Suffice it to say that I consider myself fortunate to have joined the Galli group early on and spent many stimulating years basking in her positive presence. I truly cannot imagine a more fulfilling Ph.D. experience than under her mentorship.

My graduate years have also benefited from the wonderful scientific atmosphere created by the other members from the Galli group. I extend my heartfelt thanks to two instrumental mentors: Prof. Marco Govoni and Dr. He Ma, whose support and guidance shaped my early Ph.D. years. I am also grateful to Dr. Nan Sheng and Jonah Nagura, whose creative and collaborative spirit opened up my academic horizon. I would especially like to acknowledge Dr. Yu Jin, co-author with me on half of the works presented in this thesis. I have time and time been blown away by his broad knowledge and clarity of thought. I cannot imagine where the projects in this thesis would have ended up without his vital involvement.

I would like to thank many other external collaborators whose insights are imprinted upon this body of research. I am particularly grateful to Dr. Pra Bhattacharyya, Dr. Bryce Kobrin, Dr. Satcher Hsieh, Weijie Wu, Srinivas Mandyam, and Prof. Norman Yao for patiently sharing with me their knowledge of spin defects and high-pressure physics. I thank Zhongyuang Liu, Reginald Gong, and Prof. Chong Zu for providing their critical feedback on my simulations from an experimental perspective. I thank Dr. Xinghan Guo and Prof. Alex High for their careful verification of my theoretical predictions. I thank Senrui Chen and Prof. Liang Jiang for their generous help in solving my puzzles about quantum computing. I thank Dr. Ji Liu for our fully remote brainstorming on quantum error mitigation. Finally, I would like to thank Dr. Sam McArdle, Dr. Tim Chen, Dr. Brajesh Gupt, Anh Tran and Dr.

Martin Suchara for mentoring me during my internship at Amazon and ensuring that my academic training will be put to good use after graduation, especially Sam, who plays the role of my second research advisor in the past two years. I am looking forward to working with them for years to come!

My gratitude extends to the entire UChicago chemistry department for providing a vibrant academic community. I would like to thank my thesis committee members, Prof. David Mazziotti and Prof. David Awschalom for their wisdom and inspiration I have received. I would also like to thank Frank Gao, Guan Wang, Cheng Ji, Chris Chi, Nick Herringer, and the other members of my graduate cohort for keeping my life balanced and playing soccer on weekends.

Looking back, I would like to acknowledge many other encouraging figures from my undergraduate days in Nankai and during my exchange in Minnesota. I am indebted to Prof. Don Truhlar for providing me with my first taste for research and exemplifying for me what it means to be a great scientist. I thank the members of the Truhlar group at that time, especially Dr. Sijia Dong (with whom I re-unite again later in Chicago), Dr. Jie Bao, Dr. Bo Yang, and Dr. Zoltán Varga, for their patience and mentorship as I fumbled my way through the early stages of research. I thank my professors, Zhenfeng Shang, Ruifang Li, and Hongwei Sun, for guiding me through my undergraduate years and giving me the confidence to pursue graduate school. Particularly, I appreciate the friendship with Sylvia Bintrim, my acquaintance with who magically started in Minnesota and then revived in Chicago, and has helped me navigate through the stressful days of my Ph.D.

Above all, I am grateful for the loving support I have received from my family, as I have spent many years chasing my dreams. Despite always being faced with unrealistic dreams of their son, my parents have consistently encouraged me to follow my heart and provided me with every conceivable opportunity for success. I hope they forgive me for not being able to visit them back in China in the past 5 years.

ABSTRACT

Recent years have witnessed exponential growth in the development of quantum technologies for computation, sensing, and communication. Much of this progress stems not only from new experimental fabrication and characterization tools but also from a better and deeper theoretical understanding of hardware platforms. In particular, ab initio calculations can be used to predict materials' properties and even guide experimental realizations of more advanced quantum technologies. This dissertation explores the interplay between theory, first-principles calculations, and experiments for quantum technology applications, with a particular emphasis on solid-state spins. We address several questions: What makes solid-state spins better quantum sensors than their classical counterparts? How can we interpret the response of spin defects to environmental perturbations? From a complementary perspective, how can we harness the power of quantum computation to improve the prediction of properties of solid-state spins? By investigating these questions, this dissertation sheds light on connecting a rich variety of topics—including electronic structure theory, condensed matter physics, and quantum information science. More broadly, it showcases first-principle simulations as powerful frameworks for guiding our exploration of quantum physics.

CHAPTER 1

INTRODUCTION

This dissertation introduces efforts in realizing quantum technologies, ranging from sensing, and communication to computing from a computational perspective. In this Chapter, we start by introducing the potential benefits of quantum technology applications and describe the status of their realizations using various platforms. We then focus on one specific realization, e.g., spin qubits, which are widely acknowledged as promising candidates for quantum sensing and communication. We further introduce the theoretical foundation for first-principle simulations, which serves as the working horse for all the works presented in this dissertation.

In Chapter 2, we investigate the negatively charged nitrogen-vacancy (NV) center in diamond, as a high-pressure quantum sensor. We combine computational condensed matter and computational chemistry methods to accurately estimate the intersystem crossing rates under various stress conditions at room temperature. Finally, we employ a rate model to simulate the optically detected magnetic resonance (ODMR) spectrum and predict the optimal NV orientation for sensing purposes.

In Chapter 3, we study the temperature dependence of the spin properties, e.g., zero-field splitting (ZFS) tensor and the hyperfine tensor, of the negatively charged boron vacancy (V_B^-) in hexagonal boron nitride with different isotopes. We pinpoint its microscopic origin to second-order spin-phonon coupling and identify representative phonon modes responsible for its spin properties and also spin relaxation time T_1. The experiments suggest that this defect would be a perfect candidate for temperature sensing.

In Chapter 4, we predict the strain-dependent energy susceptibilities of the Tin-vacancy in diamond, which stands out among all the group IV vacancies as a promising candidate for quantum communications. Strain turns out to be a viable solution to greatly extend its coherence time.

In Chapter 5, we switch gears and discuss quantum computations. Our discussion includes working knowledge of quantum operations/gates, circuits, and measurements, which is crucial for understanding quantum algorithms, and in seeking the ultimate goal of realizing quantum advantages over classical computations.

Chapters 6-8 summarize our efforts in performing proof of principle simulations of both molecular and solid-state systems on near-term quantum computers. We improve state-of-the-art fermion-to-qubit mapping and circuit design for solving the eigenvalue problem in the context of electronic structure and develop various noise mitigation techniques to mitigate hardware errors.

Finally, Chapter 9 provides a summary of all my work presented in this dissertation.

1.1 Where do we stand with quantum technologies?

The last century witnessed the revolution of information technologies based on semiconductors. Smartphones and personal computers, which significantly transformed our lives are all built on "bits" to store and transmit information. For communication technologies, bits are encoded in electromagnetic waves. In computer memories, bits are magnetic domains on a ferromagnet. These bits encode information in binary form, and combined with simple Boolean logical operations, they can process complicated computational functions.

Despite amazing achievements, the information technology built on bits also faces some fundamental limits. For example, classical sensing is limited by the sensitivity/resolution of sensors and the scale they can probe. Classical communication is constantly threatened by hackers and requires better encryption. Classical computation is cursed by the exponential scaling of many existing algorithms for certain problems and thus requires an exponentially increasing number of resources to solve these problems. We also witnessed in recent years a steady deviation from Moore's law [313]. These limitations and obstacles faced by classical information technology triggered the investigation of quantum technologies, for example based on spin-qubits.

Spin is an intrinsic property of quantum objects related to their angular momentum. Different particles could have different spins. Fermions, e.g., electrons and protons, have half-integer spins while bosons, e.g., photons and phonons have integer spins. Quantum systems that can be in one of two quantum states are the analog of systems that can make a "bit". These quantum bits or "qubits" are not always in a definite $|0\rangle$ or $|1\rangle$ state, but they can be in an arbitrary superposition state $|\psi\rangle = \alpha|0\rangle + \beta|1\rangle$. It turns out that, as we'll discuss in more detail later, using these qubits to build information technologies has great potential to solve many problems we're facing today.

1.1.1 Quantum sensing

The microscopic world is properly described by quantum mechanics. As such, exquisite control and readout of qubit states could provide a window into the qubit's surrounding environment. Furthermore, entangled quantum states have phases sensitive to external perturbations. Translating these phases into variations in the amplitudes of qubit readout allows for the design of readout procedures and sensing capabilities [73]. In particular, qubits with narrow transitions allow for small changes to be detected. Sometimes one reads that "A bad qubit is a good sensor", which illustrates the need for a qubit to couple well enough with the environment to detect the specific degree of freedom while reducing its coherence. The applications of quantum sensing are wide-ranging, from nanoscale bio-sensing [15], probing phase transition of condensed matter [138], transport phenomenon on surfaces [194], and dark matter detection [49]. Strictly speaking, quantum sensing has already entered our lives! A magnetic resonance imaging (MRI) scan in a hospital is a rudimentary quantum sensing technology that performs electron spin manipulation and measures the relaxation and coherence of the hydrogen spins in our body. As you can tell, the definition of what is a quantum sensor may greatly vary.

Unlike quantum computation, which is going to be introduced below, quantum sensing doesn't typically require a large number of qubits, error correction, or even fancy algorithms. As such, there are already many near-term technologies to realize it. One important example is the superconducting quantum interference device (SQUID) detectors/magnetometers. More related to this dissertation, solid-state spins are excellent quantum sensors and have been used as gyroscopes and as nanoscale sensors of temperature [107], stress [138], electrical [166] and magnetic fields [119] even in living organisms [246].

1.1.2 Quantum communication

In a classical communication channel, an eavesdropper can tap off a tiny fraction of the communications signal and listen in. However, quantum communication can prevent that from happening. The reason is i). observing quantum states necessarily collapses them to eigenstates; ii). the "no cloning" theorem prevents making copies of quantum states. The net result is that quantum communication can be used to create a key for encryption that is secured by the law of quantum physics. Interestingly, quantum technologies provide a double-edged sword for security. Quantum computers, as will be discussed later, can break the (classical) encryption we all use today, but on the other hand, quantum communications provide us with a new way to ensure information security. These quantum communication channels are commonly achieved using telecommunication fibers which offer low signal loss around 1550 nm of light [186]. Quantum communications can also be achieved with free space optics: entangled particles have even been sent from a "quantum satellite" hundreds of kilometers above the earth to two telescope-based ground stations [340].

Current efforts to build quantum networks have achieved major advances [289, 323], but lack one key component: a quantum memory. Entangled particles can be distributed to different stations, where the entanglement can be verified by measurement. However, the distributed entanglement cannot be stored without a memory. Holding onto entanglement is necessary to send quantum states over long distances and to generate entanglement over many nodes. Sending an information-encoded photon through practical distances, e.g., from Chicago to Beijing, requires a quantum memory to keep the quantum information on the order of milliseconds [20], which is beyond the coherence time of most qubit candidates. Systems that have interfaces to photons but have long-lived quantum memories are then ideal candidates. The system investigated in Chapter 4 of this dissertation provides one such candidate.

1.1.3 Quantum computing

Quantum computers are perhaps the most well-known quantum technology. The pursuit of a quantum computer today can be dated back to Richard Feynman, who said back in the 1980s: “Nature isn’t classical, dammit, and if you want to make a simulation of nature, you’d better make it quantum”. Although originally proposed for analog simulations of quantum systems, several problems beyond the pure domain of quantum mechanics have been identified where quantum computers can provide an exponential/polynomial advantage over the classical hardware [113, 163, 288]. We’ll discuss the topic of quantum simulations for Fermionic systems in more detail in Chapter 5. However, it’s worth emphasizing that quantum computers will not improve every aspect of our lives! They only perform certain problems better than their classical counterparts.

The major issues in building a quantum computer lie in scaling to large qubit numbers while keeping errors within a threshold, reaching better connectivity, longer coherence times, finer control, and more accurate calibration, among others. A metric often quoted is “quantum supremacy/advantage”, which is the critical point where a quantum computer performs a task that is not possible to perform efficiently on any classical machines. Claims of quantum supremacy have been made [11] and later disputed [243], along with arguments about the proper metrics to aim for measuring the performance of a quantum computer.

That being said, quantum computers (based on superconducting technology) are already being developed commercially. The solid-state spin systems on which we focus on in this dissertation, however, cannot (at least for the moment) scale to the qubit number needed for useful computations.

1.2 Why spin qubits?

As we learned from the previous sections, a qubit could be built from any two-level system (TLS). In general, systems for quantum computation and communications need to meet the so-called DiVincenzo's criteria [75]. There are a few candidate platforms, e.g., superconducting circuits [172], trapped ions [41], neutral atoms [127], quantum dots [198], spin defects [335], etc., that are considered promising for realizing quantum technologies. These candidates typically have more than two levels, but as long as two levels can be well separated in energy, they may be good candidates. Most of these candidate systems have demonstrated excellent single-qubit control, but the major difference in maturity lies in two-qubit gates and scaling, with other differences being operation temperature and initialization and readout schemes.

In this dissertation, we mainly focus on employing defects in wide band-gap semiconductors for quantum technologies. Strictly speaking, no crystal is exactly perfect and is always riddled with defects. These defects can range from mesoscopic defects such as domain walls, stacking faults, and screw dislocations to individual single missing atoms or substitutional impurities in the crystal structure. For quantum technologies, it turns out that the second type of defects, e.g., single vacancy, impurity along with vacancy-impurity or vacancy-vacancy complexes at the atomic scale, offers the best opportunities.

Point defects in semiconductor and insulators can exhibit single-particle levels inside the band gap of the hosting material. Proper charge states of defects can be tuned or controlled by doping the material. Furthermore, certain defects can be "optically active" and are typically called “color centers”. These color centers cause absorption and emission (within the defect levels) in the semiconductor that differs from what is expected from the crystal alone, giving rise to specific color. These optical transitions are useful for controlling qubits. The interest this dissertation is in optically active color centers.

In general, spin defects may display long coherence times, i.e., spin-phonon relaxation time T_1 and spin-spin relaxation time T_2, up to milli-seconds [24, 130]. With some systems displaying nanoscale and room temperature operation, they are good quantum sensors and communicators but are harder to scale into quantum computers.

1.3 Theoretical background of first-principle simulations

In this section, we provide the theoretical background for the first-principle calculations we're going to use throughout this dissertation.

1.3.1 Born-Oppenheimer approximation

The behavior of a microscopic system, i.e., molecules or solids, consisting of N_{el} electrons and N_{nuc} nuclei, is described by the many-body Schrodinger equation $\hat{H}|\Phi_{\mathrm{tot}}\rangle = E_{\mathrm{tot}}|\Phi_{\mathrm{tot}}\rangle$, where E_{tot}, $|\Phi_{\mathrm{tot}}\rangle$ is the eigenvalue and eigenvector, respectively, and $\hat{H}$ is the Hamiltonian under the non-relativistic approximation $\hat{H} = \hat{T}_{\mathrm{N}} + \hat{T}_{\mathrm{e}} + \hat{U}_{\mathrm{e-e}} + \hat{U}_{\mathrm{e-N}} + \hat{U}_{\mathrm{N-N}}$. Here $\hat{U}_{\mathrm{e-e}}$, $\hat{U}_{\mathrm{e-N}}$, and $\hat{U}_{\mathrm{N-N}}$ represent the electron-electron, electron-nuclei, nuclei-nuclei Coulomb interactions, which are defined as $U_{\mathrm{e-e}}(\{\mathbf{r}\}) = \sum_{i<j}^{N_{\mathrm{el}}} \dfrac{1}{|\mathbf{r}_i - \mathbf{r}_j|}$, $U_{\mathrm{e-N}}(\{\mathbf{r}\},\{\mathbf{R}\}) = -\sum_{i=1}^{N_{\mathrm{el}}} \sum_{I=1}^{N_{\mathrm{nuc}}} \dfrac{Z_I}{|\mathbf{r}_i - \mathbf{R}_I|}$, $U_{\mathrm{N-N}}(\{\mathbf{R}\}) = \sum_{I<J}^{N_{\mathrm{nuc}}} \dfrac{Z_I Z_J}{|\mathbf{R}_I - \mathbf{R}_J|}$. Here, $\{\mathbf{r}\}$ and $\{\mathbf{R}\}$ represent coordinates of all electrons and nuclei, respectively. $\hat{T}_{\mathrm{N}}$ and $\hat{T}_{\mathrm{e}}$ are the kinetic operators of nucleus and electron. Since the mass of the nucleus is at least 3 orders of magnitude larger than the mass of the electron, the motion of the nucleus is much slower than that of the electrons. We can therefore treat $\hat{T}_{\mathrm{N}}$ as a perturbation. Under the zeroth-order approximation,

the Schrodinger equation for electrons reduces to

$$\hat{H}_{\rm el}(\{\mathbf{R}\})|\Psi_i(\{\mathbf{R}\})\rangle = E_i(\{\mathbf{R}\})|\Psi_i(\{\mathbf{R}\})\rangle, \tag{1.1}$$

where $\hat{H}_{\rm el}(\{\mathbf{R}\}) = \hat{T}_{\rm e} + \hat{U}_{\rm e-e} + \hat{U}_{\rm e-N} + \hat{U}_{\rm N-N}$ is the Hamiltonian of electrons which depends on the nuclear coordinates $\{\mathbf{R}\}$, and $E_i(\{\mathbf{R}\})$ is the energy of the many-electron state $|\Psi_i(\{\mathbf{R}\})\rangle$.

In the coordinate representation, for given nuclear coordinates $\{\mathbf{R}\}$, the total wavefunction $\Phi_{\rm tot}(\{\mathbf{r}\}, \{\mathbf{R}\})$ can be expanded using $\{\Psi_i(\{\mathbf{r}\}, \{\mathbf{R}\})\}$ as basis functions $|\Phi_{\rm tot}\rangle = \sum_i |\Theta_i\rangle|\Psi_i\rangle$, which is called Born-Oppenheimer expansion [37]. $|\Theta_i\rangle$ can be computed by solving the eigenvalue equation

$$\left[\hat{T}_{\rm N} + E_i(\{\mathbf{R}\})\right]|\Theta_i\rangle - \sum_j \hat{\Lambda}_{ij}|\Theta_j\rangle = E_{\rm tot}|\Theta_i\rangle, \tag{1.2}$$

where $\hat{\Lambda}_{ij}$ is the nonadiabatic coupling operator. By assuming that the coupling terms $\hat{\Lambda}_{ij}$ are approximately zero, we arrive at the Born-Oppenheimer adiabatic approximation

$$\left[\hat{T}_{\rm N} + E_i(\{\mathbf{R}\})\right]|\Theta_i\rangle = E_{\rm tot}|\Theta_i\rangle. \tag{1.3}$$

Here, $E_i(\{\mathbf{R}\})$ is the i-th adiabatic potential energy surface (PES), which can be obtained by solving Eq 1.1, the Schrodinger equation for the electrons, at fixed nuclear coordinates $\{\mathbf{R}\}$. Within the Born-Oppenheimer approximation, nuclei move on adiabatic PES.

1.3.2 Density Functional Theory (DFT)

DFT is probably the most widely applied electronic structure theory so far. The seminal work by Hohenberg and Kohn demonstrated [137] that all the ground and excited state properties of a system of interacting electrons are completely determined by its ground state electron density and that the ground state electron density can be obtained by minimizing the total energy functional:

$$E[n] = \int V_{\text{ext}}(\mathbf{r})n(\mathbf{r})d\mathbf{r} + F[n] \tag{1.4}$$

where $F[n]$ is a universal functional of the electron density n. Most DFT calculations performed today are based on the Kohn-Sham scheme [169], which casts the solution of the above equation into the solution of the Kohn-Sham equation $\hat{H}_{\text{KS}}|\phi_i\rangle = \varepsilon_i|\phi_i\rangle$. The Kohn-Sham equation is a Schrodinger equation for independent electrons with density equal to that of the physical system, governed by the Hamiltonian $\hat{H}_{\text{KS}} = \hat{T} + \hat{V}_{\text{ion}} + \hat{V}_H + \hat{V}_{\text{xc}}$, where $\hat{T}$ denotes the kinetic energy operator and $\hat{V}_{\text{ion}}, \hat{V}_H, \hat{V}_{\text{xc}}$ denote ionic, Hartree and exchange-correlation potential, respectively. The exchange-correlation potential $\hat{V}_{\text{xc}}$ is defined as the functional derivative of the so-called exchange-correlation functional E_{xc} with respect to electron density n $\hat{V}_{\text{xc}} = \frac{\delta E_{\text{xc}}[n]}{\delta n}$.

The exact form of the exchange-correlation functional is unknown, and approximate forms are required to perform practical DFT calculations. The development of exchange-correlation functionals is one of the central topics of DFT research. In the past decades, more than 200 approximate forms of E_{xc} has been proposed, which are sometimes classified using the Jacob's ladder for DFT. The first rung of the Jacob's ladder denotes the local density approximation (LDA), where E_{xc} is a functional of the electron density only. Higher rungs of Jacob's ladder correspond to more sophisticated functionals where E_{xc} depends also on derivatives of the electron density and contains non-local terms derived from wavefunction theory.

DFT is a mean-field theory. The Kohn-Sham formulation of DFT solves the Kohn-Sham equation that describes the Kohn-Sham reference system of non-interacting electrons, and yields the exact energy and electron density of the system if the exact exchange-correlation functional were used. The eigenvalues and eigenvectors of the Kohn-Sham reference system, in principle, do not have any physical meaning. In practical calculations, however, one often associates Kohn-Sham eigenvalues and their differences to various excitation energies of the physical system, which in many cases lead to reasonable predictions and provide valuable insights to the physical system. However, such association is not theoretically rigorous, and by using it one is attaching physical meaning to the mean-field solutions of the Kohn-Sham reference system.

1.3.3 Fermi's golden rule

In studying spin defects, we're not only interested in the eigenvalues and eigenstates of their time-independent Hamiltonian but also in dynamical properties, e.g., various transition rates, since the spin defects need to be operated to perform sensing and communication tasks. In general conceptual terms, a transition rate depends upon the strength of the coupling between the initial and final state of a system and upon the number of ways the transition can happen (i.e., the density of the final states). The Fermi's golden rule is a formula that describes the transition rate from one energy eigenstate of a quantum system to a number of energy eigenstates in a continuum, as a result of a weak perturbation. This transition rate is effectively independent of time, as long as the strength of the perturbation is independent of time, and is proportional to the strength of the coupling between the initial and final states of the system, as well as the density of states.

CHAPTER 2

ELUCIDATING THE ELECTRON PARAMAGNETIC RESONANCE OF NITROGEN-VACANCY CENTERS UNDER MEGABAR PRESSURE

This chapter is in part adapted with permission from P. Bhattacharyya, W. Chen, X. Huang, S. Chatterjee, **B. Huang**, B. Kobrin, Y. Lyu, T. Smart, M. Block, E. Wang, Z. Wang, W. Wu, S. Hsieh, H. Ma, S. Mandyam, B. Chen, E. Davis, Z. Geballe, C. Zu, V. Struzhkin, R. Jeanloz, J. Moore, T. Cui, G. Galli, B. Halperin, C. Laumann, N. Yao. Nature (2024): 1-7. Copyright (2024) by Springer Nature. https://doi.org/10.1038/s41586-024-07026-7. It also contains content from **B. Huang**, S. Mandyam, B. Kobrin, P. Bhattacharyya, W. Wu, Y. Jin, M. Block, E. Wang, Z. Wang, B. Chen, C. Zu, N. Yao, and G. Galli. "Elucidating the optically detected magnetic resonance of nitrogen-vacancy centers under megabar pressure" (in preparation, 2024).

By directly altering microscopic interactions, pressure provides a powerful tuning knob for the exploration of condensed phases and geophysical phenomena [209]. The megabar regime represents an exciting frontier, where recent discoveries include novel high-temperature superconductors, as well as structural and electronic phase transitions [199, 333]. However, at such high pressures, many conventional measurement techniques fail. Recently, Bhattacharyya et al. [35] have demonstrated the ability to perform local magnetometry inside of a diamond anvil cell with sub-micron spatial resolution at megabar pressures. This approach utilizes a shallow layer of Nitrogen-Vacancy (NV) color centers implanted directly within the anvil [138, 183, 300]; crucially, a crystal cut compatible with the intrinsic symmetries of the NV center is chosen to enable functionality at megabar pressures. A recently discovered hydride superconductor, CeH_9 [55] has also been characterized by this newly developed tool.

2.1 Introduction

The recent proliferation of work on superhydride materials—hydrogen-rich compounds containing rare-earth or actinide elements—is part of a long-standing search for superconductivity at room temperature [79, 80, 205]. The intuition underlying this search dates back nearly half a century [13]: hydrogen's minimal mass and covalent bonding lead to the presence of both high-frequency phonons and strong electron-phonon interactions. The combination of these features is predicted to favor the formation of Cooper pairs, and thus superconductivity, at relatively high temperatures [14]. This strategy has been fruitful, leading to the discovery and characterization of nearly a dozen superconducting hydrides in the last decade [190, 328]. The synthesis of these materials relies upon the application of megabar (~ 100 GPa) pressures using diamond anvil cells (DACs). This requirement naturally constrains the size and homogeneity of the samples, significantly complicating attempts at *in situ* characterization. For example, it is extremely challenging for conventional probes to image the geometry of superconducting grains or to measure local properties.

This challenge is particularly acute for studying the magnetic signatures of superconductivity [90, 135]. Typical probes of magnetism average over the entire DAC geometry thereby discarding information encoded in local spatial features. The ability to perform spatially-resolved magnetometry near the hydride sample would overcome these challenges and enable both enhanced field sensitivities, as well as local measurements of the Meissner effect and flux trapping. Doing so together with resistance measurements would allow one to simultaneously probe the key electrical and magnetic signatures of superconductivity.

In Ref. [35], Bhattacharyya et al. developed a novel platform for metrology at megabar pressures based upon the nitrogen-vacancy (NV) color center in diamond [138, 183, 300, 341]. By instrumenting diamond anvils with shallow ensembles of NV centers, they directly imaged both the local diamagnetic response and flux trapping with sub-micron resolution in a cerium superhydride (CeH_9). Specifically, by utilizing NVs embedded in a [111]-crystal cut anvil

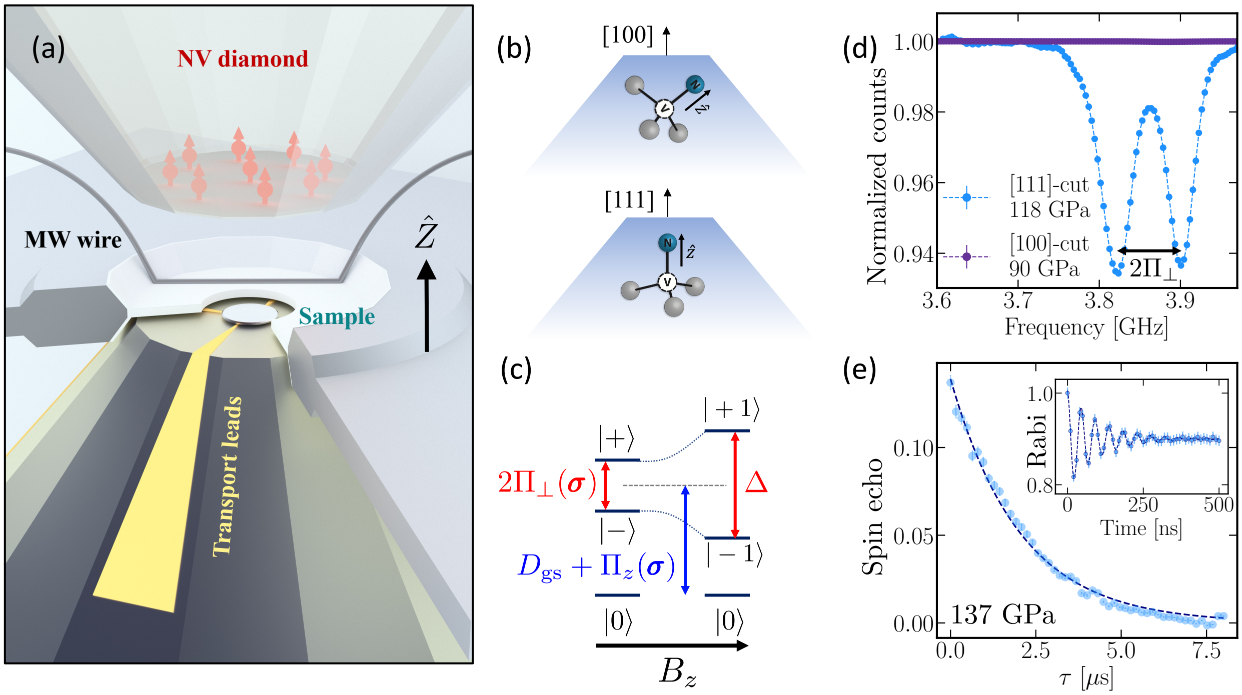

Figure 2.1: **NV sensing at megabar pressures.** **(a)** Schematic of the sample loading showing CeH_9 compressed between two opposing anvils. The top anvil contains a shallow layer of NV centers ($\sim$ 1 ppm density) approximately 50 nm below the culet surface. For ODMR measurements, a platinum wire is placed on the top culet to deliver microwaves. **(b)** The quantization axis ($\hat{z}$) of the NV center defines its local frame. The crystal cut of the diamond anvil determines the projection of culet stresses in the NV frame. For a [100]-cut anvil (top), the dominant culet stresses (σ_{ZZ} and $\sigma_\perp$) break the C_{3v}-symmetry of all four NV subgroups. For a [111]-cut anvil (bottom), these stresses preserve the C_{3v}-symmetry of the specific NV subgroup whose quantization axis is coincident with the loading axis (shown). For this particular NV subgroup, we observe excellent ODMR contrast up to pressure of $\sim$ 140 GPa. **(c)** Schematic depiction of the NV's spin sublevels in the presence of stress and magnetic field. Symmetry preserving stresses, quantified by Π_z, directly add to the zero field splitting, D_{gs}, while symmetry breaking stresses induce a splitting, $2\Pi_\perp$. An axial magnetic field B_z induces a Zeeman splitting that adds in quadrature to the stress splitting. **(d)** A continuous wave ODMR measurement on a [111]-cut anvil (sample S1) showing $\sim 6\%$ contrast at $\approx$ 118 GPa and a splitting, $2\Pi_\perp \sim (2\pi) \times 78$ MHz (blue data points). For comparison, the ODMR contrast in a [100]-cut anvil at $\approx$ 90 GPa is $\sim 0.01\%$ (purple data points). **(e)** A spin echo (i.e. pulsed) measurement on sample S2 at 137 GPa yields an NV coherence time, $T_2^{\mathrm{echo}} = 2.04(4)$ µs. We demonstrate Rabi frequencies of up to $\sim (2\pi) \times 25$ MHz (inset).

[Fig. 2.1], they demonstrated the ability to perform both DC and AC magnetometry at pressures up to $\sim$ 140 GPa.

The extension of NV sensing to megabar pressures has been a long-standing challenge due to several factors: reduction in NV fluorescence, inhomogeneous broadening of ODMR spectra, and significant loss of ODMR contrast [65, 77]. We compare NV measurements under pressure for [100]-cut and [111]-cut anvils, shown in Fig. 2.2. We refer to the lab frame by $\{X, Y, Z\}$ where Z is the loading axis, and to the local frame of the NV subgroups by $\{x, y, z\}$. For the [100]-cut anvil, Ref. [35] observed a significant loss in the ODMR contrast with increasing pressure as shown in Fig. 2.2(a). In addition, at pressures above ~ 50 GPa, they observed a surprising inversion of ODMR contrast for one of the resonances shown in Fig. 2.2(b). However, for the [111]-cut anvil, neither of these effects is observed. Notably, for this anvil cut, the ODMR contrast at pressures up to ~ 140 GPa remains comparable to that typically achieved under ambient conditions as shown in Fig. 2.2(d).

A microscopic understanding of the observed changes in the ODMR contrast requires a careful analysis of the NV center's ISC mechanism in the presence of stress [101]. In this work, we develop a physical model of the ODMR experiment based on group theory analysis and perturbation theory. Combining with parameters computed from ab initio calculations, we're able to explain the observed contrast change under various stress conditions.

2.2 Theory of NV's optical cycle

The NV center in diamond is a crystallographic defect comprising a substitutional nitrogen atom adjacent to a lattice vacancy [76]. The electronic ground state of the negatively charged NV center is a spin triplet ($S = 1$). In the absence of external perturbations, the ground-state spin Hamiltonian is given by $H = D_{\mathrm{gs}} S_z^2$, where $D_{\mathrm{gs}} = (2\pi) \times 2.87$ GHz is a temperature-dependent zero-field splitting between the $|m_{\mathrm{s}} = 0\rangle$ spin sub-level and the degenerate $|m_{\mathrm{s}} = \pm 1\rangle$ spin sub-levels, and $\{S_x, S_y, S_z\}$ are spin-1 operators quantized along the NV axis (z). While for the (triplet) excited state, the Hamiltonian becomes much more

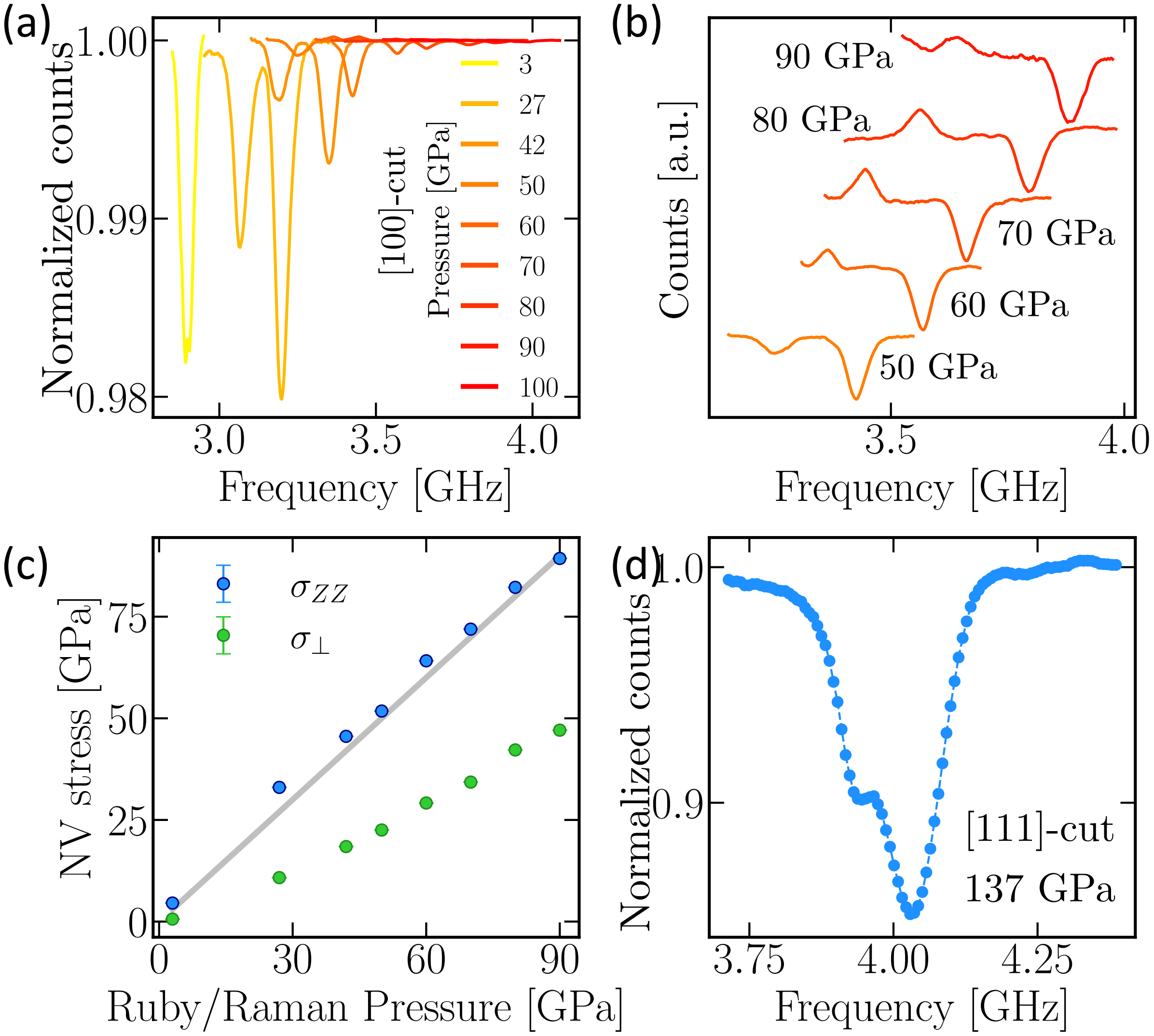

Figure 2.2: **Pushing NV sensing to megabar pressures.** **(a)** ODMR measurements under pressure in a [100]-cut anvil exhibit a drastic reduction in contrast with increase in pressure. The dominant culet stresses $\{\sigma_{ZZ}, \sigma_{\perp}\}$ have degenerate symmetry-preserving and symmetry-breaking projections on each NV subgroup, thereby inducing both a shift, Π_z, and a splitting, $2\Pi_{\perp}$, with increasing pressure. **(b)** In a [100]-cut anvil, we see a surprising inversion of contrast for one of the ODMR peaks at pressures above $\sim$ 50 GPa. **(c)** In a [100]-cut anvil, we see good agreement between the values of the loading stress σ_{ZZ} extracted from NV measurements (blue points) and values of the sample pressure calibrated via a combination of ruby and culet Raman spectra [7, 307]. For comparison, $x = y$ line is plotted in grey. We also measure an increase in the $\sigma_{\perp}$ stress (green points) consistent to cupping of the diamond culet [184]. **(d)** In a [111]-cut culet, we show $\sim$ 15% contrast at 137 GPa pressure for the [111] NV subgroup.

complicated and the effect of spin-orbit coupling (SOC) can't be ignored. We have

$$H_{\mathrm{soc}} = \lambda_z L_z S_z + \lambda_\perp \left(L_x S_x + L_y S_y \right), \tag{2.1}$$

where $\lambda_z, \lambda_\perp$ are the diagonal and transverse SOC due to the $\mathrm{C_{3v}}$-symmetry of the system and L, S are the NV's orbital and spin angular momentum operators. The quantization axis may be oriented along any of the diamond bonds resulting in four subgroups of NV centers. A magnetic field $\vec{B}$ couples with the Hamiltonian $H_B = \gamma_B \vec{B} \cdot \vec{S}$, where $\gamma_B = (2\pi) \times 2.8$ MHz/G is the NV's gyromagnetic ratio and $\vec{B}$ is expressed in the local frame of the NV center [76, 212].

A stress tensor, $\boldsymbol{\sigma}$, couples with the Hamiltonian [26, 138],

$$H_{\mathrm{s}} = \Pi_z S_z^2 + \Pi_x (S_y^2 - S_x^2) + \Pi_y (S_x S_y + S_y S_x), \tag{2.2}$$

where $\Pi_i = \Pi_i(\boldsymbol{\sigma})$ are functions of the stress tensor:

$$\Pi_z = \alpha_1 \left(\sigma_{xx} + \sigma_{yy}\right) + \beta_1 \sigma_{zz} \tag{2.3}$$

$$\Pi_x = \alpha_2 \left(\sigma_{yy} - \sigma_{xx}\right) + \beta_2 \left(2\sigma_{xz}\right) \tag{2.4}$$

$$\Pi_y = \alpha_2 \left(2\sigma_{xy}\right) + \beta_2 \left(2\sigma_{yz}\right) \tag{2.5}$$

and they are expressed in terms of the stress components in the NV's local frame. Here, $\{\alpha_1, \beta_1, \alpha_2, \beta_2\} = (2\pi) \times \{8.6(2), -2.5(4), -1.95(9), -4.50(8)\}$ MHz/GPa are the stress susceptibilities. Stress components that preserve the $\mathrm{C_{3v}}$-symmetry of the NV center maintain the degeneracy of the $|m_{\mathrm{s}} = \pm 1\rangle$ spin-sublevels and induce an overall energy shift of Π_z. Stress components that break $\mathrm{C_{3v}}$-symmetry lift the degeneracy between the $|m_{\mathrm{s}} = \pm 1\rangle$ spin-sublevels and induce a splitting $2\Pi_\perp = 2\sqrt{\Pi_x^2 + \Pi_y^2}$. In addition, symmetry breaking stress components mix the $|m_{\mathrm{s}} = \pm 1\rangle$ states into eigenstates $|\pm\rangle = (|m_{\mathrm{s}} = 1\rangle \pm e^{i\phi_\Pi} |m_{\mathrm{s}} = -1\rangle)/\sqrt{2}$, where $\phi_\Pi = \arctan(\Pi_y/\Pi_x)$.

In the experiments, electronic transitions in the NV center were excited using laser light with wavelength $\lambda = 532$ nm. Radiative transitions involved in electronic excitation and fluorescent relaxation are spin-conserving processes [76, 101]. In addition to these radiative transitions, the NV center also shows a non-radiative inter-system crossing (ISC) mechanism, whereby the $|m_\text{S} = \pm 1\rangle$ spin sub-levels of the electronic excited state can transition into the singlet manifold. Further non-radiative relaxation from the singlet manifold back to the electronic ground state is not highly spin selective [76, 101]. This leads to two important consequences. First, it enables optical polarization to the $|m_\text{S} = 0\rangle$ spin sub-level under continuous laser excitation. Second, it causes a reduction in the fluorescence rates of the $|m_\text{S} = \pm 1\rangle$ spin sub-levels compared to the $|m_\text{S} = 0\rangle$ spin sublevel. Indeed, the signal contrast of an optical detected magnetic resonance (ODMR) measurement depends on the difference between the fluorescence intensity of these spin sub-levels. As we will discuss in the next section, the ISC mechanism — and thus the ODMR contrast — is sensitive to the applied stress and can be significantly altered at high pressures.

In addition to ODMR measurements, where one measures direct-current (DC) magnetic fields through the Zeeman splitting of the ODMR resonances, the NV center can also be used to measure alternating-current (AC) magnetic fields. Here, protocols inspired by pulsed nuclear magnetic resonance (NMR) techniques can be translated to the case of electron spin resonance of the NV center [278]. The main idea of these AC magnetometry techniques is to first, create a coherent superposition of spin states and subsequently, use pulse sequences to lock the evolution of the NV's electron spin to a specific frequency ω. A fluorescence contrast measurement is used to read out the final state of the NV, allowing for the determination for AC magnetic fields of the form $Be^{i\omega t}$. Ref. [35] demonstrated a spin echo measurement at megabar pressures, as shown in Fig. 2.1(e).

2.2.1 Inter-system crossing

The spin dynamics of the NV center under optical pumping are driven by radiative transitions between states of the same spin multiplicity as well as nonradiative ISCs between states of different spin multiplicity, see Fig. 2.3(a). ISCs can be spin-selective and thus vital for the observed ODMR contrast and optical initialization of NV as a qubit. There are two distinct ISCs in the optical cycle of the NV: i). from the optically excited ^3E manifold to the singlet $|^1A_1\rangle$, and ii). from the $|^1E\rangle$ back to the ground state $^3A_2$ manifold.

The former may occur from either $|A_1\rangle$ with rate Γ_{A_1} or from $|E_{1,2}\rangle$ with rates $\Gamma_{E_{1,2}}$. These two rates have quite different mechanisms. The Γ_{A_1} process occurs in two stages: (1) an energy-conserving transition from the initial state within the ^3E manifold to a resonant excited vibrational level of the $|^1A_1\rangle$ state, and (2) relaxation of the excited vibrational level to the ground of $|^1A_1\rangle$. The first stage requires a change in both the electron spin and orbital states as well as the lattice vibrational state, and is thus mediated by a combination of SOC and electron-phonon interactions. The second stage is mediated by phonon-phonon interactions, which enable the vibrational excitation to dissipate into propagating phonon modes. The vibrational overlap $F(\Delta)$ between the ^3E manifold and the $|^1A_1\rangle$ state has been approximated by the phonon sideband band between the ^3E and $^3A_2$ manifolds in the past [101] since the $|^1A_1\rangle$ state belongs to the same electronic configuration as the ground $^3A_2$ manifold, and their electron densities should be similar. We verified this approximation by explicitly computing the (artificial) sideband between ^3E and $|^1A_1\rangle$ using Time-Dependent Density Functional Theory (TDDFT) [150] and the results are shown in Fig. 2.3(c). We note that electron-phonon interactions with A_1-symmetric phonon modes do not couple electronic states, but allow transitions between the vibrational levels of each electronic state. According to first-order Fermi's golden rule, we have

$$\Gamma_{A_1} = 4\pi\hbar\left|\lambda_\perp\right|^2 F(\triangle). \tag{2.6}$$

A first-order ISC process cannot describe the ISC transition from $|E_{1,2}\rangle$ because there is no SOC connecting it to $|^1A_1\rangle$. Although $\lambda_\perp$ could couple $|E_{1,2}\rangle$ to $|^1E\rangle$, the actual rate of this transition should still be negligible because the energy spacing between $|E_{1,2}\rangle$ and $|^1E\rangle$, i.e., 1190 meV [4] is too large compared to the energy scale of the phonon sideband. Instead, the ISC decay from $|E_{1,2}\rangle$ is the result of a second-order process wherein phonons of E symmetry couple $|E_{1,2}\rangle$ to $|A_1\rangle$ and $|A_1\rangle$ is SOC coupled to $|^1A_1\rangle$. These rates from $|E_{1,2}\rangle$ using second-order Fermi's golden rule are defined as

$$\Gamma_{E_{1,2}} = 8\hbar^2 |\lambda_\perp|^2 \eta \int_0^\Omega \omega \left\{ [n(\omega)+1]\, F(\Delta-\omega) + n(\omega) F(\Delta+\omega) \right\} d\omega, \tag{2.7}$$

where $n(\omega) = \left(e^{\hbar\omega/k_BT} - 1\right)^{-1}$ is the thermal occupation of a phonon mode with frequency ω and $\Omega = 80\text{meV}$ [101] is the phonon cutoff energy.

Direct ISCs from $|E_{x,y}\rangle$ and $|A_2\rangle$ are forbidden up to second order, and their rates are therefore negligible compared to $\Gamma_{A_1}, \Gamma_{E_{1,2}}$ at cryogenic temperatures [101]. The ISC from the ^3E manifold is thus highly spin-selective.

The ISC to the $^3A_2$ manifold occurs from $|^1E\rangle$ to either $|0\rangle$ with rate Γ_0 or $|\pm\rangle$ with rate $\Gamma_\pm$. The underlying mechanisms of the lower ISCs are more complicated than the upper case. For Γ_0, it comes from the pseudo Jahn-Teller effect that couples $|^1E\rangle$ with $|^1A_1\rangle$, while $|^1A_1\rangle$ couple to $^3A_2^0$ via λ_z. For $\Gamma_\pm$, it stems from the Coulomb repulsion that connects $|1^E\rangle$ to the higher $|^1E'\rangle$ singlet state which can couple to $|^3A_2^\pm\rangle$ via $\lambda_\perp$. These two mechanisms are of similar strength and the ratio $\Gamma_0/\Gamma_\pm$ appears to vary between centers with observed values in the range $1.1 \sim 2$ [261, 312]. While further investigations are required, it is clear that there is no strong spin selectivity of the ISC to the $^3A_2$ manifold.

Temperature dependence— Extension of the ISC model to higher temperatures requires two modifications to the ISC calculation: i). Because of phonon-induced orbital averaging [91, 263], which is significant even at $T \sim 20\text{K}$ [78], the observed ISC rate will be the average ISC rate from all ^3E states with $|m_s| = 1$. ii). The A_1-symmetric phonon modes that

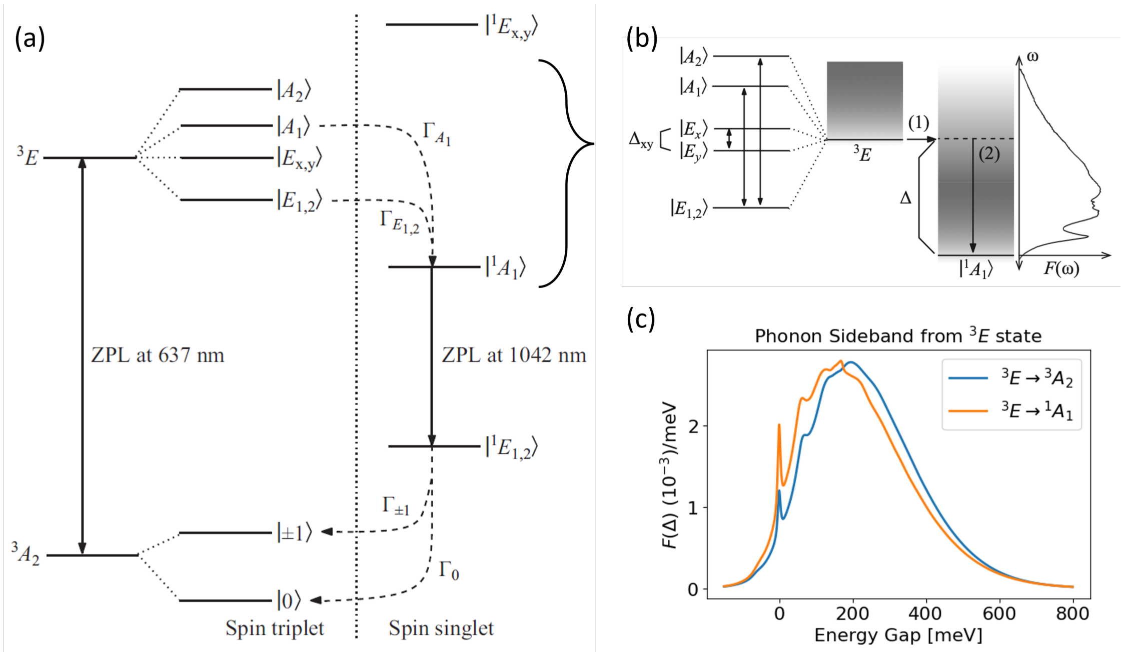

Figure 2.3: **NV's inter-system crossing model. (a)** A detailed schematic of the intersystem crossing (ISC) reproduced from Ref. [101]. Γ_{A_1} and $\Gamma_{E_{1,2}}$ represent the transition rates from the sublevels of the ^3E excited manifold to the $|^1A_1\rangle$ singlet state. Goldman et al. [101] modeled the former transition as a first-order process mediated by transverse spin-orbit coupling $\lambda_\perp$. The latter transition occurs at second order due to the electron-phonon mixing within the ^3E manifold and subsequent spin-orbit transition to the $|^1A_1\rangle$ state. **(b)** The channel to the singlet state was modeled as a resonant transition from the ^3E manifold to the phononic excitations of the $|^1A_1\rangle$ state (shown here as a vibrational overlap function $F(\Delta)$ approximated by the photoluminescence lineshape between $|^3E\rangle$ and $|^3A_2\rangle$). A decrease in Δ increases the density of states on resonance and enhances the ISC transition. **(c)** The vibrational overlap function between $|^3E\rangle$ and $|^1A_1\rangle$ computed from TDDFT [150] confirms that using the experimentally measured photoluminescence is a good approximation. Note: Images (a) and (b) are reproduced from Ref. [101].

are primarily responsible for shifting the lattice have non-negligible thermal occupations, so the vibrational overlap function $F(\Delta)$ becomes broader and flatter at higher temperatures. To address these two modifications, we calculate the orbital-averaged ISC rate

$$\Gamma_{\text{ISC}} = \frac{1}{4}\left(\Gamma_{A_1} + 2\Gamma_{E_{1,2}}\right), \tag{2.8}$$

and computed the temperature-dependent phonon sideband within the above rates using the Huang-Rhys theory [149].

Stress dependence— The above analysis applies not only to the ambient conditions but also to the situations when the system is experiencing non-negligible symmetry-preserving stress, e.g., hydrostatic or the uniaxial [111] stress. However, symmetry-breaking stress could completely alter the aforementioned model, by introducing new upper and lower ISC routes and therefore, modifying the spin selectivity. In this Chapter, we only explore the modeling of ISC rates under the symmetry-preserving case and the discussion of symmetry-breaking situations is described in the paper.

2.2.2 Rate model for ODMR spectrum

The full model of the ODMR spectrum at room temperature can be well described by classical rate equations [91], which integrate all transition rates and allow the simulation of the dynamics of state populations. The ODMR contrast is defined as

$$C = 1 - \frac{\bar{I}(\Gamma_{\text{mw}})}{\bar{I}(\Gamma_{\text{mw}} = 0)}, \tag{2.9}$$

where Γ_{mw} indicates whether the microwave driving the transitions between $|0\rangle$ and $|\pm\rangle$ sublevels at the ground state is turned on or not, and $\bar{I}$ is the steady-state photoluminescence

(PL) intensity defined as

$$\bar{I}(\Gamma_{\mathrm{mw}} = 0) = \gamma \sum_{i \in {}^3E} \sum_{j \in {}^3A_2} \Gamma_{ij} n_i, \tag{2.10}$$

where γ is the collection coefficient dependent on the experimental setup, and Γ_{ij} denotes the transition rate from state i to j. To determine the steady-state solution, we solve the classical rate equations

$$\frac{dn_i}{dt} = \sum_j \left(\Gamma_{ji} n_j - \Gamma_{ij} n_i \right). \tag{2.11}$$

Under symmetry-preserving stress at room temperature, the optical cycle of the NV center can be well approximated by a seven-orbit model [312], as shown in Fig. 2.4(a). Estimating these rates, i.e., ISC rates and spontaneous emission rates require having access to parameters that can be obtained by ab initio calculations.

2.3 Simulation results

In this section, we discuss how we performed first principle calculations to estimate the SOC, energy detuning, vibrational overlap and transitional dipole moment to obtain different rates and to finally simulate the ODMR contrast.

2.3.1 Spin-orbit coupling

Computing the spin-orbit coupling of the NV center poses a technical challenge for conventional materials' simulation software packages with periodic boundary conditions. We instead adopt a cluster model for the NV center, and terminating the surface of the cluster with hydrogen atoms. Specifically, we considered both a 70-atom and a 162-atom cluster [32], with the diamond structure optimized with the SCAN functional [304] using DFT. The effect of stress was modeled with supercell at the DFT level.

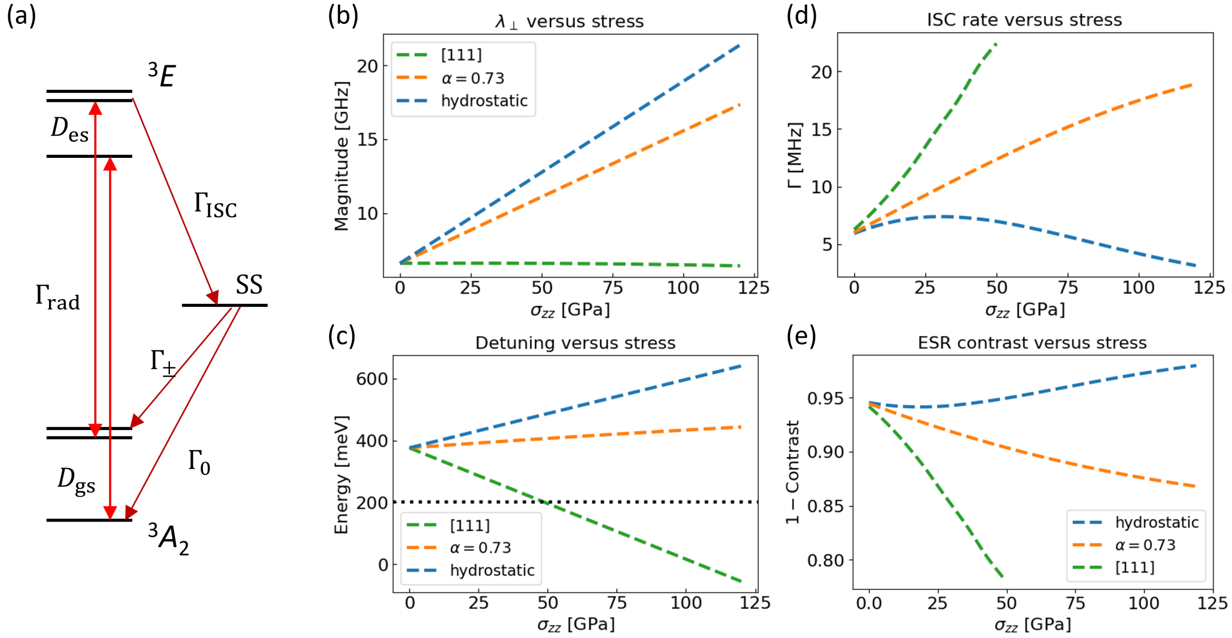

Figure 2.4: **NV's ODMR simulation results.** We computed the ODMR spectrum with its required parameters under hydrostatic stress, uniaxial [111] stress and an mixture of these two with $\alpha \sim 73\%$ hydrostatic component. The stress tensor is defined in the local NV frame with a diagonal form. **(a)** An effective seven-orbit model describing the optical cycle of NV center under only symmetry-preserving stress at room temperature. The ^3E excited manifold is experiencing strong orbital averaging. The $|0\rangle$ and $|\pm\rangle$ sublevels in the triplet states are now separated by zero-field splitting (D). The upper inter-system crossing (ISC) only happens between the spin $|\pm\rangle$ sublevels at ^3E and $\Gamma_{\mathrm{ISC}} = \frac{1}{4}\left(\Gamma_{A_1} + 2\Gamma_{E_{1,2}}\right)$. The singlet states $|^1A_1\rangle, |^1E\rangle$ is now approximated by a single shelving state. **(b)** The computed transverse spin-orbit coupling (SOC) $\lambda_\perp$ using the cluster model of NV center. Under hydrostatic stress, $\lambda_\perp$ will increase with larger stress. While for [111], $\lambda_\perp$ roughly stays unchanged. **(c)** The computed detuning Δ between ^3E and $|^1A_1\rangle$. Under hydrostatic stress, Δ will increase with larger stress leading to smaller vibrational overlap. While for [111] it's the other way around. **(d)** The simulated (upper) ISC rates with varying stress by plugging in the computed SOC and detuning parameters computed from first principle. **(e)** The computed ODMR spectrum by computing Eq. 2.9 by solving the steady-state of the rate equations 2.11. The lower ISC rates take the experimental value from Ref. [312] and are assumed to stay unchanged, as they show no state selectivity.

Once the cluster is obtained, we used the complete active space self-consistent field (CASSCF) [265] method with the Douglas-Kroll-Hess (DKH) relativistic correction [230] to compute the SOC. We choose a (6e, 6o) active space [32] and the cc-pVDZ-DK basis set implemented in the ORCA software package [233]. The $\lambda_\perp$ at ambient condition is estimated as $6.4, 6.8$ GHz from the 70-atom and 162-atom cluster, respectively, which is in reasonable agreement with the 7.5 GHz prediction from Ref. [213]. We also found that the computed SOC's stress susceptibilities have little dependence on the size of the cluster, and the results from the 162-atom cluster are plotted in Fig. 2.4(b).

2.3.2 Detuning between ^3E and $^1A_1$

The spacing between triplet and singlet states of the NV center has been controversial for a long time, with different levels of theories [32, 151, 185, 285] giving different predictions and a lack of direct experimental approach to validate the theory. The detuning between ^3E and $^1A_1$ has been indirectly estimated from experiments [101] to be $321 \sim 414$ meV with a central value of $\Delta_0 = 376$ meV. In our calculations, we use the detuning at ambient condition as Δ_0 estimated from experiment (see below).

However, the stress susceptibilities necessitate first principle calculations. Ideally, we have to consider the geometry relaxation of both the ^3E manifold and $|^1A_1\rangle$ state. Since $|^1A_1\rangle$ state has the same electronic configuration as the $^3A_2$ ground manifold, we'll ignore its geometry relaxation and use the vertical excitation energy instead. For ^3E, however, its relaxation can't be ignored and has a ~ 200 meV difference compared to the vertical excitation energy even at the ambient condition. The relaxation of ^3E can be estimated by using the constrained DFT approach applied to a 511-atom supercell (which gives perfect agreement with experiment [68]), while the vertical excitation energy of $|^1A_1\rangle$ can be estimated by either CASSCF or QDET [285]. Therefore the energy detuning between ^3E and $|^1A_1\rangle$ is computed as

$$\Delta = E_{\mathrm{ZPL}}^{\mathrm{DFT}} - E_{|^1A_1\rangle}^{\mathrm{CASSCF/QDET}} + E_{\mathrm{correction}}, \tag{2.12}$$

where the last term represents a correction to align the computed detuning to Δ_0 at ambient condition. The results with $E_{|^1A_1\rangle}$ computed with a 162-atom supercell is plotted in Fig. 2.4(c).

2.3.3 Comparison with experiments

By using the parameters we computed from first principle, we solve for the steady states of the rate equations and plot the simulated ODMR spectrum, as shown in Fig. 2.4(e). Under symmetry-preserving stress, the contrast is due to ISC, especially the upper one since it's spin-selective. Since the ISC rate is determined by the joint effect of SOC and vibrational overlap, its stress dependence is a combination of those two effects. For hydrostatic and uniaxial [111] stress, it's interesting that the effects of SOC and vibrational overlap are competing with each other. Specifically, for the hydrostatic case, the SOC dominates at small stress and reaches the largest contrast around 20 GPa, then vibrational overlap takes over, and the contrast gradually decays. We also simulated a mixture of 73% hydrostatic and 27% [111] stress, to better mimic the conditions of experiment.

For symmetry-preserving stress, the contrast has been measured from various experiments [65, 77, 134]. Fig. S7(c) of Ref. [134] gave the contrast change under increasing hydrostatic pressure, where a critical point around 25 $\sim$ 50 GPa can be seen. Ref. [329] on the other hand provided 6 times enhanced contrast [Fig. 2(f)] under a mixture of hydrostatic and [111] stress with loading stress going from 1.5 GPa to 128.6 GPa. Our prediction gave qualitatively good agreement with those reported measured data, and the deviation might be due to having neglected the Jahn-Teller effects when computing the upper ISC rates or overestimating the Δ_0. We also direct the interested reader to the paper for more detailed comparisons with ongoing experiments performed by our collaborators from Prof. Norman Yao's group.

2.4 Conclusions

In summary, we provided a detailed physical picture of the ISC effects of NV center under symmetry-preserving stress at room temperature, compared to previous work [101]. Uniaxial [111] stress has been confirmed to be the "winning strategy" for sensing at high pressures. However, the application of stress comes at the cost of sacrificing signals from the remaining three NV groups that are not oriented along the loading axis. With our ability to measure just two numbers (shift and splitting of the [111] NV group), it is only possible to get an estimate of the combined symmetry-preserving stresses ($\sigma_{ZZ}, \sigma_{\perp}$) and symmetry breaking stresses. In the case of magnetometry, it will only be possible to measure the axial and transverse components of the magnetic field ($B_Z, B_{\perp}$). The latter component is suppressed by the zero-field splitting D_{gs} and the magnitude of the symmetry-preserving stress. Nevertheless, for most of the experiments at megabar pressures, this may be a sufficient approach to probing both magnetism and stress.

The other cuts of NV are still useful. Uniaxial [100] stress leads to reduction and inversion of contrast, but the degeneracy of the four NV groups under stress can simplify the interpretation of the ODMR spectrum. In this case, a direct measurement of the $\{\sigma_{ZZ}, \sigma_{\perp}\}$ stress components provides a clean technique for pressure calibration. This can be advantageous for experiments up to $\sim$ 50 GPa, where a thorough measurement of the full stress tensor using carefully applied magnetic fields is unnecessary.

We also comment on the case of uniaxial [110] stress, although we didn't investigate this case in detail. There are two sets of doubly degenerate NV groups, with their behaviors dramatically different. For two NV groups with their z axes lying in the plane of the culet, the stress is wholly transverse. In this set of NV groups, both branches of the ^3E manifold are blue-shifted and this leads to a consequent loss in contrast. However, for the other set, comprising two NV groups with their z axes lying in the plane perpendicular to the culet, the ^3E manifold gets red-shifted. The measured contrasts are consistent with this picture;

wherein at high pressures ($\geq$ 30 GPa), we see nearly degenerate resonances stemming from two NV groups (from the second set). This ability to measure four numbers (shift and splitting of two NV groups) with better SNR than in [100] cut culets affords the ability to perform vector magnetometry at high pressures. In addition, with a little work and knowledge of the orientation of the NV groups relative to the lab frame, it may also be feasible to extract all three diagonal stress components and some measure of the shear stress in the culet.

Despite the success of recent efforts in pushing NV sensing to megabar pressures, many open questions remain. Most importantly, a physical picture of the electronic excited state under stress that leads to contrast inversion still needs to be completed. We believe there is much opportunity for further work in high-pressure sensing based on NV centers (and more broadly using other color centers) [136]. NV sensing up to megabar pressures enables studies of crystal stress for different culet cuts and pressure media on the one hand, and measurements of magnetism in various condensed matter systems on the other. The ability to do pulsed measurements up to these pressures lends access to a vast array of quantum sensing protocols!

CHAPTER 3

TEMPERATURE DEPENDENT SPIN-PHONON COUPLING OF BORON-VACANCY CENTERS IN HEXAGONAL BORON NITRIDE

This Chapter is adapted from Z. Liu, R. Gong, **B. Huang**, Y. Jin, X. Du, G. He, E. Janzen, L. Yang, E. Henriksen, J. Edgar, G. Galli, C. Zu. "Temperature Dependent Spin-Phonon Coupling of Boron-Vacancy Centers in Hexagonal Boron Nitride." *arXiv preprint arXiv:2404.15493* (2024).

The negatively charged boron vacancy center (V_B^-) in hexagonal boron nitride (hBN) has recently emerged as a highly promising quantum sensor. Compared to the nitrogen-vacancy (NV) center in diamond, the change with temperature of the spin transition energy of V_B^- is more than an order of magnitude larger, making it a potential nanoscale thermometer with superior sensitivity. In this work, using isotopically purified $h^{10}B^{15}N$, we systematically characterize the temperature dependent zero-field splitting, hyperfine interaction and spin relaxation time of V_B^- from 10 to 350 K. We carry out first-principle calculations of the V_B^- spin-phonon interaction and we show that a second-order effect from finite-temperature phonon excitations is responsible for the observed changes in experiments. By fitting our experimental results to a physically motivated model, we extract the dominant phonon mode which agrees well with our simulations. Finally, we investigate the dynamic nuclear spin polarization process at cryogenic temperatures. Our results provide key insights in V_B^- centers and their utilization as nanoscale thermometers and phonon sensors.

3.1 Introduction

Optically-addressable solid state spin defects are promising platforms for quantum applications [6, 17, 19, 69, 73, 76, 122, 128, 138, 167, 229, 249, 255, 314, 317, 335, 348], and when residing in atomically-thin van der Waals materials they may exhibit properties superior to those of their conterparts in three-dimensional materials[21, 44, 259]. Among a wide-range of contestants, the negatively charged boron vacancy center, V_B^-, in hexagonal boron nitride (hBN) is one of the defects that has attracted much growing interest [102, 106, 108]. Several interesting properties of the host material, including the large bandgap and excellent stability, as well as the readily controllable spin degree of freedom at room temperature, makes V_B^- in h-BN well-suited as a platform for technologies[228].

When compared with its three-dimensional counterparts, for example the Nitrogen-Vacancy (NV) center in diamond, the ground state zero-field splitting (ZFS) of V_B^- exhibits $a \sim 25$ times larger variation from cryogenic to room temperatures, placing it in an advantageous position for nanoscale thermometery [107, 196, 322]. However, the underlying mechanism of such a large temperature response remains an open question. In particular, in hBN the first-order lattice displacement with temperature can account only partially for the changes in the measured ZFS of V_B^- [46, 107, 309]; higher-order spin-phonon interactions should be included to quantitatively capture the experimental results.

In this letter, we experimentally characterize the temperature dependence of the ZFS, hyperfine interaction, and spin relaxation time T_1 of V_B^- in isotopically purified $h^{10}B^{15}N$, showing much narrower V_B^- spin transitions and substantially improved measurement resolution [60, 103, 148], compared to conventional hBN. We then carry out first-principle calculations of the temperature-induced phonon-mediated interaction of V_B^- , motivated by recent investigations of the NV centers in diamond [46, 309]. Our combined experimental and theoretical study allows for the identification of the main mechanism responsible for the observed temperature dependence of the properties of V_B^- , namely a second-order spin-phonon coupling with a characteristic phonon mode energy around 18 meV. We also investigate the dynamic nuclear spin polarization of the nearest three ^{15}N and find that the polarization persists down to 10 K. This is in contrast to the case of NV centers in diamond,

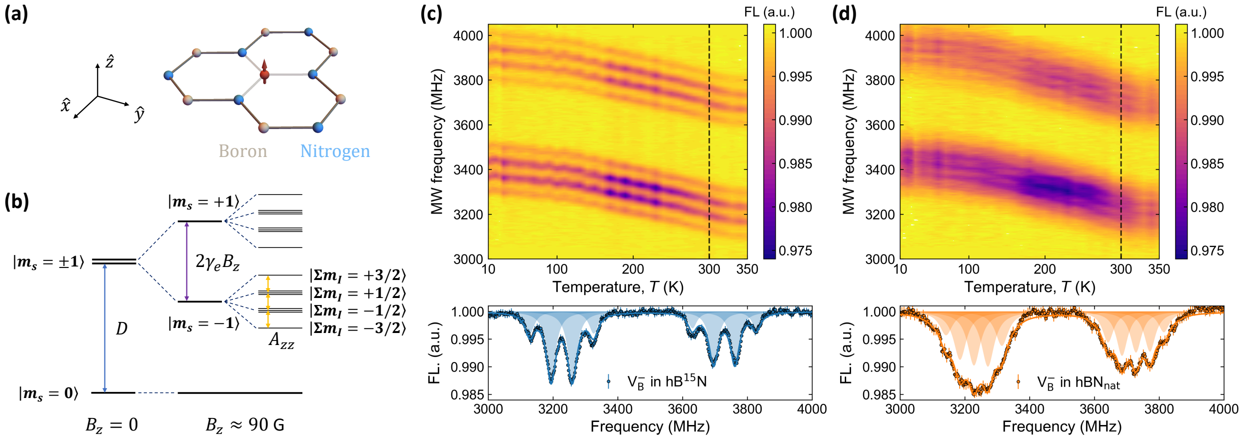

Figure 3.1: **Temperature dependence of optically detected magnetic resonance spectra of V_B^- .** (a) Schematic representation of a single V_B^- center (red spin) in the hBN honeycomb lattice. $\hat{z}$ is defined as the out-of-plane direction, while $\hat{x}$ and $\hat{y}$ live in the lattice plane. (b) The V_B^- electronic ground state energy level diagram with the presence of three nearest ^{15}N nuclear spins in isotopically purified h^{10}B^{15}N flakes. The $|m_s = \pm1\rangle$ is separated from $|m_s = 0\rangle$ by a zero-field splitting D. The hyperfine interaction further divides each spin transition into four transitions with spacing A_{zz} and degeneracy of {1, 3, 3, 1}. (c) ODMR spectrum of V_B^- in h^{10}B^{15}N flakes under magnetic field $B_z \approx 90$ G at temperatures ranging from 10 K to 350 K. The normalized fluorescence (FL) contrast is marked in the colobar. The bottom panels of (c) and (d) display the ODMR spectrum at 300 K, corresponding to the black dashed line on the top panels. The spectrum is fitted with two groups of equally spaced Lorentzians to extract the values of ZFS and hyperfine splitting. (d) ODMR spectrum of V_B^- in hBN$_{\text{nat}}$ flakes in the 10-350 K temperature range.

where the nuclear polarization vanishes at low temperatures [94, 166].

3.2 Experimental results

To investigate the temperature-dependent spin properties of V_B^-, we load the samples into a closed-cycle optical cryostat (Fournine Design) for temperature control from $10 - 350$ K. A small external magnetic field $B_z \approx 90$ G is used to lift the degeneracy between $|m_s = \pm1\rangle$. Figure 1c,d show the ODMR spectra as a function of temperature. We fit the spectra with two groups of equally spaced Lorentzians, corresponding to $|m_s =\rangle \leftrightarrow |m_s = \pm1\rangle$ transition respectively. The ZFS, $D(T)$, can be extracted from the average frequency of the two transition groups, while the hyperfine splitting, $A_{zz}(T)$, is obtained from the fitted spacing between adjacent resonances in each group (Fig. 3.2a). In addition, we also perform spin relaxation measurements and extract the T_1 timescale for different temperatures of the sample (Fig. 3.2b).

We find that the ZFS of $\mathrm{V_B^-}$ exhibits a dramatic change of more than 200 MHz from 10 to 350 K, which is around 30 times larger than the change observed for NV centers [46]. We determine the susceptibility of $\mathrm{V_B^-}$ at room temperature, $\chi(T = 300\ \mathrm{K})$, to be -880 ± 65 kHz/K for $\mathrm{hBN_{nat}}$, and -784 ± 35 kHz/K for $\mathrm{h^{10}B^{15}N}$. These results highlight the potential use of $\mathrm{V_B^-}$ as an ultra-sensitive nanoscale thermometer. Furthermore, within our measured temperature range, we observe a slightly smaller change of ZFS in $\mathrm{h^{10}B^{15}N}$ compared to $\mathrm{hBN_{nat}}$, which can be ascribed to the fact that the heavier nuclei in $\mathrm{h^{10}B^{15}N}$ lead to atomic displacements less sensitive to the temperature change. The isotope effect is further evidenced by the measured T_1 timescales, limited by spin-phonon interaction [45, 82, 108]: for heavier nuclei and thus weaker spin-phonon coupling strength, the T_1 of $\mathrm{V_B^-}$ in $\mathrm{h^{10}B^{15}N}$ is further extended at lower temperatures. We also note that while it remains a challenge to resolve the hyperfine interaction strength from the broad ODMR spectra of conventional $\mathrm{hBN_{nat}}$ [103], the substantially better resolved resonances of $\mathrm{h^{10}B^{15}N}$ enable an accurate characterization of $A_{zz}(T)$ (see Supplementary Materials). The measured amplitude of $A_{zz}(T)$ displays a noticeable increase from 64 MHz to 67 MHz with decreasing temperature, whereas the hyperfine interaction of NV centers to the nearby nuclear spins has been measured to be nearly constant with temperature [27, 337]. Finally, we observe that the ODMR contrast of $\mathrm{V_B^-}$ in both hBN samples reaches a maximum around 210 K and persists to low temperatures, without any substantial quenching. This behaviour is again in opposite to that of the NV center in diamond, whose contrast suffers from a significant drop below 90 K [94], hindering its sensing performance at cryogenic temperatures.

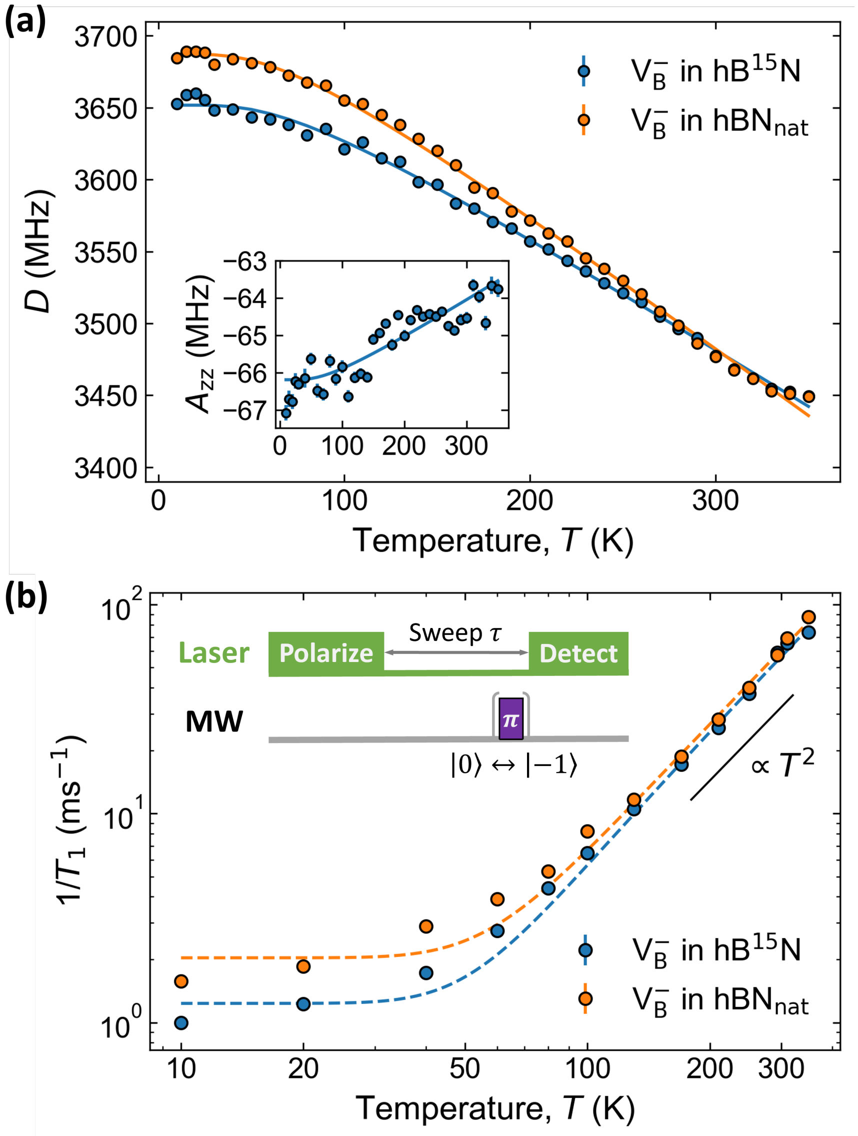

Figure 3.2: **Temperature-dependent properties of V_B^- in different hBN samples.** (a) The temperature dependence of the ZFS $D(T)$ of V_B^- in the range 10-350 K. The solid lines represent a fit to a physically motivated model using Eq. 3.2. Inset: hyperfine interaction $A_{zz}(T)$ of V_B^- in $h^{10}B^{15}N$ within the same temperature range, fitted by the same model with one fixed phonon energy 18.4 meV extracted from the fit of the ZFS. (b) Spin relaxation rate $1/T_1$ of V_B^- in the temperature range 10-350 K. Setting the phonon energy at $\hbar\omega_{\text{exp}}$, the dotted lines qualitatively reproduce the T_1 temperature-dependence by the model Eq. 3.3. In the high temperature regime, the relaxation rate is approximated by a power-law scaling $1/T_1 \propto T^2$. The experimental T_1 pulse sequence is given in the inset.

3.3 Theoretical model

To understand the observed temperature dependence of V_B^- spin properties, we adopt a theoretical model which was originally developed to study NV centers in diamond [309]. In particular, we write the electronic and nuclear spin transitions as the sum of two terms,

$$\nu = \nu_0(a(T)) + \frac{1}{2}\sum_i \frac{\partial^2 \nu}{\partial q_i^2}\frac{\hbar}{M_i \omega_i}\left(\frac{1}{e^{\hbar\omega_i/k_B T} - 1} + \frac{1}{2}\right), \tag{3.1}$$

where ν is the transition frequency (e.g., ZFS and hyperfine interaction) and $a(T)$ is the lattice constant of hBN as a function of temperature [107], q_i, M_i, ω_i are the normal mode of the crystal, mode-specific effective mass, and frequency, respectively. Here the first-order term, $\nu_0(a(T))$, corresponds to the thermal expansion of the hBN lattice, while the second-order term represents vibrational contributions caused by finite-temperature phonon excitations near the equilibrium geometry.

We carry out first-principle simulations using density functional theory (DFT) [169] with the Perdew-Burke-Ernzerhof (PBE) functional [244] to compute the temperature-dependent hyperfine interaction, $A_{zz}(T)$, between V_B^- and the nearest three ^{15}N nuclei. Interestingly, we find that the variation of the lattice constant with temperature only results in an extremely small change in the magnitude of $A_{zz}(T)$. On the other hand, the second-order term accounts for the observed effect of temperature on the value of $A_{zz}(T)$ observed experimentally.

Figure 3.3a shows the calculated second-order derivative of the energy of the crystal for each phonon mode. We find a phonon mode with the largest amplitude at energy around

Table 3.1: **Zero field splitting fitting parameters.** For each isotope, the extracted parameters are averaged over four sets of data in different sample spacial positions, fitted with same model as Eq. 3.2.

Isotopes	D_0 (MHz)	c (MHz)	$\hbar\omega_{\text{exp}}$ (meV)
^{15}N	3742 ± 10	-175 ± 13	18.4 ± 1.0
^{14}N	3777 ± 26	-201 ± 42	18.8 ± 2.8

$\hbar\omega_{\mathrm{th}} \approx 16$ meV, corresponding to an out-of-plane vibration shown in the inset. The computed temperature dependence of $A_{zz}(T)$ agrees well with our experimental results (Fig. 3.3b). For a direct comparison with the NV center, we also investigate the phonon mode associated with the hyperfine coupling between the NV center and its first shell ^{13}C nuclear spin [309]. In the case of the NV center, the dominant phonon-mode energy is $\simeq 70$ meV [45, 195], requiring a much higher activation temperature than $\mathrm{V}_{\mathrm{B}}^{-}$. Hence the variation of A_{zz} with temperature is much larger for the $\mathrm{V}_{\mathrm{B}}^{-}$ center than that observed for the NV center within the range $(10 - 350$ K) investigated in our experiment.

The dominant phonon mode found theoretically at $\hbar\omega_{\mathrm{th}} \approx 16$ meV can also be independently determined by fitting the experimentally measured spin properties to a physically motivated model [46],

$$\nu(T) = \nu_0 + c_\nu \left(\frac{1}{e^{\hbar\omega/kT} - 1} + \frac{1}{2} \right), \tag{3.2}$$

where $\nu(T = 0) = \nu_0 + \frac{1}{2}c_\nu$ is the transition energy (e.g. ZFS D and hyperfine A_{zz}) at 0 K and $n = (e^{\hbar\omega/kT} - 1)^{-1}$ is the occupation number of the phonon mode.

We apply this model to the measured ZFS and hyperfine interaction of $\mathrm{V}_{\mathrm{B}}^{-}$. For ZFS, the observed temperature dependence of $D(T)$ for both h^{10}B^{15}N and hBN$_{\mathrm{nat}}$ samples can be accurately fitted using our model, from which we extract the characteristic phonon energy to be $\hbar\omega_{\mathrm{exp}} = 18.4 \pm 1.0$ meV and 18.8 ± 2.8 meV respectively (Fig. 3.2a and Table 3.1), in agreement with our theoretical results. The measured hyperfine interaction, $A_{zz}(T)$, shows a temperature dependence that is also consistent with the model with phonon energy set to 18.4meV (Fig. 2a Inset). Interestingly, the agreement between $\hbar\omega_{\mathrm{exp}}$ and the calculated $\hbar\omega_{\mathrm{th}}$ suggests that the temperature dependence of ZFS and of the hyperfine interaction originate from the coupling of the electronic spin to the same vibrational phonon mode.

We now turn to investigate the temperature dependence of the spin relaxation time T_1. Within the temperature range $(10-350$ K) considered here, T_1 of $\mathrm{V}_{\mathrm{B}}^{-}$ is dominated by Raman scattering processes, where the energy difference between phonon absorption/emission is

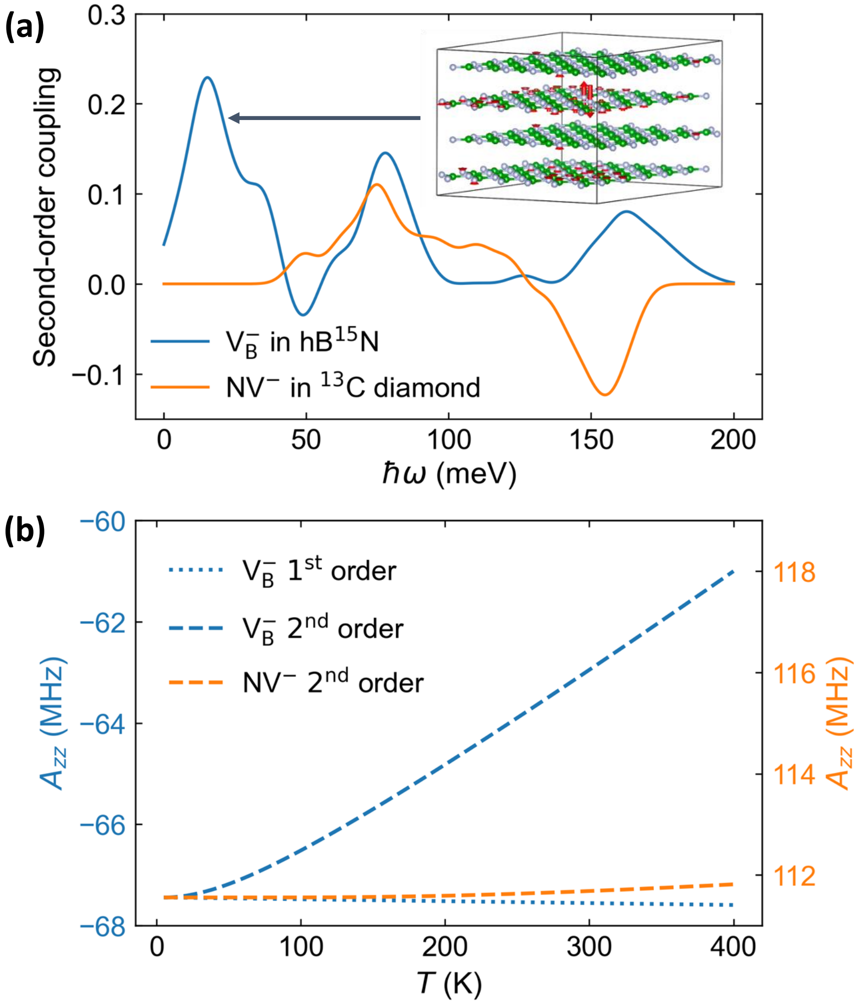

Figure 3.3: (a) The second-order vibrational coupling, i.e., $\frac{\partial^2 A_{zz}}{\partial q_i^2}\frac{\hbar}{M_i\omega_i}$ as a function of phonon frequencies of the nearest ^{15}N in hBN (blue) and ^{13}C in diamond (orange) to the vacancy, respectively. The first peak of V_B^- in hBN is identified as an out-of-plane vibrational mode (inset). (b) The computed $A_{zz}(T)$ of the nearest ^{15}N in hBN (blue) from both the first and second order vibrational contribution, respectively. We also plotted the computed $A_{zz}(T)$ of the nearest ^{13}C in NV$^-$ in diamond (orange) from the second-order vibrational contribution as a comparison.

equal to the ZFS of V_B^-, leading to spin depolarization (see Supplementary Materials) [45]. Therefore the spin relaxation rate of V_B^- can be approximated as [45]

$$\Gamma(T) = 1/T_1 \approx An(n+1) + A_S, \tag{3.3}$$

where $n = (e^{\hbar\omega/kT} - 1)^{-1}$ and A are the phonon occupation number and coupling coefficient associated with the effective mode, and A_S is a sample-related constant that might vary slightly between experiments. Using the phonon energy $\hbar\omega_{\mathrm{exp}} = 18.4$ (18.8) determined above, the model of Eq. 3.3 faithfully reproduces the experimentally measured spin relaxation rates from $50 - 350$ K (Fig. 3.2b). The small discrepancy below 50 K may be due to the activation of lower-energy phonon modes as well as processes beyond Raman scattering. We note that a prior theoretical study has predicted a power-law scaling of $T_1 \sim T^{-2}$ [224], which is consistent with our experimental results in the high temperature regime (Fig. 3.2b).

3.4 Dynamic nuclear polarization at low temperature

With the temperature-dependent $\mathrm{V_B^-}$ spin properties in hand, we now turn to investigate the dynamical polarization of the three nearest-neighbor ^{15}N nuclear spins at low temperatures. Nuclear spins feature exceptional isolation from noisy environments, making them ideal candidates for quantum storage applications [38]. At room temperature, several prior works have demonstrated the polarization of proximate ^{14}N or ^{15}N with an upper limit of $\sim$ 30 %; however how to further improve the polarization fidelity remains an open question [96, 103, 267]. Low temperature offers two potential advantages: $\sim$ 100x longer $\mathrm{V_B^-}$ electronic spin lifetime T_1 and stronger hyperfine interaction strength.

To enable resonant spin exchange between electronic and nuclear spins (known as electronic spin level anti-crossing, esLAC) [96, 103, 211], we apply an external magnetic field $B_z \approx 760$ under which the energy levels corresponding to $\mathrm{V_B^-}$ excited state $|m_s = 0\rangle$ and $|m_s = -1\rangle$ are nearly degenerate (see Supplementary Materials). We fit the measured hyperfine resonances between $\mathrm{V_B^-}$ $|m_s = 0\rangle \leftrightarrow |m_s = +1\rangle$ in the ODMR spectra as a function of the laser power to extract the nuclear spin polarization fidelity (Fig.3.4a). We find that the nuclear spin polarization at both 10 K and 300 K saturate around 30% with similar laser powers ($\sim$ 10 mW) (Fig.3.4b), suggesting that the $\mathrm{V_B^-}$ spin lifetime T_1 and hyperfine

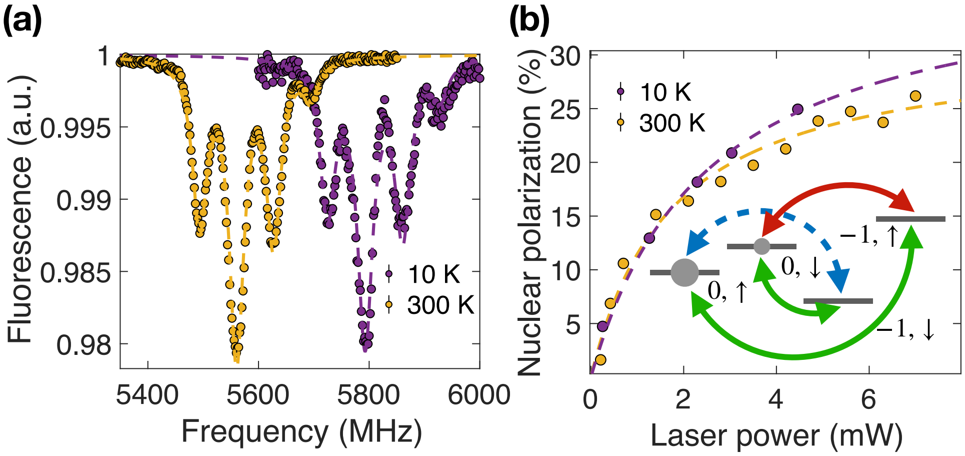

Figure 3.4: **Dynamic nuclear polarization at low temperature** (a) Near esLAC level ODMR Spectra of the $|m_s = 0\rangle \leftrightarrow |m_s = -1\rangle$ transition at 10 K and 300 K. The spectra both exhibit similar asymmetry toward the left peaks, indicating a polarization of nuclear spins. (b) Polarization level of the three nearest ^{15}N nuclear spins near esLAC level as a function of the normalized laser power under room/cryogenic temperature. Inset: schematic representation of the polarization process. The strong spin-conserving optical polarization (green arrow) continuously pumps state from $|m_s = -1\rangle$ to $|m_s = 0\rangle$, and the two hybridization processes (red arrow and dashed blue arrow) differ in strength, resulting in the polarization of $|m_I = \uparrow\rangle$ state.

interaction strength are not the limiting sources for nuclear polarization.

The spin polarization may be limited from the spin non-conserving terms in the hyperfine interaction (see Supplementary Materials), which are temperature insensitive. In addition, the observed nuclear spin polarization of $\mathrm{V_B^-}$ persists down to 10 K, in sharp contrast to the case of NV centers where the dynamic nuclear polarization process is substantially suppressed at $T \lesssim 50$ K, due to the lack of thermal averaging between NV excited states originating from different orbitals [94]. For $\mathrm{V_B^-}$, the lifting of the double degeneracy of excited states leads to a sufficiently large energy gap between the states, which renders the system insensitive to dynamic Jahn–Teller distortions [211].

3.5 Conclusion and Outlook

In summary, our research offers a comprehensive investigation of the temperature-dependent spin-phonon interaction of $\mathrm{V}_{\mathrm{B}}^{-}$ centers in isotopically purified $\mathrm{h}^{10}\mathrm{B}^{15}\mathrm{N}$. Our results will be of critical importance in designing experiments to make use of $\mathrm{V}_{\mathrm{B}}^{-}$ centers as nanoscale thermometers and phonon sensors. Moreover, although we focus on $\mathrm{V}_{\mathrm{B}}^{-}$, the methodologies developed here can be readily applied to a broad family of spin defects in two-dimensional materials.

3.6 Computational technical details

3.6.1 Electronic structure

The electronic structure calculations employ the projector-augmented-wave (PAW) method implemented in the open-source plane-wave-based Quantum ESPRESSO software package (QE) [97, 98] with a kinetic energy cutoff of 75 Ry. Spin-unrestricted calculations are performed using the Perdew-Burke-Ernzerhof (PBE) functional [244] in the computation of relaxed atomic geometries, phonons from the frozen-phonon approach [52], and hyperfine tensor A. The threshold of energy convergence is set to 10^{-8} eV, and that for force on atoms is set to 0.005 eV/Å for geometry optimization calculations.

As discussed in the main text, the temperature dependence can be captured via phonons. We note that for Eq. (3.2) in the main text, only diagonal terms are considered for the second-order contributions, leaving out the off-diagonal terms. This simplification proves to be good for the study of NV^{-} center in diamond [309] and V_{B}^{-} in hBN.

The phonon calculation for V_{B}^{-} in hBN is performed using a 287-atom supercell with only Γ-point sampling. The lattice parameters are taken from experiments at 0 K [242]. A total of 861 phonon modes are obtained, including 3 trivial modes corresponding to translations with no contribution to the temperature dependence. Therefore, all the 858 non-trivial phonon modes are then used to calculate the second-order derivative according to Eq. (2) in the main text, with the step of displacement δq_i set to 0.1 Å.

3.6.2 Hyperfine tensor

The hyperfine interaction between nuclear spin and electron spin includes the isotropic (Fermi contact) term at the nucleus site N and the anisotropic dipole-dipole interaction term near the nucleus site N

$$A_{\text{iso}}(N) = \frac{2\mu_0}{3} g_e \mu_e g_N \mu_N \rho_{\text{spin}}(\mathbf{R}), \tag{3.4}$$

$$A_{\text{aniso}}(N) = \frac{\mu_0}{4\pi} g_e \mu_e g_N \mu_N \int d^3 r \rho_{\text{spin}}(\mathbf{r}) \frac{3\cos^2\theta - 1}{2r^3}, \tag{3.5}$$

where μ_0 is the permeability of vacuum, g_e, g_N is the electron and nuclear Landé g-factor, μ_e, μ_N is the Bohr and nuclear magneton. $\mathbf{r}$ is the displacement between the electron and the nucleus at $\mathbf{R}$. ρ_{spin} denotes the electronic spin density computed from DFT, and θ is the angle between $\mathbf{r}$ and z axis.

The temperature dependence of the full hyperfine tensor of the three nearest ^{15}N atoms computed via the method discussed in the previous subsection are plotted in Fig. 3.5. Only second-order contribution is considered since the lattice expansion effect is negligible. Note that $A_{\text{yz}} = A_{\text{zx}} = 0$ due to the point group symmetry of the defect center.

3.6.3 Zero field splitting

The ZFS originates from the dipolar spin-spin interaction between electrons and can be computed as

$$D_{ab} = \frac{\mu_0 g_e^2 \mu_e^2}{4\pi} \sum_{i<j}^{\text{occ.}} \chi_{ij} \left\langle \Psi_{ij} \left| \frac{r^2 \delta_{ab} - 3 r_a r_b}{r^5} \right| \Psi_{ij} \right\rangle, \tag{3.6}$$

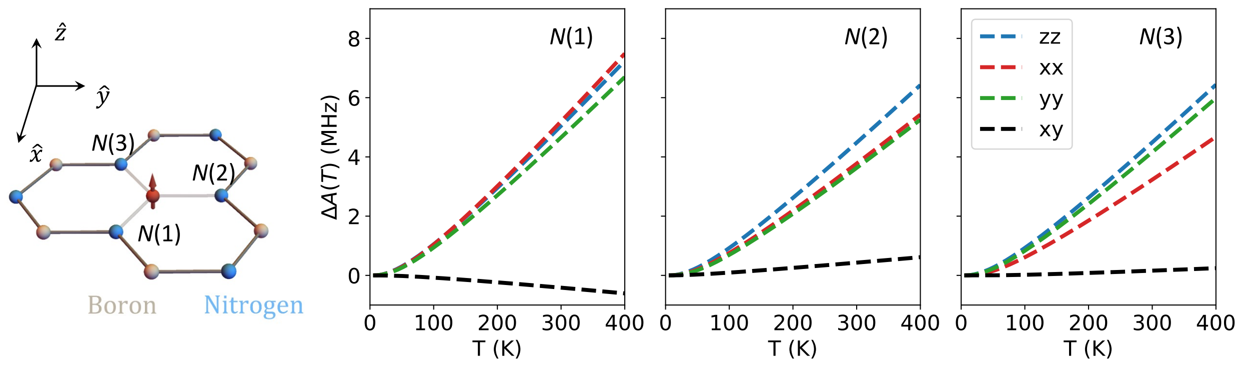

Figure 3.5: Temperature dependence of the full hyperfine tensor of three nearest ^{15}N computed from the second-order spin-phonon coupling.

where $|\Psi_{ij}\rangle$ represents a two-particle Slater determinant constructed from the Kohn-Sham ground state and $\chi_{ij} = \pm 1$ when i, j have the same/different spins. And the summation runs over all the possible electron pairs.

It has been noted by Ivády et al. [145] that it's necessary to apply hybrid functionals [132] to a 971-atom supercell, together with a post-correction for spin contamination [36], to obtain a reasonable estimation of ZFS. This calculation is computationally expensive and impractical for the investigation of temperature dependencies, which involves hundreds of single point calculations.

To qualitatively understand this temperature dependence, we focus on the coupling between spin and local phonon modes around the V_B^- center. Specifically, we cut a cluster (passivated with hydrogen atoms) with 7.5 Å radius [224] from the supercell, and apply local phonon displacements on top of it. Then we performed DFT calculations with the PBE0 [5] functional and the def2-SVP basis set to compute the ground state and the ZFS using the ORCA package [233], and the results are shown in Fig. 3.6. It can be noticed that the absolute values of the computed ZFS and the magnitude of the variation as a function of temperature are underestimated compared to the experiments. This discrepancy could be attributed to i). ignoring the contributions of a large number of non-local phonon modes, and ii). approximating the supercell using the cluster model in the calculation of the ZFS.

Despite these deficiencies, the decreasing trend in D with increasing temperature is correctly captured by our present calculations, and the difference between the two isotopes is also well reproduced, which again solidifies the phenomenological model that we've been fitting throughout this work.

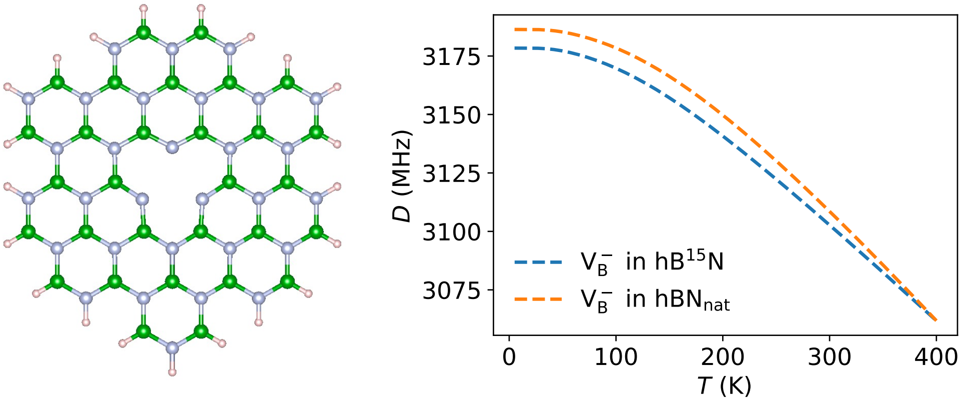

Figure 3.6: Temperature dependence of the zero field splitting of both $h^{10}B^{15}N$ and hBN_{nat} (right), computed from the cluster model (left) by only considering the second-order coupling between spin and local phonon modes near the defect. Here, we aligned the two curves at around 400 K for a better comparison with experiments.

We also note that Péter et al. [320] have studied the effects of lattice strain on the ZFS. From Supplementary Fig. 2 of Ref. [320], we can extract that the first-order contribution to the ZFS's temperature dependence is also negligible, which aligns with our expectations. Their supplementary Fig. 4b also corroborates our conclusion that the first-order contribution to the hyperfine tensor is negligible.

3.6.4 Spin relaxation time

The spin relaxation of a defect could be credited to multiple possible mechanisms. Different mechanisms could play important roles in different temperature ranges. Since the ZFS of V_B^- in hBN is $\sim$ 3.5 GHz, it's well below the typical phonon energies of hBN [224]. For temperatures well above 0 K, the one-phonon (direct) process can be safely ignored. Therefore, we mainly focus on the two-phonon processes. For the standard Orbach process [239], it's also unlikely to happen for V_{B}^{-}, because the lowest-lying excited state is $\sim$ 800 meV higher than the triplet ground state [258], well beyond the phonon cutoff frequency which is $\sim$ 200 meV in hBN [256].

One other possible two-phonon process is the Raman scattering process and it could be driven by either first-order or second-order spin-phonon interactions. Ref. [45] proposed a criterion to distinguish which of the two is dominant, namely the ratio between these two contributions, i.e., $(2\pi D/\omega)^2$, where D is the ZFS and ω is the acoustic phonon energy. Ref. [45] also showed that for NV$^-$ center in diamond, $(2\pi D/\omega)^2 \sim 10^{-7}$ and therefore the dominant driving force is second-order spin-phonon interactions. For V_{B}^{-} in hBN, we can also estimate its value as 10^{-5}, where we've taken the acoustic phonon energy as $\sim$ 26 meV [174]. We can, therefore, conclude safely that the major mechanism responsible for the spin relaxation in V_{B}^{-} is the Raman scattering driven by second-order spin-phonon interactions, and our analysis is corroborated by Ref. [224].

In this scenario, the spin relaxation rate can be modeled as

$$\Gamma(T) = 1/T_1 = \sum_i A_i n_i(n_i + 1) + A_S, \tag{3.7}$$

which is a more general form than Eq. 4 in the main text. Since we only identified a single representative phonon mode for the temperature dependence of ZFS, we only fit a single set of A, n.

CHAPTER 4

MICROWAVE-BASED QUANTUM CONTROL AND COHERENCE PROTECTION OF TIN-VACANCY SPIN QUBITS IN A STRAIN-TUNED DIAMOND MEMBRANE HETEROSTRUCTURE

This chapter is adapted with permission from X. Guo, A. Stramma, Z. Li, W. Roth, **B. Huang**, Y. Jin, R. Parker, J. Martínez, N. Shofer, C. Michaels, C. Purser, M. Appel, E. Alexeev, T. Liu, A. Ferrari, D. Awschalom, N. Delegan, B. Pingault, G. Galli, F. Heremans, M. Atatüre, A. High. Physical Review X 13.4 (2023): 041037. Copyright (2023) by the American Physical Society.
https://doi.org/10.1103/PhysRevX.13.041037.

Robust spin-photon interfaces in solids are essential components in quantum networking and sensing technologies. Ideally, these interfaces combine a long-lived spin memory, coherent optical transitions, fast and high-fidelity spin manipulation, and straightforward device integration and scaling. The tin-vacancy center (SnV) in diamond is a promising spin-photon interface with desirable optical and spin properties at 1.7 K. However, the SnV spin lacks efficient microwave control and its spin coherence degrades with higher temperature. In this work, we introduce a new platform that overcomes these challenges – SnV centers in uniformly strained thin diamond membranes. The controlled generation of crystal strain introduces orbital mixing that allows microwave control of the spin state with 99.36(9) % gate fidelity and spin coherence protection beyond a millisecond. Moreover, the presence of crystal strain suppresses temperature dependent dephasing processes, leading to a considerable improvement of the coherence time up to 223(10) µs at 4 K, a widely accessible temperature in common cryogenic systems. Critically, the coherence of optical transitions is unaffected by the elevated temperature, exhibiting nearly lifetime-limited optical linewidths. Combined with the compatibility of diamond membranes with device integration, the demonstrated platform is an ideal spin-photon interface for future quantum technologies.

4.1 Introduction

Color centers in diamond are a leading platform in quantum technologies, key achievements such as the demonstration of a quantum register [299], distant entanglement generation between three nodes [249], quantum teleportation [131], along with myriad landmarks in quantum sensing [175, 287]. In recent years, group IV centers have gained much attention due to their excellent optical properties [33, 146, 165, 210, 232, 269, 327]. Their D_{3d} symmetry renders optical transitions insensitive to first-order charge noise [71, 129]. Additionally, a favorable Debye Waller factor leads to the majority of photons being emitted into the zero-phonon line, critical for spin-photon entanglement [290]. However, the electronic structure of group IV centers – a spin 1/2 system with two ground state orbital branches – renders the electron spin susceptible to phonon-driven transitions between the two branches [147]. This temperature-dependent spin dephasing can be mitigated by operating at millikelvin temperatures [30, 303] or by engineering the local phonon density of states through nanostructuring [221, 294]. Alternatively, dephasing can be mitigated by qubit engineering such as working with group IV centers with high spin-orbit coupling and thus large orbital splitting [319], or by leveraging spin-strain interaction in randomly-, or controllably strained group IV centers[294, 299]. With a spin-orbit coupling significantly higher than those of the silicon vacancy (SiV) and the germanium vacancy (GeV) centers, the SnV center has the highest reported spin coherence time at 1.7 K [72]. However, efficient microwave (MW) control of group IV spins requires the magnitude of spin-strain interaction to be comparable with the spin-orbit interaction, which for SnV necessitates strain approaching 0.1 %. This degree of strain is challenging to achieve in microelectrical mechanical structures (MEMS) such as diamond cantilevers, with reported values on the order of 0.015 % [221]. Therefore, a controlled

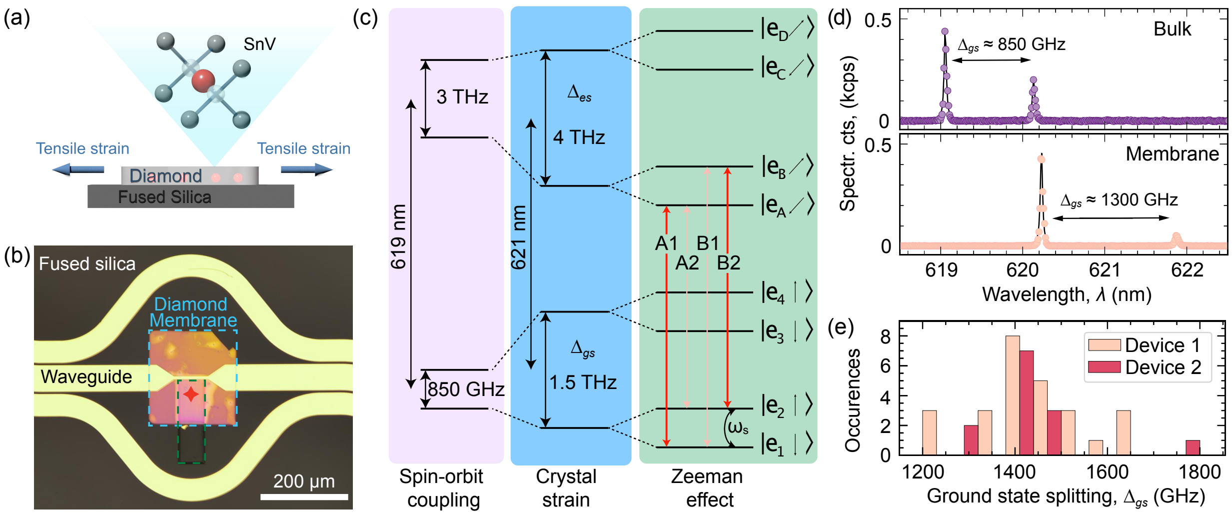

Figure 4.1: Strained SnV in diamond membrane heterostructures. (a) Schematics of the diamond-fused silica heterostructure. The static, tensile strain inside the membrane is generated from the disparity of thermal expansion ratios of diamond and fused silica. (b) The microscope image of the diamond membrane (dashed cyan region) bonded to the fused silica substrate. A trench (dashed green region) was fabricated prior to bonding. The gold coplanar waveguide is fabricated post bonding to introduce microwave signals. The location of the SnV center used in this study is highlighted by a red star. (c) Energy level of strained SnVs. Unstrained centers, strained centers and strained centers in the presence of a magnetic field are colored in purple, blue and green, respectively. (d) The PL spectrum of a strained SnV center (orange), showing a red-shifted zero-phonon line (ZPL) wavelength with a much larger ground-state splitting compared with the values in bulk diamond (purple). (e) The statistics of the SnV ground-state splitting. Two different devices with identical layout were measured. Device 1 (orange) was used for all-optical spin control (discussed in the SI) and device 2 (purple) was used for microwave spin control.

process to generate ≈0.1 % strain in diamond is desired to improve SnV qubit performance by both increasing the operational temperature and enabling efficient MW driving.

In this work, we utilize heterogeneous integration of diamond membranes to to generate strain-tuned SnVs. By bonding SnV incorporated pristine diamond membranes to a glass substrate, we leverage the heterogeneous thermal expansion coefficients of the two materials to generate a uniform, in-plane strain in the diamond to the order of 0.1 %. This strain greatly increases the energy splitting between the two orbital levels of the SnV and induces orbital mixing in the spin ground state. We demonstrate MW manipulation of the spin with 99.36(9) % Rabi fidelity at 4.50(2) MHz for 24 dBm MW input power. At 1.7 K, the implementation of dynamical decoupling allows the SnV to reach millisecond coherence time, which is largely preserved even at 4 K, owing to the strain-induced increased ground state orbital splitting. In combination with near lifetime-limited optical linewidths up to 7 K, our spin-photon interface is compatible with broadly utilized low-infrastructure and cost-effective portable cryogenic systems. Additionally, the demonstrated strained-membrane heterostructure maintains robustness and flexibility for additional photonic, electronic, and micro-electro-mechanical systems (MEMS) integration. Our SnV-based diamond membrane platform greatly reduces the technological barrier for establishing quantum nodes for networking.

4.2 Results

4.2.1 SnVs in strained diamond

This work relies on strain engineering to improve SnV qubit performance. First, we demonstrate that heterogeneous thermal expansion disparities between diamond and glass in a diamond-membrane heterostructure are sufficient to generate uniform strain of the magnitude necessary to beneficially impact SnV. The diamond membranes used in this work were generated via the "smart-cut" method combined with isotopically purified (^{12}C) overgrowth. The membrane thickness is nominally 150 nm, with pristine crystal quality and atomically smooth surfaces [116]. To introduce a positive tensile strain inside the diamond membrane, we bond them onto 500 µm-thick fused silica substrates—a material with a low thermal expansion coefficient ($< 1 \times 10^{-6}\mathrm{K}^{-1}$) – using a layer of hydrogen silsesquioxane (HSQ). The schematic of this strain generation method is shown in Figure 4.1 (a). The device is then annealed at 600 °C, beyond the temperature at which the HSQ solidifies to glass, bonding the heterostructure in a "zero-strain" condition. Due to the mismatch in thermal contraction between diamond and fused silica and the negligible thickness of the diamond membrane compared to that of the fused silica substrate, cooling down the device to cryogenic temperature regime generates a positive (tensile), static strain profile in the diamond membrane with an estimated magnitude of 0.05 % to 0.1 %. This passive, uniform, and membrane-compatible strain generation is complimentary to recent demonstrations of electro-mechanically-induced strain on suspended diamond beams [67, 294].

Figure 4.1 (b) is the microscope image showing the layout of our diamond-membrane heterostructure device. Prior to the membrane bonding, we patterned and etched a 5 µm deep trench on the fused silica to suspend part of the membrane and mitigate background fluorescence from the HSQ resist. To study MW control of the SnV centers, we patterned and deposited gold coplanar waveguides following membrane bonding.

The strain monotonically increases the orbital splitting of the SnV centers in the membranes, which can be directly verified in the photoluminescence (PL) spectra at 1.7 K. The energy level diagram of the strained SnV is shown in Figure 4.1 (c), highlighting the ground state orbital splitting (Δ_{gs}) and the respective contributions of spin-orbit coupling, strain, and magnetic Zeeman interaction in purple, blue, and green boxes. Figure 4.1 (d) compares the spectra of a strained (unstrained) SnV center in a diamond membrane (bulk diamond) with Δ_{gs} ≈1300(850) GHz. This particular strained center is used in further optical, microwave and spin characterizations in this work. Remarkably, we note that all color centers in the membrane are comparably strained. As shown in Figure 4.1 (e), we observed a distribution of the orbital branches splitting centered around 1500 GHz across different devices with a minimum (maximum) value of 1200(1800) GHz. We carried out density functional theory (DFT) calculations to compute strain-susceptibilities and characterize the SnV spin-strain interaction; our results show that the increase of the splitting between orbital branches from 850 GHz to 1500 GHz due to strain, corresponds to a diamond membrane strain magnitude of 0.075 %(see section 1.2 in the SI for details). The consistent strain generation, in combination with our ability to perform additional integration and nanofabrication following membrane bonding [43, 117], highlights the robustness and versatility of our platform.

4.2.2 Optical properties of SnV under strain

To investigate the potential of strained SnV as a spin-photon interface, we first verify that the symmetry of the defect is preserved even under considerable strain by characterizing the optical transitions as a function of the magnetic (B) field orientation. Using the $\langle 111\rangle$ crystallographic axis – the high symmetry axis of the SnV as the reference, we rotate the B field in both polar (θ) and azimuthal (ϕ) angles at the same magnitude (0.2 T). The absolute energy splitting between the two spin-conserving transitions (A1-B2) with respect to θ and ϕ is shown in Figure 4.2 (a), indicating that large splittings at moderate values of magnetic field are achievable which is ideal for later SnV spin initialization and control. Similarly to the unstrained case, we observe a ϕ rotational symmetry of the splitting with respect to $\langle 111\rangle$, which corresponds to the intrinsic spin quantization axis. We further verify that the polarization of the SnV transitions (i.e. dipole operator matrix elements) remain along the $\langle 111\rangle$ direction, as in the unstrained case [129].

From the B-field scan of the strained SnV, we note that besides the normal A1-B2 splitting maximum along the quantization axis, an additional local maximum at $\theta = 90^\circ$ – the equator plane perpendicular to the quantization axis – is observed, with the relative A1-B2 position being inverted, as verified by coherent population trapping measurements. This differs from the unstrained case. The novel feature arises from the moderate crystal strain (comparable in magnitude to the spin-orbit coupling) which increases the difference in effective Zeeman shift between ground and excited states, mostly visible for a magnetic field orthogonal to the spin-orbit-dictated quantization axis. As is the case for moderately strained SiV centers [303] for MW-based control, we roughly align the B-field towards the quantization axis to achieve highly cycling optical transitions with cyclicity reaching $\eta \approx 2500$. We note that η can

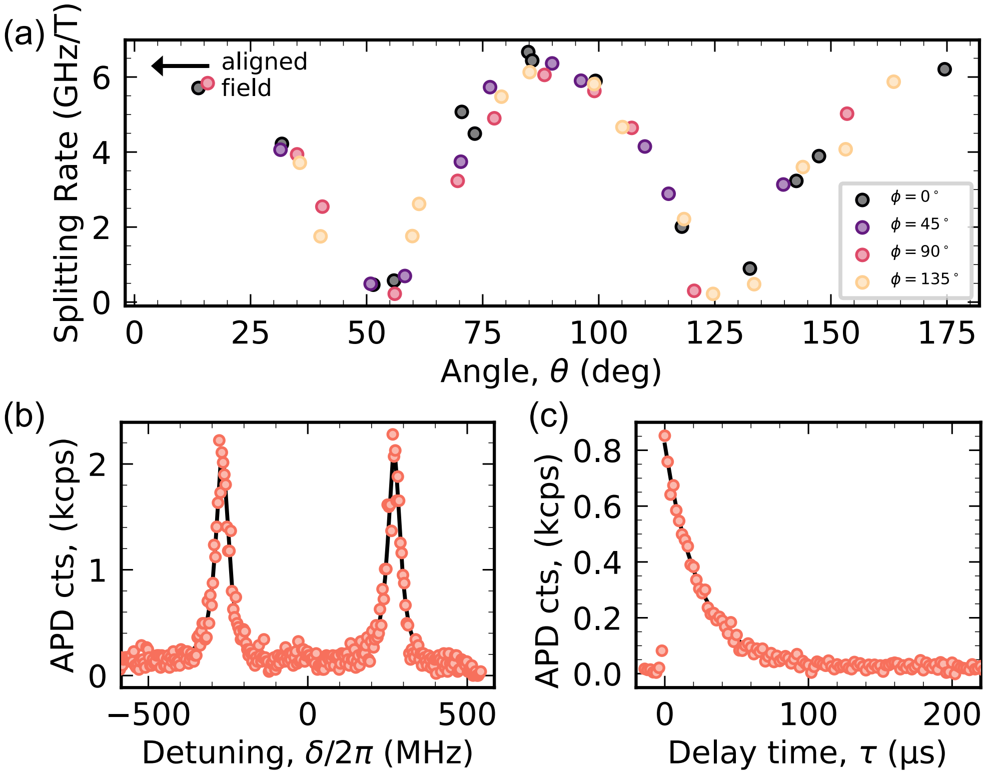

Figure 4.2: Optical properties of the strained SnV center under applied magnetic fields at 1.7 K. (a) The energy splitting rate between the A1-B2 spin conserving transitions with respect to the polar angle θ of the applied magnetic field at different azimuthal angle ϕ. The aligned field is highlighted with a black arrow. (b) PLE scan, averaged over 20 s, of the {A1, B2} transitions at an aligned B-field with a magnitude of 81.5 mT. The average linewidth for both transitions are below 48 MHz, which is less than 1.5 times of the lifetime limited value (32.26(19) MHz). (c) The initialization curve of the A1 transition, showing a time constant of 24.2(3) µs and an initialization fidelity of 98.82 %.

be as low as 6 when the B field is perpendicular to the quantization axis, which is ideal for Raman-based all-optical control of strained SnV. We provide a theoretical justification for the observed phenomenon by constructing and diagonalizing the total Hamiltonian with varying B-field orientations in Sec. 4.4. Moreover, by comparing the dependence on θ of the A1-B2 splitting with calculated results, we are able to determine the Stevens reduction factor g_L for ground and excited states mentioned in [315]. This model is then used to explain the optically detected magnetic resonance (ODMR) frequency of the strained SnV discussed below.

Additionally, our measurements reveal near-transform limited optical linewidths, thereby showing that the application of strain does not alter the excellent coherence properties of the optical transitions, as previously demonstrated with unstrained centers [232, 319]. As shown in Figure 4.2 (b), the 20 s average scan returns a mean linewidth of 47.4(16) MHz, only 40 % more than the lifetime-limited value of 32.26(19) MHz (4.933(190) ns optical lifetime). The long term frequency stability of the {A1, B2} transitions returns a center frequency standard deviation of σ_c =23.8(1) MHz and a A1-B2 splitting standard deviation of σ_s =13.28(6) MHz. This linewidth and peak stability is comparable to that of other measurements of group IV color centers in nanostructures [270, 299, 327] and thus confirms the excellent potential of these defects for quantum photonic applications.

The resolvable splitting and narrow optical transitions are crucial for the spin initialization and readout of the SnV qubit. The spin initialization curve with subtracted background is shown in Figure 4.2 (c), indicating a fitted exponential decay constant of 24.2(3) µs. The initialization pulse duration was set to 200 µs allowing us to reach a fidelity of 98.8 %. We note that with a cyclicity of over 2500, this platform is a prime candidate for single shot readout if the signal counts can be improved via on-chip structures (nanophotonics, fiber couplers or grating couplers, solid immersion lenses) [34, 115, 176, 270] or external methods (microcavities) [260, 268, 318].

4.2.3 Efficient MW control of the SnV spin

A critical component of a spin-photon interface is high-fidelity spin control, commonly achieved through MW driving of the electron spin. In the case of group IV centers, a MW field can only drive the spin transition in the presence of strain [221, 248]. This arises due to the orthogonality of orbital states associated with the electron spin qubit of group IV centers [129]. Strain that is comparable in strength to spin-orbit coupling relaxes this orthogonality, enabling microwave control. SnV, with larger spin-orbit coupling (850 GHz)

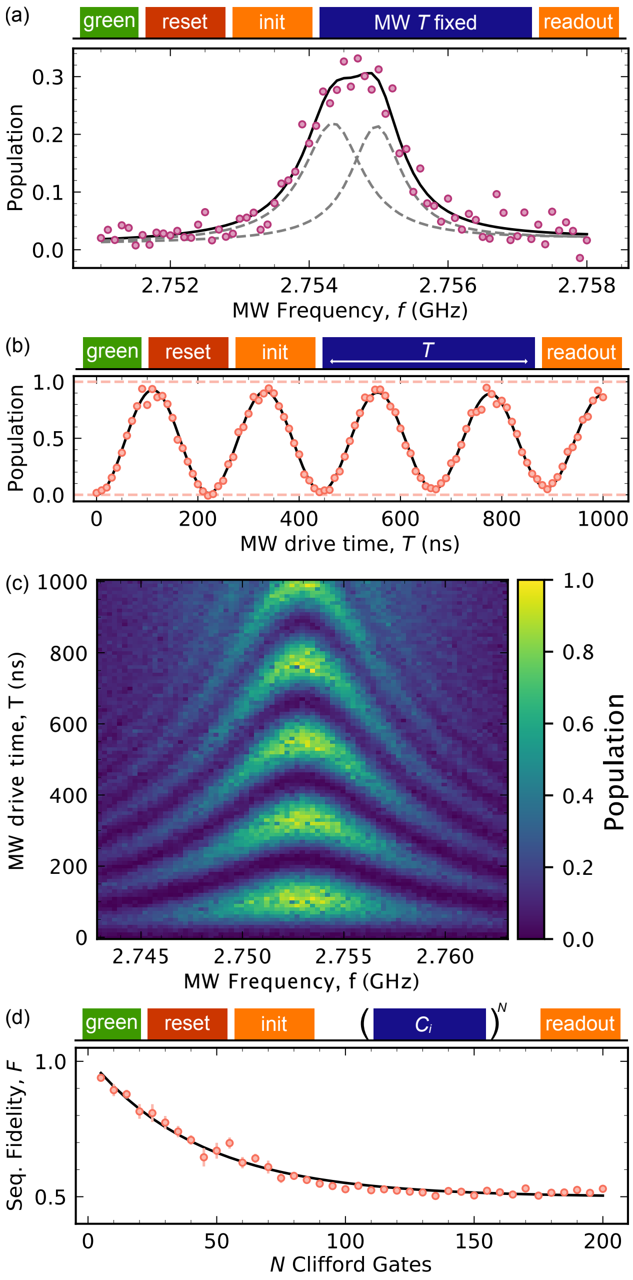

Figure 4.3: MW control of the strained SnV center at 1.7 K. (a) Pulsed ODMR spectrum with scanned MW frequency. The data (purple dots) is fitted with two Lorentzian functions (dashed line) split by 628(182) kHz and with a linewidth of 1047(208) kHz and 891(197) kHz, respectively. (b) Rabi oscillation of the SnV at zero detuning, indicating a Rabi frequency $\Omega/2\pi$ of 4.50(2) MHz with a fidelity of 99.36(9) %. (c) Rabi oscillation as a function of the MW driving frequency. (d) Randomized benchmarking at 1.7 K, showing an average gate fidelity of 97.7(1) %. The Rabi frequency is set to 2.8 MHz to avoid excess heating effects.

and smaller strain susceptibility than SiV and GeV, requires large crystal strain to meet this criteria. This strain requirement goes beyond the achievable magnitude demonstrated via active strain tuning [221] or implantation-induced strain [299].

To demonstrate efficient MW control, we utilize the nominal 0.1 % crystal strain in the diamond membrane. We estimate an effective Landé factor g of 1.62 for the transverse microwave field with the external magnetic field roughly aligned to the SnV quantization axis. This value is relatively high compared with spin-orbit-dominated regime for unstrained centers ($\leq$0.3) and is close to the free electron value ($g = 2$). In addition, we tapered the MW waveguide around the measurement area by shrinking its width to 6 µm to enhance the microwave amplitude, as shown in Figure 4.1 (b). The distance between the target SnV and the waveguide is $\approx$4 µm, ensuring an efficient exposure to the MW driving field.

We begin the MW control characterization by initializing the spin via optical pumping and scan the frequency of a MW field across the expected spin resonance while monitoring the fluorescence intensity of the spin readout at 1.7 K. In Figure 4.3 (a) we observe clear signature of optically detected magnetic resonance (ODMR) for the target SnV center. The 81.5 mT external magnetic field is aligned to the quantization axis by polarisation measurements and 3D field scan. The ODMR shows a profile with two overlapping peaks separated by 628(182) kHz, indicating an interaction between the electronic spin of the SnV with another system in the vicinity, likely a ^{13}C nuclear spin or the electron spin of a P1 center. Further investigation is needed to understand the nature of this interaction. By driving both power-broadened ODMR transitions, we are able to resonantly manipulate the spin state of the SnV with a Rabi frequency $\Omega/2\pi$ of 4.50(2) MHz. The Rabi oscillation curve and the chevrons (Rabi oscillations with varied driving frequency) are shown in Figure 4.3 (b) and (c). We observe a long-time averaged Rabi π-gate fidelity of 99.36(9) %, improving significantly from previously demonstrated optical Raman-based spin control value [72]. We note that the MW power delivered to the device is approximately 24 dBm (250 mW) which is comparable to previous demonstrations on strained SiV [299]. We also characterized the power dependence of the Rabi rate. Starting from a linear dependence, the Rabi rate deviates to sub-linear when the power surpasses 24 dBm due to excessive heating, which could be optimized by replacing gold with superconducting metals (such as niobium or NbTiN) to deliver the MW signal.

We further characterize the single qubit gate fidelity of MW control via randomized benchmarking. For this, we use the following set of Clifford gates: $\{I, \pi_x, \pi_y, \pi_x/2, -\pi_x/2, \pi_y/2, -\pi_y/2\}$ (see section 5.1 in SI). To prevent excessive heating effect during benchmarking which would lead to undesired spin decoherence, we apply a slightly slower Rabi rate (2.8 MHz, 18 dBm) which requires no time buffer between gates. The benchmarking result is shown in Figure 4.3 (d). We extract an average Clifford gate fidelity of 97.7(1) %, indicating power efficient MW control with high fidelity under stringent randomized benchmarking.

4.2.4 SnV spin coherence properties

We next utilize microwave control to characterize the SnV coherence at 1.7 K. We perform a Ramsey measurement as shown in Figure 4.4 (a). The Gaussian envelope of the Ramsey oscillations corresponds to a spin dephasing time T_2^* of 2.5(1) µs. Similar to ODMR, we observe interaction with a proximal spin in the Ramsey measurement, and we verify that this does not originate from the detuning of the MW signal via phase dependent readout (see section 5.2 in SI). Possible decoherence sources could be nearby vacancies and defects in the diamond membrane, as well as surface spins from both sides of the membrane [274].

Advanced pulse sequences, such as dynamical decoupling via CPMG (Carr-Purcell-Meiboom-Gill) and XY pulse sequences [70, 295], allow us to extend the spin coherence to millisecond timescales. The CPMG results are shown in Figure 4.4 (b). The $T_{2,\mathrm{echo}}$ returns a value of 100(1) µs, which is already longer than 35.5(30) µs measured using all-optical spin echo process, in the absence of optically induced dephasing mechanisms. The $T_{2,\mathrm{CPMG128}}$, com-

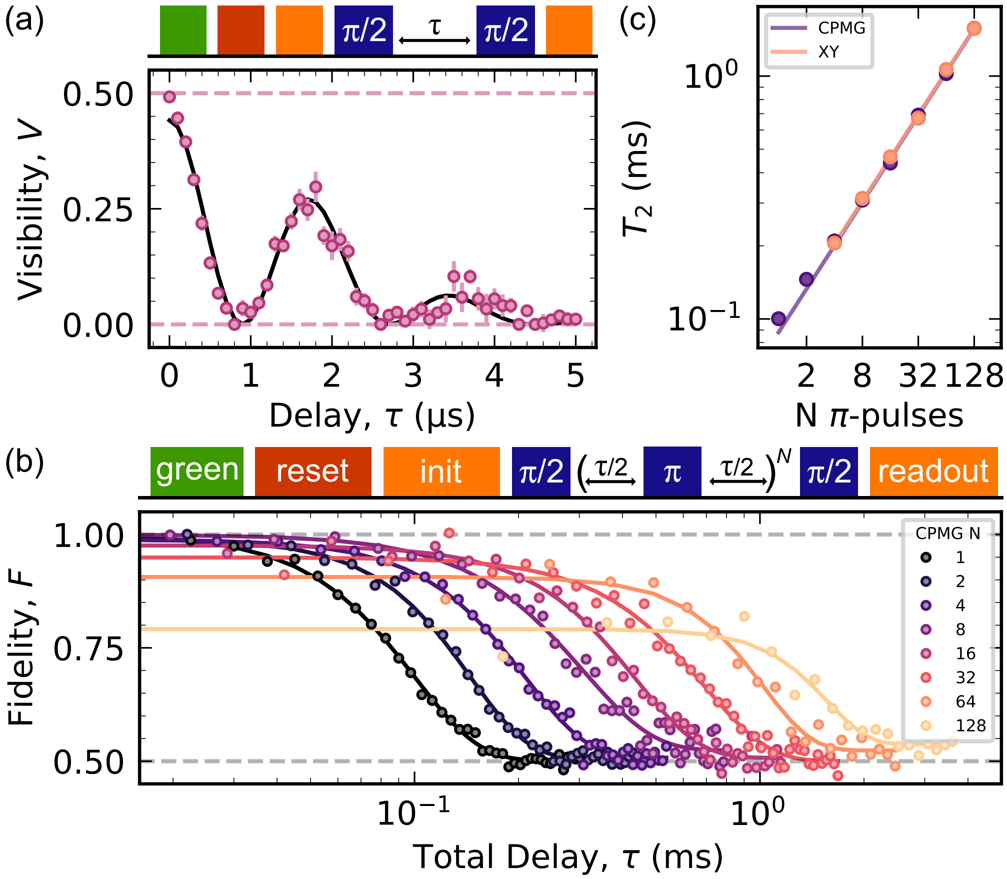

Figure 4.4: Spin coherence of the strained SnV at 1.7 K. (a) T_2^* Ramsey of the SnV center, showing a dephasing time of 2.5(1) µs. The extra beating pattern of 554(5) kHz is estimated to be an interaction with the electron or nuclear spin in the vicinity. (b) Dynamical decoupling of the SnV via CPMG pulses. The CPMG-1 (spin-echo) returns a $T_{2,\text{echo}}$ of 100(1) µs, while the CPMG-128 reaches a $T_{2,\text{CPMG128}}$ of 1.57(8) ms. (c) The scaling of T_2 with the number of CPMG and XY pulses, showing a sub-linear dependence.

prising 128 refocusing microwave pulses, prolongs the SnV spin coherence to 1.57(8) ms. We note that with no signal normalization being applied, the CPMG figure indicates a high signal fidelity of ≈80 % for up to 128 pulses. Future developments on the MW driving fidelity including superconducting metals and faster Rabi pulses can further improve the signal fidelity to higher numbers of pulses. We plot the relationship between the T_2 and the number of CPMG or XY pulses N in Figure 4.4 (c) and fit it with $T_2 \sim N^{\beta}$. The fitting curve returns a sub-linear dependence with a β factor of 0.593(8). We observed minimal T_2 differences between CPMG and XY sequences. XY sequences are more resilient to control pulse errors compared to CPMG [295], verifying that the observed coherence is not limited by our control.

4.2.5 Spin-photon interface at 4 K

Finally, we demonstrate that our strained SnV platform shows state-of-the-art spin coherence for Group IV color centers at 4 K. For Group IVs, the dominant decoherence source of the electronic spin is the electron-phonon interaction (phonon-mediated decay) between orbital branches [147, 248]. The electron-phonon interaction rate depends on the temperature-dependent phonon population and the energy splitting Δ_{gs} between orbital branches. Therefore, enhanced coherence of the group IV centers can be achieved via either cooling down to millikelvin temperature [30, 303], increased energy splitting by using heavier group IV elements [319], engineering of the phonon density of states [177], or strain engineering [294]. Here we utilize both a heavy element (Sn as compared to Si and Ge) and crystal strain in diamond to improve electron spin coherence at elevated temperatures.

The Rabi oscillation of the SnV at 4 K is shown in Figure 4.5 (a). The fidelity is characterized to be 97.7(5) %, only slightly lower than the value at 1.7 K due to background heating limitations. We characterize the average gate fidelity via randomized benchmarking at 4 K using the same 2.8 MHz Rabi rate, returning a gate fidelity of 95.7(3) %, confirming the maintained high performance spin manipulation of the strained SnV at 4 K.

Equipped with high fidelity Rabi control, we investigate the spin coherence of the SnV centers at elevated temperatures. Due to the much larger splitting Δ_{gs} of the strained SnV (≈1300 GHz) compared with bulk SnV (≈850 GHz), electron-phonon dephasing onsets at higher temperatures. Figure 4.5 (c) shows the T_1^{spin}, T_2^*, $T_{2,\text{echo}}$ and $T_{2,2XY8}$ versus temperature. Fitting the same β factor in $T_2 \sim N^\beta$ using Hahn-echo and XY4 coherence times returns a value of 0.391(8) at 4 K and 0.014 at 4.5 K, indicating that the dominant decoherence mechanism becomes phonon-induced orbital transitions instead of the spin bath.

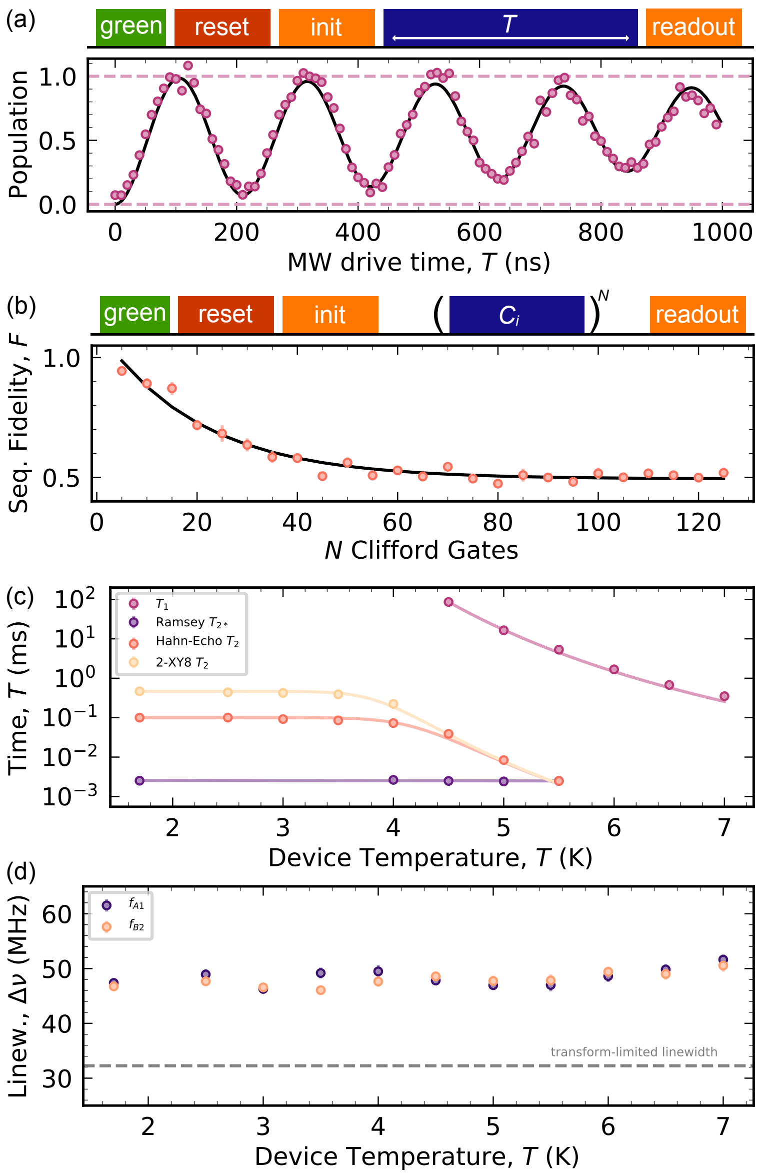

Figure 4.5: Performance of the strained SnV center at 4 K. (a) Rabi oscillation of the SnV center, showing a gate fidelity of 97.7(5) % (b) Randomized benchmarking at 4 K, showing an average gate fidelity of 95.7(3) %. (c) Temperature dependence of the spin decay time T_1^{spin}, dephasing times T_2^*, $T_{2,\text{echo}}$, and $T_{2,\text{2XY8}}$. (d) ZPL linewidths of the two spin conserving transitions (A1, B2) with respect to the temperature, showing negligible broadening with the maximum linewidth below 52.0(8) MHz. The transform-limited linewidth is shown with a dashed line.

From Figure 4.5 (c) we notice a much lower dephasing time compared with the decay time T_1^{spin} [262]. This feature originates from the fact that only spin-flipping transitions between the lower and upper orbital branch drive T_1^{spin}, whereas T_2 is sensitive to dephasing by the spin-conserving transitions due to different precession frequencies in the orbital branches [221]. In our case, the phonon transitions are highly cycling due to the aligned magnetic field. Nevertheless, T_2^* at 4 K remains at 2.7(1) µs – comparable to the 1.7 K value, and $T_{2,echo}$ only decreases slightly to 74(2) µs, with $T_{2,2XY8}$ reaching the depolarization-limited T_2 – 223(10) µs. It is worth emphasizing that all of these are record high values for all group IV spin qubits at 4 K to date.

To demonstrate the potential of the strained SnV center as a promising spin-photon interface at elevated temperature, we investigate the temperature dependence of the SnV optical coherence. As shown in Figure 4.5 (d), we observe that the ZPL linewidth remains unchanged for both A1 and B2 transitions up to 7 K with the maximum linewidth remaining below 52.0(8) MHz—only 60 % higher than lifetime-limited values. In the future, modest Purcell enhancement of SnV emission rates with on-chip nanophotonics or microcavities can generate fully lifetime-limited photons suitable for efficient entanglement generation.

4.3 Conclusions

In this work, we demonstrate that SnV in strained diamond membranes is a promising platform for quantum technologies. We create simple heterostructures that leverage differences in thermal expansion to passively generate significant strain of 0.05 % to 0.1 % in diamond, enabling efficient, high fidelity microwave control of the SnV spin. The presence of the strain also suppresses the phonon-mediated decay and improves the spin coherence of the SnV at 4 K, which greatly reduces the technological barrier for quantum networking applications. We reach a Rabi π gate fidelity of 99.36(9) % (97.7(5) %) with a randomized single qubit gate fidelity of 97.7(1) % (95.7(3) %) at 1.7 K (4 K). Dynamical decoupling sequences allow the SnV spin coherence to reach 1.57(8) ms at 1.7 K and 223(10) µs at 4 K. In the future this value can be further enhanced by generating higher strain through heterostructure optimization and/or additional active tuning. Our platform, derived from scalable diamond membrane generation, is compatible with further on-chip integration, such as microwave coplanar waveguides, integrated photonics [117], and MEMS. Finally, 4 K cryostats are relatively affordable and less infrastructure-intensive in comparison to cryogen-free 1.7 K and mK dilution-fridge systems. Therefore, the demonstrated spin-photon interface at 4 K can reduce barriers to widespread utilization and deployment of solid-state quantum technologies.

4.4 Computational technical details

In this section, we outline the basics of SnV$^-$, present our calculation on its strain susceptibility and conclude by explaining what happened between the $A1, B2$ transitions during the B-field scanning.

4.4.1 Hamiltonian of the strained SnV$^-$

The SnV$^-$ center is a spin-1/2 system. In a mean-field orbital picture, the system has three electrons in four spin orbitals ($\{|e_x \uparrow\rangle, |e_x \downarrow\rangle, |e_y \uparrow\rangle, |e_y \downarrow\rangle\}$). Both its electronic ground and excited states are doubly-degenerate; the degeneracy may be lifted by applying strain and/or by spin-orbit interaction. We write the spin Hamiltonian of the system in the minimum model of 4 electrons and 3 orbitals, for the ground (g) and excited (u) state $H_{g,u}$, as the sum of four terms: spin-orbit (SO) interaction ($\hat{H}_{\text{SO}}$); electron-phonon interaction due to the Jahn-Teller effect; strain field, and interaction with an external, static magnetic field B (Zeeman effect, $\hat{H}_Z$). Following Ref [129], we write the term arising from Jahn-Teller distortions in the same form as that describing the strain interaction. Below we merge the two terms into one, that for simplicity we call $\hat{H}_{\text{strain}}$. Hence the Hamiltonian is written as:

$$\hat{H}_{\text{sys}} = \hat{H}_{\text{SO}} + \hat{H}_{\text{strain}} + \hat{H}_Z. \tag{4.1}$$

In the following three subsections, we discuss each term of the Hamiltonian.

Spin-orbit coupling

The component of the orbital angular momentum operator $\hat{L}_x, \hat{L}_y$ vanish for the Hamiltonian expressed in the $\{|e_x\rangle, |e_y\rangle\}$ basis [129] and only the following term is non-zero: $\hat{L}_z = \begin{bmatrix} 0 & -i \\ i & 0 \end{bmatrix}$, where we have set $\hbar$ to 1. Therefore, using the $\{|e_x \uparrow\rangle, |e_x \downarrow\rangle, |e_y \uparrow\rangle, |e_y \downarrow\rangle\}$ basis, the SO Hamiltonian can be represented as:

$$\hat{H}_{SO} = \lambda \hat{L}_z \hat{S}_z = \frac{\lambda}{2} \begin{bmatrix} 0 & -i \\ i & 0 \end{bmatrix} \otimes \begin{bmatrix} 1 & 0 \\ 0 & -1 \end{bmatrix} = \begin{bmatrix} 0 & 0 & -i\lambda/2 & 0 \\ 0 & 0 & 0 & i\lambda/2 \\ i\lambda/2 & 0 & 0 & 0 \\ 0 & -i\lambda/2 & 0 & 0 \end{bmatrix}. \tag{4.2}$$

Strain field

The term of the Hamiltonian representing the presence of a strain field can be written as:

$$\hat{H}_{\text{strain}} = \begin{bmatrix} \varepsilon_{A_1} - \varepsilon_{E_x} & \varepsilon_{E_y} \\ \varepsilon_{E_y} & \varepsilon_{A_1} + \varepsilon_{E_x} \end{bmatrix} \otimes \mathbb{I}_2. \tag{4.3}$$

The elements $\{\varepsilon_{A_1}, \varepsilon_{E_x}, \varepsilon_{E_y}\}$ represent the energy response induced by strain belonging to the different irreducible representations A_1, E_x, E_y of the D_{3d} point group of the defect, and are expressed in the SnV$^-$ center's local frame, where the z-axis corresponds to the high symmetry axis of the SnV$^-$ which is the quantization axis. For example, $\varepsilon_{A_1} = \langle\Psi|(H - H_0)|\Psi\rangle$, where H_0 is the electronic Hamiltonian in the absence of strain and H is the electronic Hamiltonian, which includes the strain field applied to the supercell by changing the lattice parameters. Here $|\Psi\rangle$ represents a Slater determinant expressed in the $\{|e_x \uparrow\rangle, |e_x \downarrow\rangle, |e_y \uparrow\rangle, |e_y \downarrow\rangle\}$ basis.

We can write each term of the above equation as a linear combination of the components of the strain tensor (ϵ):

$$\begin{aligned} \varepsilon_{A_1} &= t_{\perp}\left(\epsilon_{xx}+\epsilon_{yy}\right)+t_{\|}\epsilon_{zz}, \\ \varepsilon_{E_x} &= d\left(\epsilon_{xx}-\epsilon_{yy}\right)+f\epsilon_{zx}, \\ \varepsilon_{E_y} &= -2d\epsilon_{xy}+f\epsilon_{yz}, \end{aligned} \tag{4.4}$$

where $\epsilon_{xx}, \epsilon_{yy}, \epsilon_{zz}$ represent the diagonal components of the strain tensor in the x, y, z directions and $\epsilon_{xy}, \epsilon_{yz}, \epsilon_{zx}$ represent the shear strain components; $t_{\perp}, t_{\|}, d$, and f are partial derivatives written as $\frac{\partial \varepsilon_{A_1}}{\partial(\epsilon_{xx}+\epsilon_{yy})}, \frac{\partial \varepsilon_{A_1}}{\partial \epsilon_{zz}}, \frac{\partial \varepsilon_{E_x}}{\partial(\epsilon_{xx}-\epsilon_{yy})}, \frac{\partial \varepsilon_{E_x}}{\partial \epsilon_{zx}}$, respectively. These four strain-susceptibility parameters completely describe the strain-response of the ground and excited electronic states. In the following, we ignore the diagonal term ϵ_{A_1}, which amounts to a global emission wavelength shift. Hence, the strain Hamiltonian has the following form:

$$\hat{H}_{\text{strain}} = \begin{bmatrix} -\varepsilon_{E_x} & \varepsilon_{E_y} \\ \varepsilon_{E_y} & \varepsilon_{E_x} \end{bmatrix} \otimes \mathbb{I}_2 = \begin{bmatrix} -\varepsilon_{E_x} & 0 & \varepsilon_{E_y} & 0 \\ 0 & -\varepsilon_{E_x} & 0 & \varepsilon_{E_y} \\ \varepsilon_{E_y} & 0 & \varepsilon_{E_x} & 0 \\ 0 & \varepsilon_{E_y} & 0 & \varepsilon_{E_x} \end{bmatrix}. \tag{4.5}$$

Zeeman effect

Due to the D_{3d} symmetry of the defect, the orbital component $H_{Z,L}$ of the Hamiltonian H_Z only includes a term $\hat{L}_z B_z$ [129], with a pre-factor q [315], called in the literature *effective reduction factor*, accounting for: (i) electron-phonon interaction (so-called Ham term), and (ii) the symmetry of the defect being lower than $O(3)$ (so-called Steven's factor). Note that both terms have different values for the ground and excited states and hence the q parameter is different in the ground and excited states. The H_Z Hamiltonian is written as the sum of an orbital $H_{Z,L}$ and spin component $H_{Z,S}$

$$\hat{H}_Z = \hat{H}_{Z,L} + \hat{H}_{Z,S} = q\mu_B\gamma_L\hat{L}_zB_z + g\mu_B\hat{\mathbf{S}}\cdot\mathbf{B} - 2\mu_B\delta_f\hat{S}_zB_z, \tag{4.6}$$

where μ_B is the Bohr magneton and B_x, B_y, B_z are the components of the external, static magnetic field along the crystal frame x, y, z directions, respectively. The last term on the right hand side of Eq. 4.6 originates from correcting with a factor δ the electronic Landé g factor to account for spin-phonon interaction mediated by spin-orbit coupling [315]. For all the experimental interpretations, we'll only use the Ham factor and set the Steven's factor as 1 except section 4.4.3 where we gave estimates on the possible values of Steven's factor.

4.4.2 Strain susceptibility

In the presence of a strain field, the degeneracy of the ground (gs) and excited (es) states is lifted and we call $\triangle_{\mathrm{gs(es)}}$ the energy difference between the two states split by the degeneracy. By diagonalizing the strain Hamiltonian defined in Eq. 4.5, we obtain:

$$\triangle_{\mathrm{gs(es)}} = 2\sqrt{[d_{\mathrm{gs(es)}}(\epsilon_{xx} - \epsilon_{yy}) + f_{\mathrm{gs(es)}}\epsilon_{zx}]^2 + [-2d_{\mathrm{gs(es)}}\epsilon_{xy} + f_{\mathrm{gs(es)}}\epsilon_{yz}]^2}, \tag{4.7}$$

where the strain-susceptibilities are computed from density functional theory (DFT) calculations. We performed DFT calculations employing both the PBE [244] and SCAN [304] functionals, and a 511-atom supercell with a [0.5, 0.5] occupation number for the $|e_x\downarrow\rangle, |e_y\downarrow\rangle$ orbitals. We approximated the splittings by the energy difference of the corresponding Kohn-Sham (KS) orbitals. The strain susceptibilities $d_{\mathrm{gs}}, d_{\mathrm{es}}, f_{\mathrm{gs}}, f_{\mathrm{es}}$ can be obtained from Eq. 4.7 by varying the lattice parameters of the supercell to generate $(\epsilon_{xx} - \epsilon_{yy})$ and ϵ_{zx} strain, respectively. Our results are summarized in Table. 4.1. Note the similarity of results obtained with the two different functionals.

Functional	d_{gs}	d_{es}	f_{gs}	f_{es}
PBE	0.787	0.956	-0.562	-2.555
SCAN	0.834	0.921	-0.563	-2.592

Table 4.1: Computed strain susceptibilities (see text) of the SnV$^-$ defect in diamond, in units of PHz/strain, obtained with the PBE and SCAN functionals.

4.4.3 Optical splitting with external B field

We scan the magnetic field over the whole sphere at fixed magnitude. The path between the approximately equidistant points is numerically minimised. The hysteresis of the B-field is on the order of 10 % as estimated from linear sweeps along a single magnet axis.

The splitting of the $A1, B2$ optical transitions with varying B fields can be computed by diagonalizing the system Hamiltonian H_{sys} of Eq. 4.1, and the results are shown in Fig 4.6 (b) and (c). When constructing the Hamiltonian, we considered the Steven's term g_L in the reduction factor q as a free parameter. The Steven's term, as discussed in subsection 4.4.1, originates from the defect symmetry being lower than $O(3)$. Here we determined the range of g_L by matching the experiments. We plot the difference of the splitting when the B field is aligned with the defect quantization axis ($\theta_B = 0$), and aligned along the equator ($\theta_B = \pi/2$) with varying $g_L \in [0, 1]$ in Fig 4.6 (c). The white region in the plot (values close to zero) corresponds to the two splittings being close in energy, matching the experimental observations. Therefore our calculations enabled the narrowing down of the the possible values of Steven's factor to $g_{L,\mathrm{gs}} \in [0.5, 1.0]$ and $g_{L,\mathrm{es}} \sim 2g_{L,\mathrm{gs}} - 1$.

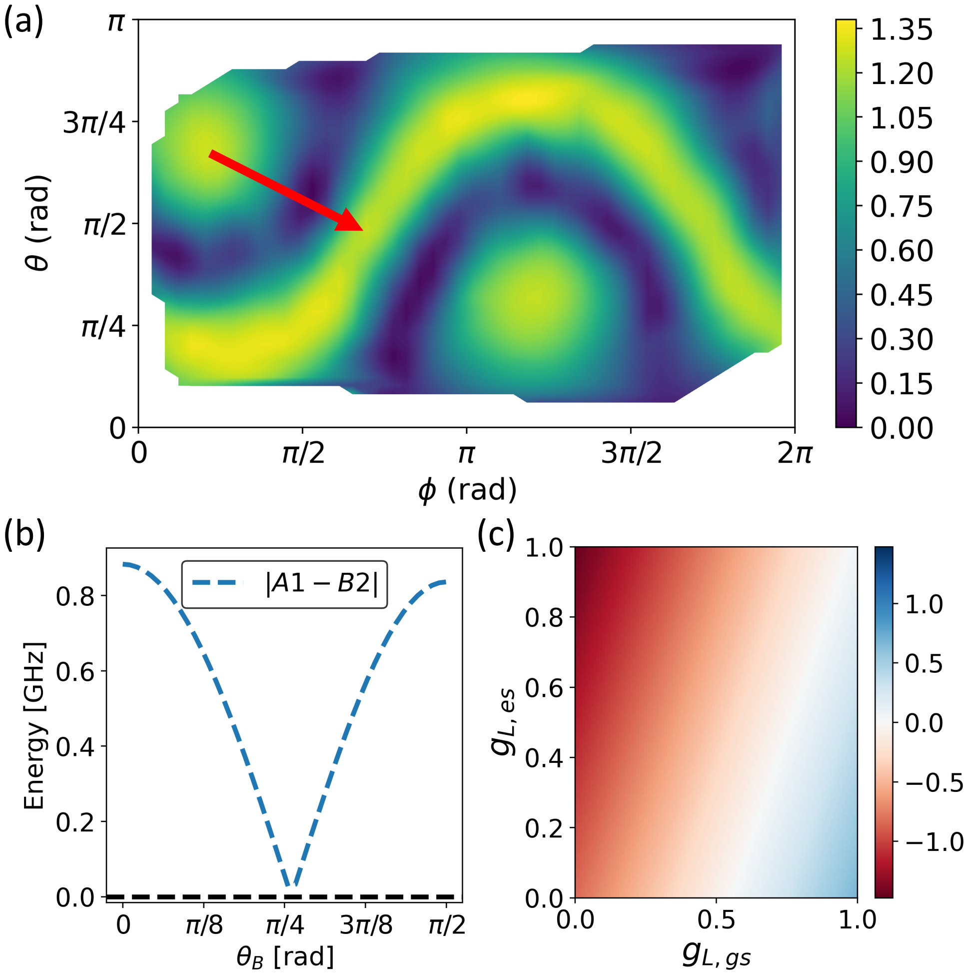

Figure 4.6: Experimental measured and simulations of the spin-conserving optical transitions $A1, B2$ with varying external magnetic field B. (a) Scanning of the splittings of $A1, B2$ transitions with varying B field directions. The magnitude of B is set to 0.2 T. The x, y axis represents the azimuthal (ϕ) and polar angle (θ) of the B field in the Lab frame. The two poles on the plot represent directions along the quantization axis of the SnV^{-} and the belt represents the equator. (b) Simulated splittings of the $A1, B2$ transitions by diagonalizing the system Hamiltonian along a chosen path of varying B fields, where the path is depicted as a red arrow in (a). The x axis represents the polar angle of the B field in the defect frame. Simulation agrees qualitatively with experiments with the magnitude of splitting underestimated by 0.4 GHz. (c) The differences between the $A1, B2$ splittings at $\theta_B = 0$ and $\theta_B = \pi/2$ with varying Steven's reduction factor. The white region corresponds to pairs of Steven's reduction factor for ground and excited states, when taken into the diagonalized Hamiltonian, that match the experimental observations.

CHAPTER 5

BASICS OF QUANTUM SIMULATIONS FOR FERMIONIC HAMILTONIANS

5.1 Motivations

As we've learned from the previous Chapters, accurately estimating the energy gaps of many-body electronic states of spin defects is crucial for understanding its mechanical/optical properties and subsequent engineering processes for realizing various quantum technologies. However, DFT as a mean-field theory doesn't always provide a quantitatively accurate prediction of these gaps, especially for systems beyond the weak correlation limit. In classical computational chemistry, several higher-level of methods have been developed to provide better accuracy, namely the coupled-cluster theory [28], configuration interaction [234] and multi-reference theories [265], with more expensive computational costs. The most accurate method given a certain basis set is the full configuration interaction (FCI) method. As its name suggests, its idea is to expand the total wavefunction to not only include the ground state Slater determinant configuration but also singly-excited, doubly-excited, up to those with all-electron excited configurations and finally diagonalize the FCI Hamiltonian matrix. This expansion is important to describe systems with strong correlations whose ground state wavefunction is highly entangled. However, the shortcoming of this approach is that it scales exponentially with system sizes.

The eigenvalue problem of the electronic structure is not the only problem where the curse of dimensionality exists. Turning to the dynamics problem, the textbook example of a separable wave function in terms of time and spatial domain points to an exponential dependence on the time variable, which holds in the adiabatic approximation (assuming the Hamiltonian stays constant in time). Thus, in simple terms, configuration interaction methods are amenable only for implementation within a computing paradigm where information can be stored and processed exponentially with the number of resources available.

Quantum computing is an emerging technology with the potential to revolutionize computational studies in chemistry and materials science. The initial idea for quantum computing came from Richard Feynman, who is often credited for conceiving the idea that a computing device working under the laws of quantum mechanics could be exponentially faster than a classical machine for certain classes of problems, an idea which was independently reached by Manin. One of the most immediate and natural applications of a quantum computer envisioned by Feynman was the simulation of other quantum systems. This opens the door to the solution of many problems that would otherwise be "practically impossible". The phrase "practically impossible" means that problems whose resource demands do not scale polynomially with the size/time of the simulation. The question of which problems are practically possible is addressed in a rich field of theoretical computer science known as computational complexity theory. However, such questions are beyond this dissertation and will not be addressed here. In light of Feynman's proposal and keeping in mind that chemistry is also governed by the laws of quantum mechanics, quantum chemistry has been seen by many as one of the first fields to showcase a tangible advantage from the employment of quantum computers, which comes from the superposition and entanglement found among qubits. In recent years, there has been a growing interest in exploring new ways to apply quantum computing to chemistry. In this Chapter, we'll review the basics of quantum computing, which will pave the way for subsequent discussions on more advanced topics.

5.2 The basics

5.2.1 Quantum gates and operations

In Chapter 1, we have introduced the basic processing units of quantum computers—the qubits, the next question is: How do we make them compute? From quantum mechanics, we learned that the evolution of any (closed) quantum system is unitary. That is, suppose a quantum computation starts with an initial state $|\psi_{\text{initial}}\rangle$, then the final state of the computation $|\psi_{\text{final}}\rangle$ must be the result of a unitary transformation U, which gives $|\psi_{\text{final}}\rangle = U|\psi_{\text{initial}}\rangle$. In classical computing, the basic components of a circuit that transforms a string $0, 1^{\otimes n}$ to another string are called gates. Analogously, in quantum computing, a unitary transformation U that transforms a system from $|\psi_{\text{initial}}\rangle$ to $|\psi_{\text{final}}\rangle$ can also be decomposed into sequential applications of basic unitary operations called quantum gates. Experimentally, the implementation of a quantum gate largely depends on the device and technique used for representing a qubit. For example, if a qubit is physically represented by the state of a trapped ion, then the quantum gate is executed by an incident laser pulse that perturbs the trapped atom(s) and alters its state; if the qubit states are encoded in the polarization states of photons, then a quantum gate consists of optical components that interact with photons and alter their polarization states as they travel through the components.

A number of widely used quantum gates include Pauli gates:

$$X = \begin{pmatrix} 0 & 1 \\ 1 & 0 \end{pmatrix}, \quad Y = \begin{pmatrix} 0 & i \\ -i & 0 \end{pmatrix}, \quad Z = \begin{pmatrix} 1 & 0 \\ 0 & -1 \end{pmatrix}, \tag{5.1}$$

where we have $X|0\rangle = |1\rangle$, $X|1\rangle = |0\rangle$. Therefore, the sheer effect of applying X to a qubit is to flip its state from $|0\rangle$ to $|1\rangle$. Other commonly used gates include the Hadamard gate H, Z rotation gate, phase gate S, and $\frac{\pi}{8}$ gate T:

$$H = \frac{1}{\sqrt{2}} \begin{pmatrix} 1 & 1 \\ 1 & -1 \end{pmatrix}, \quad S = \begin{pmatrix} 1 & 0 \\ 0 & i \end{pmatrix}, \quad T = \begin{pmatrix} 1 & 0 \\ 0 & e^{i\pi/4} \end{pmatrix}. \tag{5.2}$$

If a quantum gate involves two qubits, it can be represented by a 4×4 matrix. For example, in matrix form, the CNOT gate is defined as

$$U_{\mathrm{CNOT}} = \begin{pmatrix} 1 & 0 & 0 & 0 \\ 0 & 1 & 0 & 0 \\ 0 & 0 & 0 & 1 \\ 0 & 0 & 1 & 0 \end{pmatrix}. \tag{5.3}$$

Hence, the effect of a CNOT gate is equivalent to a conditional X gate. In classical computing, an arbitrary mapping from bits to bits can be executed by a sequence of basic gates such as AND, OR, NOT, and so on. Similarly in quantum computing, an arbitrary unitary transformation U can also be decomposed as a product of basic quantum gates. A complete set of such basic quantum gates is called a universal gate set.

5.2.2 Quantum measurements

The laws of quantum mechanics state that we cannot directly observe a state or wavefunction, but are restricted to performing measurements of these observables and that these measurements in turn collapse the state onto one of the eigenstates of the measured observable. Closely related in quantum information is the famous no-cloning theorem, which states that it is impossible to make copies of quantum states. This is an immediate consequence of how quantum measurement works, and it has drastic consequences for quantum computing. Specifically, the measurement of an observable O is given by the expectation value $\langle O \rangle = \langle \psi | O | \psi \rangle$. Unless $|\psi\rangle$ is prepared as an eigenstate of O, a series of measurements are needed to probe the distribution of eigenstates that compose $|\psi\rangle$, with each of the eigenvectors being associated with a probability of being measured. We can represent the state by $|\psi\rangle = \sum c_k |\phi_k\rangle$, with probability p_k that the state will collapse onto $|\phi_k\rangle$. Projecting $|\psi\rangle$ along $|\phi_k\rangle$ with the projector $P_k = |\phi_k\rangle\langle\phi_k|$ leads to $p_k = |\langle\phi_k|\psi\rangle|^2$.

It is important to note here that, although these are basic principles that guide quantum measurement in general, qubit states do not comprise a perfect closed system, thus projective measurements like the ones shown above are largely pedagogical and, even though they serve as the basis for how measurement is performed in quantum computers, operation of these devices require more elaborate strategies—-the projectors P_k can be replaced by more general measurement operators which still follow the basic premises above, but are not necessarily unitary. Also, one needs to choose the basis on which the measurement will take place, with the Z basis often being an obvious choice.

5.2.3 Quantum noise

The current age of quantum computing is typically referred to as the "noisy intermediate scale quantum" (NISQ) era [252], in which the best quantum processors have a few tens to a few hundred noisy qubits (although IBM recently proposed the concept of "quantum utility" era [157], with advancements in scaling the number of qubits beyond 1000). The most important character of NISQ is quantum noise. Noise refers to the multiple factors that can affect the accuracy of the calculations performed on a quantum computer. The noise has various sources, for example, fluctuations in magnetic field, local charge noises, cosmic rays, and even the influence of neighboring qubits (crosstalk) exerted on each other by mere proximity. These disruptions cause the information a qubit holds to fade away. Lastly, during a quantum operation, qubits can also suffer from errors that cause them to change by the wrong amount. In all cases, the final state of the quantum computer is not precisely the state one expects in the absense of noise. Unless one can reverse the action of the noise (which is termed coherent noise), the information in the quantum system can become random or erased. This phenomenon is known as decoherence.

Noise effects on quantum computing are typically described by the theory of open quantum systems and Kraus operators [59]. Prototypical noise channels that have been extensively studied include but are not restricted to depolarizing, bit-flip, and phase-flip channels [236]. Since quantum information is highly prone to decoherence, the outlook for quantum computing may appear confusing. Fortunately, a powerful technique known as quantum error correction [105] (QEC) provides a path forward: information is redundantly encoded into multiple physical qubits such that the effects of noise on the system can be, as the name suggests, corrected. QEC is a rich subject, but a key difficulty to reaching fault-tolerant quantum computing (wherein the probability of logical errors can be made arbitrarily small) is that current schemes require a large overhead in the total number of qubits and the error rate for individual physical qubit needs to be kept within a certain threshold beyond current physical platforms.

5.2.4 Quantum circuit and algorithms

A quantum circuit is a sequence of quantum gates. When an algorithm needs to be implemented on a quantum computer, it must first be translated to a quantum circuit to be executed on the quantum hardware.

Quantum phase estimation

The quantum phase estimation (QPE) algorithm is a general quantum routine that targets a certain eigenvalue in the spectrum of an observable. This can be readily identified with the problem of finding the ground state energy of a given molecule, that is, the QPE algorithm can be used to target the lowest energy eigenvalue of molecular Hamiltonians. The problem that the QPE algorithm attempts to solve can be stated as follows: for an arbitrary unitary U, one of its eigenvalues can be estimated as the phase U introduces into a given state. Mathematically $U|\psi\rangle = e^{2\pi i\theta}|\psi\rangle$.

A set of qubits is designated for state preparation purposes, while a second qubit register is used to tune in the precision of the measured phase. QPE makes extensive use of controlled operations. The phase is thus imparted via phase kickback, where the state of the control, not the target, is modified by a controlled operation. Upon an inverse quantum Fourier transform onto the control qubits, the phase can be estimated by measurement on the computational basis of the second qubit register. QPE is a very demanding algorithm, as the precision is determined by the number of times the oracle U is applied to $|\psi\rangle$, each one requiring an extra control qubit and adding to the depth of the circuit. To achieve a precision of ϵ, QPE requires $\mathcal{O}(\log(1/\epsilon))$ control qubits, limiting its application to small systems. A more widespread adoption would require a large number of qubits for increased precision and proper error correction. While QPE is often relegated to a coming fault-tolerant regime, a considerable amount of work has been done in the estimation of resources to enable QPE simulations in chemistry [22, 302].

Hamiltonian simulation

Unitary time evolution can be thought of as a natural application of quantum computers for the simulation of Hamiltonian dynamics. The task of Hamiltonian simulation is to approximately compile the evolution under a Hamiltonian $H(t)$, for time t, into a sequence of quantum gates. For a time-independent Hamiltonian, solving the Schrödinger equation yields a time evolution operator $U(t) = e^{-iHt}$. More generally, the unitary that describes the dynamics at time t (assuming it starts at $t = 0$) has the form $U(t) = \exp\left(-i\int_0^t H(t')dt'\right)$. The hamiltonian simulation does not give full access to the amplitudes of the wavefunction during the simulation, unlike classical approaches based on exact diagonalization (or similar methods). Instead, we are only able to measure observables with respect to the time-evolved state, or use the state as an input to other quantum subroutines. Nevertheless, there are no known efficient classical methods that achieve this for general local or sparse Hamiltonians, suggesting an exponential quantum speedup. In fact, as a quantum computation can be expressed as a time evolution under a sequence of local (time-dependent) Hamiltonians, quantum simulation (i.e. time evolution and measurement of a given observable) is a BQP (bounded-error quantum polynomial time)-complete problem [66]. Hamiltonian simulation algorithms require access to the Hamiltonian. Typically the Hamiltonian is given classically as a sum of products of Pauli operators, e.g. $H = \sum_k g_k H_k$, where g_k are coefficients and H_k are multi-qubit Pauli products.

A few different algorithms for Hamiltonian simulation purposes have been proposed, ranging from Trotterization [197], Linear combination of unitaries [31], qDRIFT [47], and quantum signal processing [201], each algorithm has its advantages and disadvantages.

Variational quantum algorithms

So far we talked about quantum algorithms aimed at fault-tolerant quantum computing, which is beyond the hardware we have access to today. In the current NISQ era, one does not have enough qubits or low enough error rates to carry out fault-tolerant quantum computation, and so one is limited to running low-depth quantum circuits. Under these constraints, structured quantum algorithms with prescribed circuits and provable guarantees are unknown. In light of this, variational quantum algorithms (VQAs) have been proposed, which could also be run on fault-tolerant devices. Whilst many VQAs have been proposed for a wide range of applications, they all share a similar core primitive. The main idea is to encode the target problem into an optimization task of minimizing the expectation value of some parametrized quantum circuit, or a function thereof. In each optimization step, a quantum computer is used to evaluate expectation values at chosen parameter values, which are read by a classical optimizer that updates the parameters for the next step. The motivation for this framework is to offload some of the computational complexity onto the classical optimization algorithm, with an aim for the quantum subroutines to perform classically intractable calculations.

CHAPTER 6

SIMULATING THE ELECTRONIC STRUCTURE OF SPIN DEFECTS ON QUANTUM COMPUTERS

This chapter is adapted with permission from **B. Huang**, M. Govoni, and G. Galli. Physical Review X Quantum 3.1 (2022): 010339. Copyright (2022) by the American Physical Society. https://doi.org/10.1103/PRXQuantum.3.010339.

In this chapter, we present calculations of both the ground and excited state energies of spin defects in solids carried out on a quantum computer, using a hybrid classical/quantum protocol. We focus on the negatively charged nitrogen vacancy center in diamond and on the double vacancy in 4H-SiC, which are of interest for the realization of quantum technologies. We employ a recently developed first-principle quantum embedding theory to describe point defects embedded in a periodic crystal, and to derive an effective Hamiltonian, which is then transformed to a qubit Hamiltonian by means of a parity transformation. We use the variational quantum eigensolver (VQE) and quantum subspace expansion methods to obtain the ground and excited states of spin qubits, respectively, and we propose a promising strategy for noise mitigation. We show that by combining zero-noise extrapolation techniques and constraints on electron occupation to overcome the unphysical state problem of the VQE algorithm, one can obtain reasonably accurate results on near-term-noisy architectures for ground and excited state properties of spin defects.

6.1 Introduction

Quantum simulations of the physical and chemical properties of molecules and solids [152] are crucial to gain insight into a wide range of complex problems, for example catalytic reactions [120] and the search for optimal materials for sustainable energy sources [180] and quantum technologies [332, 335]. One of the essential ingredients of quantum simulations is the solution of the electronic structure problem for molecules and solids, namely the time-independent Schrödinger equation of interacting electrons in the field of atomic nuclei. Such solution provides the basis for the evaluation of numerous ground and excited state properties of matter. However, the algorithms used at present on classical computers to solve the electronic structure problem, especially those based on wavefunction methods, face serious computational bottlenecks due to the exponential growth of the dimension of the many-body wavefunction as a function of system size [48].

Quantum computers hold promise to drastically improve our ability to carry out quantum simulations of many-electron systems by taking advantage of superposition and entanglement principles offered at the hardware level by quantum bits (qubits) [29, 48, 123]. N qubits can represent 2^N complex numbers, which would require 2^{N+7} bits to be represented in double precision on classical computers, and some problems, such as the solution of the Schrödinger equation, may benefit from the memory scaling. Whether one can achieve quantum advantage in solving useful chemistry and physics problems on quantum computers is still under debate. However, efforts to develop algorithms to simulate molecules and solids on quantum computers [16, 126, 154, 241, 254] have been flourishing in the last decade, and several interesting results on ground and excited states of small molecular systems (containing up to a dozen atoms) have appeared in the literature [188, 231, 275, 292].

The number of degrees of freedom and hence the number of atoms that can be handled at present on near intermediate scale quantum (NISQ) computers is limited, due to the availability of hardware architectures with only a small number of low-fidelity qubits (a 127-qubit device was recently announced but devices used for most calculations appeared in the literature have few tens of qubits). In particular, the hardware limitation poses a challenge for quantum simulations of heterogeneous solids which require the use of supercells with hundreds of atoms. Recent studies have focused on two fronts: (i) reducing the complexity of the simulations of condensed phases by using an effective Hamiltonian to represent a fragment (or active part) of a solid [203], thus effectively reducing the number of degrees of freedom; and (ii) developing techniques to mitigate the noise present in NISQ hardware [88] which affects the results of calculations on quantum computers. These techniques are based on different methods, including zero-noise extrapolation (ZNE) [187], symmetry verification [273], quasi-probability methods [87, 311], or stochastic error mitigation [305]. An alternative strategy to complexity reduction is the use of model Hamiltonians, e.g., Hubbard, Heisenberg [164, 321].

Recently, we proposed a computational framework [325] to carry out the calculation of the electronic structure of an active site in a periodic system using a quantum embedding theory which we call here quantum *defect* embedding theory (QDET) [203, 204] that is suitable, for example, for the study of spin-defects. Spin-defects in semiconductors and insulators are promising candidates for the realization of quantum technologies [138, 332, 335], including quantum sensing and communication. The electronic states of spin-defects usually exhibit a multi-reference nature, which requires methods beyond mean-field theories for a proper description.

In this work, we present calculations of both ground and excited states of two spin-defects, i.e., the NV^- center in diamond and the double vacancy (VV) in 4H-SiC described by QDET using a hybrid classical/quantum protocol on a real quantum computer. To the best of our knowledge, the calculations of excited state are reported here for the first time. In addition, we present the application of a correction scheme to impose physical constraints on the output of quantum simulations, and we propose an extrapolation strategy to carry out error mitigation.

The rest of this chapter is organized as follows: in chapter 6.2 we present the classical and quantum algorithms used in this work and in chapter 6.3 the results of our calculations, including error analysis and mitigation techniques. Chapter 6.4 concludes the work with a summary and outlook.

6.2 Methods

As mentioned in the introduction, there are numerous problems in condensed matter physics and chemistry, including point defects in semiconductors, that can be naturally formulated in terms of active regions surrounded by a host medium. These problems can be addressed using embedding theories [189] where the electronic structure of the host and the active region are described at different levels of theory, in particular a higher level of theory is chosen for the active region, which can describe the multi-reference character of wavefunctions. The QDET proposed in Ref [203, 204] is an example of embedding theories formulated in terms in Green's functions, and it has been shown to accurately describe the low-lying excitations of several spin-defects in insulators [203]. The computational strategy of our work is centered on QDET and on calculations of the electronic structure of spin defects on quantum computers. Fig. 6.1 summarizes the methods adopted in this work to carry out mean-field calculations for a chosen supercell, followed by QDET calculations for a defect, and the definition of an effective Hamiltonian for the active space of the defect. The calculation of the ground and excited states of the effective Hamiltonian are carried out on a quantum computer with a variational quantum eigensolver (VQE) and the quantum subspace expansion (QSE), respectively. These methods, starting with QDET, are briefly summarized below.

6.2.1 Quantum Defect Embedding Theory to obtain effective Hamiltonians

We first define a periodically repeated arrangement of several hundreds of atoms (or supercell) representing the point-defect of interest within a given solid, and we compute the electronic structure of the supercell from first principles with Density Functional Theory (DFT) or hybrid-DFT. We then select a sub-set of single particle wave-functions which are localized around the defect and physically represent its electronic states. This sub-set defines an active space whose excitations are described by an effective Hamiltonian H_{eff}. The effective potential entering H_{eff} is evaluated by computing the effect of the environment onto the active space with many-body perturbation theory techniques; two-body interactions are evaluated using constrained DFT either within the constrained random-phase approximation (cRPA) [12] or by including explicitly exchange-correlation effects [202, 235]. The effective Hamiltonian includes correlation effects between the electronic states of the active space. In this work we use QDET to describe strongly correlated electronic states of point-defects that are not properly described by single-determinant wavefunctions, and hence by DFT.

In essence, using QDET one can reduce the complexity of evaluating many-body states of a small guest region embedded in a large host system: the problem is reduced to diagonalizing a many-body Hamiltonian simply defined on an active space, where the number of degrees of freedom is smaller than that required to describe the entire supercell of hundreds of atoms.

The active spaces of the systems discussed in this work contain less than ten electrons, and H_{eff} can be solved using the full configuration interaction (FCI) [124] method on a classical computer. However FCI scales exponentially with system size and it has so far been limited to active spaces with up to 22 electrons and 22 orbitals [324]. Hence, in order to solve more complex problems, the opportunity offered by quantum computers appears worth exploring, as the overall scaling of FCI may eventually be overcome with quantum architectures.

6.2.2 Variational Quantum Eigensolver to obtain ground state energies

As mentioned in the introduction, quantum computers have an exponential memory advantage over classical hardware, which in principle may be harnessed to compute the eigenstates of a Fermionic Hamiltonian representing a many-body system of electrons. For example, the quantum phase estimation (QPE) [16] algorithm has been proven to be exponentially faster in finding eigenvalues of unitary operators than any available algorithm on a classical computer [2, 3, 163]. However, calculations using QPE are still impractical in the absence of error correction and require quantum resources that exceed the current capability of NISQ hardware [85]. An alternative algorithm to QPE is the variational quantum eigensolver (VQE) [245], where the properties of many-body states are measured on a quantum device, but the parameters that define such states are stored on a classical computer. Therefore, VQE allows one to use shallower circuits than QPE and hence to perform calculations on non fault-tolerant quantum computers [50].

In the last decade VQE has been successfully applied to several quantum chemistry problems [126, 154, 241, 245, 254], including the calculation of the total energies of small molecules, the evaluation of forces by finite differences from Hartree-Fock total energies for the H_2 molecule [92], and the calculations of the zero-field NMR spectrum of the methyl group of acetonitrile on a trapped-ion quantum computer [281].

When using VQE, the ground state of the Hamiltonian is approximated by a normalized trial state $|\Psi(\vec{\theta})\rangle = U(\vec{\theta})|\Psi_0\rangle$, where the unitary operator $U(\vec{\theta})$ is constructed using a set of classical parameters $\vec{\theta} = (\theta_1, \ldots, \theta_n)$ and $|\Psi_0\rangle$ is a (usually unentangled) initial state. The expectation value $\langle E(\vec{\theta})\rangle = \langle\Psi(\vec{\theta})|\hat{H}|\Psi(\vec{\theta})\rangle$ provides an upper bound to the ground state energy of the system. The energy expectation value is optimized on a classical computer by variationally optimizing the parameters $\vec{\theta}$, with all inputs (energy values) evaluated on a quantum computer. Here we used VQE to find the ground state energy and corresponding eigenvector of effective Hamiltonians obtained using the QDET.

The physical Hamiltonian (H_{eff}) is mapped onto a qubit Hamiltonian $\hat{H}_q$, e.g., by using the Jordan-Wigner [334], Bravyi-Kitaev [40], or parity [39] mapping: $\hat{H}_q = \sum_i g_i \hat{P}_i$, where g_i are coefficients determined by one and two-electron integrals, and $\hat{P}_i = \{I, X, Y, Z\}^{\otimes N}$ are Pauli correlators acting on N qubits. In general, the mapping from H_{eff} to $\hat{H}_q$ does not insure that the Hilbert space of the qubit Hamiltonian is the same as that of the original Hamiltonian and hence it is necessary to impose constraints on the many-body wavefunction through an ansatz to avoid introducing “unphysical states” in the space of $\hat{H}_q$, i.e., states that are not present in the Hilbert space of H_{eff}. Furthermore, a proper ansatz should satisfy additional, multiple requirements. It is of course important to choose variational parameters spanning a manifold of states that can accurately approximate the ground state of the system. In addition, the chosen unitary operator $U(\vec{\theta})$ should be constructed in such a way that it can be implemented with the current capacity of gates and qubit connectivity of NISQ computers. There are two classes of ansätze explored in the literature: hardware efficient ones, designed specifically by taking into account the hardware characteristics [154], and chemistry-inspired ones. The former class usually enables the use of short depth quantum circuits at the expense of including a large number of variational parameters, while chemical inspired ones attempt to minimize the number of variational parameters, leading to the need for deeper circuits.

In this work, we chose the Unitary Coupled Cluster Singles and Doubles (UCCSD) ansatz [245, 264], which belongs to the chemically inspired class and originates from coupled cluster theory [28, 124]. The UCCSD ansatz involves the definition of a unitary operator through the exponential of a couple cluster operator that contains pertinent single and double electronic excitations:

$$|\Psi\rangle = e^{\hat{T}-\hat{T}^\dagger} |\Psi_0\rangle \, , \; \hat{T} = \sum_{i\in\mathcal{A}, a\in\mathcal{V}} \theta_i^a \hat{a}_a^\dagger \hat{a}_i + \frac{1}{4} \sum_{i,j\in\mathcal{A};\; a,b\in\mathcal{V}} \theta_{i,j}^{a,b} \hat{a}_a^\dagger \hat{a}_b^\dagger \hat{a}_j \hat{a}_i, \tag{6.1}$$

where i, j are occupied single particle orbitals (belonging to subspace $\mathcal{A}$), a, b are virtual orbitals (belonging to subspace $\mathcal{V}$), $\hat{a}^\dagger, \hat{a}$ are the fermionic creation and annihilation operators, and $\theta_i^a, \theta_{i,j}^{a,b}$ are variational parameters. A straightforward implementation of Eq. 6.1 is challenging as the operators describing electronic excitations may not commute. A numerically manageable solution may be obtained by introducing a so called "trotterized" version of the unitary operator defining the UCC ansatz. We consider two electronic excitation operators

$\hat{A}$ and $\hat{B}$ that do not commute and the Trotter-Suzuki formula:

$$e^{\hat{A}+\hat{B}} = \lim_{n\to\infty} \left(e^{\frac{\hat{A}}{n}} e^{\frac{\hat{B}}{n}} \right)^n . \tag{6.2}$$

The evaluation of the right-hand side of Eq. 6.2 requires large values of n, which is expected not to be practical for NISQ computers as it would require long circuits. An approximation widely adopted in the literature is to use $n = 1$ i.e., $e^{\hat{A}+\hat{B}} \approx e^{\hat{A}} e^{\hat{B}}$ (one-step first-order Trotter-Suzuki approximation). Such an approximation introduces an error (Trotter error) and we notice that the ordering of A and B on the right-hand side could have an impact on this error, as discussed in Ref. [110].

6.2.3 Quantum Subspace Expansion to obtain excited state energies

We now turn to the discussion of the calculations of excited states, for which different algorithms are required. The excited states of a fermionic Hamiltonian may be computed on a quantum computer starting from the output of VQE optimizations by using, e.g., the variational quantum deflation (VQD) [133] or quantum subspace expansion (QSE) algorithms. The former is a constrained variational approach where a penalty term $\langle \Psi_i | \Psi \rangle$ is added to the energy expectation value to enforce orthogonality among states. A prerequisite for using VQD is that the target excited states should be included in the manifold of states spanned by the variational wavefunction defined by the chosen ansatz; such a requirement is not straightforward to insure. The QSE is an alternative strategy to VQD and can be viewed as a quantum analog of FCI. Once a reference wavefunction $|\Psi\rangle$ is prepared, a set of expansion operators $\{\hat{O}_i\}$ is chosen, which act on $|\Psi\rangle$ to form a basis given by $\{\hat{O}_i |\Psi\rangle\}$, where $\hat{O} \in \{\hat{a}_a^\dagger \hat{a}_i ,\ \hat{a}_a^\dagger \hat{a}_b^\dagger \hat{a}_j \hat{a}_i | i, j \in \mathcal{A};\ a, b \in \mathcal{V}\}$. We evaluate the Hamiltonian and overlap matrix elements using such basis:

$$H_{ij}^{\mathrm{QSE}} = \langle \Psi | \hat{O}_i^\dagger \hat{H} \hat{O}_j | \Psi \rangle , \quad S_{ij}^{\mathrm{QSE}} = \langle \Psi | \hat{O}_i^\dagger \hat{O}_j | \Psi \rangle . \tag{6.3}$$

Using the matrices defined above, we then solve the generalized eigenvalue problem in the well conditioned subspace given by

$$H^{\mathrm{QSE}} C = S^{\mathrm{QSE}} C \varepsilon, \tag{6.4}$$

where C is the matrix of eigenvectors and ε the diagonal matrix of eigenvalues. As mentioned in section 6.2.2, the Fermion-to-qubit mapping is used to transform the Fermion operators $\hat{a}_i^\dagger, \hat{a}_j$ into Pauli operators acting on N qubits, and the matrix elements are evaluated as weighted sums of the expectation values of Pauli correlators. The reference $|\Psi\rangle$ is usually taken to be the ground state. The effectiveness of the QSE relies on a careful choice of creation and annihilation operators which should enable the description of the desired excitations.

In our work, we use QSE to compute excited states for two reasons: (i) the construction of the Hamiltonian H^{QSE} and overlap matrix S^{QSE} elements may be carried out using the same quantum circuit as those used for VQE [217] calculations of the ground state, and (ii) the procedure does not require additional quantum resources, but only additional measurements [61].

6.3 Results

In this section we describe the results for the many-body ground and excited states of the NV$^-$ center in diamond and VV in 4H-SiC obtained using the IBM Qiskit package [253] on the *ibmq_ casablanca* quantum computer.

6.3.1 Reference results on classical hardware

The single particle electronic structure of the NV$^-$ center in diamond and the VV in 4H-SiC is computed with hybrid DFT using 216-atom and 200-atom periodic supercells, respectively.

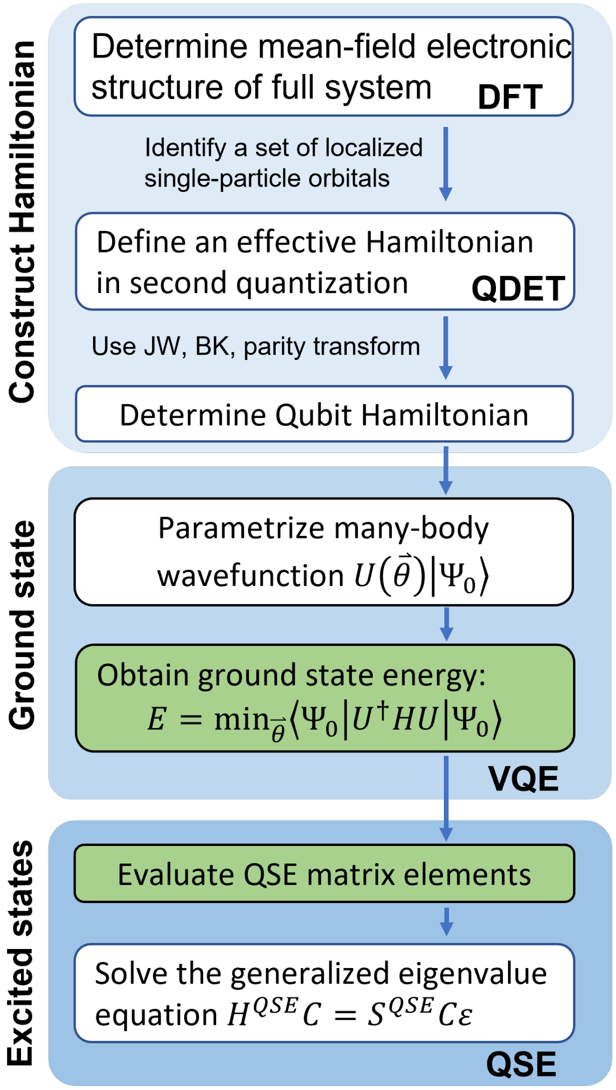

Figure 6.1: Workflow used to simulate the ground and excited state energies of spin defects, with operations executed on a quantum computer indicated in green. The transformation from a second quantized to a qubit Hamiltonian may be obtained with a Jordan-Wigner (JW), Bravyi-Kitaev (BK) or parity transformation. DFT and QDET denotes calculations carried out using Density Functional Theory and the quantum defect embedding theory, respectively. VQE and QSE denotes the variational quantum eigensolver and quantum subspace expansion algorithms used for ground and excited state calculations, respectively. See text for definition of the equations.

We use the plane-wave pseudopotential method as implemented in the Quantum Espresso code [97], dielectric-dependent hybrid functionals (DDH) [291], and a kinetic energy cutoff of 50 Ry. For both systems the active space contains the single particle states localized at

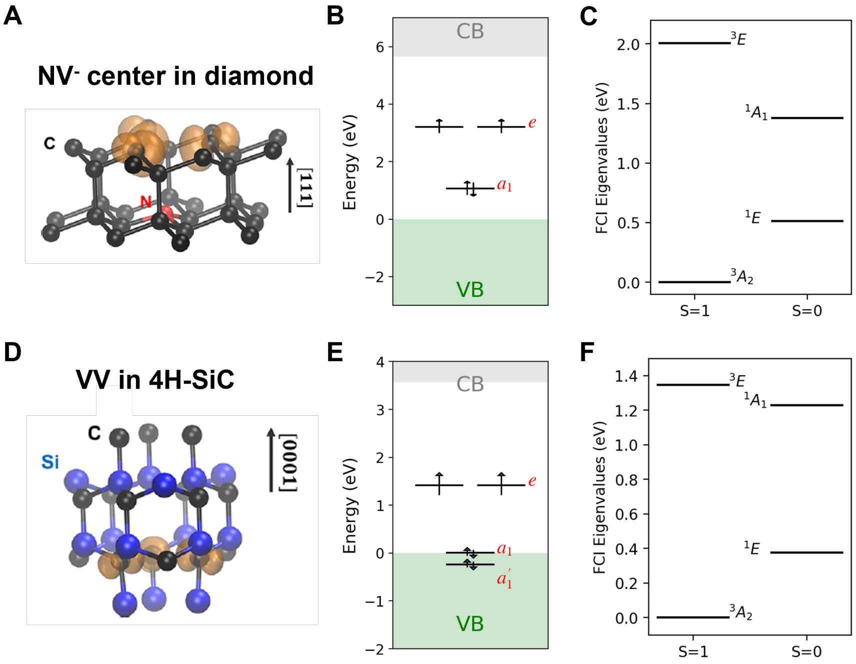

Figure 6.2: Spin defects studied in this work: the NV$^-$ center in diamond and the VV in 4H-SiC. Panels A and D show a ball-and-stick representation of the defects, where orange iso-surfaces are total spin densities. Panels B and E show single particle states obtained by solving the Kohn-Sham equations for the entire periodic solid, where gray and green shaded areas represent the conduction (CB) and valence band (VB), respectively; the single particles states shown as black lines were used to build the (4e, 3o) and the (6e, 4o) minimum models for the active spaces of the NV$^-$ and VV centers, respectively. Panels C and F show the low-lying many-body energy levels obtained by solving the effective Hamiltonians using the FCI method on classical hardware.

the defect site and we refer to the use of this active space as the “minimum model”, which at present represents the best compromise between accuracy and efficiency (see Fig. 6.2). We adopt the QDET embedding scheme as implemented in the WEST [109] code and we evaluate the dielectric screening beyond the random-phase approximation by coupling the WEST and Qbox [118] codes, as in Ref. [204]. The effective Hamiltonian is diagonalized with FCI using the PySCF code [306] on a classical hardware and the eigenvalues obtained in this way are considered as reference results for our calculations on a quantum computer. The atomic and electronic structures of the defects studied here, chosen active spaces, and FCI results are summarized in Fig. 6.2.

6.3.2 Calculation of the ground state using a quantum computer

The ground state of the effective Hamiltonian constructed for both the NV$^-$ center in diamond and the VV in 4H-SiC is a $^3A_2$ triplet state. Using the minimum models described above (see Fig. 6.2), the $m_s = 0$ component may be written as a linear superposition of two Slater determinants [203]:

$$\left|^3A_2, m_s = 0; \mathrm{NV}\right\rangle = \frac{1}{\sqrt{2}}\left(\left|a_1\bar{a}_1e_x\bar{e}_y\right\rangle + \left|a_1\bar{a}_1\bar{e}_xe_y\right\rangle\right), \tag{6.5}$$

$$\left|^3A_2, m_s = 0; \mathrm{VV}\right\rangle = \frac{1}{\sqrt{2}}\left(\left|a_1'\bar{a}_1'a_1\bar{a}_1e_x\bar{e}_y\right\rangle + \left|a_1'\bar{a}_1'a_1\bar{a}_1\bar{e}_xe_y\right\rangle\right), \tag{6.6}$$

for the NV$^-$ and the VV center, respectively. In Eq.s 6.5-6.6, a_1', a_1, e_x, e_y (spin-up) and $\bar{a}_1'$, $\bar{a}_1$, $\bar{e}_x$, $\bar{e}_y$ (spin-down) denote the single particle orbitals.

We first focus on the NV$^-$ center and consider two initial states that are used as trial wavefunctions for the VQE algorithm: (a) $|a_1\bar{a}_1e_x\bar{e}_x\rangle$, or (b) $\left|a_1\bar{a}_1e_x\bar{e}_y\right\rangle$. The UCCSD expression of Eq. 6.1 is used as an ansatz for the unitary operator applied to the trial state. In case (a) the ansatz leads to a trial wavefunction with six variational parameters, whereas in case (b) the trail wavefunction contains only $\theta_{e_x\bar{e}_y}^{e_y\bar{e}_x}$ as variational parameter (for convenience of notation, we refer to this parameter as θ since all additional parameters may be set to zero to enforce from the start a triplet solution). The effective Hamiltonian of both systems is transformed onto a qubit representation using the parity mapping [39].

Fig. 6.3 shows the convergence of the ground state energy as a function of the number of VQE iterations, starting from either trial states. We obtain convergence to the same results as obtained with FCI when using a quantum simulator (i.e., in the absence of noise) for both trial states; however, we obtain two different values when using *ibmq_ casablanca*, due to the presence of hardware noise. Not surprisingly the impact of noise on the results depends on the choice of the initial state. In case (a), where there are six variational parameters and the circuit depth is 26, we obtain a ~0.07 eV error, while in case (b), where there is only one variational parameter and the circuit depth is 6, the error is smaller (~0.02 eV). For case (b), i.e., when the initial state $|\Psi_0\rangle = \left|a_1\bar{a}_1 e_x \bar{e}_y\right\rangle$, the variational wavefunction in the UCCSD ansatz reads:

$$|\Psi(\theta)\rangle = \cos\left(\frac{\theta}{2}\right)\left|a_1\bar{a}_1 e_x \bar{e}_y\right\rangle + \sin\left(\frac{\theta}{2}\right)\left|a_1\bar{a}_1 \bar{e}_x e_y\right\rangle. \tag{6.7}$$

As expected, the energy has a minimum when $\theta = \frac{\pi}{2}$, i.e., for $\left|\Psi(\frac{\pi}{2})\right\rangle = \left|{}^3A_2, m_s = 0; \mathrm{NV}\right\rangle$. In the following, we choose the initial state as in (b) above, and use a simultaneous perturbation stochastic approximation (SPSA) [297] optimizer, which has been shown to be robust to noise [154]. The corresponding quantum circuit is depicted in Fig. 6.4. We choose physical qubits such that the mapping leads to a qubit configuration minimizing faulty CNOT gates.

The energy obtained with VQE as a function of the number of iterations is reported in Fig. 6.5 A and B (blue dots). We find that several measurements of the energy yield a value smaller than the FCI result, and the number of occurrences is larger for the VV than the NV$^-$ center. These incorrect results are a manifestation of the so called unphysical state problem [216, 276], where in some cases quantum circuits yield states with an incorrect number of electrons causing an inaccurate evaluation of the energy. The unphysical state problem was first pointed out by Sawaya et al. [276] using simple noise models to study second row dimers, and several methods to correct for unphysical states were recently proposed, including error detection using ancilla qubits [216].

We found that the apparent violation of the variational principle does pose a serious problem to the applicability of the VQE algorithm to the calculations of the electronic properties of spin defects in materials. The severity of this problem also depends on the chosen Fermion-to-qubit transformation, which in turn determines the extent to which the qubit Hilbert space differs from the configuration state space spanned by the Fermionic Hamiltonian [284].

We adopt a post-selection method to enforce the validity of the variational principle

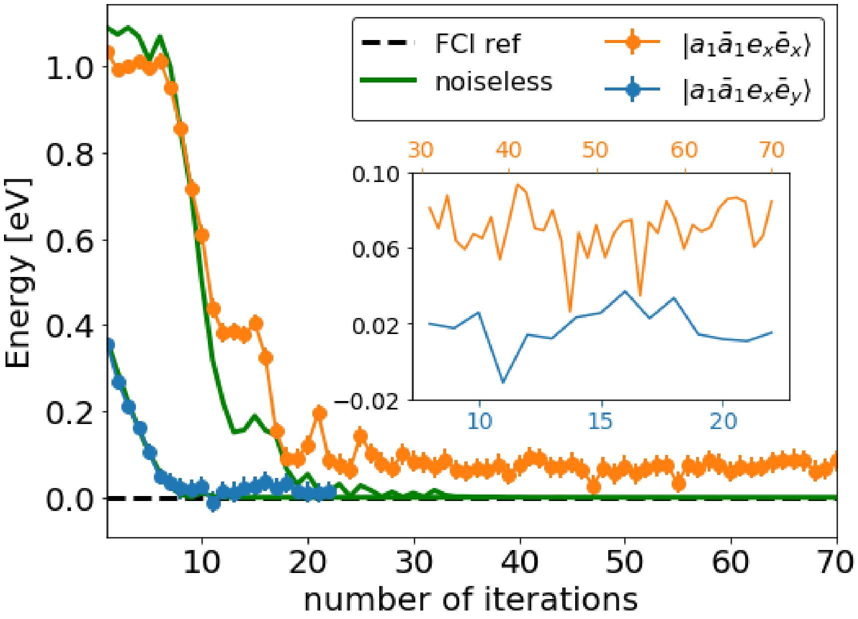

Figure 6.3: Optimization of the $|^3A_2, m_s = 0\rangle$ state of the NV$^-$ center using the variational quantum eigensolver (VQE) on *ibmq_casablanca* and on a noiseless simulator using four qubits. The strongly-correlated $\frac{1}{\sqrt{2}}(|a_1\bar{a}_1e_x\bar{e}_y\rangle + |a_1\bar{a}_1\bar{e}_xe_y\rangle)$ state is obtained starting from: the $|a_1\bar{a}_1e_x\bar{e}_x\rangle$ state, or the $|a_1\bar{a}_1e_x\bar{e}_y\rangle$ state. We used the parity transformation to obtain the qubit Hamiltonian acting on four qubits; the optimization was carried out with the COBYLA algorithm [251]. The noiseless simulation was performed with the QASM simulator [64]. The zero of energy is the result obtained on classical hardware with the full configuration interaction (FCI) method. In the inset we compare the converged energies obtained from the two chosen trial states.

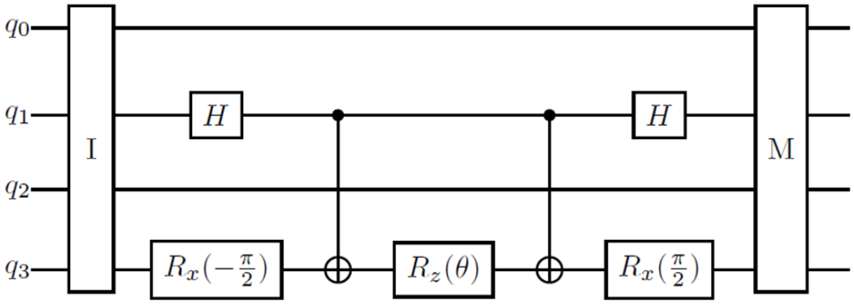

Figure 6.4: Quantum circuit executed on four qubits (q_0 to q_3): I, and M represent the state initialization and measurement blocks, respectively. The measurement block includes Pauli correlators so as to enable the measurement of observables, e.g., the energy and the electron number. The symbol H represents a Hadamard gate; $R_{x,z}(\theta)$ represents the rotation of the variational parameter θ (see text) around the x, z axis.

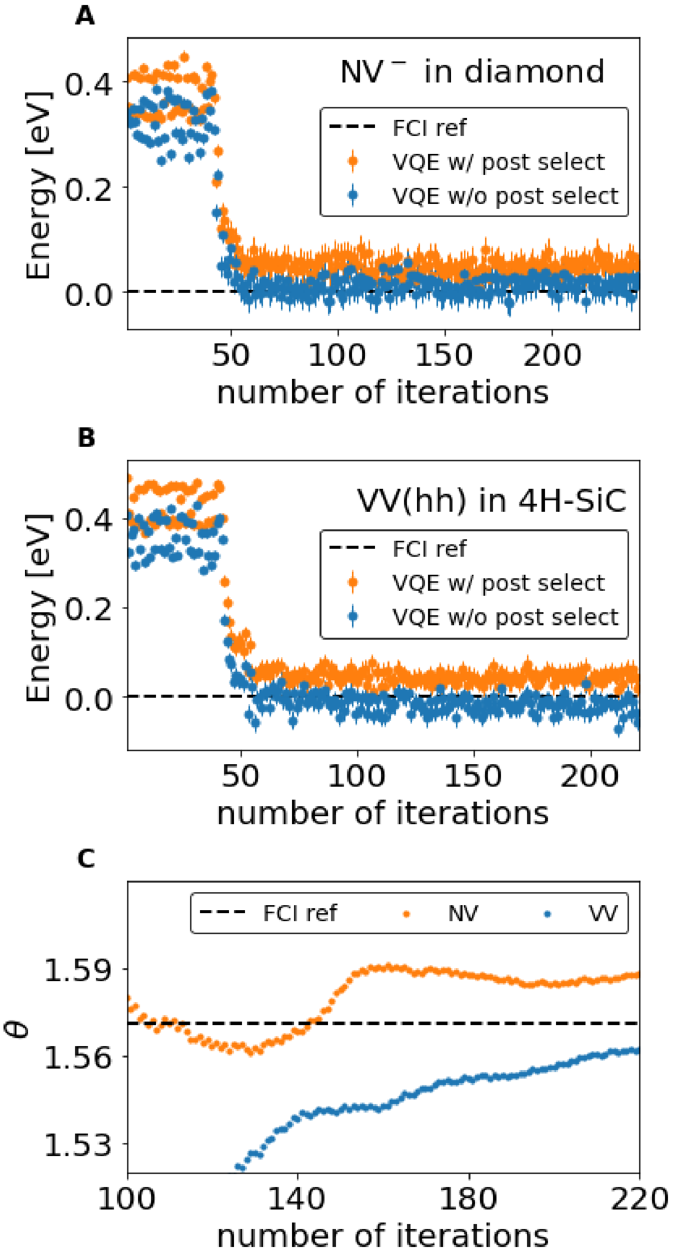

Figure 6.5: Optimization of the ground state energy of the NV$^-$ in diamond A and VV(hh) in 4H-SiC B carried out with the variational quantum eigensolver (VQE) algorithm using four and six qubits respectively on *ibmq_casablanca*, with (orange dots) and without (blue dots) post-selection of states (see text). The full configuration interaction (FCI) energy is reported for reference. In panel C we show the variation of the parameter θ (see Eq. 6.7) in the VQE optimization; the value is obtained from averaging the parameter at the end of the VQE optimization. The dashed line corresponds to the exact solution, i.e., $\theta = \frac{\pi}{2}$.

during the VQE optimization. After using the Fermion-to-qubit transformation, the energy is evaluated on the quantum hardware as the weighted sum of the expectation values of Pauli correlators, i.e., $E = \sum_i g_i \langle \hat{P}_i \rangle$. The expectation values of all Pauli correlators were obtained by measuring 8192 times N_c independent circuits, where N_c is the number of groups of Pauli correlators that contain commuting operators. The number of electrons may be determined simultaneously from the group of operators that only contains diagonal Pauli correlators (those with only I and Z gates) [86]. In our calculations we discard all measurement outcomes that do not conserve the number of electrons. Interestingly, the weights g_i of diagonal Pauli correlators lead to the dominant contribution to the energy. The orange curves in Fig. 6.5 A and B show the convergence of the VQE algorithm when energy measurements are obtained with the post-selection method, and Fig. 6.5 C shows the convergence of the variational parameter θ with a relative error of less than 2%. Upon enforcement of the post-selection rule all measured energies turn out to be higher than the reference value for the ground state. Interestingly, the same post-selection method has also been adopted in the calculation of the total energy of LiH [86], yielding a notable improvement in the accuracy of energy measurements, with a small overall error of about 1 kcal/mol.

In Fig. 6.6 we further analyze the effects of noise on the results by scanning the total energy as a function of θ: $E(\theta = \frac{\pi}{2})$ is the energy of the ground state and $E(\theta = -\frac{\pi}{2})$ that of an excited state. In the region close to the minimum (ground state) the values obtained with post selection (orange curve) are higher than the noiseless reference values (dashed black curve): indeed the post-selection process removes states that, due to the presence of noise, do not correspond to the correct number of electrons; hence, in virtue of the variational principle, one obtains an energy higher than the reference value. However in the region close to $\theta = -\frac{\pi}{2}$ (excited state) where the variational principle does not hold, even after post-selection one may obtain errors of different signs. Therefore a spurious cancellation of errors may occur and the overall error on the energy for $\theta < 0$ appears to be smaller than in

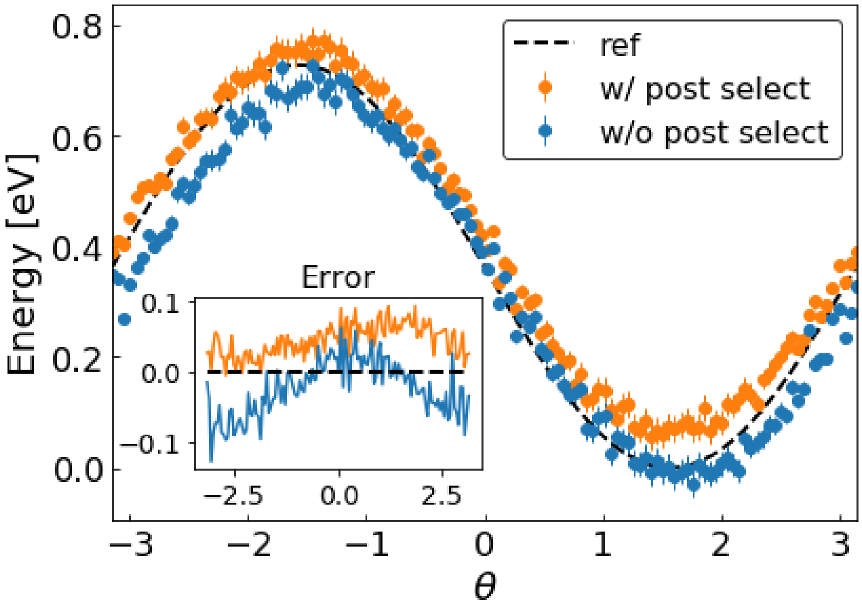

Figure 6.6: Energy variation of the ground state of the NV$^-$ center in diamond as a function of the parameter θ (see Eq. 6.7 in text) using *ibmq_ casablanca*. We show results with (orange) and without post-selection of states (blue). The straight black line (ref) indicates the energy obtained with a noiseless simulator. Inset: difference between the energy evaluated on quantum and classical hardware.

proximity of the ground state ($\frac{\pi}{2}$)).

To improve the accuracy of energy measurements, numerous mitigation schemes have been developed, including the quasi-probability method [87, 311], individual error reduction [240], and learning-based error mitigation [301]. These methods require complete information of the noise channel or a large number of quantum measurements. We note that quantum noise is usually described using the language of open quantum systems and Kraus operators, and exact forms of the these operators [88] are required in order to obtain a complete information of the noise channel, which is a difficult task for realistic hardware architectures. Here, we adopt the zero-noise extrapolation (ZNE) method, which is straightforward to implement and does not require additional qubits. The essence of the method is the expansion of the expectation value of an observable, for instance the energy E, as a power series of noise around its zero-noise value E^* [88, 155]:

$$E(\lambda) = E^* + \sum_{k=1}^{n} a_k \lambda^k + O(\lambda^{n+1}). \tag{6.8}$$

Here λ is an appropriately small ($\lambda \ll 1$) noise parameter, and the coefficients in the expansion a_k depend on specific details of the noise (i.e., on the unknown form of the Kraus operators describing the specific noise channels). The basic idea of ZNE is to amplify the noise of the circuit to various controllable levels and obtain the zero noise limit by extrapolation. Error mitigation via ZNE has been explored in several pioneering papers [81, 155] investigating small molecules and Ising Hamiltonians. Popular ways to artificially boost the error include identity insertions [121], unitary folding [99], and re-scaling of the Hamiltonian [155, 311].

Here, we propose a simple technique to boost the error for the ZNE, which we call exponential block replication. The method is applicable to all cases where the UCC ansatz [93, 181, 193] is used. As discussed in Chapter 6.2.2, UCC ansätze are typically implemented using the approximation $e^{\hat{A}+\hat{B}} \approx e^{\hat{A}} e^{\hat{B}}$. In this case multiple consecutive applications of n exponential blocks lead to the following expression: $e^{\hat{A}+\hat{B}} \approx e^{\hat{A}} e^{\hat{B}} = \left(e^{\frac{\hat{A}}{n}}\right)^n \left(e^{\frac{\hat{B}}{n}}\right)^n$. This expression is different from that obtained with a n-step first-order Trotter decomposition, where $e^{\hat{A}+\hat{B}} \approx \left(e^{\frac{\hat{A}}{n}} e^{\frac{\hat{B}}{n}}\right)^n$. By adopting this procedure we successfully increase the overall depth of the circuit by integer multiples of the original block and we artificially amplify the noise level without modifying the expression of the many-body wave-function or affecting the Trotter error.

Our extrapolation procedure is shown in Fig. 6.7. We considered $n = [1, 2, 3, 4, 5]$, and for each value of n we repeated the 8192 measurements of each circuit 50 times (for a total of $50 \times 8192 = 409{,}600$ measurements), in order to improve the stability of the extrapolation procedure. Repeating the measurement of each circuit 25 times instead of 50 leads to a small difference of ∼0.012 meV in the computed energy. The difference between the ground

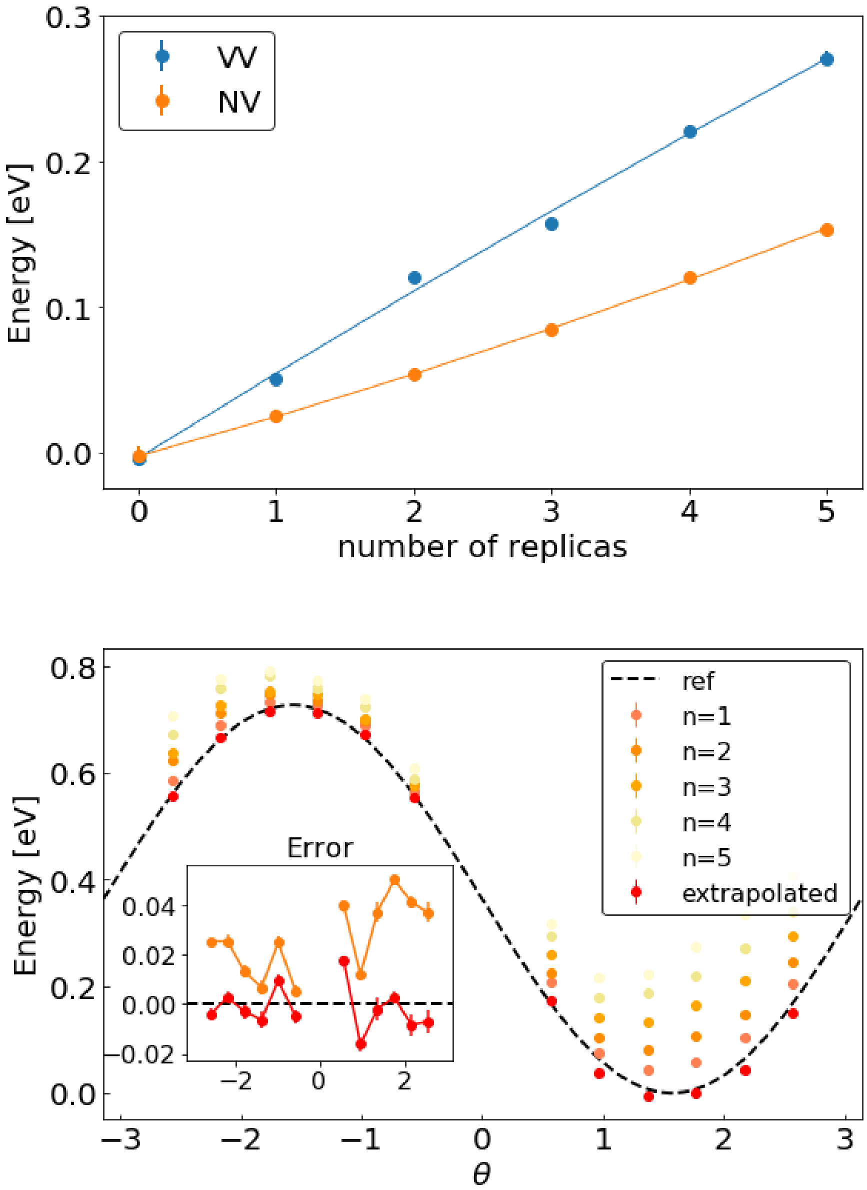

Figure 6.7: The upper panel shows the ground state energy of the NV$^-$ center and the VV in 4H-SiC as a function of number of replicas used in the zero-noise extrapolation (see text). The reference, noiseless result has been set at 0. The lower panel shows the total energy of the NV$^-$ center as a function of the parameter θ (Eq. 6.7 in text). The different colors correspond to using $n = [1, 2, 3, 4, 5]$ replicas of exponential blocks and the red dots denote the linearly extrapolated energy ($n \to 0$). In the inset we show the difference between noisy energies ($n = 1$) or extrapolated values ($n \to 0$) and the noiseless reference energy. Both panels are obtained using *ibmq_ casablanca*.

state energy obtained with 50 repetitions and the reference value obtained on a quantum simulator is ∼0.002 eV for the NV$^-$ center and ∼0.005 eV for the VV in SiC, one order of magnitude smaller than in the case where ZNE is not applied.

Fig. 6.7 also shows the results of ZNE for the energy of the NV$^-$ center as a function of θ. The extrapolation is performed considering an increasing number of replicas (n), and averaging over 24 repetitions of 8192 measurements for each replica. The choice of 24 instead of 50 repetitions is a compromise between efficiency and accuracy: scanning $E(\theta)$ (i.e., computing 12 values of the energy with a 50 time repetition rate) would require a time to completion during which we could not insure a constant noise level on the available hardware. Since we showed earlier that 25 repetitions yielded an acceptable result for the ground state, we used a similar number for the calculation of the function $E(\theta)$. The inset of Fig. 6.7 shows the difference between noisy results ($n = 1$) and extrapolated values ($n \to 0$) and the noiseless reference. Overall we see that results obtained with ZNE are in closer agreement with the reference results.

6.3.3 Calculation of the excited states using a quantum computer

We computed excited states of the NV$^-$ and VV centers using the QSE algorithm. To avoid propagating the errors introduced by VQE, we used the exact energy of the $^3A_2$ state with $m_s = 0$ as ground state energy.

We constructed a quantum subspace that is identical to the configuration state space, so the dimension of the QSE matrices is the same as that of their classical FCI counterpart. The QSE matrix is built by evaluating, on the quantum hardware, the expectation values of all Pauli correlators; in addition we adopted the post-selection and the ZNE techniques described above. To perform ZNE we used a linear extrapolation for the off-diagonal elements of the QSE matrix and we computed diagonal elements with linear, quadratic, or exponential extrapolations. The number of repetition of the same circuit with 8192 measurements was reduced from 50 to 10 for the VV due to the computational cost. The QSE matrix was diagonalized on a classical computer.

The results are summarized in Table 6.1. The accuracy of the energy of non-degenerate excitations is in general improved when using the ZNE, with the only exception being the $^3A_2 \leftrightarrow {}^3E$ transition of NV^- in diamond obtained with a quadratic extrapolation scheme. We note that overall different choices of extrapolation functions lead to similar results, and hence linear extrapolation is a desirable choice, since a smaller number of parameters is expected to lead to a more stable fit. Unfortunately, we find that the degeneracy of states is spuriously lifted on the quantum hardware due to the presence of noise, even after applying the ZNE, showing that it is not possible to resolve energy differences smaller than the standard deviation (σ) associated to the mean of our measurements. In our calculations with 50 repetitions $\sigma \simeq 3$ meV.

6.4 Conclusions

In summary, we presented electronic structure calculations of strongly correlated ground states and, for the first time, of excited electronic states of point defects in semiconductors on a near-term quantum computer. We focused on two spin-defects, i.e., the NV^- center in diamond and the VV in SiC. Our computational protocol includes first principles calculations of the electronic structure of a spin defect in a solid containing hundreds of atoms using hybrid DFT, followed by the use of the quantum defect embedding theory to define an effective Hamiltonian that represents electronic excitations localized within the point-defect. The Hamiltonian is then mapped into a qubit Hamiltonian which is solved using VQE and QSE hybrid quantum/classical algorithms to obtain the ground and excited many-body electronic states of the defect, respectively. We discussed the merits of these algorithms in the case of spin qubits; however, establishing which algorithms are better suited to obtain, in general, many-body energies of electronic states in solids on NISQ hardware remains an open area of

Table 6.1: Excitation energies [eV] of the NV$^-$ and VV centers calculated using the quantum subspace expansion (QSE) method. The first column shows transition between states labeled using the representation of the point group C_{3v}, following [203]. The second column shows results obtained with a noiseless simulator that are identical to those of classical full configuration interaction (FCI) calculations on a classical computer. The 3rd to 6th columns display results obtained using QSE on the quantum hardware, and using post-selection of states with different extrapolation strategies and the zero noise extrapolation technique.

NV$^-$ center	FCI/noiseless	No extrap.	Linear[1]	Quadratic[2]	Exponential[3]
$^3A_2 \leftrightarrow {}^1E$ [4]	0.512	0.470	0.511	0.508	0.509
$^1E \leftrightarrow {}^1E$ [5]	0.000	0.076	0.074	0.084	0.080
$^3A_2 \leftrightarrow {}^1A_1$	1.380	1.282	1.391	1.373	1.378
$^3A_2 \leftrightarrow {}^3E$ [4]	2.008	1.964	1.989	1.946	1.974
$^3E \leftrightarrow {}^3E$ [5]	0.000	0.177	0.119	0.059	0.091
VV in SiC	FCI/noiseless	No extrap.	Linear[1]	Quadratic[2]	Exponential[3]
$^3A_2 \leftrightarrow {}^1E$ [4]	0.378	0.338	0.367	0.363	0.365
$^1E \leftrightarrow {}^1E$ [5]	0.002	0.083	0.069	0.065	0.067
$^3A_2 \leftrightarrow {}^1A_1$	1.228	1.141	1.212	1.207	1.202
$^3A_2 \leftrightarrow {}^3E$ [4]	1.348	1.313	1.337	1.333	1.334
$^3E \leftrightarrow {}^3E$ [5]	0.002	0.010	0.080	0.079	0.078

[1] Linear extrapolation of both diagonal and off-diagonal elements of the QSE matrix (Eq. 6.8 in the text).

[2] Quadratic extrapolation of the diagonal, and linear of the off-diagonal elements of the QSE matrix.

[3] Exponential extrapolation of the diagonal, and linear of the off-diagonal elements of the QSE matrix.

[4] Energy of the degenerate states is computed as the average of the two energies obtained on quantum hardware.

[5] Energy gap between two states which should be degenerate, due to the presence of noise.

research [29]. For example, recent papers have proposed methods to find the eigenstates of a Fermionic Hamiltonian that are not based on the variational principle and therefore do not require the definition of an ansatz or involve an optimization procedure [227]. In particular, Ref [171] proposed an algorithm to prepare approximate ground states with shallow circuit and just one parameter.

We also discussed two main problems arising from the presence of noise on quantum hardware: (i) the apparent violation of the variational principle in VQE calculations due to unphysical states arising when the number of electrons is not conserved, and (ii) the presence of persisting errors on energies obtained on quantum computers even after correcting for the presence of unphysical states. We successfully applied a post-selection method based on partial constraints on the number of electrons to correct for problem (i) and we proposed an error mitigation technique within the ZNE scheme to reduce the effect of quantum errors. The technique uses an exponential block repetition to boost the quantum error of UCC type ansätze in a controllable fashion. The error mitigation protocol adopted here has several advantages: (1) it is readily applicable without any knowledge of the source of hardware noise and without increasing the number of qubits; (2) it does not affect the scaling of the quantum algorithm, although it may affect the prefactor. However, the UCC type ansätze require the use of relatively deep circuits thus limiting the applicability of ZNE strategies with a large number of replicas. As a proof of principle of the strategies adopted here to solve useful materials problems, we obtained results with small active spaces and shallow circuits. Work is in progress to expand the applicability of the method to systems that require larger active spaces appropriate to investigate, for example, adsorbates on surfaces and ions or nanostructures in solution. Based on our work, we further envision a feedback loop, where quantum simulations of materials properties on a quantum device lead to the prediction of new materials and properties for the design of improved quantum computers, which will in turn result in enhanced property predictions and applications, therefore establishing a tight connection between quantum computations and materials' predictions.

CHAPTER 7

QUANTUM SIMULATIONS OF FERMIONIC HAMILTONIANS WITH EFFICIENT ENCODING AND ANSATZ SCHEMES

This chapter is adapted with permission from **B. Huang**, N. Sheng, M. Govoni, and G. Galli. Journal of Chemical Theory and Computation 19.5 (2023): 1487-1498. Copyright (2023) by the American Chemical Society. https://doi.org/10.1021/acs.jctc.2c01119.

In this chapter, we propose a computational protocol for quantum simulations of Fermionic Hamiltonians on a quantum computer, enabling calculations on spin defect systems which were previously not feasible using conventional encodings and unitary coupled-cluster ansatz of variational quantum eigensolvers. We combine a qubit-efficient encoding scheme mapping Slater determinants onto qubits with a modified qubit-coupled cluster ansatz and noise-mitigation techniques. Our strategy leads to a substantial improvement in the scaling of circuit gate counts and in the number of required qubits, and to a decrease in the number of required variational parameters, thus increasing the resilience to noise. We present results for spin defects of interest for quantum technologies, going beyond minimum models for the negatively charged nitrogen-vacancy center in diamond and the double vacancy in 4H silicon carbide (4H-SiC) and tackling a defect as complex as negatively charged silicon vacancy in 4H-SiC for the first time.

7.1 Introduction

Obtaining accurate solutions of the electronic structure of many-body systems is a major challenge in computational science, and an important endeavor that may benefit problems in several fields, ranging from catalysis [120] and drug discovery [153] to quantum technologies [73, 178]. In addition to steady efforts in the development of algorithms to solve the electronic structure problem on classical computers, research into the use of quantum computers to solve the time-independent Schrödinger equation has been flourishing in the past decades [16, 144, 191, 227, 245]. The motivation behind this trend is the promise that a fault-tolerant quantum computer may be able to solve the electronic structure problem for many-body systems [48] in polynomial time, for example using a quantum phase estimation (QPE) [2, 3, 163] algorithm. The latter is a probabilistic method to obtain the eigenstate of a unitary operator that assumes that the initial state of a given system, prepared on a quantum computer, has a non-vanishing overlap with the target state.

The possibility of reaching exponential quantum advantage for quantum chemistry problems remains controversial [182]. However, it is interesting to explore whether quantum computers may in fact turn out to be advantageous over classical ones, even in the absence of exact polynomial scaling, and in particular whether even today's noisy intermediate scale quantum (NISQ) platforms may be utilized for interesting problems. Recent efforts [144, 338, 345] to incorporate quantum computations into quantum Monte Carlo methods [226] suggest new route for such benefits to be achieved, in practice, even with noisy hardware. Specifically, Ref [144] reported a calculation of the atomization energy of the strongly correlated square H_4 molecule, using a quantum-classical hybrid quantum Monte Carlo method on the Sycamore quantum processor [11], which achieved accuracy that is competitive with state-of-the-art classical methods. The algorithm relies on the preparation of a so called *a priori* quantum trial state on the quantum hardware, which is considered as an approximation to the target ground state. Therefore it appears that one strategy to obtain computational advantage on both NISQ and fault-tolerant quantum devices, relies on the efficient preparation of an accurate initial state; this strategy has been explored for both molecular [83, 126, 142, 154, 155, 241, 245, 254, 292] and condensed systems [139, 203].

An appealing and popular protocol to obtain the ground state of Fermionic systems is that of writing the Hamiltonian in second quantization and using a variational quantum eigensolver (VQE) [218, 245]. This algorithm parameterizes the many-body wavefunction through a quantum circuit, and the energy is measured on a noisy hardware. Upon optimization of the parameters on classical hardware, one obtains a variational upper bound on the ground state energy. The efficiency and reliability of VQE depend on the number of available qubits on the quantum hardware, on the qubit coherence time and usually VQE faces optimization challenges due to the hardware noise. However, despite theses challenges, this algorithm has been successfully applied to study systems with up to 12 electrons [254].

In a recent paper, we utilized VQE to solve the electronic structure of the minimum model of realistic solid-state systems with strongly correlated states, and we carried out calculations on a quantum computer. In particular we considered spin-defects in solids, i.e. the negatively charged nitrogen-vacancy center (NV^-) in diamond and the neutral di-vacancy (VV^0) in 4H-SiC [139], which are of interest for quantum information applications [332, 335], including quantum sensing [138], communication [9] and bioimaging [286]. Although we obtained encouraging results, we also identified several problems awaiting for more efficient and accurate solutions. For example, the so called unphysical state problem [276], caused by an imperfect conservation of the number of particles on a noisy hardware, leads to values of the energy that lie below the exact classical reference value. We solved this problem by post selecting [143] the measured values of the energy and considering only those corresponding to the correct number of particles. The combination of post-selection and zero-noise extrapolation (ZNE) techniques [87, 88, 187, 311] led us to solve the electronic structure of realistic spin-defects. However, we could do so only for minimum models, as the ansatz circuit used in VQE usually leads to a large gate count and hence calculations are hard to scale.

Here we propose a computational strategy leading to an improved scaling with gate counts of VQE optimizations, thus enabling electronic structure calculations of complex spin-defects previously not feasible with conventional VQE algorithms. In particular, we combine a qubit-efficient encoding (QEE) scheme [284] with a modified qubit-coupled cluster (QCC) ansatz [271] and noise-mitigation techniques. Such a protocol leads to a substantial decrease in the number of required variational parameters in VQE calculations, thus increasing the resilience to noise and enabling calculations of spin defects beyond the minimum model [139]. The rest of the paper is organized as follows. In Chapter 7.2 we discuss the quantum algorithms adopted to solve the electronic structure of systems whose parametrized Hamiltonian is expressed in second quantization. In Chapter 7.3, we present calculations on a real quantum computer of three spin defect systems, i.e. NV^- in diamond, VV^0 and a new defect–negatively charged silicon vacancy ($\mathrm{V}_{\mathrm{Si}}^-$) in 4H-SiC, which for some applications [173, 296] is a promising alternative to NV centers. Chapter 7.4 concludes our work with a summary and outlook.

7.2 Methods

The workflow adopted here to obtain the ground and excited states of a Fermionic Hamiltonian $\hat{H}_{\mathrm{elec}}$ on a quantum computer is summarized in Fig. 7.1 and consists of the following steps: (i) define a Fermionic Hamiltonian using a quantum defect embedding theory (QDET), (ii) derive a qubit Hamiltonian by mapping selected electronic configurations (Slater determinants) of the Fermionic Hamiltonian onto qubits, (iii) compute the ground state energy of the qubit Hamiltonian using VQE, (iv) compute the excited states using the quantum subspace expansion (QSE) algorithm. The qubit Hamiltonian $\hat{H}_{\mathrm{q}} = \sum_i g_i \hat{P}_i$ contains coefficients g_i obtained from the one- and two- body terms of $\hat{H}_{\mathrm{elec}}$ multiplied by Pauli strings, i.e., $\hat{P}_i \in \{I, X, Y, Z\}^{\otimes N_q}$, where N_q is the number of qubits and I, X, Y, Z are Pauli operators. When using a VQE algorithm, an ansatz circuit, usually a parametrized unitary operator $\hat{U}(\vec{\theta})$, is defined and applied to a chosen initial state $|\Psi_0\rangle$. Finally, the ground state energy E_g is variationally obtained by optimizing the parameters $\vec{\theta}$ of the ansatz such that $E_g = \min_{\vec{\theta}} \langle\Psi_0|\hat{U}^{\dagger}(\vec{\theta})\hat{H}\hat{U}(\vec{\theta})|\Psi_0\rangle$. As mentioned above, excited states are obtained with the QSE algorithm.

For a detailed discussion of the derivation of a Fermionic Hamiltonian describing spin

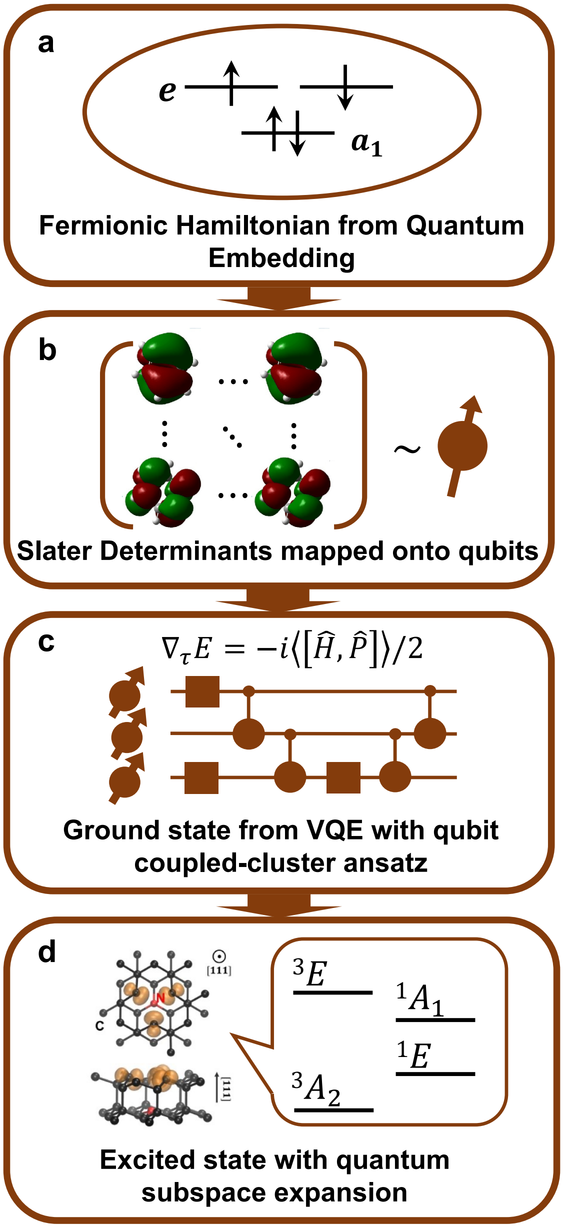

Figure 7.1: Workflow used to simulate the ground and excited state energies of spin defects on a quantum computer. **a** The effective Hamiltonian in second quantization describing the electronic structure of spin defects is obtained from a quantum defect embedding theory (QDET), see Sec 7.3.1 for detail. **b** The Slater determinants are mapped onto qubits using a qubit-efficient encoding scheme, where the molecular orbitals represent a Slater Determinant. **c** The ground state of the effective Hamiltonian is obtained using a variational quantum eigensolver (VQE) and a qubit coupled-cluster (QCC) ansatz. **d** The excited states of the effective Hamiltonian are obtained using a quantum subspace expansion (QSE) algorithm.

defects in solids using QDET we refer the reader to Ref. [203, 204, 285, 325]. Below we discuss in details steps (ii–iv: see panels **b-d** of Fig. 7.1).

7.2.1 Qubit Efficient Encoding for Fermionic Mapping

The Fermion to qubit encoding is an isometry $\mathcal{E} : \mathcal{H}_{\text{elec}} \rightarrow \mathcal{H}_{\text{q}}$ [39], where $\mathcal{H}_{\text{elec}}$ and $\mathcal{H}_{\text{q}}$ represent the physical and qubit Hilbert space spanned by the eigenvectors of $\hat{H}_{\text{elec}}$ and $\hat{H}_{\text{q}}$, respectively. Commonly used encoding schemes such as the Jordan–Wigner (JW) [334], Bravyi–Kitaev (BK) [40] and parity encoding methods [39] require $N_q = N$ qubits for a system with N spin-orbitals, and generate a 2^N-dimensional $\mathcal{H}_{\text{q}}$. However, our goal is to compute the eigenvectors and eigenvalues of $\hat{H}_{\text{elec}}$ subject to specific physical constraint on the number of electrons in the two spin channels $(m_{\uparrow}, m_{\downarrow})$. In practice this constraint can be enforced by restricting the solutions of the VQE or QSE algorithms to a subspace of the qubit Hilbert space with dimension $Q = \binom{N/2}{m_{\uparrow}} \times \binom{N/2}{m_{\downarrow}} < 2^N$. However, the JW and BK encoding maps do not enforce such a physical constraint and thus lead to a qubit Hilbert space that is larger than the physical one [276], e.g., the former contains all Fock states, some corresponding to a number of electrons different from those of the physical system. In principle, on a fault-tolerant computer the VQE algorithm should preserve the initial number of electrons throughout the optimization process; however, the noise present in NISQ devices does not guarantee the preservation of the physical constraints [86], leading to errors in ground state energies that in Ref. [139] we have mitigated with a post-selection procedure. Note that other symmetry constraints, e.g., point group symmetry [282] could also be taken into account when choosing relevant Slater determinants, which would be interesting to explore in future works.

Here we adopt instead the QEE scheme [284], a compact Fermion to qubit encoding map [51, 159, 161] that by definition excludes from the qubit Hilbert space all Fock states with nonphysical number of electrons, leading to a robust solution of the unphysical state problem. The QEE encoding has also the benefit of requiring a smaller number of qubits than the conventional encoding maps. The use of QEE has already been shown to be beneficial on quantum hardware [284] for molecules such as H_2 and LiH; here we show that its use is crucial in the case of spin-defects, where the number of qubits required to go beyond minimum models by conventional encodings would be impractical on NISQ devices.

In the QEE scheme, one pre-selects all the electronic configurations $\mathcal{F} = \{|\mathbf{f}\rangle_i | |\mathbf{f}\rangle_i \in \mathcal{H}_{\text{elec}}\}$ that satisfy the required set of physical constraints, e.g., fixed number of particles and fixed spin projection $\hat{S}_z$. The implementation of the QEE scheme requires $N_q = \left\lceil \log_2 Q \right\rceil < N$ qubits. Using the QEE isometry, configurations in $\mathcal{F}$ are mapped to $\mathcal{Q} = \{|0\rangle_q, |1\rangle_q\}^{\otimes N_q}$, the computational basis states of a N_q-qubit system. To reduce the state preparation error [284], a good practice in defining the QEE isometry $\mathcal{E}$ is to first sort both $\mathcal{F}$ and $\mathcal{Q}$ in ascending order according to the electronic energy of $|\mathbf{f}\rangle_i$ and the decimal number associated to the binary string representing the qubit state. By doing so, a correspondence $\mathcal{E}|\mathbf{f}\rangle_i = |\mathbf{q}\rangle_i$ is established. We note that in general the size Q is not necessarily a power of 2. To fit the requirements of quantum circuits, unphysical states may therefore be included in QEE so as to build a Hilbert space with a size that is a power of 2. In this case, post-selection of measurement results may be helpful to exclude results involving unphysical states.

In common Fermionic-to-qubit encoding schemes, there is a one to one correspondence of both creation and annihilation operators ($\hat{a}_p^\dagger$, $\hat{a}_q$) with qubit operators. In QEE, where by definition only states with fixed number of particles are considered, there is a one to one correspondence between the excitation operator $\hat{E}_{pq} \equiv \hat{a}_p^\dagger \hat{a}_q$ and a qubit operator $\hat{\tilde{E}}_{pq}$, where the excitation operators are first rewritten as a sum of projection of Slater determinants $|\mathbf{f}_i\rangle \langle \mathbf{f}_j|$ and then transformed into qubit space through four entry operators: $\frac{1}{2}(X+iY)$, $\frac{1}{2}(X-iY)$, $\frac{1}{2}(I-Z)$, $\frac{1}{2}(I+Z)$, see Ref [284] for detail. The qubit Hamiltonian can then be constructed using $\hat{\tilde{E}}_{pq}$. For a generic Hamiltonian, where the projection operators would lead to a linear combination of up to an exponential number of Pauli operators, and in principle one needs to consider an exponentially large number of determinants, no quantum advantage would be achieved. QEE therefore should be considered as an intermediate solution for NISQ hardware. However, we note that both the size of the qubit Hamiltonian and the total number of Slater determinants scale polynomially as a function of N for the systems considered in our study, as we explain in the Section 7.3.1.

7.2.2 Qubit Coupled-Cluster Ansatz for Variational Quantum Eigensolvers

After constructing a qubit Hamiltonian using the QEE encoding, we discuss the choice of the wavefunction ansatz. One popular ansatz used in the literature is the unitary coupled-cluster (UCC) ansatz [110, 245, 264], inspired by coupled-cluster theory [124]. Such an ansatz can yield accurate results for many-body systems, but it leads to calculations suffering from poor scaling as a function of the number of gates, due to the inclusion of all possible electronic excitations. A typical implementation of the UCC ansatz on quantum computers leads to the following expression in terms of Pauli strings (entanglers) $\hat{P}_k$:

$$\hat{U}_{\mathrm{UCC}} = \prod_k \hat{U}_k = \prod_k e^{-i\theta_k \hat{P}_k/2}, \;\; \hat{P}_k \in \{I, X, Y, Z\}^{\otimes N_q}. \tag{7.1}$$

The number of entanglers required when using the UCC ansatz may be large even for intermediate scale systems with $4 \sim 6$ electrons. The QCC ansatz [271] bypasses the formulation of the ansatz in physical space, and instead directly implements Eq. 7.1 in the qubit space. In particular, the QCC method proposed in Ref. [271] implements a screening process to select and retain the entanglers that contribute the most to the evaluation of the energy.

In QCC, the variation of the energy induced by each entangler is evaluated by expanding the energy to second order in the parameter θ_k:

$$\delta E[\theta_k; \hat{P}_k] = E[\theta_k; \hat{P}_k] - E_0 \approx \theta_k \frac{dE[\theta_k; \hat{P}_k]}{d\theta_k}\bigg|_{\theta_k=0} + \frac{\theta_k^2}{2} \frac{d^2 E[\theta_k; \hat{P}_k]}{d\theta_k^2}\bigg|_{\theta_k=0}, \tag{7.2}$$

where $E[\theta_k; \hat{P}_k] = \langle \Psi_0 | \hat{U}_k^\dagger \hat{H} \hat{U}_k | \Psi_0 \rangle$ and $E_0 = \langle \Psi_0 | \hat{H} | \Psi_0 \rangle$. The first derivative in Eq. 7.2 can be efficiently computed through quantum measurements as

$$\left.\frac{dE[\theta_k; \hat{P}_k]}{d\theta_k}\right|_{\theta_k=0} = \left\langle \Psi_0 \middle| -\frac{i}{2}\left[\hat{H}, \hat{P}_k\right] \middle| \Psi_0 \right\rangle, \tag{7.3}$$

which results from the similarity-transformed Hamiltonian being in closed form [179]

$$\hat{U}_k^\dagger \hat{H} \hat{U}_k = \hat{H} - i\frac{\sin\theta_k}{2}\left[\hat{H}, \hat{P}_k\right] + \frac{1}{2}\left(1 - \cos\theta_k\right)\hat{P}_k\left[\hat{H}, \hat{P}_k\right]. \tag{7.4}$$

The expression of the second order derivative can be found in Ref. [271].

The implementation of the QCC method proceeds by ranking the entanglers according to the magnitude of their first-order derivative and sign of the second-order derivative, and by considering only the entanglers with highest rank. This amounts to screening the value of the first and second derivative of the energy for each of the $\sim 4^N$ entanglers and choosing those with values of the first derivatives substantially different from zero or second derivatives substantially smaller than zero. By using a qubit basis state as $|\Psi_0\rangle$ we can reduce the dependency of the total number of $\hat{P}_k$ with respect to the number of qubits from exponential to polynomial. The reduction is achieved by grouping the terms in the Hamiltonian and performing the pre-screening within each group; see Ref. [272] for detail. In practice, the second derivatives could also be neglected to decrease computational cost [272], as we did in this work.

The quantum circuit is finally constructed using a ladder-like block procedure [25], as shown in Fig. 7.2. As pointed out by Ref. [271], for molecules like LiH and H_2O, the two-qubit gate count is greatly reduced compared to that of the UCC ansatz by bypassing any explicit Fermionic construction of electronic excitations and thus saving as many quantum resources as possible.

In the original proposal of the QCC [271] method, only entanglers with more than one

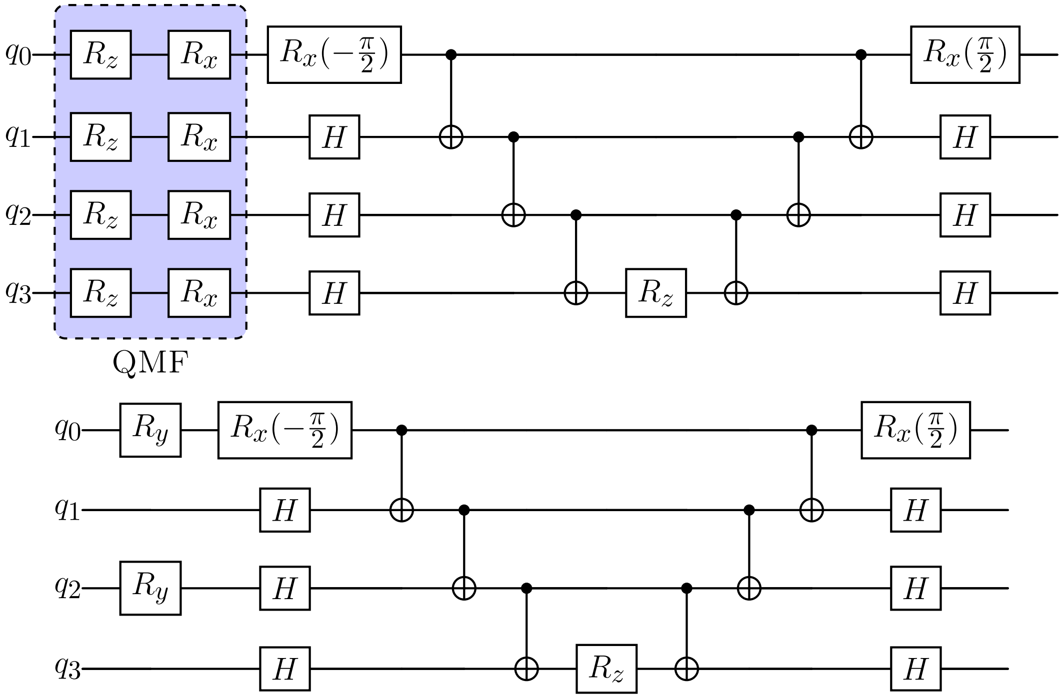

Figure 7.2: The upper panel shows a representative quantum circuit representing the qubit coupled-cluster ansatz with 4 qubits. The box circled by the dashed line shows the qubit mean-field (QMF) part of the circuit, which enables the construction of any product states. The circuit component following the QMF part enbales the construction of the exponential of entangler $XXXY$, and it is built with the CNOT gate ladders. The lower panel shows a circuit representative of the modified ansatz, where the three entanglers are $IIIY, IYII, XXXY$, as defined in the pre-screening process.

non-identity gate (X, Y, Z) were considered, and the quantum circuit was started with a qubit mean-field (QMF) component, as shown in Fig. 7.2. This QMF component consists of single R_x and R_z rotations on each qubit, allowing for access to any point on the Bloch sphere. Although it remains to be investigated whether such an implementation suffers from the Barren plateau problem [220], the QMF component resembles the hardware-efficient ansatz [154] and might pose optimization challenges [330] due to the large number of required variational parameters ($2N_q$). In addition, R_x and R_z rotations are likely redundant degrees of freedom, since often times both the Hamiltonian and wavefunction of many-body systems of interest are real.

To solve the potential optimization challenges introduced by the QMF component, we propose a modification of the original QCC ansatz. We simply discard the QMF component, and consider all the possible entanglers when performing the screening operation, regardless of the number of qubits that the entangler involves. In this way, the number of necessary variational parameters are reduced and eventually a quantum circuit only contains exponentials of entanglers, as shown in the bottom panel of Fig. 7.2.

The QCC ansatz is suitable for NISQ devices, where a trade off between circuit depth and number of quantum measurements is desirable. We note that similar ideas to construct efficient ansatz circuits using gradient methods have been explored in recent years, including iterative QCC [272], ADAPT-VQE and its several variants [111, 310], e.g. Cluster-VQE [344], factorized-form of UCC [53], and projective quantum eigensolver [298]. Besides being hardware friendly, an additional benefit of the QCC ansatz is that it leads to differentiable potential energy surfaces given its functional dependence on the entanglers, and the gradients can be estimated using the parameter-shift rule [63, 280]. The QCC ansatz has shown the correct size-consistent behavior when applied to study the dissociation of H_2, LiH and H_2O in Ref [271]. However, there is no guarantee that it will always yield the correct behavior for any systems since it depends on how the entanglers are truncated when the circuit is constructed. We also speculate that in general size-extensivity may be satisfied as entanglers for noninteracting fragments act only on each fragment, and, therefore, commute and we thus have $E(2A) = 2E(A)$.

7.2.3 Quantum Subspace Expansion for Excitation Energies

We now turn to the discussion of the calculations of excitation energies, for which subspace type methods [61, 62, 89, 160, 219, 316] are suitable. These methods can be viewed as a quantum analog of CI and its variants, e.g., selected CI approach [42]. Here we choose the quantum subspace expansion (QSE) algorithm [61, 217, 219], which uses the same quantum circuit as the one to obtain the ground state and involves only additional quantum measurements [61]. Specifically for the ground state $|\Psi\rangle$, a set of expansion operators $\{\hat{O}_i\}$ is chosen, which act on $|\Psi\rangle$ to form a basis given by $\{\hat{O}_i\,|\Psi\rangle\}$, where $\hat{O} \in \{\hat{a}_a^\dagger \hat{a}_i,\ \hat{a}_a^\dagger \hat{a}_b^\dagger \hat{a}_j \hat{a}_i | i, j \in \mathcal{A};\ a, b \in \mathcal{V}\}$. We use this basis to evaluate the Hamiltonian and overlap matrix elements:

$$H_{ij}^{\mathrm{QSE}} = \langle\Psi|\, \hat{O}_i^\dagger \hat{H} \hat{O}_j \,|\Psi\rangle\,, \quad S_{ij}^{\mathrm{QSE}} = \langle\Psi|\, \hat{O}_i^\dagger \hat{O}_j \,|\Psi\rangle\,. \tag{7.5}$$

Note that the expansion operators are not limited to double excitations, and we did not include additional excitations as double ones are sufficient to obtain the FCI spectrum of our systems. Using the matrices defined above, we then solve the generalized eigenvalue problem in the well-conditioned subspace given by $H^{\mathrm{QSE}}C = S^{\mathrm{QSE}}C\varepsilon$, where C is the matrix of eigenvectors and ε the diagonal matrix of eigenvalues. As mentioned in section 7.2.1, the QEE encoding is used to transform the excitation operators $\hat{a}_i^\dagger \hat{a}_j$ into Pauli strings acting on N_q qubits, and the matrix elements are evaluated as weighted sums of the expectation values of these Pauli strings. The cost of QSE has two components: i) determining the matrix elements through measurements, and ii) solving the generalized eigenvalue problem. In the QEE-QCC scheme adopted in this work, the measurement cost is negligible since the majority of Pauli operators have been measured already when computing the ground state. Therefore the cost of the QSE calculations mainly comes from ii). We also note that the effectiveness of QSE is achieved with a careful choice of creation and annihilation operators, which would be facilitated by using chemical intuition, e.g., by identifying the most dominant excitations.

7.3 Results

In this section we present results for the many-body ground and excited states of the NV$^-$ center in diamond, VV^0 and V$_{\mathrm{Si}}^-$ in 4H-SiC. Using the methods described in Sec. 7.2, we performed calculations on the *ibmq_guadalupe* quantum computer using the IBM Qiskit package [253]. We have applied measurement error mitigation [74, 206] to all the measurements.

7.3.1 Reference results on classical hardware

We use QDET to obtain the effective second quantized Hamiltonian, which is then used as input for our quantum computations [204, 285, 325]. As a first step we define a periodic supercell with hundreds of atoms, representing a crystal with a defect center embedded in it, and we compute its electronic structure using Kohn-Sham (KS) density functional theory (DFT) with the PBE functional, the G_0W_0 approximation, and the Quantum Espresso [97, 98] and WEST [109] codes. A subset of KS orbitals localized around the defect is then chosen based on the localization criterion defined in Ref. [285]. This subset constitutes the so-called active space A spanned by the second quantized effective Fermionic Hamiltonian $\hat{H}_{\mathrm{elec}} = \sum_{ij}^{A} t_{ij}^{\mathrm{eff}} \hat{a}_i^\dagger \hat{a}_j + \frac{1}{2}\sum_{ijkl}^{A} v_{ijkl}^{\mathrm{eff}} \hat{a}_i^\dagger \hat{a}_j^\dagger \hat{a}_l \hat{a}_k$. The effective two-body matrix elements v_{ijkl}^{eff} are computed using the constrained random-phase approximation (cRPA) method. The effective one-body matrix elements t_{ij}^{eff} are computed from the G_0W_0 Hamiltonian removing a double counting term. Notably, in Ref. [285] we rigorously derived an expression of the double counting term within the G_0W_0 approximation.

We computed the electronic structure of NV^-, VV^0 and $\mathrm{V}_{\mathrm{Si}}^-$ using a 215-, 198- and 127-atom supercell, respectively. We performed restricted closed-shell plane wave DFT calculations with the optimized structure from unrestricted open-shell calculations. We used the PBE [244] exchange-correlation functional, SG15 norm-conserving pseudopotentials [279], and a 50 Ry kinetic energy cutoff for the plane wave basis set. The active space was defined considering all KS orbitals with highest localization factor $L_V(\psi_n^{\mathbf{KS}}) = \int_V |\psi_n^{\mathbf{KS}}(\mathbf{x})|^2 d\mathbf{x}$, where the integration is performed on a predefined volume V around the defect center (see Fig. 7.4), as originally defined in Ref. [285]. In our full-frequency G_0W_0 calculations we used

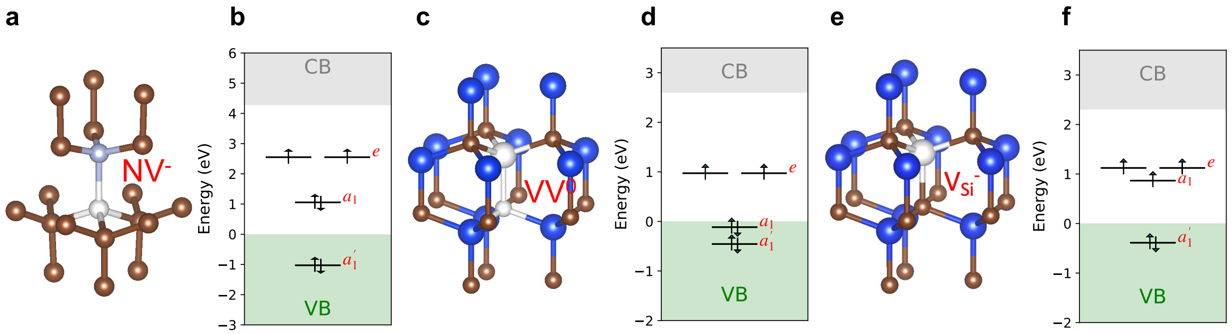

Figure 7.3: Spin defects studied in this work: the NV^- center in diamond, the VV^0 and V_{Si}^- in 4H-SiC. Panels **a**, **c** and **e** show a ball-and-stick representation of the defects. Panels **b**, **d** and **e** show single particle states obtained by solving the Kohn-Sham equations for the entire periodic solid, where gray and green shaded areas represent the conduction (CB) and valence band (VB), respectively; the single particles states are shown as black lines.

512 projective dielectric eigenpotentials (PDEPs) to represent the dielectric response. The QDET method is implemented in the WEST code [109, 342].

In Fig. 7.4 we show the convergence of vertical excitation energies of the three defects w.r.t. the localization threshold, which sets a lower bound for the KS orbitals to be included in the active spaces. We note that the energies are relatively well converged at 10%, 10% and 20% threshold in the three cases, corresponding to (14e, 8o), (22e, 12o) and (9e, 6o) active spaces, respectively. Due to the limitation in quantum resources, a compromise had to be made in selecting the active space to generate the effective Hamiltonians for the three defects: we chose the (14e, 8o) active space for VV^0 and NV^-. For NV^-, the convergence threshold for the (14e, 8o) active space lies between 20% and 10% and its excitation energies differ by approximately 0.1 eV from those obtained with a 10% localization threshold. Considering the complexity of the V_{Si}^-, for this defect we had to resort to a 30% localization threshold, leading to a (5e, 4o) active space, which we refer to as the “minimum model”.

We also note that when the localization threshold is lowered, the size of the active space N is increased by the inclusion of additional occupied orbitals. The total number of Slater determinants with a constant number of holes in each spin channel, $c_{\uparrow(\downarrow)} = \frac{N}{2} - m_{\uparrow(\downarrow)}$, scales polynomially as $O(N^{(c_\uparrow + c_\downarrow)}$. This leads to an encoded effective Hamiltonian which is

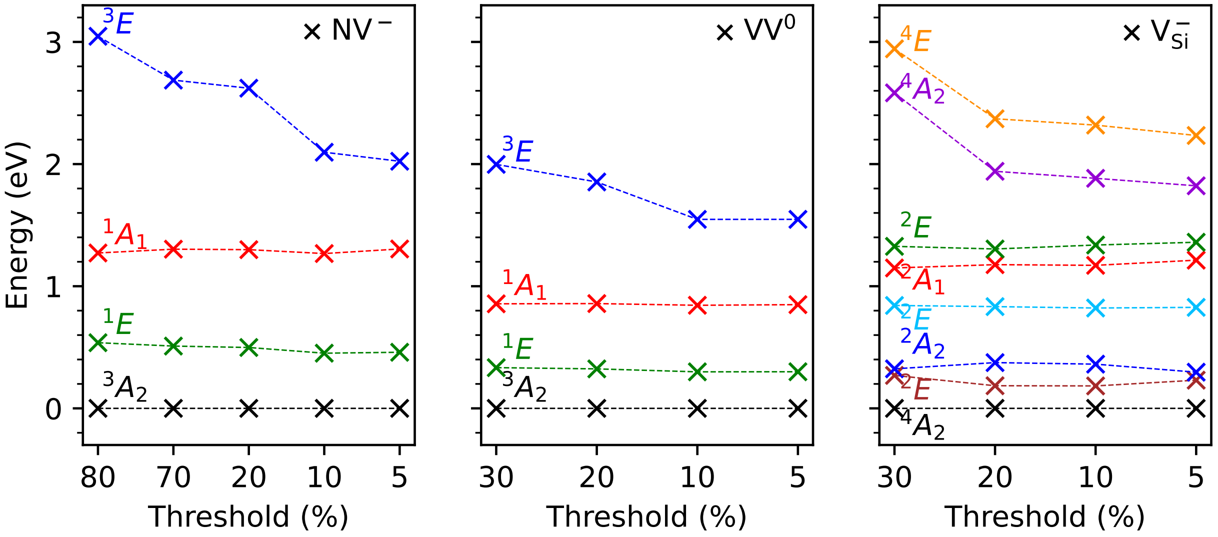

Figure 7.4: The left, middle and right panel show computed vertical excitation energies for the NV$^-$ center in diamond, VV^0 and V$_{\mathrm{Si}}^-$ in 4H-SiC as a function of the chosen localization threshold. States are labeled using the irreducible representation of the C_{3v} point group. We note that the largest threshold corresponds to a (4e, 3o), (8e, 5o) or (5e, 4o) active space for the three defects, respectively, and the smallest threshold corresponds to a (26e, 14o), (64e, 33o) or (57e, 30o) active space, respectively.

expressed as a linear combination of up to $O(N^{2(c_\uparrow + c_\downarrow)})$ Pauli operators. The size of the QEE Hamiltonian and its corresponding classical preprocessing step do not pose a computational challenge for the systems considered here, where $c_{\uparrow(\downarrow)} \leq 2$.

7.3.2 Calculation of the ground state using a quantum computer

VV^0 in 4H-SiC and NV$^-$ in diamond

The ground state of the effective Hamiltonian constructed for both the VV^0 in 4H-SiC and the NV$^-$ center in diamond is a $^3A_2$ triplet state, whose $m_S = 0$ state has a multi-reference character. To obtain such a state on quantum computers using VQE, a good guess for the initial wavefunction is key to achieving fast convergence [139]. These systems are open-shell with the highest occupied molecular orbitals (HOMOs) in the active space being e orbitals; hence it is wise to use $|\Psi_0\rangle = |..a_1\bar{a}_1 e_x \bar{e}_y\rangle$ due to Hund's Rule, where a_1, e_x, e_y (spin-up) and $\bar{a}_1$, $\bar{e}_x$, $\bar{e}_y$ (spin-down) denote the single-particle orbitals in the active space, as shown in Fig. 7.3.

As mentioned above, we choose the (14e, 8o) active space for both defects, leading to a total of 64 Slater determinants, and requiring the use of 6 qubits to span the full qubit Hilbert space, i.e., $\mathcal{H}_{\text{eff}} \subseteq \mathcal{H}_{\text{q}}$. To construct the QCC ansatz, we first measure the energy gradients of different entanglers using Eq. 7.3. The amplitude of these gradients are obtained both on a real quantum device (noisy) and on a simulator (noiseless). They are listed in Tab. 7.1 for VV^0. We find that the difference between noisy and noiseless results is negligible (within $1 \sim 2\%$). This is due to the fact that the measurement circuits does not contain two-qubit gates, which are major sources of error in NISQ devices. We also note that the four entanglers with top rank correspond to entanglers with the identity gate I at the two left-most qubit indices. Because of the chosen QEE scheme, the two left-most qubit indices control Slater determinants with the highest excitation energy, and originate from transitions from the lowest four occupied single particle orbitals. This suggests that we can use the frozen core approximation [266] to reduce the computational cost without sacrificing accuracy. Therefore we freeze the lowest four occupied orbital and in practice we work with 4 qubits, 4 entanglers, and a qubit Hamiltonian with 136 terms. The QCC circuit is constructed using 14 CNOT gates in total. The UCC counterpart, however, would require ~ 400 CNOT gates, indicating the critical advantage of the QCC method. For NV^-, the same logic applies and its circuit has 10 CNOT gates. Note that in the interest of generality, during the construction of the QCC ansatz, we did not take into consideration the point group symmetry of the ground state so as to design calculations that would be viable also for systems under strain or for moderately disordered lattices. If symmetry is invoked, both UCC and QCC can be reduced to a simple circuit with a single parameter and only two CNOT gates [139].

Results from the VQE optimization of VV^0 and NV^- are shown in the upper and middle panel of Fig. 7.5. The energy is evaluated on the quantum hardware as the weighted sum

Table 7.1: Top entanglers for the electronic structure calculation of VV^0 and $\mathrm{V}_{\mathrm{Si}}^-$ from Eqn. 7.3 before the frozen core approximation is carried out, with their magnitude computed using a noiseless simulator and a quantum hardware *ibmq_guadalupe* (Atomic units)

Rank	VV^0			$\mathrm{V}_{\mathrm{Si}}^-$		
	Entanglers	Noiseless	Noisy	Entanglers	Noiseless	Noisy
1	$IIIIXY$	0.009243	0.009170	$IXYII$	0.006969	0.006754
2	$IIXIYZ$	0.008177	0.008100	$IIIYI$	0.006693	0.006601
3	$IIXXIY$	0.008165	0.008065	$IIIIY$	0.004352	0.004352
4	$IIXIXY$	0.006587	0.006529	$IIIXY$	0.004350	0.004350

of the expectation values of Pauli strings, i.e., $E = \sum_i g_i \langle \hat{P}_i \rangle$. The expectation values of all Pauli strings were obtained by measuring 8192 times N_c independent circuits so that the standard deviation (σ) of measurement is within 15 meV, where N_c is the number of groups that contain mutually commuting strings. In the case of VV^0 (NV^-), we find that the VQE calculation converges to a state that is ~ 0.5 (0.4) eV higher than the FCI reference energy obtained on a classical computer. The fluctuations are more pronounced for the NV^- center because our calculations were carried out at different times and the hardware environment was not identical for each measurement. The insets in Fig. 7.5, where the reference values are from noiseless simulations, show that in our optimization procedure we indeed converge to the ground state of the system. We find that for both VV^0 and NV^-, only the parameter associated with entangler $IIXY$ is nonzero ($\pi/2$), indicating that the other ones are negligible in determining the ground state, thus reducing the circuit to one exponential block of $IIXY$. This simplified circuit is exactly what we obtained in Ref. [139] by taking into consideration the point group symmetry of the lattice.

To obtain an accurate estimate of the ground state energy, error mitigation is required and here we adopted the ZNE method. The latter is straightforward to implement and does not require additional qubits. The basic idea of ZNE is to amplify the noise of the circuit to various controllable levels and obtain the zero noise limit by extrapolation. The key to success of ZNE lies in how noise is artificially boosted. We employ a split exponential technique that we originally proposed in Ref. [139] to artificially increase the circuit depth of each exponential block $e^{i\theta_k \hat{P}_k}$ of the QCC quantum ansatz, i.e., n replicas are generated with $\left(e^{i\frac{\theta_k}{n}\hat{P}_k}\right)^n$. We note that this technique is suitable for both UCC and QCC-type of ansatzes [93, 181, 193, 222, 271] and it does not affect the Trotter error [139]. The extrapolation procedure is shown in Fig. 7.7. We worked with the reduced circuit with only one entangler $IIXY$, and considered $n = [1, 2, 3, 4, 5]$. For each value of n, we increased the measurements to 320000, so σ is kept within 2.5 meV and the stability of the extrapolation procedure is improved. A quadratic function is used for extrapolation and the difference between the ground state energy and the reference value obtained on a quantum simulator is one order of magnitude smaller than in the absence of ZNE.

$\mathrm{V}_{\mathrm{Si}}^{-}$ in 4H-SiC

We now turn to the discussion of the $\mathrm{V}_{\mathrm{Si}}^{-}$ spin defect in 4H-SiC, which has a $\left|{}^4A_2\right\rangle$ ground state, with multi-reference character for $m_s = \pm\frac{1}{2}$ [296]. The HOMOs of $\mathrm{V}_{\mathrm{Si}}^{-}$ consists of three quasi-degenerate orbitals: a_1, e_x, e_y that are all singly occupied in the ground state, as shown in Fig. 7.3. Therefore the $m_s = \pm\frac{1}{2}$ spin manifold is considerably more complicated than those of VV^0 and NV^-. We use only a minimal model of (5e, 4o) for the active space to describe this system, which is adequate to demonstrate the advantages of QCC over UCC in terms of finding the ground state with a shallow circuit depth. In this minimal model, the $m_s = \frac{1}{2}$ component of the ground state wavefunction consists of 6 Slater determinants

$$\begin{aligned}\left|\Psi_g\right\rangle &= \alpha\left(\left|a_1'\overline{a_1}'\overline{a_1}e_xe_y\right\rangle + \left|a_1'\overline{a_1}'a_1\overline{e_x}e_y\right\rangle + \left|a_1'\overline{a_1}'a_1e_x\overline{e_y}\right\rangle\right)\\ &+ \beta\left(\left|\overline{a_1}'a_1\overline{a_1}e_xe_y\right\rangle + \left|a_1'a_1\overline{a_1 e_x}e_y\right\rangle + \left|a_1'a_1\overline{a_1}e_x\overline{e_y}\right\rangle\right),\end{aligned} \tag{7.6}$$

where we have only used two coefficients, α and β because of symmetry. From the FCI solutions on a classical computer we know that the first three configurations with doubly occupied a_1' are dominant ($|\alpha| = 0.576,\ |\beta| = 0.0391$), hence we use one of them as the initial state of our VQE optimization. Specifically, we use $|\Psi_0\rangle = \left|a_1'\overline{a_1}'\overline{a_1}e_xe_y\right\rangle$.

When adopting the UCCSD ansatz, one needs to explicitly construct the relevant electronic excitations, whose associated parameters are $\theta^{a_1}_{a_1'}, \theta^{a_1\overline{e_x}}_{e_x\overline{a_1}}, \theta^{a_1\overline{e_y}}_{e_y\overline{a_1}}, \theta^{a_1\overline{e_x}}_{e_x\overline{a_1}'}, \theta^{a_1\overline{e_y}}_{e_y\overline{a_1}'}$. The resulting circuit requires ~200 CNOT gates, and with the UCCSD ansatz we only obtained the exact ground state on a noiseless simulator. A reasonable approximation is to assume $\beta = 0$, which would require only the first two parameters with a corresponding reduction of the number of CNOT gates to ~80. This approximation leads to an error of ~11 meV, as shown in 7.6. However, both circuits are beyond the capability of NISQ quantum devices.

Here the QCC ansatz presents a remarkable advantage and we were able to simulate the $\mathrm{V}_{\mathrm{Si}}^{-}$ defects on a real quantum processor. The screening of entanglers are summarized in Tab. 7.1. We selected the entanglers with top rank to construct the circuit for the ansatz, which contains only a total of 4 CNOT gates. The VQE optimization on a real quantum processor is shown in Fig. 7.5, where the error due to noise is about ~0.2 eV. We note that also in this case the ZNE is applied at the end of the VQE optimization to obtain a more accurate ground state energy, as shown in Fig. 7.7.

7.3.3 Calculation of the excited states using a quantum computer

As mentioned earlier, we computed excited states of the VV^0 and NV^- using the QSE algorithm. To avoid propagating the errors introduced by VQE, we used the exact energy of the ${}^3A_2$ state with $m_s = 0$ as the ground state energy.

We constructed a quantum subspace that is identical to the configuration state space, so the dimension of the QSE matrices is the same as that of their classical FCI counterpart. The QSE matrix is built by evaluating, on the quantum hardware, the expectation values of all Pauli strings. In our zero noise mitigation, we used a linear extrapolation for the off-diagonal elements of the QSE matrix and we computed diagonal elements with linear and quadratic extrapolations. The number of measurements was 320000 for both defects. The QSE matrix was finally diagonalized on a classical computer.

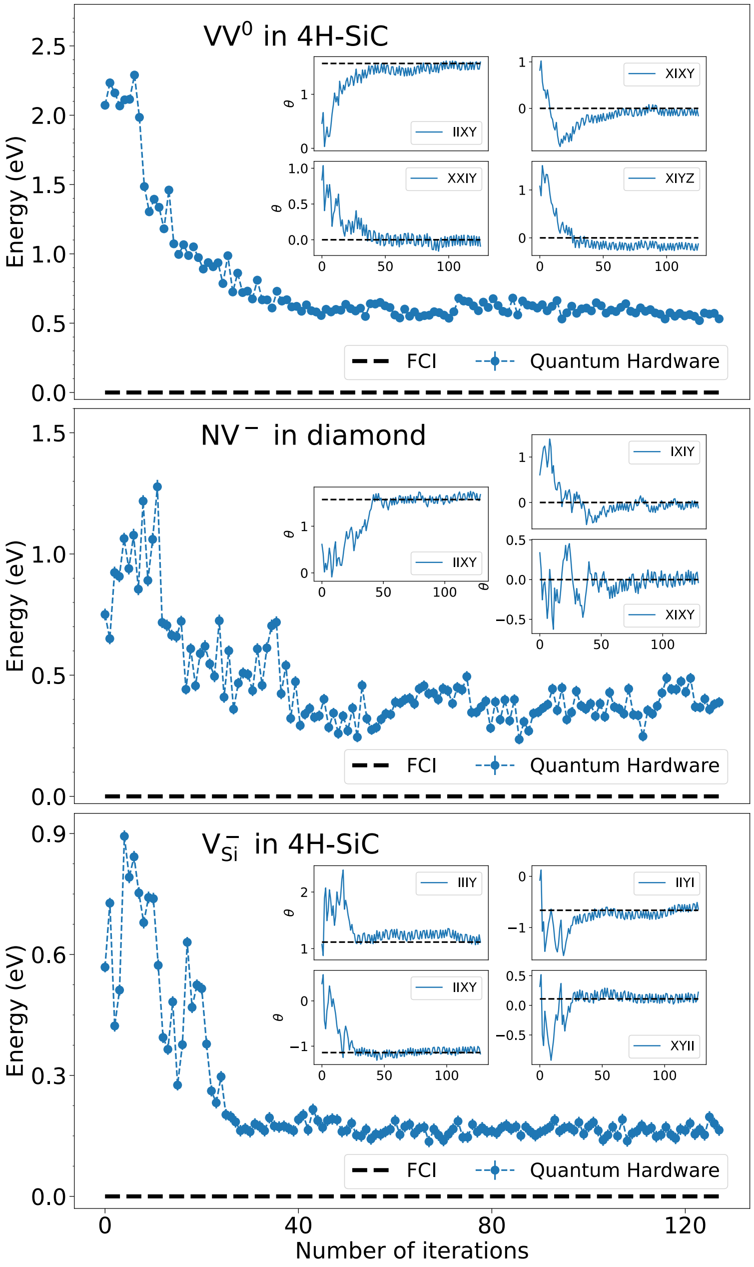

Figure 7.5: The upper, middle and bottom panel show the total energy as a function of the number of iterations during an optimization of the ground state energy of the VV^0 in 4H-SiC, the NV$^-$ in diamond and the V$_{\text{Si}}^-$ in 4H-SiC carried out with the variational quantum eigensolver (VQE) algorithm on *ibmq_guadalupe* (quantum hardware); the variation of parameters associated with each entangler of the qubit coupled cluster (QCC) ansatz is plotted in the inset. The full configuration interaction (FCI) energy is reported for reference.

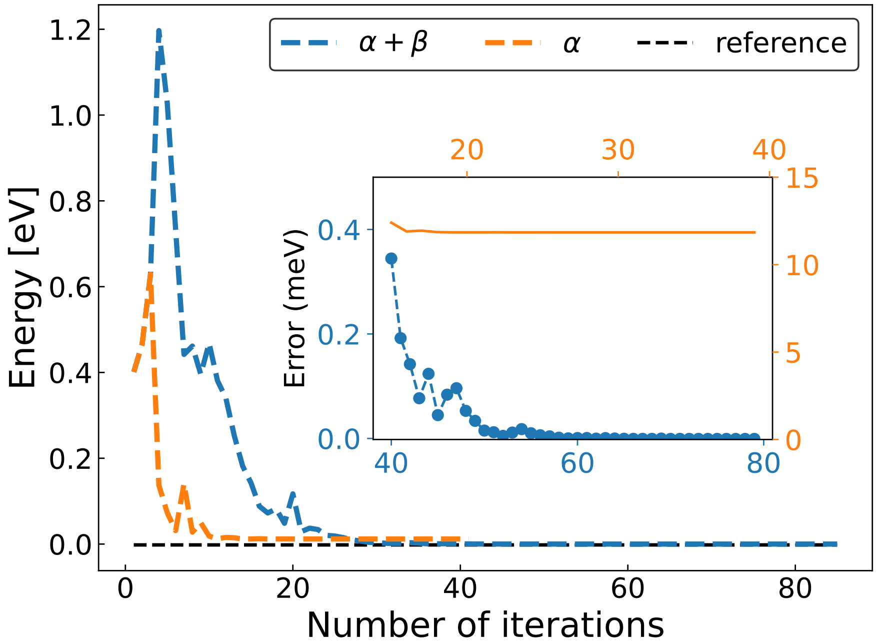

Figure 7.6: Total energy as a function of the number of iterations used to optimize the ground state energy of V_{Si}^{-} in 4H-SiC using the variational quantum eigensolver (VQE) algorithm on a noiseless simulator, with a unitary coupled cluster (UCC) ansatz and the COByLA optimizer [251]. The blue and orange curves represent results using two variants of the ansatz circuit with different levels of approximation; see text. The inset shows the error of different VQE optimizations relative to the reference energy. The full configuration interaction (FCI) energy (dashed black line) is reported for reference.

The errors of excitation energies with and without extrapolation are summarized in Fig. 7.8. The accuracy of the energy of non-degenerate excitations is in general improved when using the ZNE. We note that overall different choices of extrapolation functions lead to similar results, and hence linear extrapolation is a desirable choice, since a smaller number of parameters is expected to lead to a more stable fit. The degeneracy of states is spuriously lifted on the quantum hardware due to the presence of noise, though it is slightly mitigated after applying the linear ZNE.

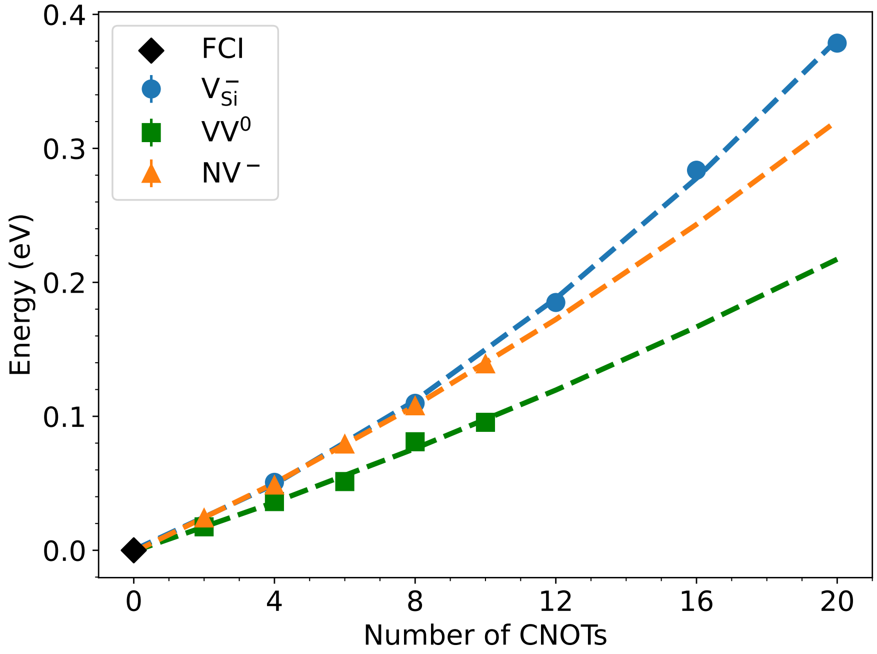

Figure 7.7: The ground state energy of the NV^- center and the VV^0 and V_{Si}^- in 4H-SiC as a function of the number of replicas used in the zero-noise extrapolation (see text), obtained using *ibmq_guadalupe*. The x axis is scaled with the number of CNOT gates used in the quantum circuit for clarity of comparison. The reference, noiseless result has been set to 0.

7.4 Conclusions

In summary, we presented a computational protocol to diagonalize Fermionic Hamiltonians on noisy-intermediate-quantum computers, which combines the QEE scheme to map electronic excitations onto qubits, a modified QCC ansatz for VQE optimizations of the ground state and noise mitigation techniques. The QEE mapping offers a robust solution to the unphysical state problem and the QCC ansatz provides a relatively short quantum circuit suitable for calculations on near-term intermediate-size quantum devices. We applied our protocol on quantum hardware to compute the electronic structure of strongly correlated ground and excited states of three spin defects, i.e., the NV^- center in diamond, the VV^0 and V_{Si}^- in 4H-SiC, and we presented calculations that would have been unfeasible with con-

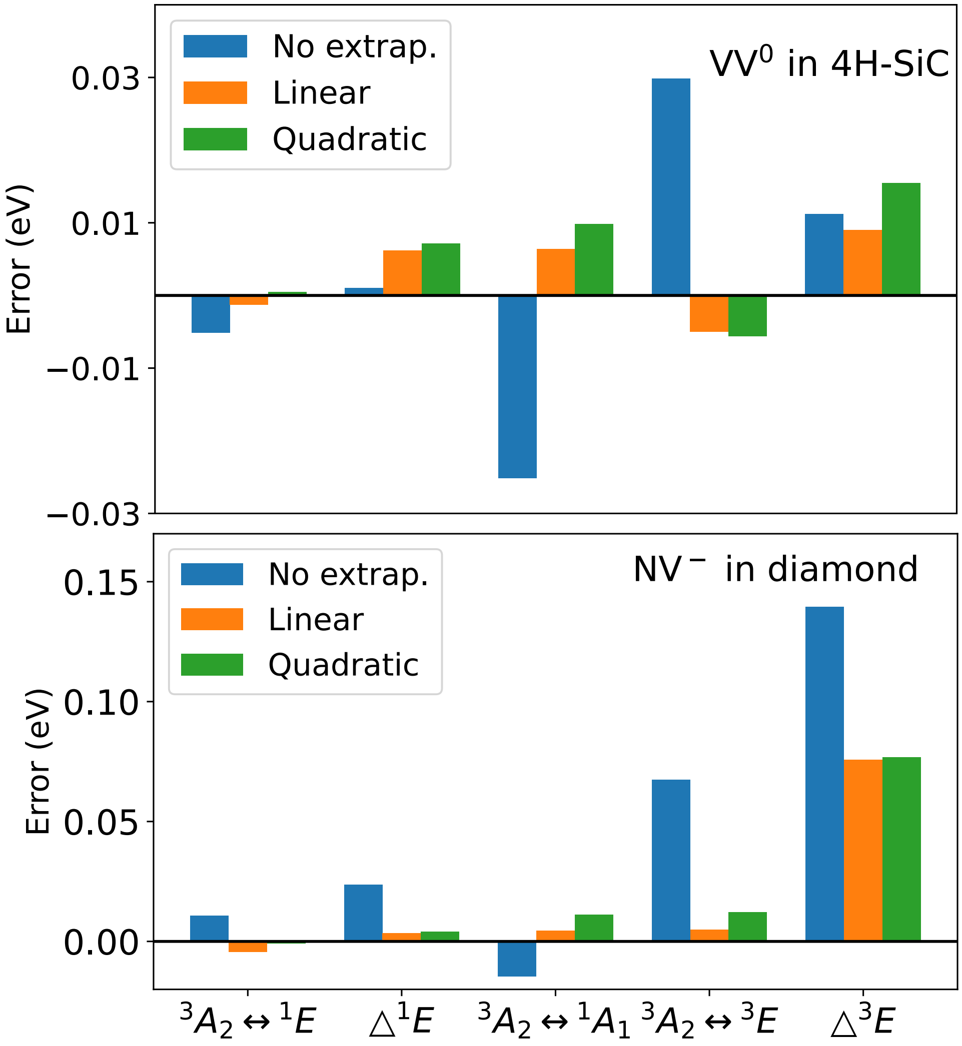

Figure 7.8: The upper and bottom panel show the error in the excitation energies (eV) of the VV^0 and NV$^-$ defects calculated using the quantum subspace expansion (QSE) method on *ibmq_guadalupe*. The x axis shows transitions between states labeled using the representation of the point group C_{3v}, following Ref. [203]. Δ^1E and Δ^3E indicate the breaking of degeneracy due to noise (see text). The reference values are obtained with a noiseless simulator and are identical to those of classical full configuration interaction (FCI) calculations on a classical computer. The blue, orange and green bar represent results obtained using no extrapolation, linear and quadratic zero-noise extrapolation techniques, respectively. For the results labeled with "quadratic extrapolation", we only carried out a quadratic extrapolation for the diagonal elements of the QSE matrix elements, and a linear extrapolation was applied to the off-diagonal elements.

ventional algorithms. In particular, we could go beyond the minimum models for the NV^- and VV^0 and tackle a complex defects such as $\mathrm{V}_{\mathrm{Si}}^-$ for the first time. Work is in progress to improve the efficiency of the measurements of $\langle H \rangle$ on quantum architectures, for example by adopting advanced measurement techniques with different term groupings [114, 339], fragmentation procedures [57, 58] and classical shadows [141], and to extend the applicability of our protocol to larger active spaces appropriate, e.g. to investigate adsorbates on surfaces or ions and nanostructures in solution. We finally note that establishing which algorithms are better suited to achieve quantum advantage in electronic structure calculations remains an open area of research. For example, recent papers have argued that simulations in first quantization offer some important advantages over approaches in second quantization including faster convergence to the continuum limit and the opportunity for practical simulations beyond the Born-Oppenheimer approximation [302]. Interestingly, in addition to efforts towards reaching a practical advantage with quantum computers, the development of algorithms for quantum computations is having a positive impact on the development of classical algorithms in various fields, e.g., machine learning [308] and computational spectroscopy [238].

CHAPTER 8

EVALUATING A QUANTUM-CLASSICAL QUANTUM MONTE CARLO ALGORITHM WITH MATCHGATE SHADOWS

This chapter is adapted from **B. Huang**, Y. Chen, B. Gupt, M. Suchara, A. Tran, S. McArdle, and G. Galli. “Evaluating a quantum-classical quantum Monte Carlo algorithm with Matchgate shadows.” *arXiv preprint arXiv:2404.18303* (2024).

Solving the electronic structure problem of molecules and solids to high accuracy is a major challenge in quantum chemistry and condensed matter physics. The rapid emergence and development of quantum computers offer a promising route to systematically tackle this problem. Recent work by Huggins, et al. [144] proposed a hybrid quantum-classical quantum Monte Carlo (QC-QMC) algorithm using Clifford shadows to determine the ground state of a Fermionic Hamiltonian. This approach displayed inherent noise resilience and the potential for improved accuracy compared to its purely classical counterpart. Nevertheless, the use of Clifford shadows introduces an exponentially scaling post-processing cost. In this work, we investigate an improved QC-QMC scheme utilizing the recently developed Matchgate shadows technique [326], which removes the aforementioned exponential bottleneck. We observe from experiments on quantum hardware that the use of Matchgate shadows in QC-QMC is still noise resilient - and show that this noise resilience has a more subtle origin than in the case of Clifford shadows. Nevertheless, we find that classical post-processing, while asymptotically efficient, requires hours of runtime on thousands of classical CPUs for even the smallest chemical systems, presenting a major challenge to the scalability of the algorithm.

8.1 Introduction

The ability to accurately solve the Schrödinger equation for interacting electrons will help tackle a multitude of problems in physics, chemistry and materials science, relevant to applications ranging from drug discovery [192] to the design of functional materials [120, 158]. In the past century, multiple efforts have been devoted to solving the Schrödinger equation on classical computers, either by using suitable approximations and mean-field theories [170] or by employing nearly exact methods such as full configuration interaction (FCI) [124] and quantum Monte Carlo (QMC) [18, 95]. However, known algorithms for FCI scale exponentially on classical computers, while scalable solutions using QMC often suffer from the sign problem and other numerical instabilities. In essence, highly entangled many-body wavefunctions of interacting electrons are hard to represent and optimize on classical computers.

The advent of quantum computers offers a promising route to tackle the interacting electron problem. Quantum computers use quantum bits (qubits) as processing units, and have advantages over classical computers for simulating entangled states. Therefore, research in developing quantum [16] or hybrid quantum-classical algorithms [227, 245] to tackle the electronic structure problem has flourished in the past decade. One popular algorithm to compute Fermionic ground states is the variational quantum eigensolver (VQE) and its variants [23, 112, 223, 293], where a parameterized quantum circuit is used to represent the wavefunction, and its optimization is off-loaded to classical hardware. Nevertheless, current noisy intermediate-scale quantum (NISQ) hardware is limited by the depth of quantum circuits that it can implement. Moreover, VQE faces optimization challenges resulting from ansatz– or noise–induced barren plateaus in energy landscapes [330], as well as large measurement overheads.

Recently Huggins, et al. [144] proposed a hybrid quantum-classical algorithm for quantum Monte Carlo (QC-QMC) and applied it to study the dissociation of diatomic molecules on Google's Sycamore quantum processor. The Monte Carlo algorithm is driven by sampling from a trial state $|\Psi_T\rangle$ prepared on the quantum computer, with the aim of producing smaller bias and better accuracy than its purely classical counterpart. The algorithm uses classical shadows [141] with random Clifford circuits to avoid iterative communication between classical and quantum hardware, which is desirable on near-term quantum devices as it minimizes latency from quantum-classical communication. Surprisingly, an inherent noise resilience was observed [144] — spurring both academic and industrial interest in the technique [8, 156, 214, 225, 338, 345]. Nevertheless, the cost of classically post-processing the Clifford shadows was proven to scale exponentially with system size, providing a barrier to achieving quantum advantage.

The inefficiencies of Clifford shadows for QC-QMC were recently addressed in Refs. [200, 326] by replacing the Clifford circuits with Matchgate circuits [347]. The two proposals were theoretical in nature, and have not yet been numerically or experimentally evaluated in the literature. In particular, it is unclear whether these scalable methods exhibit the noise resilience that underpinned the success of the original (unscalable) Clifford shadows approach [144], as the theoretical justification for the noise resilience of Clifford shadows does not immediately extend to the Matchgate case. In addition, while these proposals are formally efficient, their practicality for studying realistic systems has yet to be established.

In this work, we numerically and experimentally study the QC-QMC algorithm, incorporating Matchgate shadows. In particular, we probe the noise resilience of the algorithm on real quantum devices. We observe a similar noise resilience to the Clifford shadows case, but with a more subtle microscopic origin. Nevertheless, while the Matchgate shadows approach reduces the classical post-processing cost from exponential to formally polynomial, it has a sufficiently high degree polynomial scaling and large constant factors that we require hours of post-processing runtime for even the smallest chemical systems, using thousands of CPUs. This fundamentally challenges the scalability of the approach. We thus validate the persistence of one of the major strengths of QC-QMC, as well as elucidate the challenges

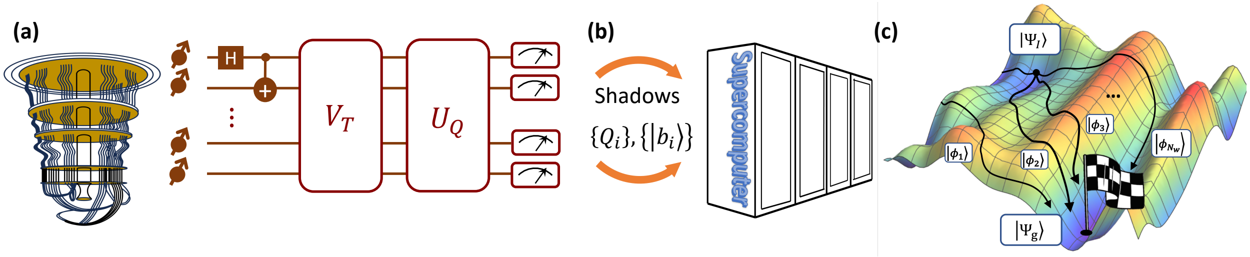

Figure 8.1: Workflow for the hybrid quantum-classical quantum Monte Carlo (QC-QMC) algorithm: (a). An equal superposition of the all-zero state $|\mathbf{0}\rangle$, and the quantum trial state $|\Psi_T\rangle$ is prepared on a quantum computer, followed by the twirling of random unitary circuits U_Q and measurements; (b). The measurement outcomes $\{|b_i\rangle\}$ and the random circuit unitary U_Q—which together constitute the information required to reconstruct classical shadows—are communicated to the classical computers; (c). The QMC procedure is carried out on a classical computer, where the walker states $|\phi_i\rangle$ evolve on the potential energy surface from the initial state $|\Psi_I\rangle$ towards the target ground state $|\Psi_g\rangle$.

that must be overcome if the technique is to provide practical quantum advantage.

The rest of the paper is organized as follows. In Sec. 8.2 we discuss how QC-QMC is performed and the basics of classical shadows, which serve as prerequisites for subsequent discussions. In Sec. 8.3, we first discuss prior work on noise robust classical shadows [54, 168] (and their recently developed Matchgate variants [336, 346]) and give an extension to these methods that mitigate state preparation noise in QC-QMC. Second, we experimentally verify the natural noise resilience of the Matchgate shadow protocol as used in QC-QMC. Finally, we apply QC-QMC to simulate the dissociation of hydrogen, and the ground state energy of a solid-state spin defect system, on different quantum hardware systems. These calculations reach agreement with the reference values even in the absence of error mitigation. In Sec. 8.4, we discuss the merits and shortcomings of QC-QMC and how it is related to other quantum-classical hybrid algorithms and purely classical QMC methods. Finally, Sec. 8.5 concludes our work with a summary.

8.2 Preliminaries

The workflow of the QC-QMC method is shown in Fig. 8.1, where the computation on quantum and classical hardware is partitioned by classical shadows. In this section, we first provide a brief overview of the auxiliary-field quantum Monte Carlo (AFQMC) algorithm [226] used in the QC-QMC method. Then we introduce the classical shadows formalism and discuss its use in QC-QMC. Readers familiar with this background material can skip to the summary of our results in Sec. 8.3.

8.2.1 Auxiliary-field quantum Monte Carlo

Within the electronic structure community, QMC refers to a family of methods that bypass the explicit optimization of the many-body wavefunction in an exponentially large Hilbert space. Specifically, probabilistic sampling is applied in a subspace of the full Hilbert space, resulting in a polynomial scaling of the memory required for the evaluation of the ground state energy of a given system. The auxiliary-field quantum Monte Carlo (AFQMC) method is one example of projector QMC methods where a stochastic imaginary time evolution of the wavefunction is carried out by propagating samples on a manifold of nonorthogonal Slater determinants. Each sample $\{|\phi_l\rangle\}$ is usually called a "walker". The ground state energy is estimated as

$$E = \frac{\sum_l w_l e^{i\theta_l} E_l^{\mathrm{loc}}}{\sum_l w_l e^{i\theta_l}}, \quad E_l^{\mathrm{loc}} = \frac{\langle\Psi_T|H|\phi_l\rangle}{\langle\Psi_T|\phi_l\rangle}, \tag{8.1}$$

where E_l^{loc} is the local energy of each walker, w_l, θ_l are its weight and phase, H is the electronic structure Hamiltonian, and $|\Psi_T\rangle$ is a trial state defined as an approximation to the true ground state. The walker wavefunction and its weight and phase are updated every time step according to functions of $\frac{\langle\Psi_T|\phi_i\rangle}{\langle\Psi_T|\phi_j\rangle}$ that perform the imaginary time evolution.

For a generic Hamiltonian, however, similar to other projector QMC methods, AFQMC suffers from the sign problem, or more precisely, the phase problem where the phases θ_l of the walkers are evenly distributed in $[0, 2\pi)$ [226, 343]. It leads to the ground state energy estimator, i.e., Eq. 8.1 (computed from the ensemble average of all the walkers) experiencing an exponentially fast decay of the signal-to-noise ratio and a large statistical error. To remedy the phase problem, a common solution is the so-called phaseless approximation (ph) [226], where $\theta_l = 0$ is enforced by a modified update rule, thus constraining the evolution of the walkers. Such an approximation, while controlling the phase problem, introduces a bias to the estimated ground state energy. The magnitude of the bias is largely determined by how well the trial state $|\Psi_T\rangle$ represents the exact ground state. On classical computers, $|\Psi_T\rangle$ is usually chosen as either a single Slater determinant, e.g., the Hartree-Fock state, or a linear combination of Slater determinants, to ensure a polynomial scaling in computational time [208].

The insight of Ref. [144] is that on a quantum computer, one may efficiently compute overlaps between Slater determinant walker states and a much wider range of trial states, e.g., the unitary coupled cluster (UCC) state [218, 245]. We refer to implementing AFQMC in this way as QC-AFQMC. Such states are potentially "closer" to the target ground state than those adopted as classical trials, and could lead to more accurate ground state energy estimations. It is currently unclear what are the best AFQMC trial states that can be prepared on a quantum computer, in low circuit depth. This is a similar issue to that of choosing a well-motivated and implementable ansatz circuit in VQE. We will discuss this problem in Sec. 8.4, and assume for now that a suitable AFQMC trial state can be efficiently prepared on a quantum computer. Then, the central issue for the QC-AFQMC scheme lies in how to evaluate the overlap amplitude $\langle\Psi_T|\phi\rangle$ for each walker, at each timestep. Efforts in the literature have branched out in two directions: Xu and Li [338] designed circuits based on the Hadamard test [84] to efficiently compute the overlap between the walker states and the trial state. On the other hand, Huggins, et al. [144] computed the amplitude by using the classical shadows technique applied to $|\Psi_T\rangle$. The former approach suffers a significant overhead in quantum computation due to the large number of walkers typically used in AFQMC. In addition, it requires iterative communication between the classical and quantum hardware, since $|\Psi_T\rangle$ is queried at every time step during the time evolution. We therefore followed the approach of Huggins et al. in this work, and we provide a detailed scaling comparison of the two approaches in Section 8.4.

8.2.2 Classical shadows

As mentioned in the previous subsection, the need to evaluate $\langle\Psi_T|\phi\rangle$ for all walkers at each time step is a key consideration for the practicality of the algorithm. In Ref. [144] it was shown that the measurements required in QC-AFQMC can be recast into the following framework. Let ρ denote the density matrix of an n-qubit quantum state that we know how to prepare, and $\{O_i\}$ denote a collection of M observables whose expectation values, i.e., $\mathrm{tr}(O_i\rho)$ we wish to estimate. Classical shadow tomography [141] provides a way to estimate these quantities with a cost that only scales logarithmically with M. Specifically, it estimates each $\mathrm{tr}(O_i\rho)$ up to some error ϵ by the following procedure: i) choose a distribution $\mathcal{D}$ of unitary transformations; ii) sample random unitaries $U \in \mathcal{D}$ from the chosen distribution and iii) measure the state $U\rho U^\dagger$ in the computational basis $\{|b\rangle\}$ (we refer to the tensor products of $\{|0\rangle, |1\rangle\}$ of each qubit as the *computational basis*, i.e., $\{|b\rangle\}_{b\in\{0,1\}^n}$) to obtain the measurement outcome $|b\rangle\langle b|$. Consider the state $U^\dagger|b\rangle\langle b|U$; in expectation, the mapping from ρ to $U^\dagger|b\rangle\langle b|U$ defines a quantum channel,

$$\mathcal{M}(\rho) := \mathop{\mathbb{E}}_{U\sim\mathcal{D}}\left[U^\dagger|\hat{b}\rangle\langle\hat{b}|U\right] = \mathop{\mathbb{E}}_{U\sim\mathcal{D}}\sum_{b\in\{0,1\}^n}\langle b|U\rho U^\dagger|b\rangle U^\dagger|b\rangle\langle b|U, \tag{8.2}$$

where $\mathbb{E}$ denotes the operation of averaging, and the hat represents a statistical estimator.

In the classical shadows framework, we require $\mathcal{M}$ to be invertible, which is true if and only if the collection of measurement operators defined by drawing $U \in \mathcal{D}$ and measuring in the computational basis is tomographically complete. Assuming that these conditions are satisfied, we can apply $\mathcal{M}^{-1}$ to both sides of above equation, yielding

$$\rho = \mathop{\mathbb{E}}_{U\sim\mathcal{D}}[\hat{\rho}] = \mathcal{M}^{-1}\left(\mathop{\mathbb{E}}_{U\sim\mathcal{D}}\left[U^\dagger|\hat{b}\rangle\langle\hat{b}|U\right]\right) = \mathop{\mathbb{E}}_{U\sim\mathcal{D}}\left[\mathcal{M}^{-1}\left(U^\dagger|\hat{b}\rangle\langle\hat{b}|U\right)\right]. \tag{8.3}$$

We call the collection $\{\mathcal{M}^{-1}(U^\dagger|\hat{b}\rangle\langle\hat{b}|U)\}$ the classical shadows of ρ. These shadows can be used to estimate the expectation values $\mathrm{tr}(O_i\rho)$,

$$\langle O_i\rangle = \mathop{\mathbb{E}}_{U\sim\mathcal{D}}\mathrm{tr}\left[O_i\mathcal{M}^{-1}\left(U^\dagger|\hat{b}\rangle\langle\hat{b}|U\right)\right], \tag{8.4}$$

each within error ϵ with probability at least $1-\delta$, with a number of samples that scales as:

$$N_{\text{sample}} = \mathcal{O}\left(\frac{\log(M/\delta)}{\epsilon^2}\max_{1<i<M}\mathrm{Var}[\hat{o}_i]\right). \tag{8.5}$$

In the above equation, we define $\hat{o}_i$ as an estimator of $\mathrm{tr}(O_i\rho)$ and $\mathrm{Var}[\hat{o}_i]$ represents the variance of estimator $\hat{o}_i$, which could be bounded by the shadow norm of O_i [141]. Importantly for QC-AFQMC, N_{sample} only scales logarithmically with the number of target observables M[1].

Formally, the condition that the measurement channel is invertible is sufficient for performing the classical shadows protocol. In practice, it is desirable that the protocol is efficient both in terms of quantum and classical resources. This means that there should be an efficient procedure to sample unitaries U from $\mathcal{D}$ and implement them on a quantum computer, and in addition the variance of the estimates $\hat{o}_i$ is polynomial in system size. Moreover, it should be efficient to compute the expectation values with respect to the shadows, $\mathrm{tr}\left[O_i\mathcal{M}^{-1}\left(U^\dagger|\hat{b}\rangle\langle\hat{b}|U\right)\right]$, on a classical computer.

---

[1] We note that the scaling in Eq. 8.5 was rigorously proven in Ref. [141] using a median-of-means estimator. For Matchgate shadows, however, it is proven in Ref. [347] that a mean estimator suffices, which we use in this work.

In QC-AFQMC, the overlap amplitude $\langle\Psi_T|\phi\rangle$ is not a physical observable. Nevertheless, it can be measured within the framework of classical shadows by rewriting it as [144]

$$\langle\Psi_T|\phi\rangle = 2\mathrm{tr}\left(|\phi\rangle\langle\mathbf{0}|\rho\right) = 2\underset{U\sim\mathcal{D}}{\mathbb{E}}\mathrm{tr}\left[|\phi\rangle\langle\mathbf{0}|\mathcal{M}^{-1}\left(U^\dagger|\hat{b}\rangle\langle\hat{b}|U\right)\right], \tag{8.6}$$

where ρ is the density matrix corresponding to the state $\frac{1}{\sqrt{2}}\left(|\mathbf{0}\rangle + |\Psi_T\rangle\right)$ and $|\mathbf{0}\rangle = |0\rangle^{\otimes n}$. Here $|\phi\rangle\langle\mathbf{0}|$ plays the role of the operator O.

Ref. [144] used random Clifford circuits to perform classical shadows, where the overlap amplitude is post-processed as

$$\langle\Psi_T|\phi\rangle = 2f^{-1}\underset{U\sim\mathrm{Cl}(2^n)}{\mathbb{E}}\left[\langle\mathbf{0}|U^\dagger|\hat{b}\rangle\langle\hat{b}|U|\phi\rangle\right]. \tag{8.7}$$

In the above equation, $f = (2^n+1)^{-1}$ is the only (non-trivial) eigenvalue of $\mathcal{M}$, since the Clifford group has only one non-trivial irreducible representation (irrep). The first term $\langle\mathbf{0}|U^\dagger|b\rangle$ can be efficiently computed using the Gottesman-Knill theorem [1], but the second term $\langle b|U|\phi\rangle$, in general, cannot be efficiently estimated due to $|\phi\rangle$ being a random Slater determinant. As noted in Ref. [144], the method of Ref. [308] could be used to efficiently estimate this quantity up to an additive error. Nevertheless, the f^{-1} prefactor exponentially amplifies this error, eliminating the efficiency of the proposed scheme.

Another interesting observation of Ref. [144] is that the evaluation of overlap ratios, which drives the AFQMC algorithm, is resilient to quantum hardware noise. This phenomenon can be understood by first noting that noise will change the prefactor f to a modified prefactor $\widetilde{f}$ (as explained in detail in Sec. 8.3.1). This prefactor cancels out when taking the ratio, recovering the noiseless result without requiring any additional error mitigation. We refer to this as having an inherent noise resilience.

Refs. [200, 326] overcame the post-processing limitations of Clifford shadows by replacing the Clifford unitaries with random Matchgate circuits. The Matchgate circuit is the qubit representation of the Fermionic Gaussian transformation assuming the Jordan-Wigner (JW) transformation [334] is used. We therefore adopt the JW mapping throughout this work. Unlike the Clifford group, the Matchgate group has $(n + 1)$ (even) irreps. The overlap amplitude can be computed as [326]

$$\langle \Psi_T | \phi \rangle = 2 \sum_{l=0}^{n} f_{2l}^{-1} \underset{Q \sim B(2n)}{\mathbb{E}} \operatorname{tr} \left[|\phi\rangle\langle 0| \Pi_{2l} \left(U_Q^{\dagger} |\hat{b}\rangle\langle \hat{b}| U_Q \right) \right], \tag{8.8}$$

where the random Matchgate circuits U_Q are prepared by sampling random signed permutation matrices Q ($Q \in B(2n)$, where B represents the Borel group). In Eq. 8.8, Π_{2l} is the projector associated with the l-th even irrep, and its eigenvalue f_{2l} is $\binom{2n}{2l}^{-1}\binom{n}{l}$. Importantly, Eq. 8.8 can be efficiently solved using the matrix Pfaffian, with a scaling of $\mathcal{O}\left((n - \zeta/2)^4\right)$ by polynomial interpolation [326], where ζ denotes the number of electrons. As such, the exponential post-processing bottleneck present in the Clifford shadows approach is eliminated through the use of Matchgate shadows.

Inherent noise resilience, analogous to that observed for overlap ratios computed via Clifford shadows, has not yet been established for overlap ratios computed via Matchgate shadows. One sufficient but not necessary condition, (following from the Clifford case), would be $\widetilde{f}_{2l} = \alpha f_{2l},\ l \in \{0, 1, \ldots, n\}$, where α is a proportionality constant. In Sec. 8.3.2 we investigate the noise resilience of overlap ratios computed via Matchgate shadows. While our experimental results do not display a universal proportionality constant between each $\widetilde{f}_{2l}$ and f_{2l}, we nevertheless find that the computed ratios are inherently robust to noise, and provide justification for this observation.

8.3 Results

In this section, we present our results, divided into three parts. We first introduce prior work on noise robust classical shadows, and provide an improvement that mitigates state preparation noise in QC-AFQMC. Second, we experimentally test for noise resilience of both overlap amplitudes and ratios of overlap amplitudes, evaluated via the Matchgate shadow technique. Notably, we observe that the ratios are resilient to the effects of noise (as was previously observed for Clifford shadows [144]). We provide a theoretical explanation for the observed noise resilience and its limitations, which has more subtle origins than in the Clifford case. Third, we apply the QC-AFQMC algorithm to compute i) the dissociation curve of the hydrogen molecule on an IBM superconducting device; and ii) the ground state of a negatively charged nitrogen-vacancy (NV) center in diamond on an IonQ trapped ion quantum computer.

We use the following notation in this section: we denote overlap amplitudes obtained from noiseless shadows with an ordinary bracket, $\langle \Psi_T | \phi \rangle$, quantities subject to quantum noise with a tilde bracket, $\widetilde{\langle \Psi_T | \phi \rangle}$, and we use a tilde plus subscript r to denote quantities obtained from a robust shadow protocol, $\widetilde{\langle \Psi_T | \phi \rangle}_r$.

8.3.1 Robust Matchgate shadow protocol

Refs. [54, 168] developed a "robust shadow protocol", showing that when the quantum noise is gate-independent, time-stationary, and Markovian (GTM), and the state preparation of ρ is perfect, a noise-free expectation value can be obtained. The protocol works by replacing the eigenvalue(s) f of $\mathcal{M}$ with modified value(s) $\widetilde{f}$ that compensates for the effect of noise. The robust scheme uses additional shadow-like circuits to estimate the value(s) of $\widetilde{f}$. It can be viewed as passive error mitigation, as the updates are made purely in the classical post-processing of the shadow expectation value. The framework was originally applied to global and local Clifford shadows. Recently, two separate works extended the robust shadow protocol to the Matchgate setting [336, 346]. The latter of these works observed a close connection between the circuit used for the robust Matchgate shadow protocol and prior work on Matchgate randomized benchmarking [125].

The robust Matchgate shadows protocol [336] estimates $\{\widetilde{f}_{2l}\}$ using the following steps: i) prepare the all-zero state $|\mathbf{0}\rangle$ on a quantum computer; ii) sample $Q \in B(2n)$ and apply the Matchgate circuit U_Q to $|\mathbf{0}\rangle$; iii) measure in the computational basis and collect measurement outcomes $|b\rangle$. The expressions used to calculate $\{\widetilde{f}_{2l}\}$ from these measurement outcomes are given in the appendix of the paper. The sample complexity is asymptotically equivalent to that used in the noiseless case [336].

The established robust shadow scheme focuses on noise in the shadow unitary (U_Q in Fig. 8.1a), and does not mitigate any noise occurring during state preparation (V_T in Fig. 8.1a). We extend the method to (partly) account for noise that occurs during the state preparation unitary. In QC-AFQMC, we evaluate the overlap amplitudes by measuring classical shadows of an equal superposition state $\frac{1}{\sqrt{2}}(|\Psi_T\rangle + |\mathbf{0}\rangle)$. This state is prepared via a circuit that first generates a superposition of the Hartree-Fock state with $|\mathbf{0}\rangle$ state, and then applies a unitary V_T, such that $V_T|\Psi_{\mathrm{HF}}\rangle = |\Psi_T\rangle$ and $V_T|\mathbf{0}\rangle = |\mathbf{0}\rangle$ [237]. As discussed above, to estimate the values of $\{\widetilde{f}_{2l}\}$ required in the robust Matchgate protocol, we apply a Matchgate shadow circuit to the initial state $|\mathbf{0}\rangle$. We can partially account for the noise in the state preparation circuit in the following way. We minimally alter the QC-AFQMC circuit in Fig. 8.1a, such that it measures $\{\widetilde{f}_{2l}\}$, by removing the initial Hadamard gate. In a noiseless setting, this modified version of V_T would still result in $\rho = |\mathbf{0}\rangle\langle\mathbf{0}|$, as required. In the noisy setting, we can treat the noise as originating in the Matchgate circuit, which is then mitigated by the robust protocol. While we do not yet have a full mathematical characterization of the noise models that can be mitigated by our enhanced robust Matchgate shadows technique, we demonstrate the efficacy of this approach through numerical simulations and experiments on quantum hardware, presented in the following subsection.

8.3.2 Noise resilience of overlap amplitudes and their ratios

As discussed previously, all of the key quantities used in the AFQMC algorithm, e.g., the local energy, can be expressed as linear combinations of the ratio of overlaps $\frac{\langle\Psi_T|\phi_i\rangle}{\langle\Psi_T|\phi_j\rangle}$. Hence we can view the propagation in imaginary time as being driven by these overlap ratios. We can estimate the individual overlaps from Matchgate shadows. In this section, we experimentally probe the impact of noise on both the overlap amplitudes, and their ratios by measuring these quantities via Matchgate shadows implemented on the IBM Hanoi superconducting quantum computer. As a test system, we consider the hydrogen molecule in its minimal STO-3G basis, mapped to four qubits via the Jordan-Wigner transform. We use a trial state of the form $|\Psi_T\rangle = \alpha|1100\rangle + \beta|0011\rangle$, which is a linear combination of the Hartree-Fock configuration and double excited state, respectively.

Evaluating the overlap amplitudes

We compute the overlaps $\langle\Psi_T|\phi_i\rangle$ between the trial state and 16 randomly sampled Slater determinants, using Eq. 8.8, as a function of the number of Matchgate shadows used. We consider both noisy Matchgate shadows, and those corrected using the robust Matchgate shadow protocol introduced in Sec. 8.3.1.

In Fig. 8.2 (upper panel) we show the mean absolute error (MAE) of the noisy and noise-robust overlaps, with respect to the ideal noiseless value. We observe that the noisy results differ significantly from the true values, and their accuracy is limited by the effects of noise. The two robust shadow approaches (accounting for state preparation error (SP) and not accounting for it) mitigate the impact of hardware noise. In particular, compensating for the effects of state preparation noise results in a much smaller deviation from the ideal noiseless values than the standard robust approach. This observation signifies the importance of considering the state preparation noise when using robust shadows on quantum hardware.

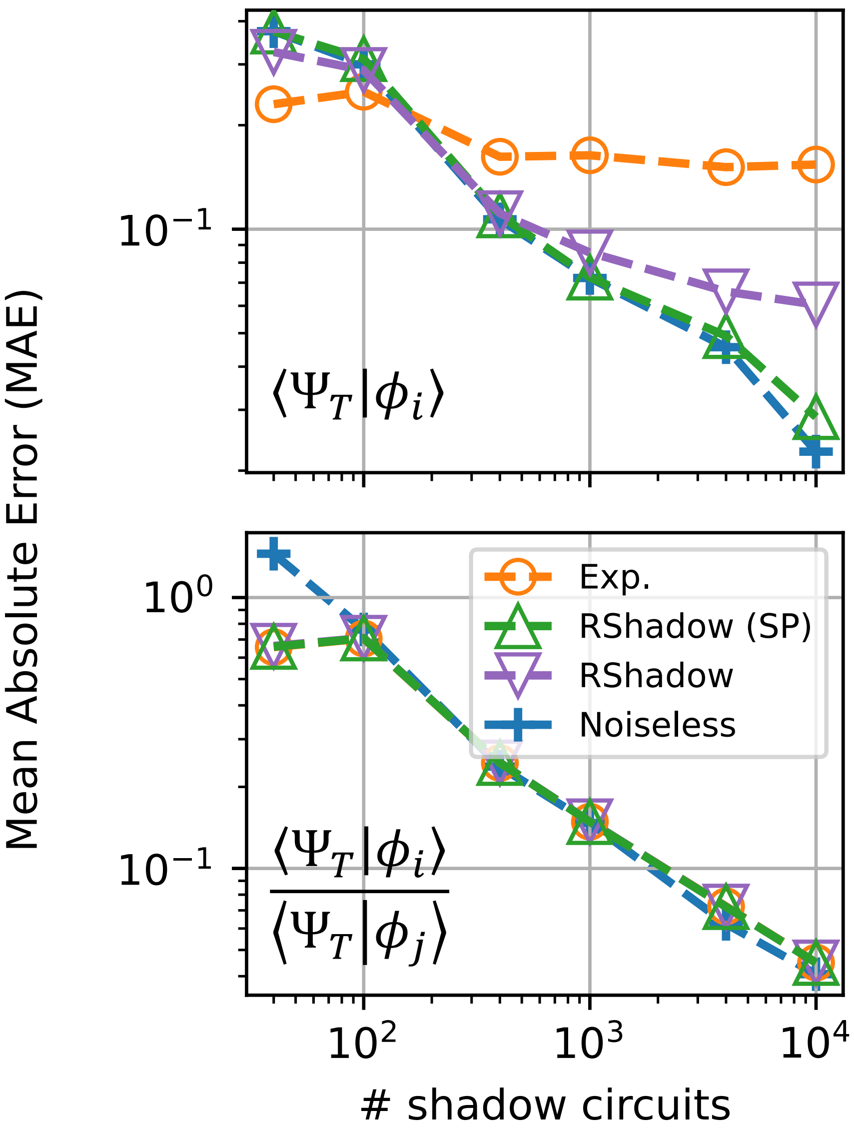

Figure 8.2: The mean absolute error (MAE) of overlap amplitudes $\langle\Psi_T|\phi_i\rangle$ and overlap ratios $\frac{\langle\Psi_T|\phi_i\rangle}{\langle\Psi_T|\phi_j\rangle}$ w.r.t. the number of Matchgate circuits, varying from 40 to 10,000. A total of 16,000 Matchgate shadow circuits are used in this experiment, each using 1024 measurement shots. The raw experimental results ("Exp.") and noiseless simulation ("Noiseless") are plotted in orange circles and blue crosses, respectively. For the two robust protocols ("RShadow" and "RShadow (SP)"), we allocated another 16,000 Matchgate circuits for each to determine the coefficients $\widetilde{f}_{2l}$, thus doubling the measurement cost.

Noise resilience in the evaluation of overlap ratios

Using the results presented in the previous section for $\{\langle\Psi_T|\phi_i\rangle\}$, we can compute the 120 possible ratios of overlaps originating from the 16 Slater determinants sampled. In Fig. 8.2

(lower panel) we show the MAE of these overlap ratios with respect to the ideal values. We observe the following behavior

$$\frac{\langle \Psi_T | \phi_i \rangle}{\langle \Psi_T | \phi_j \rangle} \approx \frac{\widetilde{\langle \Psi_T | \phi_i \rangle_r}}{\widetilde{\langle \Psi_T | \phi_j \rangle_r}} \approx \frac{\widetilde{\langle \Psi_T | \phi_i \rangle}}{\widetilde{\langle \Psi_T | \phi_j \rangle}}, \tag{8.9}$$

when the number of shadow circuits exceeds 100. This is an indication of noise resilience in evaluating the overlap ratios, suggesting that the robust shadow protocol may not be required for QC-AFQMC. We provide theoretical justification for these observations below.

The first (approximate) equality in Eq. 8.9 will not hold for all noise models, as the robust Matchgate shadow protocol is only guaranteed to correct the effects of noise if its assumptions (GTM noise, noiseless state preparation) are satisfied. Nevertheless, for cases where the robust Matchgate protocol is able to correct the effects of noise the equality of the ratios follows directly. In our experiments, we found that the robust Matchgate protocol was able to correct the individual overlaps up to a small residual error attributed to residual state preparation noise. This leads to the approximate equality between the ratios.

The second (approximate) equality shows that the ratio of any two uncorrected overlap amplitudes (which are themselves inaccurate, see Fig. 8.2 (upper panel)) yields the same results as ratios of overlaps computed via the robust Matchgate protocol. To understand this result, we first restate Eq. 8.8 for computing the overlap in the absence of noise

$$\langle \Psi_T | \phi \rangle = 2 \sum_{l=0}^{n} f_{2l}^{-1} \mathop{\mathbb{E}}_{Q \sim B(2n)} \operatorname{tr}\left[|\phi\rangle\langle \mathbf{0}| \Pi_{2l} \left(U_Q^{\dagger} |\hat{b}\rangle\langle \hat{b}| U_Q \right) \right],$$

and observe that $|\phi\rangle\langle \mathbf{0}|$ is an eigen-operator of Π_{2l} in a subspace spanned by ζ-electron basis states and the vacuum state with $\Pi_{2l}(|\phi\rangle\langle \mathbf{0}|) = b_{2l} |\phi\rangle\langle \mathbf{0}|$. The reason we restrict to this subspace is that ρ is an equal superposition of $|\mathbf{0}\rangle$ and $|\Psi_T\rangle$, and therefore the trace of ρ with operators outside this subspace will necessarily be zero. This will still hold approximately true when ρ is reconstructed from a finite number of classical shadows. This operator only appears in the classical post-processing step and is therefore not affected by noise. Therefore, the noisy overlap amplitude can be expanded as

$$\widetilde{\langle \Psi_T | \phi \rangle} \approx 2 \left(\sum_{l=0}^{n} f_{2l}^{-1} b_{2l} \right) \underset{Q \sim B(2n)}{\mathbb{E}} \left[\left\langle \mathbf{0} \middle| U_Q^\dagger \middle| \hat{\tilde{b}} \right\rangle \left\langle \hat{\tilde{b}} \middle| U_Q \middle| \phi \right\rangle \right], \tag{8.10}$$

where in deriving this equation, we have used $\operatorname{tr}\left(A\mathcal{M}^{-1}(B)\right) = \operatorname{tr}\left(\mathcal{M}^{-1}(A)B\right)$, where operators A, B are in the subspace where $\mathcal{M}$ is invertible [326]. This expression, being very similar to Eq. 8.7 of the Clifford case, has the sum over the channel index l and walker state $|\phi\rangle$ separated into a product. In order to mitigate the effects of noise with the robust Matchgate shadows approach, we could replace f_{2l}^{-1} with $\widetilde{f}_{2l}^{-1}$

$$\widetilde{\langle \Psi_T | \phi \rangle}_r \approx 2 \left(\sum_{l=0}^{n} \widetilde{f}_{2l}^{-1} b_{2l} \right) \underset{Q \sim B(2n)}{\mathbb{E}} \left[\left\langle \mathbf{0} \middle| U_Q^\dagger \middle| \hat{\tilde{b}} \right\rangle \left\langle \hat{\tilde{b}} \middle| U_Q \middle| \phi \right\rangle \right]. \tag{8.11}$$

If the noise satisfies GTM assumptions (and state preparation is noise-free), Eq. 8.11 is able to correct the effect of noise that manifests from the deviation of $\left|\hat{\tilde{b}}\right\rangle\left\langle\hat{\tilde{b}}\right|$ from $\left|\hat{b}\right\rangle\left\langle\hat{b}\right|$. If these assumptions on the noise are not satisfied, robust Matchgate shadows may not be able to perfectly recover the noiseless value. We can now observe that regardless of whether the robust procedure is used, the terms corresponding to the sum over l in Eq. 8.10 and Eq. 8.11 are both independent of $|\phi\rangle$. As such, when computing the ratios $\frac{\widetilde{\langle \Psi_T | \phi_i \rangle}_r}{\widetilde{\langle \Psi_T | \phi_j \rangle}_r}$ and $\frac{\widetilde{\langle \Psi_T | \phi_i \rangle}}{\widetilde{\langle \Psi_T | \phi_j \rangle}}$, the prefactor will cancel between the numerator and denominator, leaving behind a ratio of estimators $\underset{Q \sim B(2n)}{\mathbb{E}} \left[\dots \right]$ that is identical for the robust case and the non-robust case. As such, if the ratio of overlaps evaluated via robust Matchgate shadows is able to approximately recover the noiseless results (as observed in our data), we conclude that the ratio of overlaps evaluated via regular Matchgate shadows is also able to approximately recover the noiseless value. This explains the data shown in Fig. 8.2 (lower panel).

We emphasize that the cancellation of the pre-factor found here, i.e., $\sum_{l=0}^{n} \widetilde{f}_{2l}^{-1} b_{2l}$, should not be mistaken with that of the Clifford case, although they have a very similar form. This prefactor of Matchgate shadows, as a sum, contains the noise information of all $(n+1)$ even subspaces of the Matchgate channel. From the Clifford case, one might naturally think that the cancellation for the Matchgate shadow is due to $\widetilde{f}_{2l} = \alpha f_{2l}$ where α is independent of l. We verified that this is not the case by experimentally determining $\widetilde{f}_{2l}$. We observed that α_l could differ by up to 20% for different l. Therefore, this cancellation should be credited to the structure of $|\phi\rangle\langle\mathbf{0}|$, namely being an eigen-operator of Π_{2l}. If another observable, without this property, were chosen, any observed noise resilience would have an alternative origin. For example, Ref. [277] shows a similar contractive property in evaluating the ratios, but only for noise models that ensure $\langle\mathbf{0}|\rho_{\text{noise}}|\phi\rangle$ is zero, where ρ_{noise} is the noise corrupted part of the density matrix.

As discussed above, robust shadows have been shown to correct for noise in the shadow circuit, assuming noiseless state preparation [54], or state preparation affected by global depolarizing noise [144, 277]. In a realistic setting, the state preparation step may suffer from more complicated noise which may prevent the technique from recovering the noiseless result. We performed numerical simulations to compute overlap ratios for the water molecule in a (4e, 4o) active space (8 qubits). We employed asymmetric Pauli errors as the noise model in this simulation (including in the state preparation circuit). The results, shown in Fig. 8.3 corroborate the analysis provided above. Specifically, we observe from the upper panel that when computing $\widetilde{\langle\Psi_T|\phi_i\rangle}$ the results differ significantly from the noiseless value. In contrast, when computing $\widetilde{\langle\Psi_T|\phi_i\rangle}_r$ using the robust Matchgate protocol (with compensation for state preparation error) we are able to almost recover the noise-free value. We attribute the deviation from the noiseless value to the presence of some residual state preparation error, which violates the assumptions of the robust shadow protocol. In contrast, from the lower panel we observe that the ratios of overlaps evaluated via the robust Matchgate shadow protocol are no more accurate than those evaluated using the regular Matchgate shadow protocol. Moreover, both of these values deviate from the noiseless value by a small error

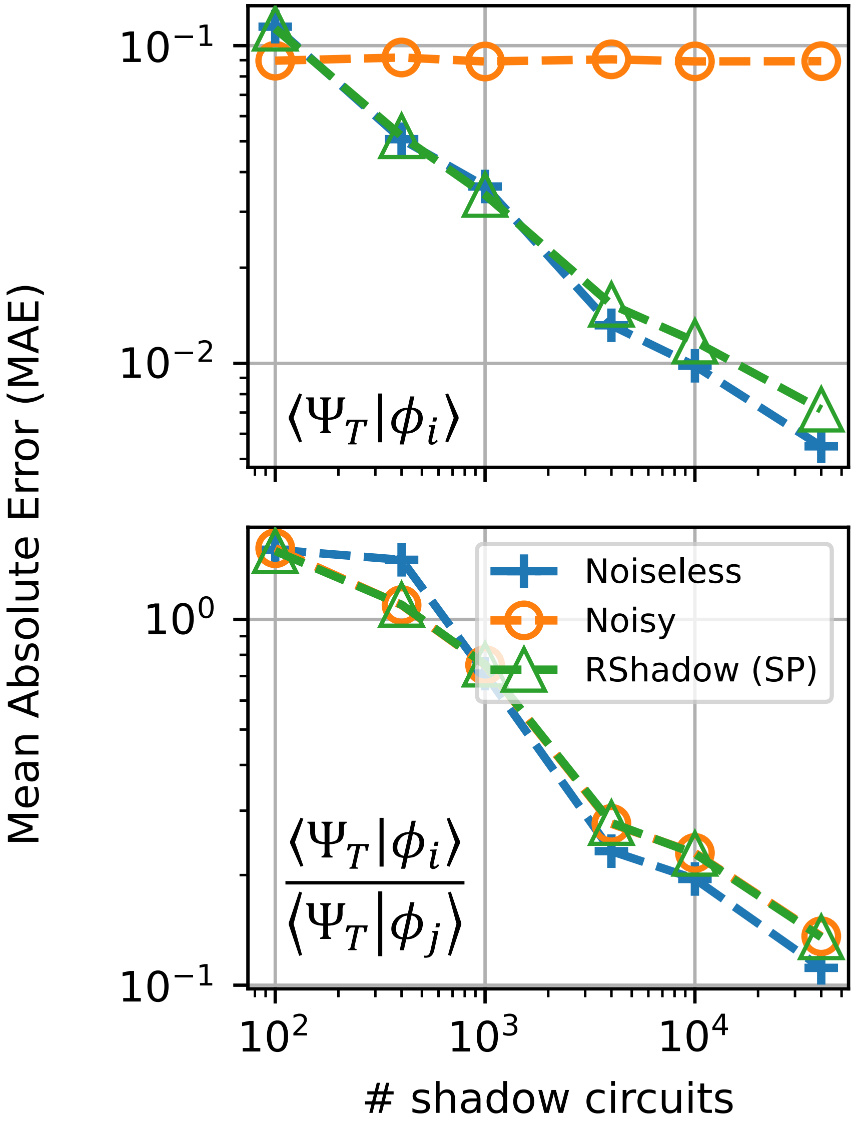

Figure 8.3: The MAE of estimating overlap amplitudes and overlap ratios w.r.t. the number of Matchgate shadow circuits for the water molecule (8 qubits). These results were obtained through numerical simulations under single-qubit asymmetric Pauli noise, where the Pauli-X, Z and Y error rates are set to 1, 3, 2%, respectively.

due to residual (uncorrectable) state preparation noise. In the case of coherent errors during state preparation, we effectively prepare $\left|\widetilde{\Psi}_T\right\rangle = U\left|\Psi_T\right\rangle$ for some unitary U. As such, while we would still observe that $\frac{\widetilde{\langle\Psi_T|\phi_i\rangle}}{\widetilde{\langle\Psi_T|\phi_j\rangle}} \approx \frac{\widetilde{\langle\Psi_T|\phi_i\rangle}_r}{\widetilde{\langle\Psi_T|\phi_j\rangle}_r}$, neither ratio would likely recover the noiseless value.

Overall, the results of this subsection highlight a limitation of the robust Matchgate protocol, and its use in QC-AFQMC. Nevertheless, these results should be seen as an attractive feature of QC-AFQMC, as they suggest that the algorithm, driven by overlap ratios, is naturally resilient to the impact of many types of noise.

8.3.3 Computing ground states with QC-AFQMC

Having established the inherent noise resilience of the overlap ratios that drive the AFQMC algorithm, we demonstrate that this property contributes to noise resilience in the overall algorithm. We first compute the dissociation curve of the four-qubit hydrogen molecule studied in the previous subsections using the QC-AFQMC algorithm implemented on the IBM Hanoi superconducting quantum processor. We then apply the QC-AFQMC algorithm to compute the ground state of an NV center in diamond, using the Aria trapped ion quantum processor from IonQ. In both settings, we emulate practical applications of QC-AFQMC by assuming a trial state generated by an imperfect VQE calculation. In both cases, we use a tailored UCCSD ansatz, which was optimized until the energy was approximately $30 \sim 80$ mHa higher than the FCI reference.

Hydrogen molecule dissociation

In Fig. 8.4 (upper panel) we show the ground state energies obtained from QC-AFQMC at 5 different molecular geometries. If we target an error $\epsilon = 10^{-2}$ on any overlap, with $\geq 99.99\%$ confidence, the rigorous sample complexity bounds presented in Eq. 8.5 imply the need to use $\sim 1.1 \times 10^5$ shadow circuits (with one measurement shot per circuit). As shown in Fig. 8.2, it was sufficient to use only 16000 circuits for each bond length, suggesting the bounds of Eq. 8.5 are overly pessimistic for the small system studied here. Given the noise resilience observed in evaluating the overlap ratios, the use of robust shadows was not necessary. In our AFQMC calculations, we used 4800 walkers for all numerical data presented here to ensure a negligible variance, and a time step $\Delta\tau = 0.005$ H.a.$^{-1}$ resulting in a negligible error. We chose the initial walker state to be the Hartree-Fock state, for each of the five distances studied here. The calculation was parallelized across 4800 CPU cores, as discussed in more detail below.

In the interest of conserving computational resources, only two of the five data points (solid points) were obtained using the scalable Matchgate shadows approach outlined above. The remaining three data points were obtained using an exponentially scaling approach used in Ref. [144], that is ultimately more efficient than the scalable Matchgate approach for small system sizes. We verified that the two schemes give the same results for overlap amplitudes. Thus, the two Matchgate-obtained points are used as a complete evaluation of the practicality of the algorithm, while the remaining three points are only presented to confirm the accuracy of the algorithm in the presence of hardware noise.

We observe that all five QC-AFQMC calculations converge to within chemical accuracy of the FCI reference value, even without the use of the robust shadow protocol. In Fig. 8.4 (lower panel) we show the variation in energy as a function of imaginary time for the 0.75 Å geometry. There is little observable difference (~ 0.1 mHa) between the noisy experiment and its noiseless classical emulation.

We further note that even when the state preparation suffers from coherent errors, the QC-AFQMC algorithm is still able to recover accurate ground state energies, providing the effective quantum trial state $|\widetilde{\Psi}_T\rangle$, reconstructed from the noisy shadows, does not appreciably deviate from $|\Psi_T\rangle$. This is a result of the dissipative nature of the imaginary time process emulated by AFQMC, which will drive any initial state towards the ground state. This further enhances the inherent noise resilience of the QC-AFQMC algorithm.

We emphasize that even for the hydrogen molecule in a minimal basis set, executing the QC-AFQMC algorithm using Matchgate shadows requires a substantial amount of resources, with classical computation dominating over the quantum subroutine. It was necessary to

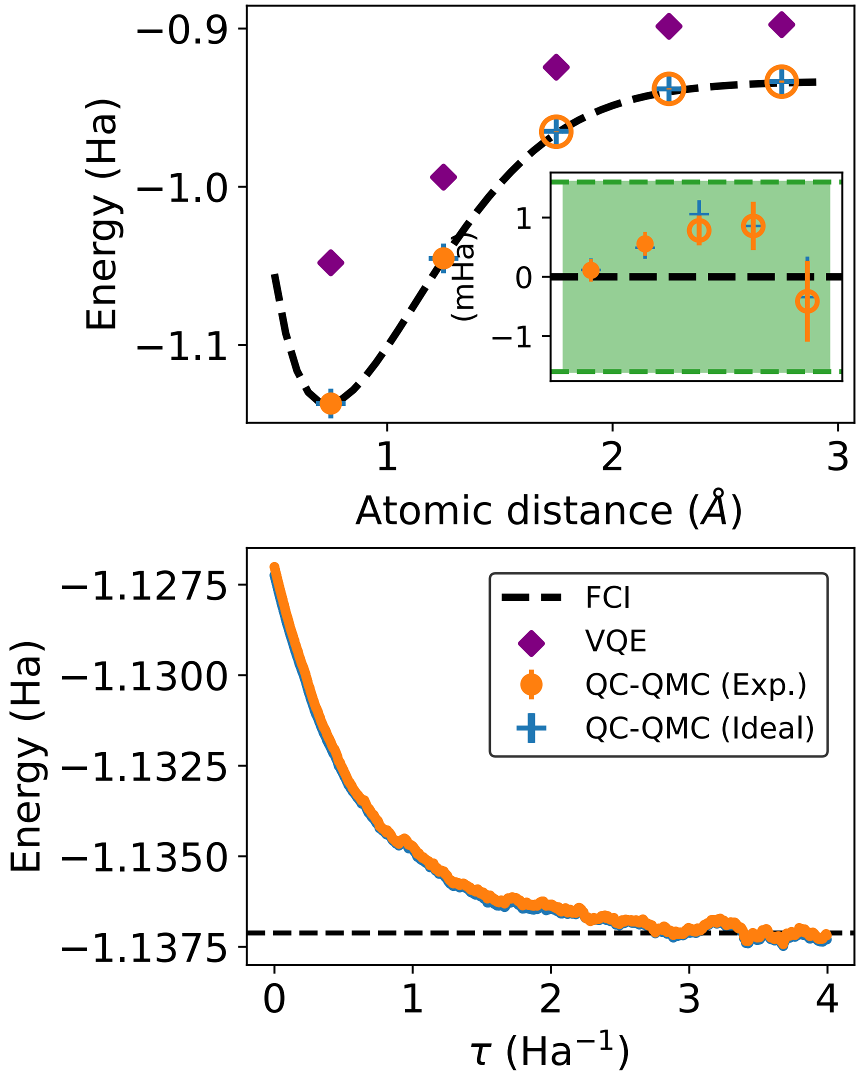

Figure 8.4: Estimations of the ground state energy of the hydrogen molecule at 5 different bond distances (upper). The QC-AFQMC calculation run on the IBM Hanoi quantum computer (solid and hollow orange circles labeled "exp.") converges within chemical accuracy for all distances (see inset), with a difference of $\sim 10^{-4}$ H.a. from its simulated noiseless counterpart (blue crosses). As discussed in the main text, filled circles denote results obtained with the scalable Matchgate shadows approach, while the empty circles denote results obtained with the non-scalable approach. The quantum trial state is obtained from a noisy VQE simulation (purple diamond). An imaginary time evolution at 0.75 Å is plotted in the lower panel, where the auxiliary fields sampled at each time step are synchronized between the raw noisy experiment and noiseless reference.

perfectly parallelize the classical AFQMC propagation, with one walker per CPU core[2] (this

---

[2] Intel Xeon Platinum Processor.

is only possible when not using population control). For each walker, it took approximately 1 minute to post-process the shadows from 16000 circuits in each timestep. As each step of the AFQMC algorithm must be performed sequentially, it could take up to hours or even days to complete the full evolution. This total runtime partly comes from the large number of shadows, which plays the role of a pre-factor and could be further improved by implementing additional parallelization among the shadows, for example, processing the shadows corresponding to a single walker in parallel across a number of cores, rather than sequentially on the same core. The total runtime also stems from a scaling as high as $\mathcal{O}(n^8)$ to evaluate the local energy of each walker. This high cost presents a practical concern for scaling this algorithm to larger systems of practical interest.

Nitrogen-vacancy center ground state

We applied the QC-AFQMC algorithm to study the electronic states of a point defect in a solid. We chose the NV center in diamond, which is widely considered a promising candidate for quantum sensing and has recently been applied to imaging high-pressure phase transitions [138] and superconducting systems [35]. To obtain multireference states we employed a quantum defect embedding theory (QDET) [285], which allows us to derive an effective Hamiltonian H_{eff}, by defining an active space. This effective Hamiltonian is used as the starting point of the QC-AFQMC calculation.

Although it has been shown [140] that a rather large active space is needed to fully converge the computed neutral excitation energies, here we only chose a minimum model of (4e, 3o) to carry out the QC-AFQMC calculations, as a proof of principle. The ground state has a $^3A_2$ irrep due to the C_{3v} symmetry of the defect and its wavefunction can be written as

$$|\,^3A_2\rangle = \frac{1}{\sqrt{2}}\left(|a_1\overline{a_1}e_x\overline{e_y}\rangle + |a_1\overline{a_1}\overline{e_x}e_y\rangle\right), \tag{8.12}$$

where a_1, e denotes the irrep of the single-particle orbital and the bar symbol represents the

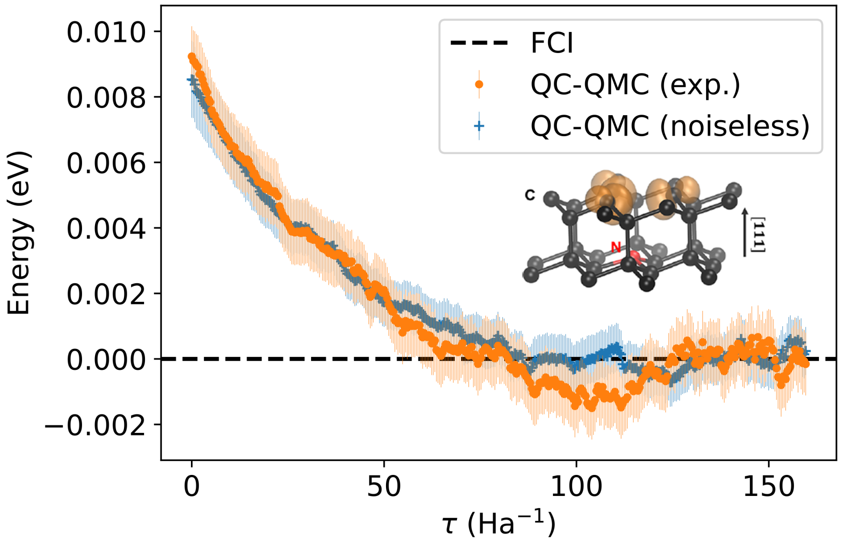

Figure 8.5: The QC-AFQMC calculation of an NV center in diamond using a noiseless quantum simulator (blue crosses), and the IonQ Aria quantum computer (orange circles). Converged results of both have an error in the order of 1 meV compared to classical reference. The inset shows an atomistic model of the defect center. Note that the y axis scale is now in eV due to the effective Hamiltonian being downfolded.

spin-down channel. In Ref. [139], a subset of the current authors investigated this system using VQE and found that error mitigation techniques were necessary to obtain an accurate ground state energy. Here, we use the tailored UCCSD ansatz as the quantum trial state for our QC-AFQMC calculations.

In QC-AFQMC, we used 4000 shadow circuits (with 100 shots each), 4800 walkers and an imaginary time step of $\Delta\tau = 0.4$ H.a.$^{-1}$. As can be seen from Fig. 8.5, the results obtained on quantum hardware (orange curve) agree with the noiseless reference (blue curve), which is within our expectation, given the noise resilience discussed in Sec. 8.3.2. Both curves converge to the classical reference FCI limit, which has been renormalized to zero.

The computation was again fully parallelized, with one walker per physical CPU core (4800 physical cores total). The total runtime required for 400 time steps was approximately 1.5 hours.

8.4 Discussion

As we discussed in Sec. 8.1, variational algorithms like VQE have been the methods of choice for quantum chemistry problems on near-term quantum computers. The QC-AFQMC scheme discussed here is complementary to VQE. Specifically, QC-AFQMC could be viewed as an error mitigation technique for VQE, where both the inaccuracy of the ansatz used and the noise effects would in principle be corrected by imaginary time evolution. In turn, the quantum trial state used in the QC-AFQMC algorithm could come from VQE calculations (in a smaller subspace, or for a reduced problem size). However, one notable difference from the VQE ansatz is that the quantum trial preparation circuit needs to satisfy $V_T|\mathbf{0}\rangle = |\mathbf{0}\rangle$, if following the approach used in this work. This additional constraint prevents the use of some popular ansatz circuits in VQE, such as qubit coupled cluster [271], and circuit simplification techniques [126]. For some ansatz circuits it may be possible to circumvent this limitation by introducing another ancilla qubit, and controlling the implementation of the ansatz (which can often be done by controlling select gates, rather than every gate), following the procedure in App. E of Ref. [336].

The possibility of achieving exponential quantum advantage in solving quantum chemistry problems remains controversial [182]. This is arguably not the direct aim of QC-AFQMC, given that phaseless-AFQMC is already a polynomially scaling method. Instead, the motivation of ph-QC-AFQMC is that the trial state used may provide energies with smaller biases than the purely classical algorithm. A full comparison requires an improved understanding of the advantages offered by quantum trial states over classical trial states. As a proxy for this, we could compare the cost of classical methods using state-of-the-art techniques [56, 247, 283, 331], such as Multi-Slater trial states. Two popular implementations using Wick's theorem have the following scaling for evaluating the local energy, $\mathcal{O}(MXn^3 + MXN_c)$ [208] and $\mathcal{O}(MXn^4 + MN_c)$ [207], where M, X, N_c are the number of walkers, Cholesky vectors, and Slater determinants in the trial, respectively. This can

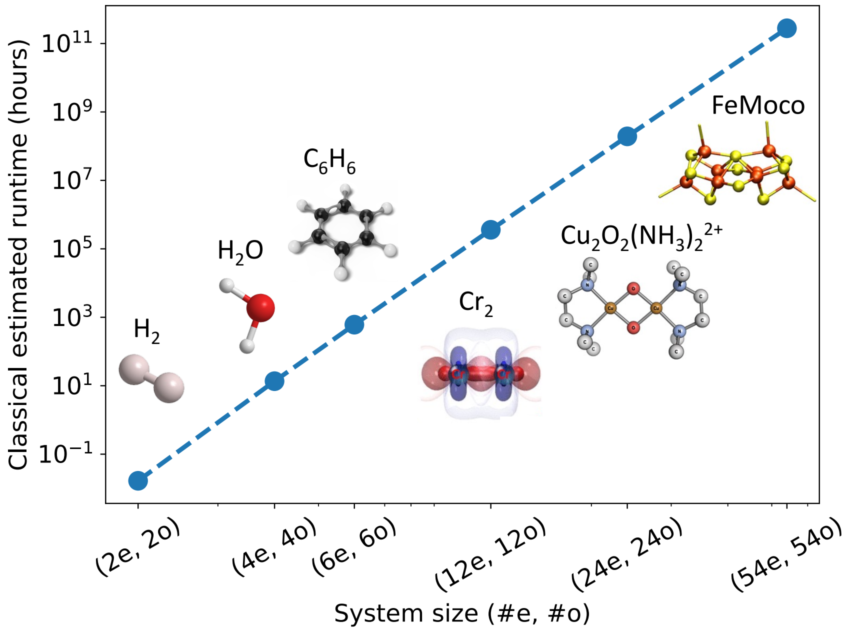

Figure 8.6: Prediction of the runtime estimation of classical post-processing for a single time step in the QC-AFQMC algorithm performed on a single CPU core. These results were extrapolated from the runtime of post-processing results from hydrogen. We make the optimistic assumptions that the error thresholds ϵ, δ in classical shadows do not need to decrease, and that the number of walkers does not need to increase, as the system size increases. The scaling is dominated by the local energy estimation. The system sizes are quantified using active spaces, taken from literature [10, 100, 217, 257, 271].

be compared against the complexities of the quantum algorithm, which is summarized in Table. 8.1 for the three different proposed approaches for measuring the overlap amplitudes. We see that the classical algorithms are more efficient in n than the classical shadows-based quantum algorithms, which scale as $\mathcal{O}(n^8)$. As such, the quantum trial state would need to lead to a much smaller bias than a classical multi-Slater trial state with a large number of determinants to be practically advantageous. It is currently an open question as to what kind of quantum trial state is best suited for QC-AFQMC. The only criterion adopted so far is the trial state energy $\langle\Psi_T|H|\Psi_T\rangle$, but there might exist other, better-suited criteria.

While Matchgate classical shadows are formally efficient, they introduce a large post-processing cost. This presents a practical challenge for scaling up the QC-AFQMC algorithm to larger system sizes. To highlight this, in Fig. 8.6 we present the classical runtime for post-processing a single timestep of the QC-AFQMC algorithm. Numerical results were obtained for hydrogen and then extrapolated to larger system sizes using the scaling of the QC-AFQMC algorithm. The results show that our implementation of the algorithm is only realistic up to four spin-orbitals (water). The numerical results assume a fixed number of walkers (4800), and allocate 1 physical CPU core to each walker. Within each CPU, computation associated with postprocessing the results of each of the shadow circuits can be further parallelized. While not investigated in this paper, parallelization between shadow circuits can potentially speed up the classical runtime. For example, using one million CPU cores [250] would drive the classical post-processing of benzene toward a realistic regime, of around 6 hours per time step. Nevertheless, for larger systems such as FeMoco, further optimizations in the algorithm and/or classical post-processing are still required to become practical. Compared to the classical shadows approach, the Hadamard-test based approach of Ref. [338] reduces the cost of classical post-processing. However, this comes at a price of an increased number of quantum circuit repetitions (scaling linearly with the number of walkers), leading to similar measurement bottlenecks as observed for VQE methods [104]. In addition, this approach requires iterative communication between quantum and classical processors, which may be subject to latencies. As such, despite the higher classical post-processing costs of the classical shadow based approach, we currently view it as the more promising approach to QC-AFQMC.

Table 8.1: Comparison of different measurement schemes for QC-AFQMC.

Method for computing $\langle\Psi_T\|\phi\rangle$	Vacuum reference [338]	Clifford shadows [144]	Matchgate shadows [326]
Only offline QC access?	×	✓	✓
Circuit sampling complexity[1]	$\mathcal{O}\left(\frac{Mn^4}{\epsilon^2}\right)$	$\mathcal{O}\left(\frac{\log(Mn^4/\delta)}{\epsilon^2}\right)$	$\mathcal{O}\left(\frac{\log(Mn^4/\delta)}{\epsilon^2}\sqrt{n}\log n\right)$
Circuit depth complexity[2]	$O(N_T + n)$		
Noise-resilient overlap ratios	×	✓	✓
$\{\langle\Psi_T\|\phi\rangle\}$ post-processing complexity	$\mathcal{O}(M)$	$\mathcal{O}(M\exp(n))$	$\mathcal{O}(Mn^4)$
$\{\langle\Psi_T\|H\|\phi\rangle\}$ post-processing complexity[3]	$\mathcal{O}(Mn^4)$	$\mathcal{O}(M\exp(n))$	$\mathcal{O}(Mn^8)$

[1] M in the scaling should be interpreted as the total number of walker states involved in the algorithm.

[2] $\mathcal{O}(N_T)$ represents the quantum trial state preparation circuit depth complexity. And the $|\phi\rangle$ preparation, random Clifford, and Matchgate circuit for the three schemes all scale as $\mathcal{O}(n)$ in depth.

[3] The local energy numerator can be computed by decomposing it into a linear combination of $\mathcal{O}(n^4)$ overlap amplitudes, due to the complexity of the Hamiltonian.

Finally, it has been acknowledged [144] and highlighted [215] that the overlap amplitudes $\langle \Psi_T | \phi \rangle$ are expected to decay exponentially with system size. Although it remains to be explored how inaccuracies in evaluating each overlap would affect the accuracy of AFQMC [162], this generally means an exponentially large number of measurements is needed to control the uncertainty in estimating these overlaps. Establishing the practical viability of QC-AFQMC will require developing an improved understanding of these challenges, and their possible solutions.

8.5 Conclusions

In this work, we carried out the first end-to-end experimental evaluation of the recently proposed Matchgate shadows [200, 326] powered QC-AFQMC algorithm for quantum chemistry [144]. We observed that the algorithm is inherently noise robust, which we find to be a consequence of the natural noise resilience of evaluating overlap ratios via Matchgate shadows. We provided a theoretical explanation for this observed phenomenon, which also elucidates limitations in recently proposed robust Matchgate shadow protocols. We also developed improvements to those protocols which can mitigate state preparation noise, and may be of independent interest. Nevertheless, despite the tantalizing noise resilience of the algorithm, our optimized practical implementations have uncovered a number of challenges to the scalability of the algorithm. Most prominently, while the Matchgate shadows protocol is asymptotically efficient, its high degree polynomial scaling for evaluating the local energy necessitates significant parallel compute resources for classical post-processing. We estimate that for larger molecules, we would require significant amounts of classical post-processing, as shown in Fig. 8.6. As such, future work should focus on developing new methods for efficiently computing the local energy in QC-AFQMC, with lower post-processing costs. Many open questions remain about the best trial states to use for QC-AFQMC, and how to ensure non-vanishing overlaps between the trial state and walker states. The merits of QC-AFQMC found in this work, together with these open research questions, motivate the importance of further study of this algorithm applied to larger system sizes, on real quantum devices.

CHAPTER 9

CONCLUSIONS

In this dissertation, we presented research projects that fall within two interwoven themes: i). first-principles studies of the electronic, optical, and mechanical properties of spin defects in semiconductors for the realization of quantum technologies; ii). development of quantum algorithms for solving the electronic structure problem of molecules and materials on near-term quantum computers.

The research presented in this dissertation heavily focused on solving real-world physical, chemical, and material problems using spin defects, which directly impact their application for quantum information technologies. Specifically, we studied the inter-system crossing of NV centers under various stresses, combining state-of-the-art computational chemistry and computational material science methods, to elucidate the defect's ODMR resolution for quantum sensing at high pressure and room temperature. We also verified for the first time several assumptions regarding NV's energy susceptibilities and optical spectrum widely adopted by experimentalists. As different spin defects have dramatically different responses to different environmental changes, we also studied the temperature dependence of the spin properties of $\mathrm{V_B^-}$ in hBN, which has been experimentally demonstrated to be much more sensitive than the NV center in diamond. We identified the underlying mechanism for the temperature dependence to be second-order spin-phonon coupling and discussed the isotope effects. We also went beyond quantum sensing applications and predicted that proper strain could significantly increase the coherence time of group-IV vacancies by lifting the degeneracy of ground and excited states and thus suppressing the spin-phonon relaxations. The theoretical interpretation of experiment and our predictions for potential improvements in the performance of spin defects as quantum information candidates greatly validate their applicability and deepen our understanding of their physical properties.

Despite the success we've achieved, there are open problems in the current computational tools. For instance, the energy gaps predicted with conventional DFT are not always to satisfactory accuracy, while more accurate methods have much worse scaling and can't be applied to large supercells or clusters. This inspired us to explore the use of quantum algorithms on quantum computers to solve the electronic structure problem. We mostly focused on using the variational quantum eigensolver method and test different fermion-to-qubit mappings and ansatz schemes. An error mitigation technique called exponential-block replication based on zero-noise extrapolation was developed that is compatible with all the unitary coupled-cluster type quantum circuits. This technique can also be used in excited state calculations. Although widely assumed to be fit for NISQ hardware, we realized that even VQE suffers from serious noise problems. This promoted us to explore the use of quantum Monte Carlo on quantum computers leveraging its stochastic nature to suppress the effects of noise. We indeed witnessed a noise resilience in this approach but also were confronted with a steep scaling in terms of classical post-processing. Therefore, there is still a long way to go in the pursuit of realizing quantum advantage for application in the areas of physics and chemistry.

Looking into the future, critical problems are awaiting to be solved to realize quantum computational advantages in solving the electronic structure problem, including:

- **Computing excited states**: Lee et al. [182] cast shadows in achieving exponential quantum advantages in solving the ground state problem on quantum computers. However, there is still hope for the solution of excited states. Current efforts in developing quantum computational chemistry algorithms mainly focus on the ground state properties. Therefore, investing efforts to compute the excited state properties might lead to better advantage of the power of quantum computation.

- **Developing more efficient/universal circuits for state preparation**: One component connecting the NISQ era and fault-tolerant quantum computing (FTQC) in terms of solving the eigenvalue problem is state preparation. Algorithms like quantum phase estimation executed in FTQC are widely acknowledged to have a polynomial scaling. But to achieve this scaling, the initial input state should have a decent overlap with the true eigenstate solution. This however is not trivial to realize and we don't yet have a universal ansatz to prepare (correlated) states for quantum chemistry, nor a good metric for that.

- **Solving hybrid fermion-boson systems**: The memory advantages in representing correlated wavefunctions using a linearly scaling number of qubits would benefit not only fermionic systems but also hybrid fermion-boson systems. However, a mapping between the bosonic degrees of freedom and qubits needs to be carefully designed.

APPENDIX A

LIST OF PUBLICATIONS

1. **B. Huang**, M. Govoni, and G. Galli. "Simulating the electronic structure of spin defects on quantum computers." *PRX Quantum* 3.1 (2022): 010339.

2. C. Vorwerk, N. Sheng, M. Govoni, **B. Huang**, and G. Galli. "Quantum embedding theories to simulate condensed systems on quantum computers." *Nature Computational Science* 2.7 (2022): 424-432.

3. **B. Huang**, N. Sheng, M. Govoni, and G. Galli. "Quantum simulations of Fermionic Hamiltonians with efficient encoding and ansatz schemes." *Journal of Chemical Theory and Computation* 19.5 (2023): 1487-1498.

4. X. Guo, A. Stramma, Z. Li, W. Roth, **B. Huang**, Y. Jin, R. Parker, J. Martínez, N. Shofer, C. Michaels, C. Purser, M. Appel, E. Alexeev, T. Liu, A. Ferrari, D. Awschalom, N. Delegan, B. Pingault, G. Galli, F. Heremans, M. Atatüre, and A. High. "Microwave-Based Quantum Control and Coherence Protection of Tin-Vacancy Spin Qubits in a Strain-Tuned Diamond-Membrane Heterostructure." *Physical Review X* 13.4 (2023): 041037.

5. P. Bhattacharyya, W. Chen, X. Huang, S. Chatterjee, **B. Huang**, B. Kobrin, Y. Lyu, T. Smart, M. Block, E. Wang, Z. Wang, W. Wu, S. Hsieh, H. Ma, S. Mandyam, B. Chen, E. Davis, Z. Geballe, C. Zu, V. Struzhkin, R. Jeanloz, J. Moore, T. Cui, G. Galli, B. Halperin, C. Laumann, and N. Yao. "Imaging the Meissner effect in hydride superconductors using quantum sensors." *Nature* (2024): 1-7.

6. **B. Huang**, Y. Chen, B. Gupt, M. Suchara, A. Tran, S. McArdle, and G. Galli. "Evaluating a quantum-classical quantum Monte Carlo algorithm with Matchgate shadows." *arXiv preprint arXiv:2404.18303* (2024)

7. Z. Liu, R. Gong, **B. Huang**, Y. Jin, X. Du, G. He, E. Janzen, L. Yang, E. Henriksen, J. Edgar, G. Galli, and C. Zu. "Temperature Dependent Spin-Phonon Coupling of Boron-Vacancy Centers in Hexagonal Boron Nitride." *arXiv preprint arXiv:2404.15493* (2024)

8. **B. Huang**, S. Mandyam, B. Kobrin, P. Bhattacharyya, W. Wu, Y. Jin, M. Block, E. Wang, Z. Wang, B. Chen, C. Zu, N. Yao, and G. Galli. “Elucidating the optically detected magnetic resonance of nitrogen-vacancy centers under megabar pressure.” *in preparation* (2024)

REFERENCES

[1] Scott Aaronson and Daniel Gottesman. Improved simulation of stabilizer circuits. *Physical Review A*, 70(5):052328, 2004. doi:10.1103/PhysRevA.70.052328.

[2] Daniel S Abrams and Seth Lloyd. Simulation of many-body fermi systems on a universal quantum computer. *Physical Review Letters*, 79(13):2586, 1997.

[3] Daniel S Abrams and Seth Lloyd. Quantum algorithm providing exponential speed increase for finding eigenvalues and eigenvectors. *Physical Review Letters*, 83(24):5162, 1999.

[4] VM Acosta, A Jarmola, E Bauch, and D Budker. Optical properties of the nitrogen-vacancy singlet levels in diamond. *Physical Review B*, 82(20):201202, 2010.

[5] Carlo Adamo and Vincenzo Barone. Toward reliable density functional methods without adjustable parameters: The pbe0 model. *The Journal of Chemical Physics*, 110 (13):6158–6170, 1999.

[6] Igor Aharonovich, Dirk Englund, and Milos Toth. Solid-state single-photon emitters. *Nature Photonics*, 10(10):631–641, 2016.

[7] Yuichi Akahama and Haruki Kawamura. Pressure calibration of diamond anvil raman gauge to 310 GPa. *Journal of Applied Physics*, 100(4):043516, 2006.

[8] Maximilian Amsler, Peter Deglmann, Matthias Degroote, Michael P Kaicher, Matthew Kiser, Michael Kühn, Chandan Kumar, Andreas Maier, Georgy Samsonidze, Anna Schroeder, et al. Classical and quantum trial wave functions in auxiliary-field quantum monte carlo applied to oxygen allotropes and a cubr2 model system. *The Journal of Chemical Physics*, 159(4), 2023. doi:10.1063/5.0146934.

[9] Christopher P Anderson, Elena O Glen, Cyrus Zeledon, Alexandre Bourassa, Yu Jin, Yizhi Zhu, Christian Vorwerk, Alexander L Crook, Hiroshi Abe, Jawad Ul-Hassan, et al. Five-second coherence of a single spin with single-shot readout in silicon carbide. *Science Advances*, 8(5):eabm5912, 2022. URL `https://www.science.org/doi/full/10.1126/sciadv.abm5912`.

[10] Robert J Anderson, Toru Shiozaki, and George H Booth. Efficient and stochastic multireference perturbation theory for large active spaces within a full configuration interaction quantum monte carlo framework. *The Journal of Chemical Physics*, 152 (5), 2020. doi:10.1063/1.5140086.

[11] Frank Arute, Kunal Arya, Ryan Babbush, Dave Bacon, Joseph C Bardin, Rami Barends, Rupak Biswas, Sergio Boixo, Fernando GSL Brandao, David A Buell, et al. Quantum supremacy using a programmable superconducting processor. *Nature*, 574 (7779):505–510, 2019. URL `https://www.nature.com/articles/s41586-019-1666-5?categoryid=2849273&discountcode=DSI19S?categoryid=2849273`.

[12] F Aryasetiawan, M Imada, A Georges, G Kotliar, S Biermann, and AI Lichtenstein. Frequency-dependent local interactions and low-energy effective models from electronic structure calculations. *Physical Review B*, 70(19):195104, 2004.

[13] Neil W Ashcroft. Metallic hydrogen: A high-temperature superconductor? *Physical Review Letters*, 21(26):1748, 1968.

[14] NW Ashcroft. Hydrogen dominant metallic alloys: high temperature superconductors? *Physical Review Letters*, 92(18):187002, 2004.

[15] Nabeel Aslam, Hengyun Zhou, Elana K Urbach, Matthew J Turner, Ronald L Walsworth, Mikhail D Lukin, and Hongkun Park. Quantum sensors for biomedical applications. *Nature Reviews Physics*, 5(3):157–169, 2023.

[16] Alán Aspuru-Guzik, Anthony D Dutoi, Peter J Love, and Martin Head-Gordon. Simulated quantum computation of molecular energies. *Science*, 309(5741):1704–1707, 2005. doi:10.1126/science.1113479.

[17] Mete Atatüre, Dirk Englund, Nick Vamivakas, Sang-Yun Lee, and Joerg Wrachtrup. Material platforms for spin-based photonic quantum technologies. *Nature Reviews Materials*, 3(5):38–51, 2018.

[18] Brian M Austin, Dmitry Yu Zubarev, and William A Lester Jr. Quantum monte carlo and related approaches. *Chemical Reviews*, 112(1):263–288, 2012. doi:10.1021/cr2001564.

[19] David D Awschalom, Ronald Hanson, Jörg Wrachtrup, and Brian B Zhou. Quantum technologies with optically interfaced solid-state spins. *Nature Photonics*, 12(9):516–527, 2018.

[20] Koji Azuma, Sophia E Economou, David Elkouss, Paul Hilaire, Liang Jiang, Hoi-Kwong Lo, and Ilan Tzitrin. Quantum repeaters: From quantum networks to the quantum internet. *Reviews of Modern Physics*, 95(4):045006, 2023.

[21] Shaimaa I Azzam, Kamyar Parto, and Galan Moody. Prospects and challenges of quantum emitters in 2d materials. *Applied Physics Letters*, 118(24), 2021.

[22] Ryan Babbush, Craig Gidney, Dominic W Berry, Nathan Wiebe, Jarrod McClean, Alexandru Paler, Austin Fowler, and Hartmut Neven. Encoding electronic spectra in quantum circuits with linear t complexity. *Physical Review X*, 8(4):041015, 2018.

[23] Unpil Baek, Diptarka Hait, James Shee, Oskar Leimkuhler, William J Huggins, Torin F Stetina, Martin Head-Gordon, and K Birgitta Whaley. Say no to optimization: A nonorthogonal quantum eigensolver. *PRX Quantum*, 4(3):030307, 2023. doi:10.1103/PRXQuantum.4.030307.

[24] Nir Bar-Gill, Linh M Pham, Andrejs Jarmola, Dmitry Budker, and Ronald L Walsworth. Solid-state electronic spin coherence time approaching one second. *Nature Communications*, 4(1):1743, 2013.

[25] Panagiotis Kl Barkoutsos, Jerome F Gonthier, Igor Sokolov, Nikolaj Moll, Gian Salis, Andreas Fuhrer, Marc Ganzhorn, Daniel J Egger, Matthias Troyer, Antonio Mezzacapo, et al. Quantum algorithms for electronic structure calculations: Particle-hole hamiltonian and optimized wave-function expansions. *Physical Review A*, 98(2): 022322, 2018. URL `https://journals.aps.org/pra/abstract/10.1103/PhysRevA.98.022322`.

[26] Michael SJ Barson, Phani Peddibhotla, Preeti Ovartchaiyapong, Kumaravelu Ganesan, Richard L Taylor, Matthew Gebert, Zoe Mielens, Berndt Koslowski, David A Simpson, Liam P McGuinness, et al. Nanomechanical sensing using spins in diamond. *Nano Letters*, 17(3):1496–1503, 2017.

[27] MSJ Barson, Prithvi Reddy, Sen Yang, NB Manson, Joerg Wrachtrup, and Marcus William Doherty. Temperature dependence of the c 13 hyperfine structure of the negatively charged nitrogen-vacancy center in diamond. *Physical Review B*, 99(9): 094101, 2019.

[28] Rodney J Bartlett and Monika Musiał. Coupled-cluster theory in quantum chemistry. *Reviews of Modern Physics*, 79(1):291, 2007.

[29] Bela Bauer, Sergey Bravyi, Mario Motta, and Garnet Kin-Lic Chan. Quantum algorithms for quantum chemistry and quantum materials science. *Chemical Reviews*, 120 (22):12685–12717, November 2020. ISSN 0009-2665. doi:10.1021/acs.chemrev.9b00829.

[30] Jonas N Becker, Benjamin Pingault, David Groß, Mustafa Gündoğan, Nadezhda Kukharchyk, Matthew Markham, Andrew Edmonds, Mete Atatüre, Pavel Bushev, and Christoph Becher. All-optical control of the silicon-vacancy spin in diamond at millikelvin temperatures. *Physical review letters*, 120(5):053603, 2018.

[31] Dominic W Berry, Andrew M Childs, Richard Cleve, Robin Kothari, and Rolando D Somma. Simulating hamiltonian dynamics with a truncated taylor series. *Physical Review Letters*, 114(9):090502, 2015.

[32] Churna Bhandari, Aleksander L Wysocki, Sophia E Economou, Pratibha Dev, and Kyungwha Park. Multiconfigurational study of the negatively charged nitrogen-vacancy center in diamond. *Physical Review B*, 103(1):014115, 2021.

[33] Mihir K Bhaskar, Denis D Sukachev, Alp Sipahigil, Ruffin E Evans, Michael J Burek, Christian T Nguyen, Lachlan J Rogers, Petr Siyushev, Mathias H Metsch, Hongkun Park, et al. Quantum nonlinear optics with a germanium-vacancy color center in a nanoscale diamond waveguide. *Physical Review Letters*, 118(22):223603, 2017.

[34] Mihir K Bhaskar, Ralf Riedinger, Bartholomeus Machielse, David S Levonian, Christian T Nguyen, Erik N Knall, Hongkun Park, Dirk Englund, Marko Lončar, Denis D Sukachev, et al. Experimental demonstration of memory-enhanced quantum communication. *Nature*, 580(7801):60–64, 2020.

[35] P Bhattacharyya, W Chen, X Huang, S Chatterjee, B Huang, B Kobrin, Y Lyu, TJ Smart, M Block, E Wang, et al. Imaging the meissner effect in hydride superconductors using quantum sensors. *Nature*, pages 1–7, 2024. doi:10.1038/s41586-024-07026-7.

[36] Timur Biktagirov, Wolf Gero Schmidt, and Uwe Gerstmann. Spin decontamination for magnetic dipolar coupling calculations: Application to high-spin molecules and solid-state spin qubits. *Physical Review Research*, 2(2):022024, 2020.

[37] Max Born and Kun Huang. *Dynamical theory of crystal lattices.* Oxford university press, 1996.

[38] Conor E Bradley, Joe Randall, Mohamed H Abobeih, RC Berrevoets, MJ Degen, Michiel A Bakker, Matthew Markham, DJ Twitchen, and Tim H Taminiau. A ten-qubit solid-state spin register with quantum memory up to one minute. *Physical Review X*, 9(3):031045, 2019.

[39] Sergey Bravyi, Jay M Gambetta, Antonio Mezzacapo, and Kristan Temme. Tapering off qubits to simulate fermionic hamiltonians. *arXiv preprint arXiv:1701.08213*, 2017.

[40] Sergey B Bravyi and Alexei Yu Kitaev. Fermionic quantum computation. *Annals of Physics*, 298(1):210–226, 2002.

[41] Colin D Bruzewicz, John Chiaverini, Robert McConnell, and Jeremy M Sage. Trapped-ion quantum computing: Progress and challenges. *Applied Physics Reviews*, 6(2), 2019.

[42] Robert J Buenker and Sigrid D Peyerimhoff. Individualized configuration selection in ci calculations with subsequent energy extrapolation. *Theoretica chimica acta*, 35(1): 33–58, 1974.

[43] Amy Butcher, Xinghan Guo, Robert Shreiner, Nazar Delegan, Kai Hao, Peter J Duda III, David D Awschalom, F Joseph Heremans, and Alexander A High. High-q nanophotonic resonators on diamond membranes using templated atomic layer deposition of tio2. *Nano Letters*, 20(6):4603–4609, 2020.

[44] Joshua D Caldwell, Igor Aharonovich, Guillaume Cassabois, James H Edgar, Bernard Gil, and DN Basov. Photonics with hexagonal boron nitride. *Nature Reviews Materials*, 4(8):552–567, 2019.

[45] M. C. Cambria, A. Norambuena, H. T. Dinani, G. Thiering, A. Gardill, I. Kemeny, Y. Li, V. Lordi, Á. Gali, J. R. Maze, and S. Kolkowitz. Temperature-dependent spin-lattice relaxation of the nitrogen-vacancy spin triplet in diamond. *Phys. Rev. Lett.*, 130:256903, Jun 2023. doi:10.1103/PhysRevLett.130.256903.

[46] M. C. Cambria, G. Thiering, A. Norambuena, H. T. Dinani, A. Gardill, I. Kemeny, V. Lordi, Á. Gali, J. R. Maze, and S. Kolkowitz. Physically motivated analytical expression for the temperature dependence of the zero-field splitting of the nitrogen-vacancy center in diamond. *Phys. Rev. B*, 108:L180102, Nov 2023. doi:10.1103/PhysRevB.108.L180102.

[47] Earl Campbell. Random compiler for fast hamiltonian simulation. *Physical review letters*, 123(7):070503, 2019.

[48] Yudong Cao, Jonathan Romero, Jonathan P. Olson, Matthias Degroote, Peter D. Johnson, Mária Kieferová, Ian D. Kivlichan, Tim Menke, Borja Peropadre, Nicolas P. D. Sawaya, et al. Quantum chemistry in the age of quantum computing. *Chemical Reviews*, 119(19):10856–10915, October 2019. ISSN 0009-2665.

[49] Daniel Carney, Gordan Krnjaic, David C Moore, Cindy A Regal, Gadi Afek, Sunil Bhave, Benjamin Brubaker, Thomas Corbitt, Jonathan Cripe, Nicole Crisosto, et al. Mechanical quantum sensing in the search for dark matter. *Quantum Science and Technology*, 6(2):024002, 2021.

[50] Marco Cerezo, Andrew Arrasmith, Ryan Babbush, Simon C Benjamin, Suguru Endo, Keisuke Fujii, Jarrod R McClean, Kosuke Mitarai, Xiao Yuan, Lukasz Cincio, et al. Variational quantum algorithms. *Nature Reviews Physics*, pages 1–20, 2021.

[51] Diana Chamaki, Mekena Metcalf, and Wibe A de Jong. Compact molecular simulation on quantum computers via combinatorial mapping and variational state preparation. *arXiv preprint arXiv:2205.11742*, 2022. URL `https://arxiv.org/abs/2205.11742`.

[52] Laurent Chaput, Atsushi Togo, Isao Tanaka, and Gilles Hug. Phonon-phonon interactions in transition metals. *Phys. Rev. B*, 84:094302, Sep 2011. doi:10.1103/PhysRevB.84.094302. URL `https://link.aps.org/doi/10.1103/PhysRevB.84.094302`.

[53] Jia Chen, Hai-Ping Cheng, and James K Freericks. Quantum-inspired algorithm for the factorized form of unitary coupled cluster theory. *Journal of Chemical Theory and Computation*, 17(2):841–847, 2021. URL `https://pubs.acs.org/doi/10.1021/acs.jctc.0c01052`.

[54] Senrui Chen, Wenjun Yu, Pei Zeng, and Steven T Flammia. Robust shadow estimation. *PRX Quantum*, 2(3):030348, 2021. doi:10.1103/PRXQuantum.2.030348.

[55] Wuhao Chen, Dmitrii V Semenok, Xiaoli Huang, Haiyun Shu, Xin Li, Defang Duan, Tian Cui, and Artem R Oganov. High-temperature superconducting phases in cerium superhydride with a T_c up to 115 k below a pressure of 1 megabar. *Physical Review Letters*, 127(11):117001, 2021.

[56] Yixiao Chen, Linfeng Zhang, Weinan E, and Roberto Car. Hybrid auxiliary field quantum monte carlo for molecular systems. *Journal of Chemical Theory and Computation*, 2023. doi:10.1021/acs.jctc.3c00038.

[57] Seonghoon Choi, Tzu-Ching Yen, and Artur F Izmaylov. Improving quantum measurements by introducing "ghost" pauli products. *Journal of Chemical Theory and Computation*, 18(12):7394–7402, 2022.

[58] Seonghoon Choi, Ignacio Loaiza, and Artur F Izmaylov. Fluid fermionic fragments for optimizing quantum measurements of electronic hamiltonians in the variational quantum eigensolver. *Quantum*, 7:889, 2023.

[59] Aashish A Clerk, Michel H Devoret, Steven M Girvin, Florian Marquardt, and Robert J Schoelkopf. Introduction to quantum noise, measurement, and amplification. *Reviews of Modern Physics*, 82(2):1155, 2010.

[60] T Clua-Provost, A Durand, Z Mu, T Rastoin, J Fraunié, E Janzen, H Schutte, JH Edgar, G Seine, A Claverie, et al. Isotopic control of the boron-vacancy spin defect in hexagonal boron nitride. *Physical Review Letters*, 131(12):126901, 2023.

[61] James I Colless, Vinay V Ramasesh, Dar Dahlen, Machiel S Blok, Mollie E Kimchi-Schwartz, Jarrod R McClean, Jonathan Carter, Wibe A de Jong, and Irfan Siddiqi. Computation of molecular spectra on a quantum processor with an error-resilient algorithm. *Physical Review X*, 8(1):011021, 2018.

[62] Cristian L Cortes and Stephen K Gray. Quantum krylov subspace algorithms for ground-and excited-state energy estimation. *Physical Review A*, 105(2):022417, 2022. URL `https://journals.aps.org/pra/abstract/10.1103/PhysRevA.105.022417`.

[63] Gavin E Crooks. Gradients of parameterized quantum gates using the parameter-shift rule and gate decomposition. *arXiv preprint arXiv:1905.13311*, 2019. URL `https://arxiv.org/abs/1905.13311`.

[64] Andrew W Cross, Lev S Bishop, John A Smolin, and Jay M Gambetta. Open quantum assembly language. *arXiv preprint arXiv:1707.03429*, 2017.

[65] Jian-Hong Dai, Yan-Xing Shang, Yong-Hong Yu, Yue Xu, Hui Yu, Fang Hong, Xiao-Hui Yu, Xin-Yu Pan, and Gang-Qin Liu. Optically detected magnetic resonance of diamond nitrogen-vacancy centers under megabar pressures. *Chinese Physics Letters*, 39(11):117601, 2022.

[66] Alexander M Dalzell, Sam McArdle, Mario Berta, Przemyslaw Bienias, Chi-Fang Chen, András Gilyén, Connor T Hann, Michael J Kastoryano, Emil T Khabiboulline, Aleksander Kubica, et al. Quantum algorithms: A survey of applications and end-to-end complexities. *arXiv preprint arXiv:2310.03011*, 2023.

[67] Chaoqun Dang, Jyh-Pin Chou, Bing Dai, Chang-Ti Chou, Yang Yang, Rong Fan, Weitong Lin, Fanling Meng, Alice Hu, Jiaqi Zhu, et al. Achieving large uniform tensile elasticity in microfabricated diamond. *Science*, 371(6524):76–78, 2021.

[68] Gordon Davies and MF Hamer. Optical studies of the 1.945 eV vibronic band in diamond. *Proceedings of the Royal Society of London. A. Mathematical and Physical Sciences*, 348(1653):285–298, 1976.

[69] E Davis, Bingtian Ye, Francisco Machado, Meynell, Weijie Wu, Thomas Mittiga, William Schenken, Maxime Joos, Bryce Kobrin, Yuanqi Lyu, Zilin Wang, Dolev Bluvstein, et al. Probing many-body noise in a strongly interacting two-dimensional dipolar spin system. *Nature Physics*, 2023.

[70] G De Lange, ZH Wang, D Riste, VV Dobrovitski, and R Hanson. Universal dynamical decoupling of a single solid-state spin from a spin bath. *Science*, 330(6000):60–63, 2010.

[71] Lorenzo De Santis, Matthew E Trusheim, Kevin C Chen, and Dirk R Englund. Investigation of the stark effect on a centrosymmetric quantum emitter in diamond. *Physical Review Letters*, 127(14):147402, 2021.

[72] Romain Debroux, Cathryn P Michaels, Carola M Purser, Noel Wan, Matthew E Trusheim, Jesús Arjona Martínez, Ryan A Parker, Alexander M Stramma, Kevin C Chen, Lorenzo De Santis, et al. Quantum control of the tin-vacancy spin qubit in diamond. *Physical Review X*, 11(4):041041, 2021.

[73] Christian L Degen, Friedemann Reinhard, and Paola Cappellaro. Quantum sensing. *Reviews of Modern Physics*, 89(3):035002, 2017. URL `https://journals.aps.org/rmp/abstract/10.1103/RevModPhys.89.035002`.

[74] Andreas Dewes, Florian R Ong, Vivien Schmitt, R Lauro, N Boulant, P Bertet, D Vion, and D Esteve. Characterization of a two-transmon processor with individual single-shot qubit readout. *Physical Review Letters*, 108(5):057002, 2012. URL `https://journals.aps.org/prl/abstract/10.1103/PhysRevLett.108.057002`.

[75] David P DiVincenzo. The physical implementation of quantum computation. *Fortschritte der Physik: Progress of Physics*, 48(9-11):771–783, 2000.

[76] Marcus W Doherty, Neil B Manson, Paul Delaney, Fedor Jelezko, Jörg Wrachtrup, and Lloyd CL Hollenberg. The nitrogen-vacancy colour centre in diamond. *Physics Reports*, 528(1):1–45, 2013.

[77] Marcus W Doherty, Viktor V Struzhkin, David A Simpson, Liam P McGuinness, Yufei Meng, Alastair Stacey, Timothy J Karle, Russell J Hemley, Neil B Manson, Lloyd CL Hollenberg, et al. Electronic properties and metrology applications of the diamond NV$^-$ center under pressure. *Physical Review Letters*, 112(4):047601, 2014.

[78] MW Doherty, SD Bennett, M Markham, DJ Twitchen, and NB Manson. Phonon-induced population dynamics and intersystem crossing in nitrogen-vacancy centers. *Physical Review Letters*, 114(14):145502, 2015.

[79] AP Drozdov, MI Eremets, IA Troyan, Vadim Ksenofontov, and Sergii I Shylin. Conventional superconductivity at 203 kelvin at high pressures in the sulfur hydride system. *Nature*, 525(7567):73–76, 2015.

[80] AP Drozdov, PP Kong, VS Minkov, SP Besedin, MA Kuzovnikov, S Mozaffari, L Balicas, FF Balakirev, DE Graf, VB Prakapenka, et al. Superconductivity at 250 K in lanthanum hydride under high pressures. *Nature*, 569(7757):528–531, 2019.

[81] Eugene F Dumitrescu, Alex J McCaskey, Gaute Hagen, Gustav R Jansen, Titus D Morris, T Papenbrock, Raphael C Pooser, David Jarvis Dean, and Pavel Lougovski. Cloud quantum computing of an atomic nucleus. *Physical Review Letters*, 120(21): 210501, 2018.

[82] A. Durand, T. Clua-Provost, F. Fabre, P. Kumar, J. Li, J. H. Edgar, P. Udvarhelyi, A. Gali, X. Marie, C. Robert, J. M. Gérard, B. Gil, G. Cassabois, and V. Jacques. Optically active spin defects in few-layer thick hexagonal boron nitride. *Phys. Rev. Lett.*, 131:116902, Sep 2023. doi:10.1103/PhysRevLett.131.116902.

[83] Andrew Eddins, Mario Motta, Tanvi P Gujarati, Sergey Bravyi, Antonio Mezzacapo, Charles Hadfield, and Sarah Sheldon. Doubling the size of quantum simulators by entanglement forging. *PRX Quantum*, 3(1):010309, 2022. URL `https://journals.aps.org/prxquantum/abstract/10.1103/PRXQuantum.3.010309`.

[84] Artur K Ekert, Carolina Moura Alves, Daniel KL Oi, Michał Horodecki, Paweł Horodecki, and Leong Chuan Kwek. Direct estimations of linear and nonlinear functionals of a quantum state. *Physical Review Letters*, 88(21):217901, 2002. doi:10.1103/PhysRevLett.88.217901.

[85] Vincent E Elfving, Benno W Broer, Mark Webber, Jacob Gavartin, Mathew D Halls, K Patrick Lorton, and A Bochevarov. How will quantum computers provide an industrially relevant computational advantage in quantum chemistry? *arXiv preprint arXiv:2009.12472*, 2020.

[86] Vincent E Elfving, Marta Millaruelo, José A Gámez, and Christian Gogolin. Simulating quantum chemistry in the seniority-zero space on qubit-based quantum computers. *Physical Review A*, 103(3):032605, 2021.

[87] Suguru Endo, Simon C Benjamin, and Ying Li. Practical quantum error mitigation for near-future applications. *Physical Review X*, 8(3):031027, 2018.

[88] Suguru Endo, Zhenyu Cai, Simon C Benjamin, and Xiao Yuan. Hybrid quantum-classical algorithms and quantum error mitigation. *Journal of the Physical Society of Japan*, 90(3):032001, 2021.

[89] Ethan N Epperly, Lin Lin, and Yuji Nakatsukasa. A theory of quantum subspace diagonalization. *SIAM Journal on Matrix Analysis and Applications*, 43(3):1263–1290, 2022.

[90] Mikhail I Eremets, Vasily S Minkov, Alexander P Drozdov, PP Kong, Vadim Ksenofontov, Sergii I Shylin, Sergey L Bud'ko, Ruslan Prozorov, Fedor F Balakirev, Dan Sun, et al. High-temperature superconductivity in hydrides: experimental evidence and details. *Journal of Superconductivity and Novel Magnetism*, 35(4):965–977, 2022.

[91] Stefan Ernst, Patrick J Scheidegger, Simon Diesch, and Christian L Degen. Modeling temperature-dependent population dynamics in the excited state of the nitrogen-vacancy center in diamond. *Physical Review B*, 108(8):085203, 2023.

[92] Dmitry A Fedorov, Matthew J Otten, Stephen K Gray, and Yuri Alexeev. Ab initio molecular dynamics on quantum computers. *The Journal of Chemical Physics*, 154 (16):164103, 2021.

[93] Dmitry A Fedorov, Yuri Alexeev, Stephen K Gray, and Matthew Otten. Unitary selective coupled-cluster method. *Quantum*, 6:703, 2022.

[94] Ran Fischer, Andrey Jarmola, Pauli Kehayias, and Dmitry Budker. Optical polarization of nuclear ensembles in diamond. *Physical Review B*, 87(12):125207, 2013.

[95] WMC Foulkes, Lubos Mitas, RJ Needs, and Guna Rajagopal. Quantum monte carlo simulations of solids. *Reviews of Modern Physics*, 73(1):33, 2001. doi:10.1103/RevModPhys.73.33.

[96] Xingyu Gao, Sumukh Vaidya, Kejun Li, Peng Ju, Boyang Jiang, Zhujing Xu, Andres E Llacsahuanga Allcca, Kunhong Shen, Takashi Taniguchi, Kenji Watanabe, et al. Nuclear spin polarization and control in hexagonal boron nitride. *Nature Materials*, 21(9):1024–1028, 2022.

[97] Paolo Giannozzi, Stefano Baroni, Nicola Bonini, Matteo Calandra, Roberto Car, Carlo Cavazzoni, Davide Ceresoli, Guido L Chiarotti, Matteo Cococcioni, Ismaila Dabo, et al. Quantum espresso: a modular and open-source software project for quantum simulations of materials. *Journal of Physics: Condensed Matter*, 21(39):395502, 2009.

[98] Paolo Giannozzi, Oliviero Andreussi, Thomas Brumme, Oana Bunau, M Buongiorno Nardelli, Matteo Calandra, Roberto Car, Carlo Cavazzoni, Davide Ceresoli, Matteo Cococcioni, et al. Advanced capabilities for materials modelling with quantum espresso. *Journal of physics: Condensed matter*, 29(46):465901, 2017. URL `https://iopscience.iop.org/article/10.1088/1361-648X/aa8f79/meta?casa_token=4_H53R5jMkAAAAAA:qN-7KBJSYdB7iVsbF3DPL1JTzO512f1q3fxvsIodt5SOlxVeHwl3JPMSPL85tT-kZcna5PmvaSU5o4RsxxI`.

[99] Tudor Giurgica-Tiron, Yousef Hindy, Ryan LaRose, Andrea Mari, and William J Zeng. Digital zero noise extrapolation for quantum error mitigation. In *2020 IEEE International Conference on Quantum Computing and Engineering (QCE)*, pages 306–316. IEEE, 2020.

[100] Joshua Goings, Luning Zhao, Jacek Jakowski, Titus Morris, and Raphael Pooser. Molecular symmetry in vqe: A dual approach for trapped-ion simulations of benzene. In *2023 IEEE International Conference on Quantum Computing and Engineering (QCE)*, volume 2, pages 76–82. IEEE, 2023. doi:10.1109/QCE57702.2023.10187.

[101] Michael Lurie Goldman, MW Doherty, Alp Sipahigil, Norman Ying Yao, SD Bennett, NB Manson, Alexander Kubanek, and Mikhail D Lukin. State-selective intersystem crossing in nitrogen-vacancy centers. *Physical Review B*, 91(16):165201, 2015.

[102] Ruotian Gong, Guanghui He, Xingyu Gao, Peng Ju, Zhongyuan Liu, Bingtian Ye, Erik A Henriksen, Tongcang Li, and Chong Zu. Coherent dynamics of strongly interacting electronic spin defects in hexagonal boron nitride. *Nature Communications*, 14 (1):3299, 2023.

[103] Ruotian Gong, Xinyi Du, Eli Janzen, Vincent Liu, Zhongyuan Liu, Guanghui He, Bingtian Ye, Tongcang Li, Norman Y Yao, James H Edgar, et al. Isotope engineering for spin defects in van der waals materials. *Nature Communications*, 15(1):104, 2024.

[104] Jérôme F. Gonthier, Maxwell D. Radin, Corneliu Buda, Eric J. Doskocil, Clena M. Abuan, and Jhonathan Romero. Measurements as a roadblock to near-term practical quantum advantage in chemistry: Resource analysis. *Phys. Rev. Res.*, 4:033154, Aug 2022. doi:10.1103/PhysRevResearch.4.033154. URL `https://link.aps.org/doi/10.1103/PhysRevResearch.4.033154`.

[105] Daniel Gottesman. *Stabilizer codes and quantum error correction.* California Institute of Technology, 1997.

[106] Andreas Gottscholl, Mehran Kianinia, Victor Soltamov, Sergei Orlinskii, Georgy Mamin, Carlo Bradac, Christian Kasper, Klaus Krambrock, Andreas Sperlich, Milos Toth, et al. Initialization and read-out of intrinsic spin defects in a van der waals crystal at room temperature. *Nature Materials*, 19(5):540–545, 2020.

[107] Andreas Gottscholl, Matthias Diez, Victor Soltamov, Christian Kasper, Dominik Krauße, Andreas Sperlich, Mehran Kianinia, Carlo Bradac, Igor Aharonovich, and Vladimir Dyakonov. Spin defects in hbn as promising temperature, pressure and magnetic field quantum sensors. *Nature Communications*, 12(1):4480, 2021.

[108] Andreas Gottscholl, Matthias Diez, Victor Soltamov, Christian Kasper, Andreas Sperlich, Mehran Kianinia, Carlo Bradac, Igor Aharonovich, and Vladimir Dyakonov. Room temperature coherent control of spin defects in hexagonal boron nitride. *Science Advances*, 7(14):eabf3630, 2021.

[109] Marco Govoni and Giulia Galli. Large scale gw calculations. *Journal of Chemical Theory and Computation*, 11(6):2680–2696, 2015.

[110] Harper R Grimsley, Daniel Claudino, Sophia E Economou, Edwin Barnes, and Nicholas J Mayhall. Is the trotterized uccsd ansatz chemically well-defined? *Journal of Chemical Theory and Computation*, 16(1):1–6, 2019.

[111] Harper R Grimsley, Sophia E Economou, Edwin Barnes, and Nicholas J Mayhall. An adaptive variational algorithm for exact molecular simulations on a quantum computer. *Nature Communications*, 10(1):1–9, 2019. URL `https://www.nature.com/articles/s41467-019-10988-2`.

[112] Harper R Grimsley, George S Barron, Edwin Barnes, Sophia E Economou, and Nicholas J Mayhall. Adaptive, problem-tailored variational quantum eigensolver mitigates rough parameter landscapes and barren plateaus. *npj Quantum Information*, 9 (1):19, 2023. doi:10.1038/s41534-023-00681-0.

[113] Lov K Grover. A fast quantum mechanical algorithm for database search. In *Proceedings of the twenty-eighth annual ACM symposium on Theory of computing*, pages 212–219, 1996.

[114] Kaiwen Gui, Teague Tomesh, Pranav Gokhale, Yunong Shi, Frederic T Chong, Margaret Martonosi, and Martin Suchara. Term grouping and travelling salesperson for digital quantum simulation. *arXiv preprint arXiv:2001.05983*, 2020. URL `https://arxiv.org/abs/2001.05983`.

[115] Cem Güney Torun, Philipp-Immanuel Schneider, Martin Hammerschmidt, Sven Burger, Joseph HD Munns, and Tim Schröder. Optimized diamond inverted nanocones for enhanced color center to fiber coupling. *arXiv e-prints*, pages arXiv–2105, 2021.

[116] Xinghan Guo, Nazar Delegan, Jonathan C Karsch, Zixi Li, Tianle Liu, Robert Shreiner, Amy Butcher, David D Awschalom, F Joseph Heremans, and Alexander A High. Tunable and transferable diamond membranes for integrated quantum technologies. *Nano Letters*, 21(24):10392–10399, 2021.

[117] Xinghan Guo, Mouzhe Xie, Anchita Addhya, Avery Linder, Uri Zvi, Tanvi D Deshmukh, Yuzi Liu, Ian N Hammock, Zixi Li, Clayton T DeVault, et al. Direct-bonded diamond membranes for heterogeneous quantum and electronic technologies. *arXiv preprint arXiv:2306.04408*, 2023.

[118] Francois Gygi. Architecture of qbox: A scalable first-principles molecular dynamics code. *IBM Journal of Research and Development*, 52(1.2):137–144, 2008.

[119] Liam T Hall, Jared H Cole, Charles D Hill, and Lloyd CL Hollenberg. Sensing of fluctuating nanoscale magnetic fields using nitrogen-vacancy centers in diamond. *Physical Review Letters*, 103(22):220802, 2009.

[120] Sharon Hammes-Schiffer and Giulia Galli. Integration of theory and experiment in the modelling of heterogeneous electrocatalysis. *Nature Energy*, 6(7):700–705, 2021. doi:10.1038/s41560-021-00827-4. URL `https://www.nature.com/articles/s41560-021-00827-4`.

[121] Andre He, Benjamin Nachman, Wibe A de Jong, and Christian W Bauer. Zero-noise extrapolation for quantum-gate error mitigation with identity insertions. *Physical Review A*, 102(1):012426, 2020.

[122] Guanghui He, Bingtian Ye, Ruotian Gong, Zhongyuan Liu, Kater W Murch, Norman Y Yao, and Chong Zu. Quasi-floquet prethermalization in a disordered dipolar spin ensemble in diamond. *Physical Review Letters*, 131(13):130401, 2023.

[123] Kade Head-Marsden, Johannes Flick, Christopher J Ciccarino, and Prineha Narang. Quantum information and algorithms for correlated quantum matter. *Chemical Reviews*, 121(5):3061–3120, 2020.

[124] Trygve Helgaker, Poul Jorgensen, and Jeppe Olsen. *Molecular electronic-structure theory.* John Wiley & Sons, 2013.

[125] Jonas Helsen, Sepehr Nezami, Matthew Reagor, and Michael Walter. Matchgate benchmarking: Scalable benchmarking of a continuous family of many-qubit gates. *Quantum*, 6:657, 2022. doi:10.22331/q-2022-02-21-657.

[126] Cornelius Hempel, Christine Maier, Jonathan Romero, Jarrod McClean, Thomas Monz, Heng Shen, Petar Jurcevic, Ben P Lanyon, Peter Love, Ryan Babbush, et al. Quantum chemistry calculations on a trapped-ion quantum simulator. *Physical Review X*, 8(3):031022, 2018.

[127] Loïc Henriet, Lucas Beguin, Adrien Signoles, Thierry Lahaye, Antoine Browaeys, Georges-Olivier Reymond, and Christophe Jurczak. Quantum computing with neutral atoms. *Quantum*, 4:327, 2020.

[128] Bas Hensen, Hannes Bernien, Anaïs E Dréau, Andreas Reiserer, Norbert Kalb, Machiel S Blok, Just Ruitenberg, Raymond FL Vermeulen, Raymond N Schouten, Carlos Abellán, et al. Loophole-free bell inequality violation using electron spins separated by 1.3 kilometres. *Nature*, 526(7575):682–686, 2015.

[129] Christian Hepp, Tina Müller, Victor Waselowski, Jonas N Becker, Benjamin Pingault, Hadwig Sternschulte, Doris Steinmüller-Nethl, Adam Gali, Jeronimo R Maze, Mete Atatüre, et al. Electronic structure of the silicon vacancy color center in diamond. *Physical Review Letters*, 112(3):036405, 2014.

[130] ED Herbschleb, H Kato, Y Maruyama, T Danjo, T Makino, S Yamasaki, I Ohki, K Hayashi, H Morishita, M Fujiwara, et al. Ultra-long coherence times amongst room-temperature solid-state spins. *Nature Communications*, 10(1):3766, 2019.

[131] SLN Hermans, Matteo Pompili, HKC Beukers, Simon Baier, Johannes Borregaard, and Ronald Hanson. Qubit teleportation between non-neighbouring nodes in a quantum network. *Nature*, 605(7911):663–668, 2022.

[132] Jochen Heyd, Gustavo E Scuseria, and Matthias Ernzerhof. Hybrid functionals based on a screened coulomb potential. *The Journal of Chemical Physics*, 118(18):8207–8215, 2003.

[133] Oscar Higgott, Daochen Wang, and Stephen Brierley. Variational quantum computation of excited states. *Quantum*, 3:156, 2019.

[134] Antoine Hilberer, Loïc Toraille, Cassandra Dailledouze, Marie-Pierre Adam, Liam Hanlon, Gunnar Weck, Martin Schmidt, Paul Loubeyre, and Jean-François Roch. Enabling quantum sensing under extreme pressure: Nitrogen-vacancy magnetometry up to 130 gpa. *Physical Review B*, 107(22):L220102, 2023.

[135] JE Hirsch and F Marsiglio. Absence of magnetic evidence for superconductivity in hydrides under high pressure. *Physica C: Superconductivity and its applications*, 584: 1353866, 2021.

[136] Kin On Ho, King Cho Wong, Man Yin Leung, Yiu Yung Pang, Wai Kuen Leung, King Yau Yip, Wei Zhang, Jianyu Xie, Swee K Goh, and Sen Yang. Recent developments of quantum sensing under pressurized environment using the nitrogen vacancy (nv) center in diamond. *Journal of Applied Physics*, 129(24), 2021.

[137] Pierre Hohenberg and Walter Kohn. Inhomogeneous electron gas. *Physical Review*, 136(3B):B864, 1964.

[138] S Hsieh, C Zu, T Mittiga, TJ Smart, F Machado, B Kobrin, TO Höhn, NZ Rui, et al. Imaging stress and magnetism at high pressures using a nanoscale quantum sensor. *Science*, 366(6471):1349–1354, 2019. doi:10.1126/science.aaw4352.

[139] Benchen Huang, Marco Govoni, and Giulia Galli. Simulating the electronic structure of spin defects on quantum computers. *PRX Quantum*, 3(1):010339, 2022. URL `https://doi.org/10.1103/PRXQuantum.3.010339`.

[140] Benchen Huang, Nan Sheng, Marco Govoni, and Giulia Galli. Quantum simulations of fermionic hamiltonians with efficient encoding and ansatz schemes. *Journal of Chemical Theory and Computation*, 19(5):1487–1498, 2023. URL `https://doi.org/10.1021/acs.jctc.2c01119`.

[141] Hsin-Yuan Huang, Richard Kueng, and John Preskill. Predicting many properties of a quantum system from very few measurements. *Nature Physics*, 16(10):1050–1057, 2020. doi:10.1038/s41567-020-0932-7.

[142] Renke Huang, Chenyang Li, and Francesco A Evangelista. Leveraging small-scale quantum computers with unitarily downfolded hamiltonians. *PRX Quantum*, 4(2): 020313, 2023.

[143] William J Huggins, Jarrod R McClean, Nicholas C Rubin, Zhang Jiang, Nathan Wiebe, K Birgitta Whaley, and Ryan Babbush. Efficient and noise resilient measurements for quantum chemistry on near-term quantum computers. *npj Quantum Information*, 7 (1):1–9, 2021. URL `https://www.nature.com/articles/s41534-020-00341-7`.

[144] William J Huggins, Bryan A O'Gorman, Nicholas C Rubin, David R Reichman, Ryan Babbush, and Joonho Lee. Unbiasing fermionic quantum monte carlo with a quantum computer. *Nature*, 603(7901):416–420, 2022. doi:10.1038/s41586-021-04351-z.

[145] Viktor Ivády, Gergely Barcza, Gergő Thiering, Song Li, Hanen Hamdi, Jyh-Pin Chou, Örs Legeza, and Adam Gali. Ab initio theory of the negatively charged boron vacancy qubit in hexagonal boron nitride. *npj Computational Materials*, 6(1):41, 2020.

[146] Takayuki Iwasaki, Yoshiyuki Miyamoto, Takashi Taniguchi, Petr Siyushev, Mathias H Metsch, Fedor Jelezko, and Mutsuko Hatano. Tin-vacancy quantum emitters in diamond. *Physical Review Letters*, 119(25):253601, 2017.

[147] Kay D Jahnke, Alp Sipahigil, Jan M Binder, Marcus W Doherty, Mathias Metsch, Lachlan J Rogers, Neil B Manson, Mikhail D Lukin, and Fedor Jelezko. Electron–phonon processes of the silicon-vacancy centre in diamond. *New Journal of Physics*, 17(4):043011, 2015.

[148] Eli Janzen, Hannah Schutte, Juliette Plo, Adrien Rousseau, Thierry Michel, Wilfried Desrat, Pierre Valvin, Vincent Jacques, Guillaume Cassabois, Bernard Gil, and James H. Edgar. Boron and nitrogen isotope effects on hexagonal boron nitride properties. *Advanced Materials*, page 2306033, 2023. doi:https://doi.org/10.1002/adma.202306033.

[149] Yu Jin, Marco Govoni, Gary Wolfowicz, Sean E Sullivan, F Joseph Heremans, David D Awschalom, and Giulia Galli. Photoluminescence spectra of point defects in semiconductors: Validation of first-principles calculations. *Physical Review Materials*, 5(8): 084603, 2021.

[150] Yu Jin, Marco Govoni, and Giulia Galli. Vibrationally resolved optical excitations of the nitrogen-vacancy center in diamond. *npj Computational Materials*, 8(1):238, 2022.

[151] Yu Jin, Victor Wen-zhe Yu, Marco Govoni, Andrew C Xu, and Giulia Galli. Excited state properties of point defects in semiconductors and insulators investigated with time-dependent density functional theory. *Journal of Chemical Theory and Computation*, 19(23):8689–8705, 2023.

[152] Robert O Jones. Density functional theory: Its origins, rise to prominence, and future. *Reviews of modern physics*, 87(3):897, 2015. doi:10.1103/RevModPhys.87.897.

[153] William L Jorgensen. The many roles of computation in drug discovery. *Science*, 303 (5665):1813–1818, 2004. doi:10.1126/science.1096361.

[154] Abhinav Kandala, Antonio Mezzacapo, Kristan Temme, Maika Takita, Markus Brink, Jerry M Chow, and Jay M Gambetta. Hardware-efficient variational quantum eigensolver for small molecules and quantum magnets. *Nature*, 549(7671):242–246, 2017.

[155] Abhinav Kandala, Kristan Temme, Antonio D Córcoles, Antonio Mezzacapo, Jerry M Chow, and Jay M Gambetta. Error mitigation extends the computational reach of a noisy quantum processor. *Nature*, 567(7749):491–495, 2019.

[156] Shu Kanno, Hajime Nakamura, Takao Kobayashi, Shigeki Gocho, Miho Hatanaka, Naoki Yamamoto, and Qi Gao. Quantum computing quantum monte carlo with hybrid tensor network toward electronic structure calculations of large-scale molecular and solid systems. *arXiv preprint arXiv:2303.18095*, 2023. doi:10.48550/arXiv.2303.18095.

[157] Youngseok Kim, Andrew Eddins, Sajant Anand, Ken Xuan Wei, Ewout Van Den Berg, Sami Rosenblatt, Hasan Nayfeh, Yantao Wu, Michael Zaletel, Kristan Temme, et al. Evidence for the utility of quantum computing before fault tolerance. *Nature*, 618 (7965):500–505, 2023.

[158] Neil P King, William Sheffler, Michael R Sawaya, Breanna S Vollmar, John P Sumida, Ingemar André, Tamir Gonen, Todd O Yeates, and David Baker. Computational design of self-assembling protein nanomaterials with atomic level accuracy. *Science*, 336(6085):1171–1174, 2012. doi:10.1126/science.1219364.

[159] William Kirby, Bryce Fuller, Charles Hadfield, and Antonio Mezzacapo. Second-quantized fermionic operators with polylogarithmic qubit and gate complexity. *PRX Quantum*, 3(2):020351, 2022. URL `https://journals.aps.org/prxquantum/abstract/10.1103/PRXQuantum.3.020351`.

[160] William Kirby, Mario Motta, and Antonio Mezzacapo. Exact and efficient lanczos method on a quantum computer. *Quantum*, 7:1018, 2023.

[161] William M Kirby, Sultana Hadi, Michael Kreshchuk, and Peter J Love. Quantum simulation of second-quantized hamiltonians in compact encoding. *Physical Review A*, 104(4):042607, 2021. URL `https://journals.aps.org/pra/abstract/10.1103/PhysRevA.104.042607`.

[162] Matthew Kiser, Anna Schroeder, Gian-Luca R Anselmetti, Chandan Kumar, Nikolaj Moll, Michael Streif, and Davide Vodola. Classical and quantum cost of measurement strategies for quantum-enhanced auxiliary field quantum monte carlo. *arXiv preprint arXiv:2312.09872*, 2023. doi:10.48550/arXiv.2312.09872.

[163] A Yu Kitaev. Quantum measurements and the abelian stabilizer problem. *arXiv preprint quant-ph/9511026*, 1995.

[164] Ian D Kivlichan, Craig Gidney, Dominic W Berry, Nathan Wiebe, Jarrod McClean, Wei Sun, Zhang Jiang, Nicholas Rubin, Austin Fowler, Alán Aspuru-Guzik, et al. Improved fault-tolerant quantum simulation of condensed-phase correlated electrons via trotterization. *Quantum*, 4:296, 2020. doi:10.22331/q-2020-07-16-296.

[165] Erik N Knall, Can M Knaut, Rivka Bekenstein, Daniel R Assumpcao, Pavel L Stroganov, Wenjie Gong, Yan Qi Huan, P-J Stas, Bartholomeus Machielse, Michelle Chalupnik, et al. Efficient source of shaped single photons based on an integrated diamond nanophotonic system. *Physical Review Letters*, 129(5):053603, 2022.

[166] B Kobrin, NL Figueroa, VM Acosta, JR Maze, et al. Optically enhanced electric field sensing using nitrogen-vacancy ensembles. *Physical Review Applied*, 16(2):024024, 2021.

[167] William F Koehl, Bob B Buckley, F Joseph Heremans, Greg Calusine, and David D Awschalom. Room temperature coherent control of defect spin qubits in silicon carbide. *Nature*, 479(7371):84–87, 2011.

[168] Dax Enshan Koh and Sabee Grewal. Classical shadows with noise. *Quantum*, 6:776, 2022. doi:10.22331/q-2022-08-16-776.

[169] Walter Kohn and Lu Jeu Sham. Self-consistent equations including exchange and correlation effects. *Physical Review*, 140(4A):A1133, 1965.

[170] Walter Kohn, Axel D Becke, and Robert G Parr. Density functional theory of electronic structure. *Journal of Physical Chemistry*, 100(31):12974–12980, 1996. doi:10.1021/jp960669l.

[171] Karen J. Morenz Korol, Kenny Choo, and Antonio Mezzacapo. Quantum approximation algorithms for many-body and electronic structure problems. *arXiv preprint arXiv:2111.08090*, 2021.

[172] Philip Krantz, Morten Kjaergaard, Fei Yan, Terry P Orlando, Simon Gustavsson, and William D Oliver. A quantum engineer's guide to superconducting qubits. *Applied physics reviews*, 6(2), 2019.

[173] H Kraus, VA Soltamov, F Fuchs, D Simin, A Sperlich, PG Baranov, GV Astakhov, and Vladimir Dyakonov. Magnetic field and temperature sensing with atomic-scale spin defects in silicon carbide. *Scientific reports*, 4(1):1–8, 2014. URL `https://www.nature.com/articles/srep05303`.

[174] Birgit Krummheuer, Vollrath Martin Axt, and Tilmann Kuhn. Theory of pure dephasing and the resulting absorption line shape in semiconductor quantum dots. *Physical Review B*, 65(19):195313, 2002.

[175] Georg Kucsko, Peter C Maurer, Norman Ying Yao, MICHAEL Kubo, Hyun Jong Noh, Po Kam Lo, Hongkun Park, and Mikhail D Lukin. Nanometre-scale thermometry in a living cell. *Nature*, 500(7460):54–58, 2013.

[176] Kazuhiro Kuruma, Benjamin Pingault, Cleaven Chia, Dylan Renaud, Patrick Hoffmann, Satoshi Iwamoto, Carsten Ronning, and Marko Lončar. Coupling of a single tin-vacancy center to a photonic crystal cavity in diamond. *Applied Physics Letters*, 118(23), 2021.

[177] Kazuhiro Kuruma, Benjamin Pingault, Cleaven Chia, Michael Haas, Graham D Joe, Daniel Rimoli Assumpcao, Sophie Weiyi Ding, Chang Jin, CJ Xin, Matthew Yeh, et al. Engineering phonon-qubit interactions using phononic crystals. *arXiv preprint arXiv:2310.06236*, 2023.

[178] Thaddeus D Ladd, Fedor Jelezko, Raymond Laflamme, Yasunobu Nakamura, Christopher Monroe, and Jeremy Lloyd O'Brien. Quantum computers. *Nature*, 464(7285): 45–53, 2010. URL `https://www.nature.com/articles/nature08812`.

[179] Robert A Lang, Ilya G Ryabinkin, and Artur F Izmaylov. Unitary transformation of the electronic hamiltonian with an exact quadratic truncation of the baker-campbell-hausdorff expansion. *Journal of Chemical Theory and Computation*, 17(1):66–78, 2020. URL `https://pubs.acs.org/doi/full/10.1021/acs.jctc.0c00170`.

[180] Dongho Lee, Wennie Wang, Chenyu Zhou, Xiao Tong, Mingzhao Liu, Giulia Galli, and Kyoung-Shin Choi. The impact of surface composition on the interfacial energetics and photoelectrochemical properties of bivo 4. *Nature Energy*, 6(3):287–294, 2021.

[181] Joonho Lee, William J Huggins, Martin Head-Gordon, and K Birgitta Whaley. Generalized unitary coupled cluster wave functions for quantum computation. *Journal of Chemical Theory and Computation*, 15(1):311–324, 2018.

[182] Seunghoon Lee, Joonho Lee, Huanchen Zhai, Yu Tong, Alexander M Dalzell, Ashutosh Kumar, Phillip Helms, Johnnie Gray, Zhi-Hao Cui, Wenyuan Liu, et al. Evaluating the evidence for exponential quantum advantage in ground-state quantum chemistry. *Nature Communications*, 14(1):1952, 2023. doi:10.1038/s41467-023-37587-6.

[183] Margarita Lesik, Thomas Plisson, Loïc Toraille, Justine Renaud, Florent Occelli, Martin Schmidt, Olivier Salord, Anne Delobbe, Thierry Debuisschert, Loïc Rondin, et al. Magnetic measurements on micrometer-sized samples under high pressure using designed NV centers. *Science*, 366(6471):1359–1362, 2019.

[184] Bing Li, Cheng Ji, Wenge Yang, Junyue Wang, Ke Yang, Ruqing Xu, Wenjun Liu, Zhonghou Cai, Jiuhua Chen, and Ho-kwang Mao. Diamond anvil cell behavior up to 4 Mbar. *Proceedings of the National Academy of Sciences*, 115(8):1713–1717, 2018.

[185] Kejun Li, Vsevolod D Dergachev, Ilya D Dergachev, Shimin Zhang, Sergey A Varganov, and Yuan Ping. Excited-state dynamics and optically detected magnetic resonance of solid-state spin defects from first principles. *arXiv preprint arXiv:2404.05917*, 2024.

[186] Xiaoying Li, Paul L Voss, Jay E Sharping, and Prem Kumar. Optical-fiber source of polarization-entangled photons in the 1550 nm telecom band. *Physical Review Letters*, 94(5):053601, 2005.

[187] Ying Li and Simon C Benjamin. Efficient variational quantum simulator incorporating active error minimization. *Physical Review X*, 7(2):021050, 2017.

[188] Zhaokai Li, Xiaomei Liu, Hefeng Wang, Sahel Ashhab, Jiangyu Cui, Hongwei Chen, Xinhua Peng, and Jiangfeng Du. Quantum simulation of resonant transitions for solving the eigenproblem of an effective water hamiltonian. *Physical Review Letters*, 122(9):090504, 2019.

[189] Florian Libisch, Chen Huang, and Emily A Carter. Embedded correlated wavefunction schemes: Theory and applications. *Accounts of chemical research*, 47(9):2768–2775, 2014.

[190] Boeri Lilia, Richard Hennig, Peter Hirschfeld, Gianni Profeta, Antonio Sanna, Eva Zurek, Warren E Pickett, Maximilian Amsler, Ranga Dias, Mikhail I Eremets, et al. The 2021 room-temperature superconductivity roadmap. *Journal of Physics: Condensed Matter*, 34(18):183002, 2022.

[191] Lin Lin and Yu Tong. Heisenberg-limited ground-state energy estimation for early fault-tolerant quantum computers. *PRX Quantum*, 3(1):010318, 2022. URL `https://journals.aps.org/prxquantum/pdf/10.1103/PRXQuantum.3.010318`.

[192] Xiaoqian Lin, Xiu Li, and Xubo Lin. A review on applications of computational methods in drug screening and design. *Molecules*, 25(6):1375, 2020. doi:10.3390/molecules25061375.

[193] Junzi Liu and Lan Cheng. Unitary coupled-cluster based self-consistent polarization propagator theory: A quadratic unitary coupled-cluster singles and doubles scheme. *The Journal of Chemical Physics*, 155(17):174102, 2021.

[194] Kristina S Liu, Alex Henning, Markus W Heindl, Robin D Allert, Johannes D Bartl, Ian D Sharp, Roberto Rizzato, and Dominik B Bucher. Surface nmr using quantum sensors in diamond. *Proceedings of the National Academy of Sciences*, 119(5): e2111607119, 2022.

[195] Mingzhe Liu, Xin Zhao, Tianyu Xie, Shaoyi Xu, Fazhan Shi, and Chang-Kui Duan. First-principles investigation of the impact of stress and lattice vibration on the hyperfine interactions of the nitrogen-vacancy center in diamond. *Physical Review B*, 108 (15):155150, 2023.

[196] Wei Liu, Zhi-Peng Li, Yuan-Ze Yang, Shang Yu, Yu Meng, Zhao-An Wang, Ze-Cheng Li, Nai-Jie Guo, Fei-Fei Yan, Qiang Li, et al. Temperature-dependent energy-level shifts of spin defects in hexagonal boron nitride. *ACS Photonics*, 8(7):1889–1895, 2021.

[197] Seth Lloyd. Universal quantum simulators. *Science*, 273(5278):1073–1078, 1996.

[198] Daniel Loss and David P DiVincenzo. Quantum computation with quantum dots. *Physical Review A*, 57(1):120, 1998.

[199] Paul Loubeyre, Florent Occelli, and Paul Dumas. Synchrotron infrared spectroscopic evidence of the probable transition to metal hydrogen. *Nature*, 577(7792):631–635, 2020.

[200] Guang Hao Low. Classical shadows of fermions with particle number symmetry. *arXiv preprint arXiv:2208.08964*, 2022. doi:10.48550/arXiv.2208.08964.

[201] Guang Hao Low and Isaac L Chuang. Optimal hamiltonian simulation by quantum signal processing. *Physical review letters*, 118(1):010501, 2017.

[202] He Ma, Marco Govoni, Francois Gygi, and Giulia Galli. A finite-field approach for gw calculations beyond the random phase approximation. *Journal of chemical theory and computation*, 15(1):154–164, 2018.

[203] He Ma, Marco Govoni, and Giulia Galli. Quantum simulations of materials on near-term quantum computers. *npj Computational Materials*, 6(1):85, 2020. URL `https://doi.org/10.1038/s41524-020-00353-z`.

[204] He Ma, Nan Sheng, Marco Govoni, and Giulia Galli. Quantum embedding theory for strongly correlated states in materials. *Journal of Chemical Theory and Computation*, 17(4):2116–2125, 2021. URL `https://doi.org/10.1021/acs.jctc.0c01258`.

[205] Liang Ma, Kui Wang, Yu Xie, Xin Yang, Yingying Wang, Mi Zhou, Hanyu Liu, Xiaohui Yu, Yongsheng Zhao, Hongbo Wang, et al. High-temperature superconducting phase in clathrate calcium hydride CaH_6 up to 215 K at a pressure of 172 GPa. *Physical Review Letters*, 128(16):167001, 2022.

[206] Filip B Maciejewski, Zoltán Zimborás, and Michał Oszmaniec. Mitigation of readout noise in near-term quantum devices by classical post-processing based on detector tomography. *Quantum*, 4:257, 2020. URL `https://quantum-journal.org/papers/q-2020-04-24-257/`.

[207] Ankit Mahajan and Sandeep Sharma. Efficient local energy evaluation for multi-slater wave functions in orbital space quantum monte carlo. *The Journal of Chemical Physics*, 153(19), 2020. doi:https://doi.org/10.1063/5.0025055.

[208] Ankit Mahajan and Sandeep Sharma. Taming the sign problem in auxiliary-field quantum monte carlo using accurate wave functions. *Journal of Chemical Theory and Computation*, 17(8):4786–4798, 2021. doi:10.1021/acs.jctc.1c00371.

[209] Ho-Kwang Mao, Xiao-Jia Chen, Yang Ding, Bing Li, and Lin Wang. Solids, liquids, and gases under high pressure. *Reviews of Modern Physics*, 90(1):015007, 2018.

[210] Jesús Arjona Martínez, Ryan A Parker, Kevin C Chen, Carola M Purser, Linsen Li, Cathryn P Michaels, Alexander M Stramma, Romain Debroux, Isaac B Harris, Martin Hayhurst Appel, et al. Photonic indistinguishability of the tin-vacancy center in nanostructured diamond. *Physical Review Letters*, 129(17):173603, 2022.

[211] Nikhil Mathur, Arunabh Mukherjee, Xingyu Gao, Jialun Luo, Brendan A McCullian, Tongcang Li, A Nick Vamivakas, and Gregory D Fuchs. Excited-state spin-resonance spectroscopy of vb- defect centers in hexagonal boron nitride. *Nature Communications*, 13(1):3233, 2022.

[212] Jeronimo R Maze, Paul L Stanwix, James S Hodges, Seungpyo Hong, Jacob M Taylor, Paola Cappellaro, Liang Jiang, MV Gurudev Dutt, Emre Togan, AS Zibrov, et al. Nanoscale magnetic sensing with an individual electronic spin in diamond. *Nature*, 455(7213):644–647, 2008.

[213] Jeronimo R Maze, Adam Gali, Emre Togan, Yiwen Chu, Alexei Trifonov, Efthimios Kaxiras, and Mikhail D Lukin. Properties of nitrogen-vacancy centers in diamond: the group theoretic approach. *New Journal of Physics*, 13(2):025025, 2011.

[214] Guglielmo Mazzola. Quantum computing for chemistry and physics applications from a monte carlo perspective. *The Journal of Chemical Physics*, 160(1), 2024. URL `10.1063/5.0173591`.

[215] Guglielmo Mazzola and Giuseppe Carleo. Exponential challenges in unbiasing quantum monte carlo algorithms with quantum computers. *arXiv preprint arXiv:2205.09203*, 2022. doi:10.48550/arXiv.2205.09203.

[216] Sam McArdle, Xiao Yuan, and Simon Benjamin. Error-mitigated digital quantum simulation. *Physical Review Letters*, 122(18):180501, 2019.

[217] Sam McArdle, Suguru Endo, Alán Aspuru-Guzik, Simon C Benjamin, and Xiao Yuan. Quantum computational chemistry. *Reviews of Modern Physics*, 92(1):015003, 2020. doi:https://doi.org/10.1103/RevModPhys.92.015003.

[218] Jarrod R McClean, Jonathan Romero, Ryan Babbush, and Alán Aspuru-Guzik. The theory of variational hybrid quantum-classical algorithms. *New Journal of Physics*, 18 (2):023023, 2016. doi:10.1088/1367-2630/18/2/023023.

[219] Jarrod R McClean, Mollie E Kimchi-Schwartz, Jonathan Carter, and Wibe A De Jong. Hybrid quantum-classical hierarchy for mitigation of decoherence and determination of excited states. *Physical Review A*, 95(4):042308, 2017. URL `https://journals.aps.org/pra/abstract/10.1103/PhysRevA.95.042308`.

[220] Jarrod R McClean, Sergio Boixo, Vadim N Smelyanskiy, Ryan Babbush, and Hartmut Neven. Barren plateaus in quantum neural network training landscapes. *Nature Communications*, 9(1):1–6, 2018. URL `https://www.nature.com/articles/s41467-018-07090-4`.

[221] Srujan Meesala, Young-Ik Sohn, Benjamin Pingault, Linbo Shao, Haig A Atikian, Jeffrey Holzgrafe, Mustafa Gündoğan, Camille Stavrakas, Alp Sipahigil, Cleaven Chia, et al. Strain engineering of the silicon-vacancy center in diamond. *Physical Review B*, 97(20):205444, 2018.

[222] Mekena Metcalf, Nicholas P Bauman, Karol Kowalski, and Wibe A De Jong. Resource-efficient chemistry on quantum computers with the variational quantum eigensolver and the double unitary coupled-cluster approach. *Journal of Chemical Theory and Computation*, 16(10):6165–6175, 2020. URL `https://pubs.acs.org/doi/abs/10.1021/acs.jctc.0c00421`.

[223] Jonathon P Misiewicz and Francesco A Evangelista. Implementation of the projective quantum eigensolver on a quantum computer. *arXiv preprint arXiv:2310.04520*, 2023. doi:10.48550/arXiv.2310.04520.

[224] Sourav Mondal and Alessandro Lunghi. Spin-phonon decoherence in solid-state paramagnetic defects from first principles. *npj Computational Materials*, 9(1):120, 2023.

[225] Ashley Montanaro and Stasja Stanisic. Accelerating variational quantum monte carlo using the variational quantum eigensolver. *arXiv preprint arXiv:2307.07719*, 2023. doi:10.48550/arXiv.2307.07719.

[226] Mario Motta and Shiwei Zhang. Ab initio computations of molecular systems by the auxiliary-field quantum monte carlo method. *Wiley Interdisciplinary Reviews: Computational Molecular Science*, 8(5):e1364, 2018. doi:10.1002/wcms.1364.

[227] Mario Motta, Chong Sun, Adrian TK Tan, Matthew J O'Rourke, Erika Ye, Austin J Minnich, Fernando GSL Brandao, and Garnet Kin-Lic Chan. Determining eigenstates and thermal states on a quantum computer using quantum imaginary time evolution. *Nature Physics*, 16(2):205–210, 2020. doi:10.1038/s41567-019-0704-4.

[228] Andrew E Naclerio and Piran R Kidambi. A review of scalable hexagonal boron nitride (h-bn) synthesis for present and future applications. *Advanced Materials*, 35 (6):2207374, 2023.

[229] Roland Nagy, Matthias Niethammer, Matthias Widmann, Yu-Chen Chen, Péter Udvarhelyi, Cristian Bonato, Jawad Ul Hassan, Robin Karhu, Ivan G Ivanov, Nguyen Tien Son, et al. High-fidelity spin and optical control of single silicon-vacancy centres in silicon carbide. *Nature Communications*, 10(1):1954, 2019.

[230] Takahito Nakajima and Kimihiko Hirao. The douglas–kroll–hess approach. *Chemical Reviews*, 112(1):385–402, 2012.

[231] Yunseong Nam, Jwo-Sy Chen, Neal C Pisenti, Kenneth Wright, Conor Delaney, Dmitri Maslov, Kenneth R Brown, Stewart Allen, Jason M Amini, Joel Apisdorf, et al. Ground-state energy estimation of the water molecule on a trapped-ion quantum computer. *npj Quantum Information*, 6(1):33, 2020.

[232] Yasuyuki Narita, Peng Wang, Keita Ikeda, Kazuki Oba, Yoshiyuki Miyamoto, Takashi Taniguchi, Shinobu Onoda, Mutsuko Hatano, and Takayuki Iwasaki. Multiple tin-vacancy centers in diamond with nearly identical photon frequency and linewidth. *Physical Review Applied*, 19(2):024061, 2023.

[233] Frank Neese, Frank Wennmohs, Ute Becker, and Christoph Riplinger. The orca quantum chemistry program package. *The Journal of Chemical Physics*, 152(22), 2020.

[234] RK Nesbet. Configuration interaction in orbital theories. *Proceedings of the Royal Society of London. Series A. Mathematical and Physical Sciences*, 230(1182):312–321, 1955.

[235] Ngoc Linh Nguyen, He Ma, Marco Govoni, Francois Gygi, and Giulia Galli. Finite-field approach to solving the bethe-salpeter equation. *Physical review letters*, 122(23): 237402, 2019.

[236] Michael A Nielsen and Isaac L Chuang. *Quantum computation and quantum information.* Cambridge university press, 2010.

[237] Thomas E. O'Brien, Stefano Polla, Nicholas C. Rubin, William J. Huggins, Sam McArdle, Sergio Boixo, Jarrod R. McClean, and Ryan Babbush. Error mitigation via verified phase estimation. *PRX Quantum*, 2:020317, May 2021. doi:10.1103/PRXQuantum.2.020317. URL `https://link.aps.org/doi/10.1103/PRXQuantum.2.020317`.

[238] Changhun Oh, Youngrong Lim, Yat Wong, Bill Fefferman, and Liang Jiang. Quantum-inspired classical algorithms for molecular vibronic spectra. *Nature Physics*, pages 1–7, 2024.

[239] R Orbach. Spin-lattice relaxation in rare-earth salts. *Proceedings of the Royal Society of London. Series A. Mathematical and Physical Sciences*, 264(1319):458–484, 1961.

[240] Matthew Otten and Stephen K Gray. Accounting for errors in quantum algorithms via individual error reduction. *npj Quantum Information*, 5(1):1–6, 2019.

[241] Peter JJ O'Malley, Ryan Babbush, Ian D Kivlichan, Jonathan Romero, Jarrod R McClean, Rami Barends, Julian Kelly, Pedram Roushan, Andrew Tranter, Nan Ding, et al. Scalable quantum simulation of molecular energies. *Physical Review X*, 6(3): 031007, 2016.

[242] W Paszkowicz, JB Pelka, M Knapp, T Szyszko, and SJAPA Podsiadlo. Lattice parameters and anisotropic thermal expansion of hexagonal boron nitride in the 10–297.5 k temperature range. *Applied Physics A*, 75:431–435, 2002.

[243] Edwin Pednault, John A Gunnels, Giacomo Nannicini, Lior Horesh, and Robert Wisnieff. Leveraging secondary storage to simulate deep 54-qubit sycamore circuits. *arXiv preprint arXiv:1910.09534*, 2019.

[244] John P Perdew, Kieron Burke, and Matthias Ernzerhof. Generalized gradient approximation made simple. *Physical Review Letters*, 77(18):3865, 1996. URL `https://journals.aps.org/prl/abstract/10.1103/PhysRevLett.77.3865`.

[245] Alberto Peruzzo, Jarrod McClean, Peter Shadbolt, Man-Hong Yung, Xiao-Qi Zhou, Peter J Love, Alán Aspuru-Guzik, and Jeremy L O'brien. A variational eigenvalue solver on a photonic quantum processor. *Nature Communications*, 5(1):4213, 2014. doi:10.1038/ncomms5213.

[246] Giulia Petrini, Ekaterina Moreva, Ettore Bernardi, Paolo Traina, Giulia Tomagra, Valentina Carabelli, Ivo Pietro Degiovanni, and Marco Genovese. Is a quantum biosensing revolution approaching? perspectives in nv-assisted current and thermal biosensing in living cells. *Advanced Quantum Technologies*, 3(12):2000066, 2020.

[247] Hung Q Pham, Runsheng Ouyang, and Dingshun Lv. Scalable quantum monte carlo with direct-product trial wave functions. *arXiv preprint arXiv:2306.15186*, 2023. doi:10.48550/arXiv.2306.15186.

[248] Benjamin Pingault, David-Dominik Jarausch, Christian Hepp, Lina Klintberg, Jonas N Becker, Matthew Markham, Christoph Becher, and Mete Atatüre. Coherent control of the silicon-vacancy spin in diamond. *Nature Communications*, 8(1):15579, 2017.

[249] Matteo Pompili, Sophie LN Hermans, Simon Baier, Hans KC Beukers, Peter C Humphreys, Raymond N Schouten, Raymond FL Vermeulen, Marijn J Tiggelman, Laura dos Santos Martins, Bas Dirkse, et al. Realization of a multinode quantum network of remote solid-state qubits. *Science*, 372(6539):259–264, 2021.

[250] Brandon Posey, Christopher Gropp, Boyd Wilson, Boyd McGeachie, Sanjay Padhi, Alexander Herzog, and Amy Apon. Addressing the challenges of executing a massive computational cluster in the cloud. In *2018 18th IEEE/ACM International Symposium on Cluster, Cloud and Grid Computing (CCGRID)*, pages 253–262, 2018. doi:10.1109/CCGRID.2018.00040.

[251] Michael JD Powell. A direct search optimization method that models the objective and constraint functions by linear interpolation. In *Advances in optimization and numerical analysis*, pages 51–67. Springer, 1994.

[252] John Preskill. Quantum computing in the nisq era and beyond. *Quantum*, 2:79, 2018.

[253] Qiskit contributors. Qiskit: An open-source framework for quantum computing, 2023.

[254] Google AI Quantum, Collaborators*†, Frank Arute, Kunal Arya, Ryan Babbush, Dave Bacon, Joseph C Bardin, Rami Barends, Sergio Boixo, Michael Broughton, Bob B Buckley, et al. Hartree-fock on a superconducting qubit quantum computer. *Science*, 369(6507):1084–1089, 2020.

[255] J Randall, CE Bradley, FV van der Gronden, Asier Galicia, MH Abobeih, Matthew Markham, DJ Twitchen, Francisco Machado, NY Yao, and Tim Hugo Taminiau. Many-body–localized discrete time crystal with a programmable spin-based quantum simulator. *Science*, 374(6574):1474–1478, 2021.

[256] S Reich, AC Ferrari, R Arenal, A Loiseau, I Bello, and J Robertson. Resonant raman scattering in cubic and hexagonal boron nitride. *Physical Review B*, 71(20):205201, 2005.

[257] Markus Reiher, Nathan Wiebe, Krysta M Svore, Dave Wecker, and Matthias Troyer. Elucidating reaction mechanisms on quantum computers. *Proceedings of the National Academy of Sciences*, 114(29):7555–7560, 2017. doi:10.1073/pnas.1619152114.

[258] Jeffrey R Reimers, Jun Shen, Mehran Kianinia, Carlo Bradac, Igor Aharonovich, Michael J Ford, and Piotr Piecuch. Photoluminescence, photophysics, and photochemistry of the v b- defect in hexagonal boron nitride. *Physical Review B*, 102(14): 144105, 2020.

[259] Shuliang Ren, Qinghai Tan, and Jun Zhang. Review on the quantum emitters in two-dimensional materials. *Journal of Semiconductors*, 40(7):071903, 2019.

[260] Daniel Riedel, Immo Söllner, Brendan J Shields, Sebastian Starosielec, Patrick Appel, Elke Neu, Patrick Maletinsky, and Richard J Warburton. Deterministic enhancement of coherent photon generation from a nitrogen-vacancy center in ultrapure diamond. *Physical Review X*, 7(3):031040, 2017.

[261] Lucio Robledo, Hannes Bernien, Toeno Van Der Sar, and Ronald Hanson. Spin dynamics in the optical cycle of single nitrogen-vacancy centres in diamond. *New Journal of Physics*, 13(2):025013, 2011.

[262] Lachlan J Rogers, Kay D Jahnke, Mathias H Metsch, Alp Sipahigil, Jan M Binder, Tokuyuki Teraji, Hitoshi Sumiya, Junichi Isoya, Mikhail D Lukin, Philip Hemmer, et al. All-optical initialization, readout, and coherent preparation of single silicon-vacancy spins in diamond. *Physical Review Letters*, 113(26):263602, 2014.

[263] LJ Rogers, RL McMurtrie, MJ Sellars, and NB Manson. Time-averaging within the excited state of the nitrogen-vacancy centre in diamond. *New Journal of Physics*, 11 (6):063007, 2009.

[264] Jonathan Romero, Ryan Babbush, Jarrod R McClean, Cornelius Hempel, Peter J Love, and Alán Aspuru-Guzik. Strategies for quantum computing molecular energies using the unitary coupled cluster ansatz. *Quantum Science and Technology*, 4(1):014008, 2018.

[265] Björn O Roos et al. The complete active space self-consistent field method and its applications in electronic structure calculations. *Advances in Chemical Physics*, 69: 399–445, 2007.

[266] Max Rossmannek, Panagiotis Kl Barkoutsos, Pauline J Ollitrault, and Ivano Tavernelli. Quantum hf/dft-embedding algorithms for electronic structure calculations: Scaling up to complex molecular systems. *The Journal of Chemical Physics*, 154(11):114105, 2021. URL `https://aip.scitation.org/doi/10.1063/5.0029536`.

[267] Shihao Ru, Zhengzhi Jiang, Haidong Liang, Jonathan Kenny, Hongbing Cai, Xiaodan Lyu, Robert Cernansky, Feifei Zhou, Yuzhe Yang, Kenji Watanabe, et al. Robust nuclear spin polarization via ground-state level anti-crossing of boron vacancy defects in hexagonal boron nitride. *arXiv preprint arXiv:2306.15960*, 2023.

[268] Maximilian Ruf, Matthew J Weaver, Suzanne B van Dam, and Ronald Hanson. Resonant excitation and purcell enhancement of coherent nitrogen-vacancy centers coupled to a fabry-perot microcavity. *Physical Review Applied*, 15(2):024049, 2021.

[269] Alison E Rugar, Constantin Dory, Shahriar Aghaeimeibodi, Haiyu Lu, Shuo Sun, Sattwik Deb Mishra, Zhi-Xun Shen, Nicholas A Melosh, and Jelena Vuckovic. Narrow-linewidth tin-vacancy centers in a diamond waveguide. *ACS Photonics*, 7(9):2356–2361, 2020.

[270] Alison E Rugar, Shahriar Aghaeimeibodi, Daniel Riedel, Constantin Dory, Haiyu Lu, Patrick J McQuade, Zhi-Xun Shen, Nicholas A Melosh, and Jelena Vučković. Quantum photonic interface for tin-vacancy centers in diamond. *Physical Review X*, 11(3):031021, 2021.

[271] Ilya G Ryabinkin, Tzu-Ching Yen, Scott N Genin, and Artur F Izmaylov. Qubit coupled cluster method: a systematic approach to quantum chemistry on a quantum computer. *Journal of Chemical Theory and Computation*, 14(12):6317–6326, 2018. doi:https://doi.org/10.1021/acs.jctc.8b00932.

[272] Ilya G Ryabinkin, Robert A Lang, Scott N Genin, and Artur F Izmaylov. Iterative qubit coupled cluster approach with efficient screening of generators. *Journal of Chemical Theory and Computation*, 16(2):1055–1063, 2020. URL `https://pubs.acs.org/doi/10.1021/acs.jctc.9b01084`.

[273] Ramiro Sagastizabal, Xavier Bonet-Monroig, Malay Singh, M Adriaan Rol, CC Bultink, Xiang Fu, CH Price, VP Ostroukh, N Muthusubramanian, A Bruno, et al. Experimental error mitigation via symmetry verification in a variational quantum eigensolver. *Physical Review A*, 100(1):010302, 2019.

[274] Sorawis Sangtawesin, Bo L Dwyer, Srikanth Srinivasan, James J Allred, Lila VH Rodgers, Kristiaan De Greve, Alastair Stacey, Nikolai Dontschuk, Kane M O'Donnell, Di Hu, et al. Origins of diamond surface noise probed by correlating single-spin measurements with surface spectroscopy. *Physical Review X*, 9(3):031052, 2019.

[275] Raffaele Santagati, Jianwei Wang, Antonio A Gentile, Stefano Paesani, Nathan Wiebe, Jarrod R McClean, Sam Morley-Short, Peter J Shadbolt, Damien Bonneau, Joshua W Silverstone, et al. Witnessing eigenstates for quantum simulation of hamiltonian spectra. *Science Advances*, 4(1):eaap9646, 2018.

[276] Nicolas PD Sawaya, Mikhail Smelyanskiy, Jarrod R McClean, and Alán Aspuru-Guzik. Error sensitivity to environmental noise in quantum circuits for chemical state preparation. *Journal of Chemical Theory and Computation*, 12(7):3097–3108, 2016.

[277] Maximilian Scheurer, Gian-Luca R Anselmetti, Oumarou Oumarou, Christian Gogolin, and Nicholas C Rubin. Tailored and externally corrected coupled cluster with quantum inputs. *arXiv preprint arXiv:2312.08110*, 2023. doi:10.48550/arXiv.2312.08110.

[278] Romana Schirhagl, Kevin Chang, Michael Loretz, and Christian L Degen. Nitrogen-vacancy centers in diamond: nanoscale sensors for physics and biology. *Annual Review of Physical Chemistry*, 65:83–105, 2014.

[279] Martin Schlipf and François Gygi. Optimization algorithm for the generation of oncv pseudopotentials. *Computer Physics Communications*, 196:36–44, 2015. URL `https://www.sciencedirect.com/science/article/pii/S0010465515001897`.

[280] Maria Schuld, Ville Bergholm, Christian Gogolin, Josh Izaac, and Nathan Killoran. Evaluating analytic gradients on quantum hardware. *Physical Review A*, 99(3):032331, 2019. URL `https://journals.aps.org/pra/abstract/10.1103/PhysRevA.99.032331`.

[281] Kushal Seetharam, Debopriyo Biswas, Crystal Noel, Andrew Risinger, Daiwei Zhu, Or Katz, Sambuddha Chattopadhyay, Marko Cetina, Christopher Monroe, Eugene Demler, et al. Digital quantum simulation of nmr experiments. *Science Advances*, 9 (46):eadh2594, 2023.

[282] Kanav Setia, Richard Chen, Julia E Rice, Antonio Mezzacapo, Marco Pistoia, and James D Whitfield. Reducing qubit requirements for quantum simulations using molecular point group symmetries. *Journal of Chemical Theory and Computation*, 16(10): 6091–6097, 2020. URL `https://doi.org/10.1021/acs.jctc.0c00113`.

[283] James Shee, John L Weber, David R Reichman, Richard A Friesner, and Shiwei Zhang. On the potentially transformative role of auxiliary-field quantum monte carlo in quantum chemistry: A highly accurate method for transition metals and beyond. *The Journal of Chemical Physics*, 158(14), 2023. doi:10.1063/5.0134009.

[284] Yu Shee, Pei-Kai Tsai, Cheng-Lin Hong, Hao-Chung Cheng, and Hsi-Sheng Goan. Qubit-efficient encoding scheme for quantum simulations of electronic structure. *Physical Review Research*, 4(2):023154, 2022.

[285] Nan Sheng, Christian Vorwerk, Marco Govoni, and Giulia Galli. Green's function formulation of quantum defect embedding theory. *Journal of Chemical Theory and Computation*, 18(6):3512–3522, 2022. doi:10.1021/acs.jctc.2c00240.

[286] Fazhan Shi, Qi Zhang, Pengfei Wang, Hongbin Sun, Jiarong Wang, Xing Rong, Ming Chen, Chenyong Ju, Friedemann Reinhard, Hongwei Chen, et al. Single-protein spin resonance spectroscopy under ambient conditions. *Science*, 347(6226):1135–1138, 2015. URL `https://www.science.org/doi/10.1126/science.aaa2253`.

[287] Fazhan Shi, Fei Kong, Pengju Zhao, Xiaojun Zhang, Ming Chen, Sanyou Chen, Qi Zhang, Mengqi Wang, Xiangyu Ye, Zhecheng Wang, et al. Single-dna electron spin resonance spectroscopy in aqueous solutions. *Nature Methods*, 15(9):697–699, 2018.

[288] Peter W Shor. Polynomial-time algorithms for prime factorization and discrete logarithms on a quantum computer. *SIAM Review*, 41(2):303–332, 1999.

[289] Jasminder S Sidhu, Siddarth K Joshi, Mustafa Gündoğan, Thomas Brougham, David Lowndes, Luca Mazzarella, Markus Krutzik, Sonali Mohapatra, Daniele Dequal, Giuseppe Vallone, et al. Advances in space quantum communications. *IET Quantum Communication*, 2(4):182–217, 2021.

[290] Alp Sipahigil, Ruffin E Evans, Denis D Sukachev, Michael J Burek, Johannes Borregaard, Mihir K Bhaskar, Christian T Nguyen, Jose L Pacheco, Haig A Atikian, Charles Meuwly, et al. An integrated diamond nanophotonics platform for quantum-optical networks. *Science*, 354(6314):847–850, 2016.

[291] Jonathan H Skone, Marco Govoni, and Giulia Galli. Self-consistent hybrid functional for condensed systems. *Physical Review B*, 89(19):195112, 2014.

[292] Scott E Smart and David A Mazziotti. Quantum-classical hybrid algorithm using an error-mitigating n-representability condition to compute the mott metal-insulator transition. *Physical Review A*, 100(2):022517, 2019.

[293] Scott E Smart and David A Mazziotti. Accelerated convergence of contracted quantum eigensolvers through a quasi-second-order, locally parameterized optimization. *Journal of Chemical Theory and Computation*, 18(9):5286–5296, 2022. doi:10.1021/acs.jctc.2c00446.

[294] Young-Ik Sohn, Srujan Meesala, Benjamin Pingault, Haig A Atikian, Jeffrey Holzgrafe, Mustafa Gündoğan, Camille Stavrakas, Megan J Stanley, Alp Sipahigil, Joonhee Choi, et al. Controlling the coherence of a diamond spin qubit through its strain environment. *Nature Communications*, 9(1):2012, 2018.

[295] Alexandre M Souza, Gonzalo A Alvarez, and Dieter Suter. Robust dynamical decoupling for quantum computing and quantum memory. *Physical Review Letters*, 106(24): 240501, 2011.

[296] ÖO Soykal, Pratibha Dev, and Sophia E Economou. Silicon vacancy center in 4 h-sic: Electronic structure and spin-photon interfaces. *Physical Review B*, 93(8):081207, 2016. URL `https://journals.aps.org/prb/abstract/10.1103/PhysRevB.93.081207`.

[297] James C Spall et al. Multivariate stochastic approximation using a simultaneous perturbation gradient approximation. *IEEE transactions on automatic control*, 37(3): 332–341, 1992.

[298] Nicholas H Stair and Francesco A Evangelista. Simulating many-body systems with a projective quantum eigensolver. *PRX Quantum*, 2(3):030301, 2021. URL `https://journals.aps.org/prxquantum/abstract/10.1103/PRXQuantum.2.030301`.

[299] P-J Stas, Yan Qi Huan, Bartholomeus Machielse, Erik N Knall, Aziza Suleymanzade, Benjamin Pingault, Madison Sutula, Sophie W Ding, Can M Knaut, Daniel R Assumpcao, et al. Robust multi-qubit quantum network node with integrated error detection. *Science*, 378(6619):557–560, 2022.

[300] LG Steele, Matthew Lawson, Michael Onyszczak, BT Bush, Ziwen Mei, AP Dioguardi, Jonathan King, Anna Parker, Alexander Pines, ST Weir, et al. Optically detected magnetic resonance of nitrogen vacancies in a diamond anvil cell using designer diamond anvils. *Applied Physics Letters*, 111(22):221903, 2017.

[301] Armands Strikis, Dayue Qin, Yanzhu Chen, Simon C. Benjamin, and Ying Li. Learning-based quantum error mitigation. *PRX Quantum*, 2:040330, 2021.

[302] Yuan Su, Dominic W Berry, Nathan Wiebe, Nicholas Rubin, and Ryan Babbush. Fault-tolerant quantum simulations of chemistry in first quantization. *PRX Quantum*, 2(4):040332, 2021. URL `https://doi.org/10.1103/PRXQuantum.2.040332`.

[303] Denis D Sukachev, Alp Sipahigil, Christian T Nguyen, Mihir K Bhaskar, Ruffin E Evans, Fedor Jelezko, and Mikhail D Lukin. Silicon-vacancy spin qubit in diamond: a quantum memory exceeding 10 ms with single-shot state readout. *Physical Review Letters*, 119(22):223602, 2017.

[304] Jianwei Sun, Adrienn Ruzsinszky, and John P Perdew. Strongly constrained and appropriately normed semilocal density functional. *Physical Review Letters*, 115(3): 036402, 2015.

[305] Jinzhao Sun, Xiao Yuan, Takahiro Tsunoda, Vlatko Vedral, Simon C Benjamin, and Suguru Endo. Mitigating realistic noise in practical noisy intermediate-scale quantum devices. *Physical Review Applied*, 15(3):034026, 2021.

[306] Qiming Sun, Timothy C Berkelbach, Nick S Blunt, George H Booth, Sheng Guo, Zhendong Li, Junzi Liu, James D McClain, Elvira R Sayfutyarova, Sandeep Sharma, et al. Pyscf: the python-based simulations of chemistry framework. *Wiley Interdisciplinary Reviews: Computational Molecular Science*, 8(1):e1340, 2018.

[307] K Syassen. Ruby under pressure. *High Pressure Research*, 28(2):75–126, 2008.

[308] Ewin Tang. A quantum-inspired classical algorithm for recommendation systems. In *Proceedings of the 51st Annual ACM SIGACT Symposium on Theory of Computing*, pages 217–228, 2019. URL `https://arxiv.org/abs/1807.04271`.

[309] Hao Tang, Ariel Rebekah Barr, Guoqing Wang, Paola Cappellaro, and Ju Li. First-principles calculation of the temperature-dependent transition energies in spin defects. *The Journal of Physical Chemistry Letters*, 14(13):3266–3273, 2023.

[310] Ho Lun Tang, VO Shkolnikov, George S Barron, Harper R Grimsley, Nicholas J Mayhall, Edwin Barnes, and Sophia E Economou. qubit-adapt-vqe: An adaptive algorithm

for constructing hardware-efficient ansätze on a quantum processor. *PRX Quantum*, 2(2):020310, 2021. URL `https://journals.aps.org/prxquantum/abstract/10.1103/PRXQuantum.2.020310`.

[311] Kristan Temme, Sergey Bravyi, and Jay M Gambetta. Error mitigation for short-depth quantum circuits. *Physical Review Letters*, 119(18):180509, 2017.

[312] Jean Philippe Tetienne, Loïc Rondin, Piernicola Spinicelli, Mayeul Chipaux, Thierry Debuisschert, Jean-François Roch, and Vincent Jacques. Magnetic-field-dependent photodynamics of single nv defects in diamond: an application to qualitative all-optical magnetic imaging. *New Journal of Physics*, 14(10):103033, 2012.

[313] Thomas N Theis and H-S Philip Wong. The end of moore's law: A new beginning for information technology. *Computing in science & engineering*, 19(2):41–50, 2017.

[314] Lucas Thiel, Zhe Wang, Märta A Tschudin, Dominik Rohner, Ignacio Gutiérrez-Lezama, Nicolas Ubrig, Marco Gibertini, Enrico Giannini, Alberto F Morpurgo, and Patrick Maletinsky. Probing magnetism in 2d materials at the nanoscale with single-spin microscopy. *Science*, 364(6444):973–976, 2019.

[315] Gergő Thiering and Adam Gali. Ab initio magneto-optical spectrum of group-iv vacancy color centers in diamond. *Physical Review X*, 8(2):021063, 2018. URL `https://journals.aps.org/prx/abstract/10.1103/PhysRevX.8.021063`.

[316] Nikolay V Tkachenko, Yu Zhang, Lukasz Cincio, Alexander I Boldyrev, Sergei Tretiak, and Pavel A Dub. Quantum davidson algorithm for excited states. *arXiv preprint arXiv:2204.10741*, 2022. URL `https://arxiv.org/abs/2204.10741`.

[317] Emre Togan, Yiwen Chu, Alexei S Trifonov, Liang Jiang, Jeronimo Maze, Lilian Childress, MV Gurudev Dutt, Anders Søndberg Sørensen, Phillip R Hemmer, Alexander S Zibrov, et al. Quantum entanglement between an optical photon and a solid-state spin qubit. *Nature*, 466(7307):730–734, 2010.

[318] Natasha Tomm, Alisa Javadi, Nadia Olympia Antoniadis, Daniel Najer, Matthias Christian Löbl, Alexander Rolf Korsch, Rüdiger Schott, Sascha René Valentin, Andreas Dirk Wieck, Arne Ludwig, et al. A bright and fast source of coherent single photons. *Nature Nanotechnology*, 16(4):399–403, 2021.

[319] Matthew E Trusheim, Benjamin Pingault, Noel H Wan, Mustafa Gündoğan, Lorenzo De Santis, Romain Debroux, Dorian Gangloff, Carola Purser, Kevin C Chen, Michael Walsh, et al. Transform-limited photons from a coherent tin-vacancy spin in diamond. *Physical Review Letters*, 124(2):023602, 2020.

[320] Péter Udvarhelyi, Tristan Clua-Provost, Alrik Durand, Jiahan Li, James H Edgar, Bernard Gil, Guillaume Cassabois, Vincent Jacques, and Adam Gali. A planar defect spin sensor in a two-dimensional material susceptible to strain and electric fields. *npj Computational Materials*, 9(1):150, 2023.

[321] Alexey Uvarov, Jacob D Biamonte, and Dmitry Yudin. Variational quantum eigensolver for frustrated quantum systems. *Physical Review B*, 102(7):075104, 2020. doi:10.1103/PhysRevB.102.075104.

[322] Sumukh Vaidya, Xingyu Gao, Saakshi Dikshit, Igor Aharonovich, and Tongcang Li. Quantum sensing and imaging with spin defects in hexagonal boron nitride. *Advances in Physics: X*, 8(1):2206049, 2023.

[323] Daniel A Vajner, Lucas Rickert, Timm Gao, Koray Kaymazlar, and Tobias Heindel. Quantum communication using semiconductor quantum dots. *Advanced Quantum Technologies*, 5(7):2100116, 2022.

[324] Konstantinos D Vogiatzis, Dongxia Ma, Jeppe Olsen, Laura Gagliardi, and Wibe A De Jong. Pushing configuration-interaction to the limit: Towards massively parallel mcscf calculations. *The Journal of Chemical Physics*, 147(18):184111, 2017.

[325] Christian Vorwerk, Nan Sheng, Marco Govoni, Benchen Huang, and Giulia Galli. Quantum embedding theories to simulate condensed systems on quantum computers. *Nature Computational Science*, 2(7):424–432, 2022. doi:10.1038/s43588-022-00279-0.

[326] Kianna Wan, William J Huggins, Joonho Lee, and Ryan Babbush. Matchgate shadows for fermionic quantum simulation. *Communications in Mathematical Physics*, pages 1–72, 2023. doi:10.1007/s00220-023-04844-0.

[327] Noel H Wan, Tsung-Ju Lu, Kevin C Chen, Michael P Walsh, Matthew E Trusheim, Lorenzo De Santis, Eric A Bersin, Isaac B Harris, Sara L Mouradian, Ian R Christen, et al. Large-scale integration of artificial atoms in hybrid photonic circuits. *Nature*, 583(7815):226–231, 2020.

[328] Dong Wang, Yang Ding, and Ho-Kwang Mao. Future study of dense superconducting hydrides at high pressure. *Materials*, 14(24):7563, 2021.

[329] Mengqi Wang, Yu Wang, Zhixian Liu, Ganyu Xu, Bo Yang, Pei Yu, Haoyu Sun, Xiangyu Ye, Jingwei Zhou, Alexander Goncharov, et al. Imaging magnetism evolution of magnetite to megabar pressure range with quantum sensors in diamond anvil cell. *arXiv preprint arXiv:2306.07840*, 2023.

[330] Samson Wang, Enrico Fontana, Marco Cerezo, Kunal Sharma, Akira Sone, Lukasz Cincio, and Patrick J Coles. Noise-induced barren plateaus in variational quantum algorithms. *Nature Communications*, 12(1):6961, 2021. doi:10.1038/s41467-021-27045-6.

[331] John L Weber, Hung Vuong, Richard A Friesner, and David R Reichman. The design of new practical constraints in auxiliary-field quantum monte carlo. *arXiv preprint arXiv:2306.09207*, 2023. doi:10.48550/arXiv.2306.09207.

[332] JR Weber, WF Koehl, JB Varley, A Janotti, BB Buckley, CG Van de Walle, and David D Awschalom. Quantum computing with defects. *Proceedings of the National Academy of Sciences*, 107(19):8513–8518, 2010.

[333] Gunnar Weck, Jean-Antoine Queyroux, Sandra Ninet, Frédéric Datchi, Mohamed Mezouar, and Paul Loubeyre. Evidence and stability field of FCC superionic water ice using static compression. *Physical Review Letters*, 128(16):165701, 2022.

[334] E Wigner and Pascual Jordan. Über das paulische äquivalenzverbot. *Z. Phys*, 47(631): 46, 1928.

[335] Gary Wolfowicz, F Joseph Heremans, Christopher P Anderson, Shun Kanai, Hosung Seo, Adam Gali, Giulia Galli, and David D Awschalom. Quantum guidelines for solid-state spin defects. *Nature Reviews Materials*, 6(10):906–925, 2021. doi:10.1038/s41578-021-00306-y.

[336] Bujiao Wu and Dax Enshan Koh. Error-mitigated fermionic classical shadows on noisy quantum devices. *arXiv preprint arXiv:2310.12726*, 2023. URL `https://arxiv.org/abs/2310.12726`.

[337] Shaoyi Xu, Mingzhe Liu, Tianyu Xie, Zhiyuan Zhao, Qian Shi, Pei Yu, Chang-Kui Duan, Fazhan Shi, and Jiangfeng Du. High-precision measurements and first-principles explanation of the temperature-dependent c 13 and n 14 hyperfine interactions of single nv- centers in diamond at room temperature. *Physical Review B*, 107(14):L140101, 2023.

[338] Xiaosi Xu and Ying Li. Quantum-assisted monte carlo algorithms for fermions. *Quantum*, 7:1072, 2023. doi:10.22331/q-2023-08-03-1072.

[339] Tzu-Ching Yen, Aadithya Ganeshram, and Artur F Izmaylov. Deterministic improvements of quantum measurements with grouping of compatible operators, non-local transformations, and covariance estimates. *npj Quantum Information*, 9(1):14, 2023.

[340] Juan Yin, Yuan Cao, Yu-Huai Li, Sheng-Kai Liao, Liang Zhang, Ji-Gang Ren, Wen-Qi Cai, Wei-Yue Liu, Bo Li, Hui Dai, et al. Satellite-based entanglement distribution over 1200 kilometers. *Science*, 356(6343):1140–1144, 2017.

[341] King Yau Yip, Kin On Ho, King Yiu Yu, Yang Chen, Wei Zhang, S Kasahara, Y Mizukami, T Shibauchi, Y Matsuda, Swee K Goh, et al. Measuring magnetic field texture in correlated electron systems under extreme conditions. *Science*, 366(6471): 1355–1359, 2019.

[342] Victor Wen-zhe Yu and Marco Govoni. Gpu acceleration of large-scale full-frequency gw calculations. *Journal of Chemical Theory and Computation*, 18(8):4690–4707, 2022. doi:10.1021/acs.jctc.2c00241. URL `https://doi.org/10.1021/acs.jctc.2c00241`. PMID: 35913080.

[343] Shiwei Zhang. 15 auxiliary-field quantum monte carlo for correlated electron systems. *Emergent Phenomena in Correlated Matter*, 2013.

[344] Yu Zhang, Lukasz Cincio, Christian FA Negre, Piotr Czarnik, Patrick J Coles, Petr M Anisimov, Susan M Mniszewski, Sergei Tretiak, and Pavel A Dub. Variational quantum eigensolver with reduced circuit complexity. *npj Quantum Information*, 8(1):96, 2022.

[345] Yukun Zhang, Yifei Huang, Jinzhao Sun, Dingshun Lv, and Xiao Yuan. Quantum computing quantum monte carlo. *arXiv preprint arXiv:2206.10431*, 2022. doi:10.48550/arXiv.2206.10431.

[346] Andrew Zhao and Akimasa Miyake. Group-theoretic error mitigation enabled by classical shadows and symmetries. *arXiv preprint arXiv:2310.03071*, 2023. doi:10.48550/arXiv.2310.03071.

[347] Andrew Zhao, Nicholas C Rubin, and Akimasa Miyake. Fermionic partial tomography via classical shadows. *Physical Review Letters*, 127(11):110504, 2021. doi:10.1103/PhysRevLett.127.110504.

[348] Chong Zu, Francisco Machado, Bingtian Ye, Soonwon Choi, Bryce Kobrin, Thomas Mittiga, Satcher Hsieh, Prabudhya Bhattacharyya, Matthew Markham, Dan Twitchen, et al. Emergent hydrodynamics in a strongly interacting dipolar spin ensemble. *Nature*, 597(7874):45–50, 2021.